Design and Numerical Simulation of the Real-time Particle Charge and Size Analyser

A thesis submitted for the degree of

Doctor of Philosophy

by

Lu Zhang (M.Sc.)

Faculty of Advanced Technology

University of Glamorgan

Sep. 2010

Abstract

The electrostatic charge and size distribution of aerosol particles play a very important role in many industrial applications. Due to the complexity and the probabilistic nature of the different charging mechanisms often acting simultaneously, it is difficult to theoretically predict the charge distribution of aerosol particles or even estimate the relative effect of the different mechanisms. Therefore, it is necessary to measure the size and also the bipolar charge distribution on aerosol particles.

The main aim of this research project was to design, implement and simulate a signal processing system for novel, fully functional measurement instrument capable of simultaneously measuring in real time the bipolar charge and size distribution of medical aerosols. The Particle Size and Charge Analyser (PSCA), investigated in this thesis, uses Phase Doppler Anemometry (PDA) technique. The PDA system was used to track the motion of charged particles in the presence of an electric field. By solving the equation of particle motion in a viscous medium combined with the simultaneous measurement of its size and velocity, the magnitude as well as the polarity of the particle charge can be obtained. Different signal processing systems in different excitation fields have been designed and implemented. These systems include: velocity estimation system using spectral analysis in DC excitation field, velocity estimation system based on Phase Locked Loop (PLL) technique working in DC as well as sine-wave excitation fields, velocity estimation system based on Quadrature Demodulation (QD) technique under sine-wave excitation method, velocity estimation system using spectral analysis in square-wave excitation field and phase shift estimation based on Hilbert transformation and correlation technique in both sine-wave and square-wave excitation fields. The performances of these systems were evaluated using Monte Carlo (MC) simulations obtained from the synthesized Doppler burst signals generated from the mathematical models implemented in MATLAB. The synthesized Doppler Burst Signal (DBS) was subsequently corrupted with the added Gaussian noise. Cross validation of the results was performed using hardware signal processing system employing Arbitrary Waveform Generator and also NASA simulator to further confirm the validity of the estimation.

It was concluded that the velocity estimation system based on spectral analysis in square-wave excitation field offers the best overall performance in terms of the working range, noise sensitivity and particle capture efficiency. The main reasons for the superiority of the square-wave excitation over the sine-wave excitation system are as follows: Firstly, in the square-wave field particles attain higher velocities and greater amplitudes of displacement, which increases their probability of crossing the measurement volume from various injection points. Secondly, the sine-wave excitation requires that the particle residence time in the measurement volume is at least equal to one period of the excitation, which effectively eliminates shorter and discontinuous burst. Thirdly, the signal processing based on FFT is less demanding in terms of the quality of DBS, which increases the likelihood of the detected particles to be successfully processed.

Acknowledgements

First of all, I would like to greatly thank my supervisor Dr. Janusz Kulon for his guidance and giving me the opportunity to undertake this Ph.D. course. His enthusiastic and open-minded approach has been a great stimulus for me throughout this project. His understanding, encouragement and patience help me to overcome the difficulties during the past years' study. I have learnt lots of from him and it will definetly benefit my future career.

I would also like to thank members of the Medical Electronics and Signal Processing Research Group at University of Glamorgan for their help and support, Dr Peter Plassman for his valuable suggestions on my PhD study, Dr Ralf Patz for arranging for me a loan of the TGA12101 100MHz Arbitrary Waveform Generator; Brian Wee and Stuart Watson for their assistance during my experimental work.

My appreciation extends to Dr. Senchun Chai, Dr. Bo Wang, Dr. Yunbo Zhao and Dr. Jian Sun for many stimulating discussions, particularly mathematical problems.

I am grateful to the University of Glamorgan for the financial support.

Lastly, special thanks to my parents, for their love, encouragement and self-giving support throughout these years.

Contents

List of Nomenclature

ACF	Autocorrelation Function
ACV	Autocovariance
CRB	Cramér Rao Bound
DBS	Doppler Burst Signal
DPI	Dry Powder Inhaler
DSP	Digital Signal Processing
E-SPART	Electrical Signal Particle Aerodynamic Relaxation Time
FFT	Fast Fourier Transform
FM	Frequency Modulation
HV	High Voltage
LDV	Laser Doppler Velocimeter
LPF	Low-pass loop Filter
MC	Monte Carlo
MDI	Metered Dose Inhaler
PCSA	Particle Charge and Size Analyser
PD	Phase Detector
PDA	Phase Doppler Anemometry
PLL	Phase Locked Loop
PMT	Photomultiplier Tube/ Photo Detector
QD	Quadrature Demodulation
VCO	Voltage Control Oscillator

List of Figures

List of Tables

List of Symbols

Symbol	*Name*	*Unit*
a	Particle acceleration	m/s^2
A	Amplitude of DBS	V
A_{pp}	Difference between maximum and minimum values of particle displacement in X direction	m
A_s	The effective cross-sectional area of the sensing volume	m^2
A_v	Amplitude of particle velocity	m/s
c_p	Particle concentration number	
C_d	Aerodynamic drag coefficient	-
C_c	Cunningham slip correction factor	-
d	Particle diamter	m
dN/dt	Particle count rate	*particles/s*
d_x	Measurement volume diameter in x direction	m
d_y	Measurement volume diameter in y direction	m
d_z	Measurement volume diameter in z direction	m
d_f	Beam waist diameter	m
d_L	Diameter of the laser beam waist before expansion	m
d_m	Beam diameter	m
D	Calibration factor	μm^{-1}
D_e	Distance between electrodes	m
D_i	Diameter of inlet	m

f_D	Doppler frequency	Hz
f_{drive}	Drive frequency of excitation field	Hz
f_L	Focal length of the front lens	m
f_s	Sampling frequency	Hz
Δf_s	Frequency resolution	Hz
G_k	Coefficient value of the interpolation curve	-
I_{DC}	Amplitude of the DC part of DBS	V
I_{AC}	Amplitude of the AC part of DBS	V
K_0	Gain of VCO	-
K_d	Gain of phase detector	-
$\mathbf{k}_1$, $\mathbf{k}_2$	Unit vectors in the direction of the incident beams	-
$\mathbf{k}_s$	Unit vector in the direction of the scattered light	-
M_p	DC component of the Signal	-
M	Number of fringes	-
M_{min}	Minimum number of fringes crossed by the particle motion in the measurement volume	-
M_x	Radius of the measurement volume in **X** direction	m
M_y	Radius of the measurement volume in **Y** direction	m
m	Mass of particle	kg
N	Number of Samples	-
N_0	Number concentration of the aerosol in particls per unit volume	$Particles/m^3$
n_{rel}	Relative refractive index	-
$n_{particle}$	Refractive index of particle	-
n_{medium}	Refractive index of medium	-

P_{signal}	Power of signal	W
P_{noise}	Power of noise	W
q	Particle charge	C
q_{GL}	Gaussian charge limit	C
q/m	Charge-to-mass ratio	C/kg
R_e	Reynolds number	-
S_{DC}	DC part of DBS	-
S_{AC}	AC part of DBS	-
S	Doppler Burst Signal	-
T	Period of the square-wave excitation field	s
T_s	Sampling period	s
T_{burst}	Time period of a burst	s
$T_{Residence}$	Particle residence time	s
t_0	Time slot of particle passing through the center of measurement volume	s
U_0	Amplitude of reference signal of PLL system	V
V_y	Particle velocity in **Y** direction	m/s
V_m	Mean flow velocity	m/s
V_{MV}	The measurement volume	m^3
$\mathbf{V}$	Particle velocity vector	-
$\mathbf{V_x}$	Particle velocity vector in **X** direction	-
$\mathbf{V_y}$	Particle velocity vector in **Y** direction	-
$\mathbf{x}$	Particle position in **X** direction	m
$\mathbf{x}_0$	Original particle position in **X** direction	m
x_{max}	Maximum value of particle displacement in X	m

	direction	
x_{min}	Minimum value of particle displacement in X direction	*m*
Y_2	Length of electrode	*m*
Y_3	Half length of electrode	*m*
λ	Wavelength of laser beam	*nm*
ρ	Particle density	kg/m^3
ρ_{air}	Air density	kg/m^3
μ_m	Electrical mobility of particle	m^2/Vs
φ	The scattering angle	*deg*
ψ	The elevation angle	*deg*
$\Delta\Phi$	Phase difference between DBSs generated by different photo detectors	*deg*
φ_0	Original phase of DBS	*deg*
γ	Angle between the velocity vector V and velocity component in Y direction	*deg*
ω_D	Doppler frequency	*rad/s*
ω_i	Angular frequency of input signal of PLL system	*rad/s*
ω_0	Angular frequency of reference signal of PLL system	*rad/s*
η	Viscosity of air	*kg/ms*
θ_i	Original phase of input signal of PLL system	*deg*
θ_0	Original phase of reference signal of PLL system	*deg*
θ_1	Instantaneous phase of input signal of PLL system	*deg*
θ_2	Instantaneous phase of reference signal of P LL system	*deg*
θ_e	Phase difference between input and reference	*deg*

	signals	
μ	Flow viscosity	m^2/s
$\sigma_n^2 = 0.01$	Noise variance	-

Chapter 1

Introduction

1.1 General Introduction

The drug delivery to the respiratory tract has become more and more important and effective method in the therapy of a variety of pulmonary diseases for the last 60 years. According to the recent statistics, there are more than 50 million patients taking inhaled therapy all over the world. It has been reported that the annual sales of medical inhalers, were approximately 6.5 billion USD in total in 2000. This amout is rapidly growing due to the increasing incidence of asthma as well as the wider employment of inhaled pharmaceuticals [1]. It is expected that the global pulmonary delivery market will grow up to 40 billion USD by 2013. Hence, there is little doubt of the importance of the investigation of the properties of aerosol particles generated by medical inhalers and its benefits to the general public.

The inhaled therapy is superior to the conventional methods because the drug can be transferred directly to the airways and its effects are more rapid. Since human lungs have large surface area and are able to rapidly absorb and transfer drug molecules into the blood stream, the lungs are an excellent entry port for the therapeutic aerosols produced by the medical devices. The efficacy of the medical aerosol is mainly determined by the amount of drug reaching the target location. It has been reported that typically, less than 20% of the total amount of drug in aerosol dose is delivered to the lower airways [2]. As shown by a number of experimental and theoretical studies [2], [3], usually the deposition of the medical aerosol in the lungs is not evenly distributed. Most of the aerosol particles remain in the extrathoracic and upper airways and thus contribute very little to the efficacy of the drug therapy. This part of aerosol is swallowed and subsequently absorbed in the gastrointestinal tract. In order to improve the medical efficacy, the amount of aerosol

deposited in the lungs is expected to be as large as possible with the decreased extrathoracic and upper airway depostion.

From the previous research, it has been shown that the dispersion and the deposition of the drug particles in the respiratory tract are affected by the following factors: anatomy of the respiratory tract, breathing patterns and characteristics of the inhaled particles such as size distribution, shape, density, hygroscopicity and electrical charge [4] [5]. The generation of therapeutic aerosols from the medical inhaler devices almost always results in charged aerosols. Before 1980, the researchers studying respiratory drug delivery didn't consider the effect of the electrostatic charge on particles. However, many studies over the last two decades have shown that the aerosol deposition changes as a function of electrostatic charge and size distribution [6]. It has been shown that the electrical charge and particle size can affect the particles' dispersion characteristic and significantly alter their respiratory deposition. Additionally, the practical significance of the electrostatic charge interactions on the functionality of therapeutic aerosols embraces most aspects of their processing and general use, including their formulation and manufacture and dosing reproducibility. Therefore, the characterization of pharmaceutical aerosols in terms of their electrical properties plays an increasingly important role in the development of drug administration devices by inhalation and prospective medications [7].

1.2 Medical Devices for Drug Delivery

Medical devices for drug delivery to the lungs are important in delivering high concentrations of drug with potential therapeutic effects directly into lung airways [9]. It can be classified into three different types, Metered-Dose Inhaler (MDIs), Dry-Powder Inhalers (DPIs) and nebulizers. MDIs and DPIs have been more popular medical devices for drug aerosol delivery because of ease of usage, small and compact size and the relative cost-effectiveness. The MDIs take about 70% and DPIs take about 20% of the whole market. The photographs of medical inhalers are shown in Fig. 1.1.

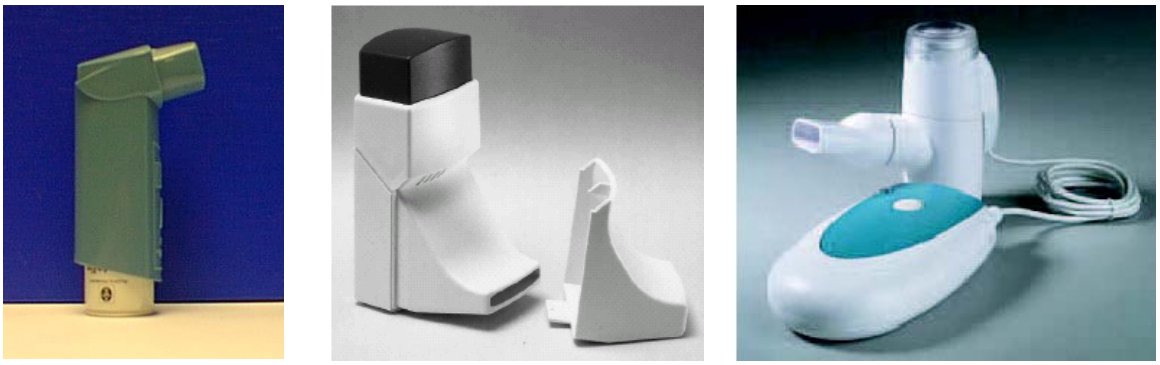

(a) MDI (b) DPI (c) Nebulizer

Fig. 1.1 Photographs of medical devices for drug delivery [10]

MDI is the most frequently used inhaler drug delivery device. It is composed of a reservoir (canister), which contains drug suspended or dissolved in liquefied gas propellant, a metering valve, spray actuator, which is next to the stem of metering valve. It comprises a twin orifice expansion chamber and spray nozzle to generate spray [10].

The generation of medical aerosol by an MDI is shown in Fig. 1.2. The canister contains the liquified propellent with medical drug in it. In the MDI, there is a valve which is used to deliver a known volume of the liquid under pressure. Next to the valve, there is a spray actuator. When the canister is pressed down into the actuator, the propellant in the canister discharges the liquid out at a high speed. Thus spray is produced by the spray nozzle in the spray actuator. Finally, the spray is dispersed into human's mouth and the medical aerosol travel into human's lung [10].

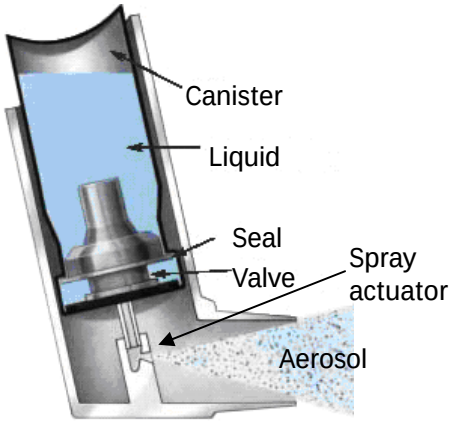

Fig. 1.2 Internal structure of MDI [11]

A DPI is a small-size, handy and portable inhaler device. It is composed of dose-metering, aerosolisation, deaggregation and adaptor. When the inhalation starts, it initiates the dispersion of particles. The pressure difference between the air contained in the powder and the motion of air passing over the powder is developed and then the powder is fluidized. Next, aggregates of carriers and drug particles are dispersed into primary particles. Ultimately, the particles move into patients' mouth through the adaptor [10].

Nebulizers have been used in medication since 19th century. The jet nebulizer is one of the nebulizers. The operating principle of it can be described as follows. A pressurized source supplies high pressure air flowing though a nozzle. The droplets are produced by disintegration of the liquid jet, called as atomization. The emitted droplet sizes depend on jet design, gas density, gas flow rate, surface tension and viscosity of drug solution [10].

The generation of therapeutic aerosols from the medical inhalers almost always results in charged aerosols [12]. It has been shown that there is a reduction in lung deposition of therapeutic drug from pressurized aerosol dispensers resulting from the static charge in plastic spacer devices [8]. The electrostatic charge is generated by the contact and separation of two dissimilar materials. The relative movement of particles with inhaler device surface provides ideal conditions for the development of charge by frictional contact or triboelectrification [13]. The mechanics of charge transfer and separation between two dissimilar surfaces are influenced by material properties, such as, particle size, shape, surface roughness, duration of contact, etc. and environmental conditions, such as, temperature and relative humidity [9], [14], [15].

1.3 Importance of the Electrostatic Charge on Medical Aerosols

The electrostatic charge and size distribution of aerosol particles play a very important role in many industrial applications, for instance, electrostatic painting, coating and printing, crop spraying, gas cleaning and many other fields. The specific charge of particle or droplet highly affects the transportation and the deposition of sprays and aerosols. It has been found that the drug particles' dispersion and deposition along the respiratory tract depend on several factors such as anatomy of the respiratory tract, breathing patterns and characteristics of the inhaled particles including size, shape, density,

hygroscopicity and electrostatic charge [16], [17]. Numerous studies have demonstrated that the electrostatic charge can affect the particles' dispersion characteristic and significantly alter their respiratory deposition [18], [19], [20], [21]. Besides the net charge, the polarity of the electrostatic charge also affects the dispersion and deposition of liquids and bulk powders [4]. There are several different charging mechanisms which play a role in the charging process during droplet and particle formation. For example, electric double layer charging or ionic charging, charging mechanism due to mechanical disruption of liquid surfaces, charging due to contact potentials between the liquid phase and solid surfaces during aerosolization, tibocharging, etc. [22]. However, due to the complexity and the probabilistic nature of different charging mechanisms often acting simultaneously, it is very difficult to predict theoretically the charge distribution of aerosol particles or even estimate the relative effect of the different mechanisms. It has become apparent that it is essential to be able to measure not only aerosols size distribution but also bipolar electrical charge profile. Such measurements are often needed in real time especially if the aerosol particles undergo rapid changes due to frequent collisions, evaporation, condensation, coagulation etc. Therefore, a non-invasive, fast and accurate experimental technique is vital to investigate the nature of aerosol electrostatics produced by medical inhalers.

1.4 Charged Particle Deposition in Human Lungs

Primary aerosol mechanisms in the transport and deposition of aerosols in human lungs consist of inertial impaction, sedimentation, diffusion and electrostatic forces. First, the inertial impaction. Particles with sufficient momentum will be affected by the centrifugal forces generated where the airway network changes direction rapidly. This mechanism is a function of Stokes number, which is directly proportional to particle size and particle velocity. This mechanism is primarily concerned in large airways (Extrathoracic and Upper bronchial regions) because of the high flow rates. Most of the large particles are deposited in these regions due to inertial impaction [6]. But for small particles, inertial impaction is not a significant mechanism. Second, the sedimentation. Because of the force of gravity in regions where the particles have a long residence time, particles of sufficient mass can be deposited. In smaller airways and alveolar regions,

sedimentation is a dominant mechanism with its maximum deposition effect in horizontal airways. Third, the diffusion. Particles of sub-micron size have a random Brownian motion due to molecular collisions with gas molecules. The movement of particles by Brownian motion can be regarded as a Markov random process [6]. The probability distribution of random distances is a function of the diffusion coefficient of the particles. For small particles, diffusion is an important mechanism. It plays a key role in the alveolar region, where distances are short and residence times comparatively long. Finally, the electrostatic forces. This mechanism concerns the effects of electrostatic forces due to the electrostatic charges. A mathematical model of lung deposition developed by Professor W. Balachandran's research group at Brunel University was used to quantify the effect of the electrostatic charge on the respiratory deposition [5], [23]. The study of particle deposition in the respiratory tract generally accounts for the space and image charge forces. The space charge is due to the mutual repulsion of particles, which is a function of concentration of particles and charge levels on the particles. The image charge force is the interaction of charged particles with the lung wall [24]. Particle whose size is larger than $5\mu m$ will be captured by the impaction and the sedimentation in the head and tracheo-bronchial region, i.e. the upper part of respiration system. It means that the smaller particles will play a dominant role in the aerosol deposition because the smaller ones can move deeper in human's respiratory system. Because of the smaller space in the deeper regions, particles are closer to airways and alveolar walls. Therefore, electrostatic charge significantly enhances the deposition.

As reported in [6], [23], [25], for particles with size larger than $5\mu m$, the electrostatic charge has no significant effect on the deposition. However, for smaller particles whose size is smaller than $5\mu m$, the charge becomes an important factor in the aerosol deposition [26], [27]. The relationship between particle charge and deposition (for $0.5\mu m$ diameter particle) is illustrated in Fig. 1.3 showing the results of the numerical modeling carried out at Brunel University. It can be seen that the deposition of $0.5\mu m$-diameter is enhanced as the charge becomes larger.

(a)

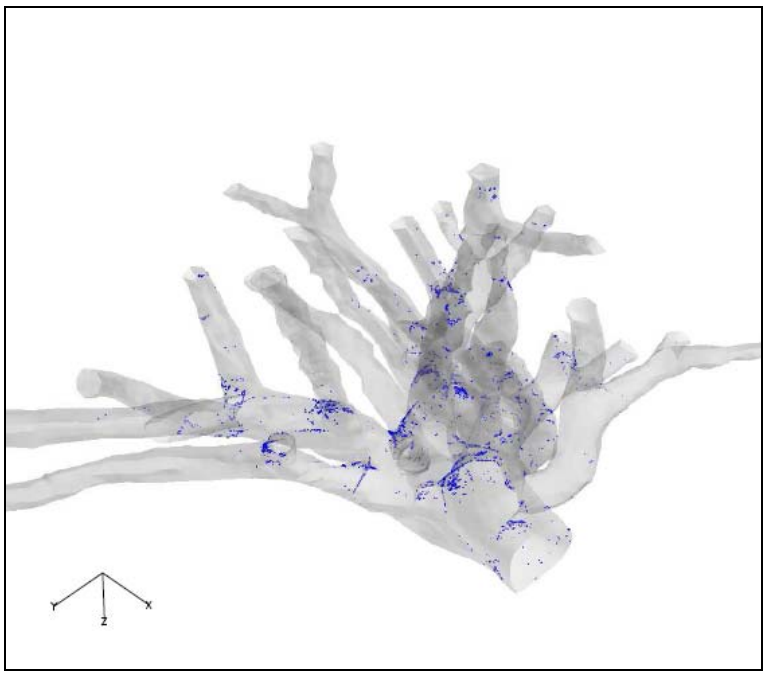

(b)

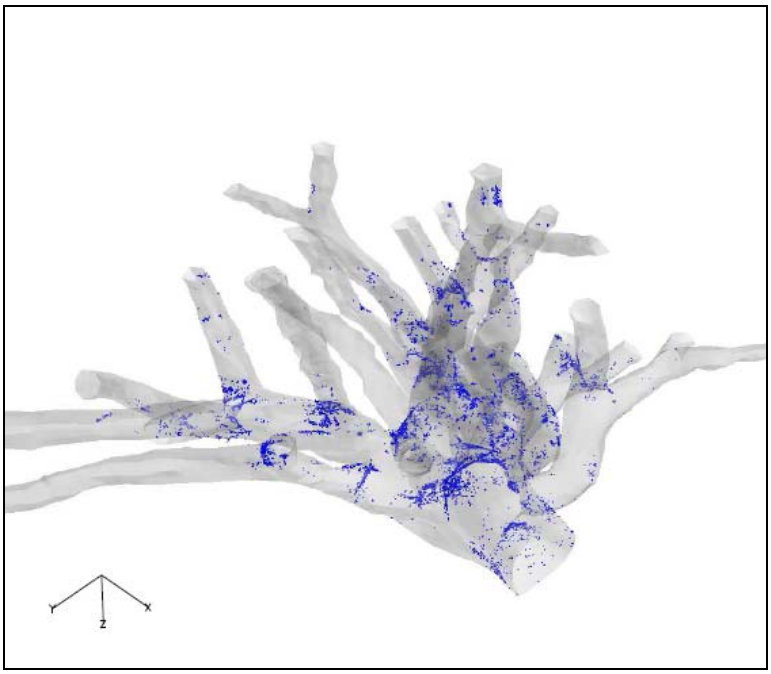

Fig.1.3 Local deposition of inhaled 0.5μm diameter charged particles in the right-upper reconstructed airway model (R_e=1750) (a) q=50e (b) q=200e [from 27]

1.5 Limitations of Existing Charge Measurement Techniques

The charge measurement techniques are divided into two different categories: static and dynamic. The principle of static measurement of particle charge is to transfer the charge to a capacitor and to measure the voltage developed [17]. This method is based on the equal electric potential of the capacitor and the particle. However, in practice, the capacitance of the capacitor is greater than the one of the particle. Therefore, most of the charge is transferred to the capacitor. Krupa and Jaworek [28] developed a system which measures the charge cumulatively by an orientated collecting wire. In their system, only large droplets (hundreds of μm in diameter) can be captured and subsequently counted. The charge measurement range of this system is limited to relatively highly charged particles. Greaves and Makin [29] proposed a method using coarse conducting grids to measure the droplets generated from an aerosol spray. This simple method is able to supply sufficient information on particle charge. The same principle was used on electrophotographic toner by Donivan and Laukaitis [9]. But only the unipolar charge could be measured since a mean charge was counted. In 1983, the simultaneous size and charge measurement technique combined with a size-selective device was implemented by Aldred [30]. But there is a problem, only the mean charge of aerosol can be measured. It means if an aerosol contains particles with equal total negative and positive charge, a result of zero total charge would be given. Some static methods employ induction to measure particle charge. Even if a particle doesn't touch the capacitor, image charge with opposite polarity will be induced. The induction has been widely used in the measurement of particle charge, such as the complete and incomplete Faraday cage. However, these methods are not suitable for measuring the bipolarly charged aerosol. Aiming to solve this problem, several instruments were designed, for instance, conducting probe, electrostatic cascade impactor and bipolar charge measurement system [9]. But these methods were still not satisfactory because they required very accurate aerosol injection into the instrument, the number of measured particles was limited or only total positive or negative charged aerosol could be measured [28]. The static methods can only measure the mean charge of populations of particles because it measures charge cumulatively. Additionally, only highly charged particles (much higher than a single electron) can be detected by static methods.

Compared to the static methods, dynamic methods are capable of measuring particles with small size and charge [8]. The dynamic methods require particle motion in an electric field. The Millikan's method was developed first and provided a method to obtain charge of electron by measuring a single droplet in an electric field. The main idea of Millikan's method is to suspend particles in an electrical and gravitational field. The charge is calculated from strength of the electric field when the drift particle velocity is zero. Compared to the single particle, the measurement of population of particles is more important. Small particles with small charge can be measured by analyzing electric mobility of a particle. In principle, the only method to measure particle mobility is to measure the response of a particle in an electric field. Daniel, Brackett and others developed several instruments based on this principle [8]. The main idea was to utilize the parallel plates to capture moving particles. Both magnitude and polarity of charge could be measured. At a low potential difference between the plates, however, some particles with low mobilities will be lost. The differential mobility analyser was designed and has been applied to singularly charged and ultrafine particles by Davison *et al*. [8]. The dead-time is a severe problem of sanning mobility analyser. Additionally, there is a compromise between speed and precision. The cumulative mobility analyser is the simplest mobility analyser. However, the dead-time of the instrument response is high. Until now, the Electronic Single Particle Aerodynamic Relaxation Time (E-SPART) Analyser is the only commercially available instrument for real-time simultaneous analysis of the aerodynamic size and both magnitude and polarity of electrostatic charge distributions of particles on a single particle basis. This instrument measures the particle size from the aerodynamic relaxation time of individual particles. Based on the analysis of charged particle motion in an electric field, the bipolar charge can be determined from particle velocity and diameter. This instrument has been used to measure the bipolarly charged toner first in acoustic and DC electric field (DC E-SPART Analyser), then in a sinusoidally oscillating AC electric field (AC E-SPART Analyser). Compared to the DC E-SPART Analyser, a better performance has been achieved by the AC E-SPART Analyser in terms of the range of operation, counting efficiency, sampling error, change of size range and noise immunity, even for highly charged particles [31]. However, the AC E-SPART Analyser suffers from several significant limitations.

Charge measurement techniques		Method / Instrument	Limitations
	Static method	Charge transfer to capacitor	Not suitable for simultaneous charge and size measurement
		Using orientated collecting wire	Limited to large droplets (hundreds of μm in diameter). Measurement range was limited to highly charged particles Only those particles that impact will be counted.
		Electrophotographic toner	Only mean charge of each particle can be deduced if the charge is unipolar.
		Simultaneous size and charge measurement technique with a size-selective device	Only net charge of aerosol could be measured
		Faraday cage	Couldn't measure bipolarly charged aerosol
		Conducting probe/ electrostatic cascade impactor / bipolar charge measurement system	Only total positive or negative charged aerosol could be measured. Number of measured particles was finite. Very accurate aerosol injection was required.
	Dynamic method	Millikan's method	Limiting the point of particle inlet and of confining particles of interest to the focal plane of the system.Considerable time to study single particle
		Parallel plates	Without sufficiently high potential difference between the plates, some ions with a low mobility will be lost.
		Differential mobility analyser	Although the classification becomes more exact by making slot thinner, the sample size will be reduced. Long sampling times - not suitable for rapidly evolving, unstable aerosols
		Scanning mobility analyser	Very long observation time. Conflict between processing speed and precision.
		Cumulative mobility analyser	The dead-time for the instrument response is high.
		E-SPART	Significant error of measurement of lowly charged particle. Low particle count rate When the charge-to-mass ratio is larger than $20\mu C/g$, there will be a significant error. The size of the E-SPART is very large which leads to difficulties in operation.

Table 1.1 Limitations of existing charge measurement technique

First, there is a significant error of measurement of lowly charged particle. Second, the low particle count rate (less than 200 particles per second) results in a poor statistical accuracy of the measurement. Third, when the particle charge-to-mass ratio is larger than $20\mu C/g$, there will be a significant error resulted from the wall loss in E-SPART Analyser [32]. Finally, the size of the E-SPART Analyser is very large, which leads to some difficulties in operation.. The Digital E-SPART Analyser was implemented by W. DiVito *et al*. The raw signal from PMT is provided to the DSP board by the analog circuitry. The DSP board samples, stores the data and signals PC to begin processing signal. Although the Digital E-SPART shows a higher resolution and precision than analog E-SPART [33] its principle of operation is very similar to the previous E-SPART Analysers.

In conclusion, none of the methods mentioned above is without its problems and significant shortcomings. The summary of the limitations of different charge measurement techniques is listed in Table 1.1. A new, improved and smaller-size instrument is needed for simultaneous measurement of particle bipolar charge and size in real time.

1.6 Aim and Objectives

The main aim of this research was to design, implement and simulate a signal processing system for novel, fully functional measurement instrument capable of simultaneously measuring in real time the bipolar charge and size distribution of medical aerosols. The specific objectives of the project are listed below:

- To study the mathematical model of Doppler Burst Signal (DBS) derived from the fringe model and complete the modeling and simulation of the measurement cell system under different scenarios of particle motion.
- To complete the spectral analysis of DBS corresponding to different excitation methods and particle motion characteristics.
- To design charge and size measurement systems used in conjunction with an application of Phase Doppler Anemometry (PDA) based on different real-time DBS processing strategies for particle velocity and size estimation in different excitation fields.
- To evaluate and compare the performance of the different proposed systems by using

Monte Carlo (MC) simulations obtained from the synthesized DBSs.

- To derive the new Cramér-Rao Bound (CRB) for the Doppler frequency estimation using 2D model of noisy DBS in DC excitation field and investigate the influences of the size of the measurement volume, the particle velocity and trajectory and the effect of the signal to noise ratio (SNR) on the value of CRB.
- To develope the numerical model of the measurement system in order to estimate the percentage of the particles captured in the measurement volume and successfully analyse the signal processing system leading to the optimization of the system parameters.

1.7 The Outline of the Thesis

This thesis has been organized in 8 chapters.

Chapter 1 describes the motivation for this research project. Background information regarding the inhalation therapy is given. The increasing popularity of inhalation medication and the therapy efficacy affected by the charge on medical aerosol are emphasized. This is followed by the brief discussion of the effect of particle charge and size on the deposition in human lungs. Then, the chapter presents the summary of the literature review of the existing charge measurement methods underlining the limitations and shortcomings of the measurement techniques with respect to simultaneous measurement of size and charge distribution on rapidly evolving aerosols. Finally, the aim and objectives of this research work and the contributions to knowledge are presented.

Chapter 2 focuses on the discussion of the underlying principles of the Particle Charge and Size Analyzer (PCSA). First, the block diagram of the whole measurement system based on Phase Doppler Anemometry (PDA) is shown and briefly described. Next, the charged particle motions in different excitation fields are investigated in order to derive the theoretical formulas for the charge calculation from real-time particle velocity and size measurement. Then, the principles of the LDA and PDA are presented providing a theoretical underpinning for the PCSA. The relationship between particle velocity and Doppler frequency is discussed,. Additionally, the principles of particle size estimation from phase shift between DBSs are also described. Finally, the advantages and

disadvantages of the DC field and the oscillatory excitation fields, sine and square wave fields are shown and discussed.

Chapter 3, 4, 5, 6 and 7 contain the main contributions of this thesis.

Chapter 3 is mainly concerned with the mathematical modeling and the simulation of the DBS in different excitation fields including DC field, sine-wave excitation field and square-wave excitation field. The main aim of this chapter is to investigate the characteristics of the DBS due to trajectory of single-particle or multi-particle via the measurement volume in different excitation fields and study the relationship between the real-time particle velocity and the instantaneous Doppler frequency. At the beginning of the chapter, the mathematical models of DBSs generated from different particle motions via the measurement volume in different fields are derived. Next, the structure of measurement cell and volume is described. Then, the simulations based on these mathematical models in different scenarios are completed. The simulation results of DBSs and the corresponding spectral analysis are presented. Thus, the relationship of the 2D particle trajecotry via the measurement volume, Gaussian envelope of DBS and instantaneous Doppler frequency are studied. Besides the ideal cases including particle motions with constant velocity, constant acceleration, sinusoidal velocity and sqaure-wave velocity, some more complex cases are also shown, for example, the discontinuous DBS and the multi-burst DBS. Furthermore, the limitations of the velocity estimation based on spectral analysis in different excitation methods and challenges in the singal processing are discussed.

Chapter 4 discusses the design of the signal processing system for the PCSA in order to obtain particle charge and size simultaneously in real time. The chapter starts with the general introduction of the simultaneous charge and size estimation system composed of velocity and phase shift estimation modules. The objective of this chapter is to describe the design and implementation of the real-time particle velocity and phase shift estimaiton systems based on different Doppler signal processing techniques in different excitation fields, such as DC excitation field, sine-wave excitation field and square-wave excitation field. Additionally, the design goals and signal processing performance requirements of the designed systems are listed. Secondly, various signal processing techniques from the published literature are comprehensively reviewed in three different working domains: time domain (counting technique), frequency domain (spectral analysis and PLL technique) and

correlation domain (auto-correlator). A comparison of these techniques has been made with regards to the working range, SNR requirement, real-time information availability. Advantaged and disadvantages of these techniques are highlighted with respect to the real-time DBS processing. Thirdly, the particle velocity and phase shift estimation systems based on different signal processing techniques (e.g. FFT tehcnique, PLL technique, QD techinque, correlation technique and Hilbert transformation) under different excitation methods are designed and implemented in SIMULINK/MATLAB. The brief description of the principles of related techniques and the block diagrams of designed systems are given. In order to improve the system performance, e.g. enlarging the working range, several design improvements are made to the conventional signal processing methods, such as AGC unit and long loop PLL.

In Chapter 5, the simulation and the performance testing results of the signal processing systems proposed in Chapter 4 are given. The main purpose of this chapter is to comprehensively compare the performance of designed estimation systems and determine the optimal one. First of all, the procedure for the generation of the analog DBS and the performance testing scheme are discussed for particle velocity and size estimation systems. Secondly, the simulation results of velocity estimation systems based on different signal processing technqiues (spectral analysis, PLL, QD and correlation technqiues) in DC, sine-wave and square-wave excitation fields are presented. The performances of these systems are evaluated using MC simulations obtained from the synthesized Doppler burst signals generated from the mathematical models implemented in MATLAB. The synthesized DBS are subsequently corrupted with the added Gaussian noise. Cross validation of the results is performed using hardware signal processing system employing Arbitrary Waveform Generator and also NASA simulator to further confirm the validity of the estimation. Thirdly, the performances of the phase shift estimation systems implemented using Hilbert transformation and correlation technique in both sine-wave and square-wave excitation fields are tested by the means of MC simulations. Fourthly, the charge ranges of different estimation systems are calculated from the estimation range of particle velocity and size based on the formulas given in Chapter 2. Finally, the performance of the systems has been compared with regards to the velocity and phase shift estimation range, charge range and SNR requirement and particle capture efficiency.

Chapter 6 derives the Cramér-Rao Bound (CRB) on frequency estimation of the noisy DBS taking into account the 2D motion of particle via the measurement volume. The CRB provides an analytical expression for the lowest variance of the estimation of Doppler frequency which can be used to validate the designed estimator. A theoretical basis of CRB is introduced first. Next, the expression of the CRB corresponding to the 2D model of DBS in DC excitation field is derived. Furthermore, the comparison between the new bound and the bounds published in the literature (Rife and Sobolev) is given. In addition, the numerical simulations of the frequency estimation performed using MC simulations are discussed. Then, from the simulation results, the conclusions are drawn regarding the effect of the particle velocity, trajectory via the measurement volume, the number of fringes, SNR and the measurement time on the accuracy of the Doppler frequency estimation.

Chapter 7 describes a numerical model of the measurement system developed to estimate the percentage of aerosol particles arriving at the measurement volume at any given time and generating a valid DBS. The purpose of the numerical modeling is to examine various measurement system configurations and to establish the optimal range of the system parameters for both excitation methods. It is assumed that the aerosol flow is laminar with a uniform distribution of randomly generated particles across the inlet. The simulated particle's size is from 0.5 to 10μm and charge from 0e to Gaussian limit. The investigation focuses on the effect of drive frequency of excitation field, amplitude of field strength, mean flow velocity, diameter of inlet and size of the measurement volume. The optimal range of system parameters for both excitation methods has been determined with the recommended values proposed for sine and square wave excitation systems.

The thesis concludes with Chapter 8 which summarizes the findings of this work and suggests areas, which could be investigated in the future.

1.8 Contributions to Knowledge

The thesis claims the original contributions to the knowledge in the following areas:

1. **The mathematical modeling of Doppler Burst Signal in different excitation fields, including the DC electric field, sine-wave excitation field and square-wave excitation field.**

   The new mathematical models of the DBS in three different excitation fields have been derived taking into account the mean flow velocity, the geometry of the measurement volume and the particle trajectory via the measurement volume. Four different kinds of particle motions in the different excitation fields and the corresponding DBSs have been investigated, such as the motion with constant velocity in the DC excitation field, the motion with a constant acceleration, the sinusoidal motion in the sine-wave excitation field and the oscillatory motion in the square-wave excitation field. The simulations of DBSs were completed in the presence of the Guassian white noise. Furthermore, the modeling of the multi-burst DBS and discontinuous bursts was accomplished in different excitation fields. In addition to the mathematical modeling and simulation, the spectrum analysis of the DBS provided the new insights into the complexity of the DBS and the subsequent signal processing.

2. **The design and implementation of simultaneous charge and size measurement systems based on the spectral analysis, PLL technique, QD technique and correlation technique in different excitation fields.**

   The signal processing systems for charge and size measurement have been separately designed and implemented in the DC, sine-wave and square-wave excitation fields. Both magnitude and the polarity of the particle charge can be determined by the designed systems. The velocity estimation systems, which were independently designed and implemented include: 1) Spectral analysis and PLL based systems working in DC field. 2), QD and PLL based systems working in sine-wave excitation field and 3) Spectral analysis based algorithm working in square-wave excitation field. In addition to the velocity estimation systems the phase shift estimation system using Hilbert transformation and correlation

technique was designed and implemented in both sine-wave and square-wave excitation fields. Finally, the design of DBS train processing algorithm was accomplished in both sine-wave and square-wave excitation field.

3. **Evaluation of the performance of the particle charge and size measurement systems by means of Monte Carlo simulations.**

   The performance of the velocity and size estimation systems was tested on simulated DBS by means of MC simulations. The DBSs used in MC tests were generated from the mathematical models implemented in MATLAB. The generated DBS were subsequently corrupted with the added Gaussian noise. Cross validation of the results was performed using hardware signal processing system employing Arbitrary Waveform Generator and also NASA simulator to further confirm the validity of the estimation. Comparison of the system performance was given in terms of the velocity and size estimation range, charge range and the noise sensitivity.

4. **Novel Cramér-Rao Bound derivation for the frequency estimation in the DC excitation field**

   The new Cramér-Rao Bound for a model of the DBS taking into the account the 2D motion of particle tracer via the measurement volume was derived. The novelty of the presented approach is in the consideration of the mean flow velocity in conjunction with the cross flow velocity instead of assuming that the particle motion is perpendicular to the fringe pattern as investigated in the previous research. The new CRB expression has been compared with the CRB derived by Rife and Sobolev [156], [157]. The respective influences of the size of the measurement volume, the particle velocity and trajectory and the effect of the signal to noise ratio (SNR) are studied and shown. The numerical results of the frequency estimation are given using FFT algorithm and Monte Carlo simulations obtained from the synthesized Doppler burst signals.

5. **Numerical modeling of the measurement system and optimization of the system parameter.**

   A new numerical model has been developed in order to estimate the percentage of particles captured in the measurement volume and successfully

analyzed by the signal processing system leading to the optimization of the system parameters. In order to determine the optimal range of system parameters, the effect of drive frequency, strength of field, mean flow velocity, the size of the inlet and the size of measurement volume on the particle capture percentage have been investigated based on the specific criteria in both sine and square wave excitation fields.

Chapter 2

Theoretical Basis for the Particle Charge and Size Analyzer

2.1 Introduction

This chapter aim is to provide a theoretical basis for the Particle Charge and Size Analyzer (PCSA). First of all, the underlying principles of the operation of the PCSA are described. Secondly, the charged particle motion in DC, sine-wave and square-wave excitation fields is discussed and the charge calculation formulae based on particle velocity and size are given. Finally, the principles of the Laser Doppler Anemometry (LDA) and Phase Doppler Anemometry (PDA) are introduced.

The next chapter will investigate the mathematical modeling of Doppler Burst Signal (DBS) and discuss the simulation results of the DBS corresponding to different particle trajectories inside the measurement volume in different excitation fields.

2.2 The Concept of the PCSA

The block diagram of the charge measurement system, Particle Charge and Size Analyzer (PCSA), proposed in this research is shown in Fig. 2.1. The measurement system consists of the measurement cell with optical windows, settling chamber, vacuum pump, high precision flow meter, the PDA system including transmitting/receiving optics and photo detectors, amplifier and band pass filter, PC with A/D card and HV power supply generating the oscillatory field. The PDA is used to track the motion of charged particles suspended in the medium in an excitation field. In the electric field the oscillating particle passing through the measurement volume generates frequency

modulated DBS, which contains the information about the amplitude of the particle velocity. There are two laser beams intersecting in the measurement cell. When the oscillating particle passing through the measurement volume in the field, three DBS with the same frequency but different signal phase are generated and received by the detectors.

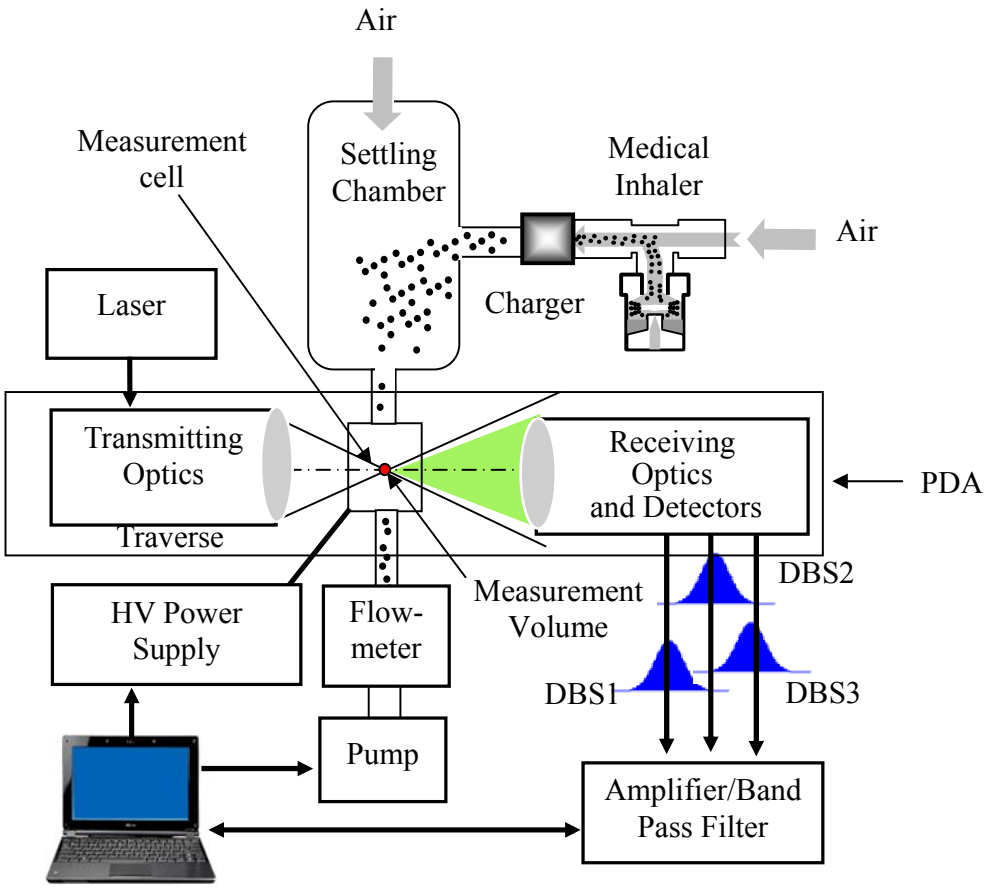

Fig. 2.1 Block diagram of PCSA

The Doppler frequency contains the information about the instantaneous particle velocity. It is given by

$$F_D(t) = F_B + f_D(t) = F_B + \frac{2V_x(t)}{\lambda}\sin\frac{\theta}{2} = F_B + DV_x(t) \qquad (2.1)$$

where $V_x(t)$ is the particle real-time velocity component perpendicular to bisector of beams, only this component contributes to the frequency of DBS, θ is the intersection

angle between the beams, λ is the wavelength of the incident beams, D is called the calibration factor, $D = \frac{1}{i} = \frac{2\sin(\theta/2)}{\lambda}$,where i is the fringe spacing, F_B is the shift frequency, which is a constant introduced to one of the beams by the Bragg cell to solve the velocity directional ambiguity [34].

DBSs are processed by the signal processing algorithm in order to obtain the particle velocity in real-time. Based on the equation of a particle motion in a viscous medium, the magnitude as well as the polarity of the particle charge can be obtained from the simultaneous measurement of the particle size and velocity. The phase shift between the signals from the different detectors is proportional to the size of spherical particles. Since phase shift is a modulo 2π function, it can't exceed 2π. Therefore, if a particle has a size that causes the phase to go beyond a 2π jump, a two-detector PDA can't discriminate between this size and a much smaller particle. The problem of 2π ambiguity is sovled by using three detectors in PDA system for validation [35].

2.3 Charged Particle Motion in the External Excitation Field

In order to obtain the magnitude and the polarity of the particle charge, the charged particles are forced to pass through an excitation field in the measurement cell.

When the charged particle is moving in the DC excitation field with a constant velocity, it is called the steady state. The motion of particle is shown in Fig. 2.2. The trajectory of the charged particle is affected by two different forces, the electric force F_e arising from the excitation field and the drag force F_{drag} due to the viscous medium. These two forces can be determined from the following equations [14]

$$F_e = qE \tag{2.2}$$

$$F_{drag} = -\frac{C_d \pi \rho_{air} d^2 V^2}{8} \tag{2.3}$$

where $C_d = 24\eta/(C_c \mathbf{V} d \rho_{air})$ is the drag coefficient, d is the particle diameter, C_c is the Cunningham slip correction factor, η is the viscosity of air, V is the relative instantaneous

velocity between the air and the particle, ρ_{air} is the air density, q is the particle charge and E is the strength of the DC field in the direction of the particle drift velocity. Small particles immediately attain equilibrium in the presence of the DC excitation field [15].

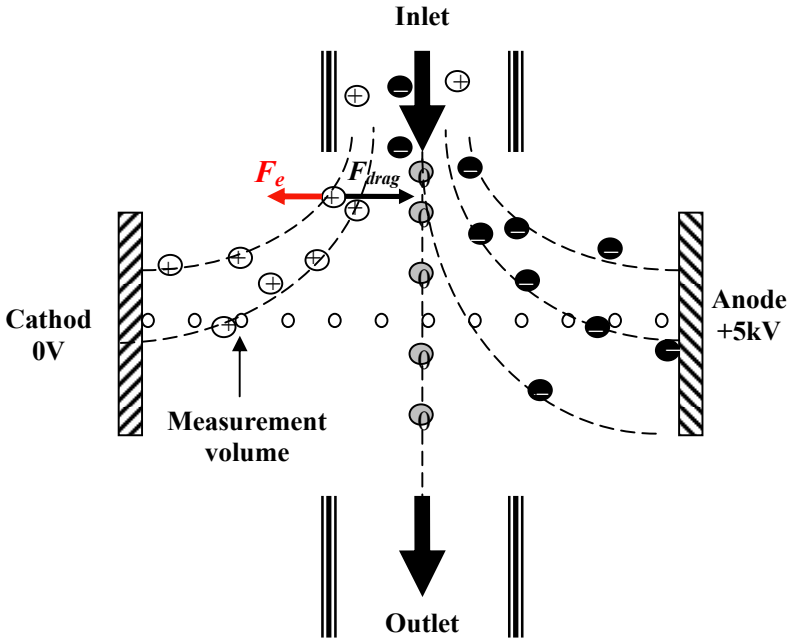

Fig.2.2 Charged particle motion in the DC excitation field in the measurement cell

$$F_e = F_{drag} \tag{2.4}$$

From (2.4), the particle charge can be calculated as

$$q = -\frac{3\pi\eta V d}{C_c E} \tag{2.5}$$

In the DC excitation field, in order to measure particles with different electric mobilities, the measurement volume must be moved between the two electrodes, as shown in Fig. 2.2. Despite this movement, however, some highly charged particles may still be deflected towards the electrodes before they reach the measurement volume. This problem can be overcome when a charged particle is subjected to the oscillatory field.

The particle trajectory in the sine-wave excitation field is shown in Fig. 2.3. In this case, the position of the measurement volume can be kept stationary in the centre of the cell. In the sine-wave excitation field, the electric charge on particle can be calculated as

follows [7]:

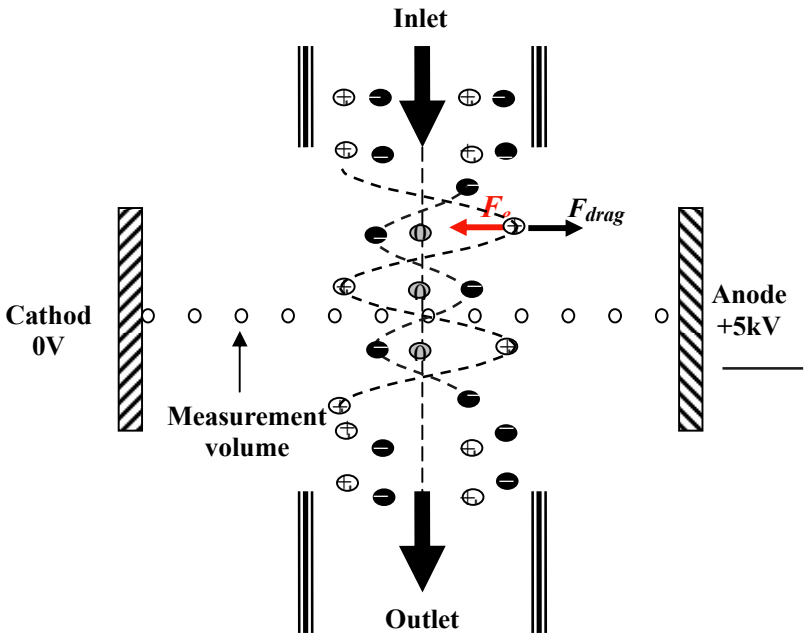

Fig.2.3 Charged particle motion in the sine-wave excitation field in the measurement cell

$$q = \frac{3\pi\eta d A_v}{C_c E}\sqrt{1+\omega^2\tau^2} \tag{2.6}$$

where E is the strength of the sine-wave excitation field, A_v is the amplitude of the particle velocity, ω is the angular frequency of excitation field and τ is the relaxation time. The polarity of the charge can be determined from the phase difference between the field excitation and the particle velocity [7]. From the examination of the particle motion it can be concluded that more highly charged particle can be captured in the sine-wave excitation field than in the DC excitation field [51].

In addition to the sine-wave excitation system, the square-wave oscillatory field was proposed and investigated in this research in order to carry out a comparative study of the performance of both methods. The charged particle motion in the square-wave field is shown in Fig. 2.4. Similar to the situation in the sine-wave excitation field the position of the measurement volume can be kept stationary in the centre of the cell. Also, more particles highly charged particles enter the measurement volume rather than being

deflected towards the electrodes as is the case with the DC field.

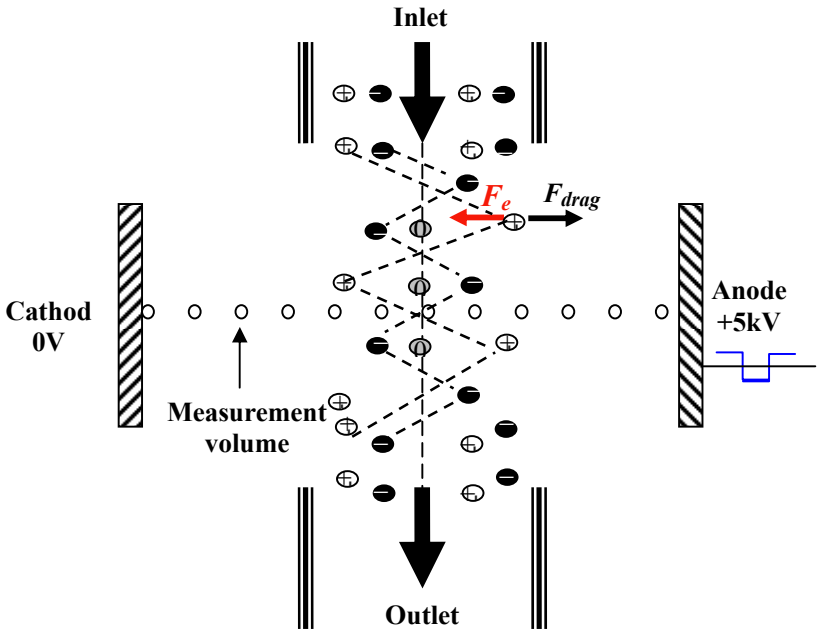

Fig. 2.4 Charged particle motion in the square-wave excitation field in the measurement cell

In the square-wave excitation field the electric charge on particle can be calculated as follows:

$$q = -\frac{3\pi\eta V d}{C_c E} \tag{2.7}$$

where E is the strength of the square-wave excitation field in the direction of particle drift velocity, V is the particle velocity. The polarity of charge can be determined by the phase difference between the field excitation and particle velocity.

2.4 Theory of Laser Doppler Anemometry

In the Section 2.2, the relationships between the particle charge and velocity in different fields was given. In order to obtain the particle velocity and size, the PDA is employed in the PCSA system. As the PDA is the development of LDA, the principles of the LDA are introduced first.

LDA is a widely used technique for fluid dynamic investigations in gases and liquids and has been used for more than three decades. Laser Doppler technique was first proposed in 1964 but came into widespread use only in the 1970s [34]. It is a well-established optical technique for measurements of particle velocities. The block diagram of LDA system is shown in Fig. 2.5.

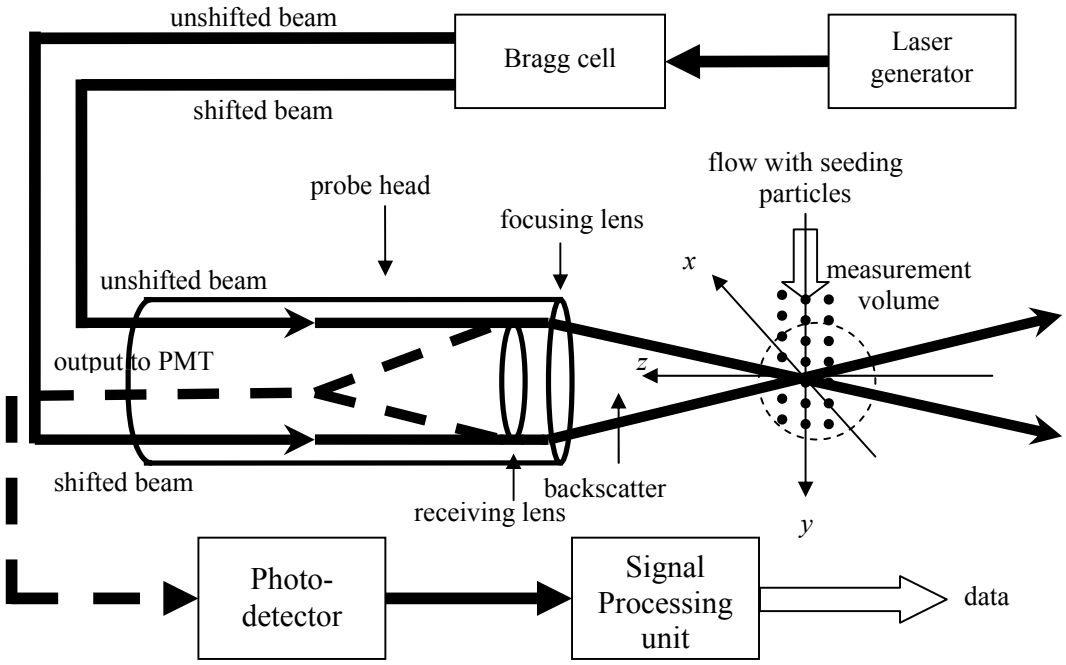

Fig. 2.5 Block diagram of Laser Doppler Anemometry system

The laser Doppler technique uses mono-chromatic laser light as the light source. In the LDA system, the Bragg cell is used as a beam splitter. The output of the Bragg cell is two beams with equal intensity but different frequencies, one shifted, the other unshifted. They are focused into optical fibers bringing them to a probe. In the probe, the parallel exit beams from the fibers are focused by the focusing lens to intersect in the measurement volume. The scattered light by the particles passing through the interference region is collected by the receiving lens and focused on the photo-detector. The interference of two beams crossing in the measurement volume or the interference of two scattering waves on the detector is contained in the scattered field due to the Doppler Effect [34], which will be discussed in the Section 2.3.1. Finally, the DBS is transmitted

to the signal processing unit from the photo-detector. The information of particle velocity can be obtained from processing DBS. Its non-intrusive principles and directional sensitivity make LDA very suitable for applications in a number of different fields, for example, medical applications, spray diagnostics [36] [37], combustion measurements [38], design of ink-jet printers and so on. The advantages of this technique are mainly non-intrusive measurement, high spatial and temporal resolution, no need for calibration and the ability to measure in reversing flow [39]. In order to give the theoretical background, the fundamental principles of LDA are introduced below. More details can be found in [40], [41], [42].

2.4.1 Doppler Effect

The Doppler Effect is employed in the velocity measurement of the LDA. The Doppler Effect accompanies any movement of either the transmitter or receiver of the electromagnetic radiation. The illustration of the principle of the Doppler Effect is shown in Fig. 2.6.

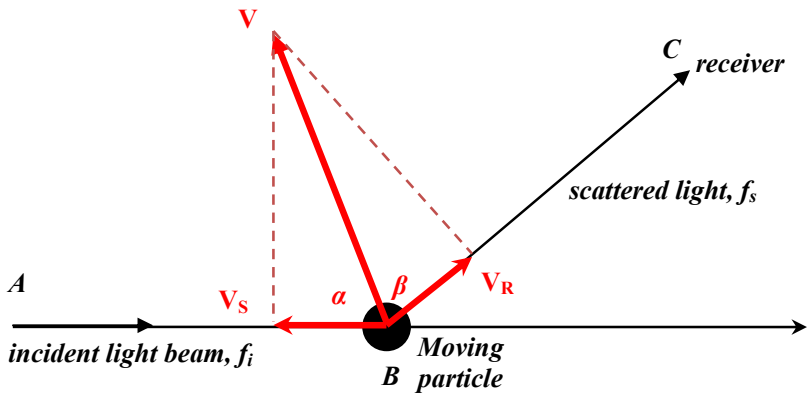

Fig. 2.6 Illustrate of Doppler Effect

When the light is reflected from a moving object, the frequency of the scattered light is shifted by an amount proportional to the speed of the object. As shown in Fig. 2.6, there is an incident plane wave light beam, with a frequency of f_i scattered by a moving particle with velocity of **V**. When the particle crosses the light beam at the origin it

scatters light with Doppler shifted frequency. The frequency shift is directly proportional to the velocity component in the propagation direction of incident light, $\mathbf{V}_S$ which is defined as,

$$\mathbf{V}_s = \mathbf{V}\mathbf{e}_i = \mathbf{V}\cos\alpha \tag{2.8}$$

where α is the angle between the velocity vector and the incident beam, $\mathbf{e}_i$ is the unit vector in the direction of the incident beam.

From the point view of the receiver, the particle can be regarded as a moving transmitter. Therefore, the movement introduces an additional Doppler-shift in the frequency of the light f_s received by the receiver. There is a directly proportional relationship between the particle velocity and the component in the receiver direction, $\mathbf{V}_R$, which is shown below,

$$\mathbf{V}_R = \mathbf{V}\mathbf{e}_s = \mathbf{V}\cos\beta \tag{2.9}$$

where β is the angle between the velocity vector and the scattered beam, $\mathbf{e}_s$ is the unit vector in the direction of the scattered beam.

Therefore, the frequency of the light received by the receiver can be expressed as,

$$f_s = f_i - \frac{1}{\lambda}\mathbf{V}\mathbf{e}_i + \frac{1}{\lambda}\mathbf{V}(\mathbf{e}_s - \mathbf{e}_i) = f_i + \frac{1}{\lambda}\mathbf{V}(\cos\alpha + \cos\beta) \tag{2.10}$$

It can be seen in Fig. 2.6 that the direction of $\mathbf{V}_s$ component is opposite to the one of the incident light. Thus it can be concluded that the frequency of the incoming light, f_i, is smaller than the frequency of the scattered light, f_s. The frequency difference between the incident and the scattered light is so called the Doppler shift, *i.e*.

$$f_D = \frac{\mathbf{V}}{\lambda}(\cos\alpha + \cos\beta) \tag{2.11}$$

From (2.11), it can be seen that the particle velocity can be estimated by measuring the frequency difference between f_i and f_s, which is the fundamental principle of the operation of the LDA. However, normally, the Doppler shift is a very small value

compared to the frequency of the incident beam in the practical applications. There is a high degree of uncertainty when estimating a small value from the difference between two large values. One exception is a direct measurement by the means of an interferometer [35] or the frequency dependent absorption cells leading to the Doppler global velocimeter (or planar Doppler velocimetry) [42] [43]. In order to improve the accuracy of the estimation, an optical heterodyning technique is proposed. This technique requires that Doppler shifted scattered light should be mixed with the incident light generated from the same light source or that the light scattered from one laser beam interference with scattered light from another beam [41]. Correspondingly, there have been two LDA systems developed, one of which is known as dual beam system, and the other is a reference beam system, and both have been successfully implemented [44], [45], [46]. This section will mainly focus on the introduction of the dual beam system. The arrangement of the dual beam LDA system is illustrated in Fig. 2.7.

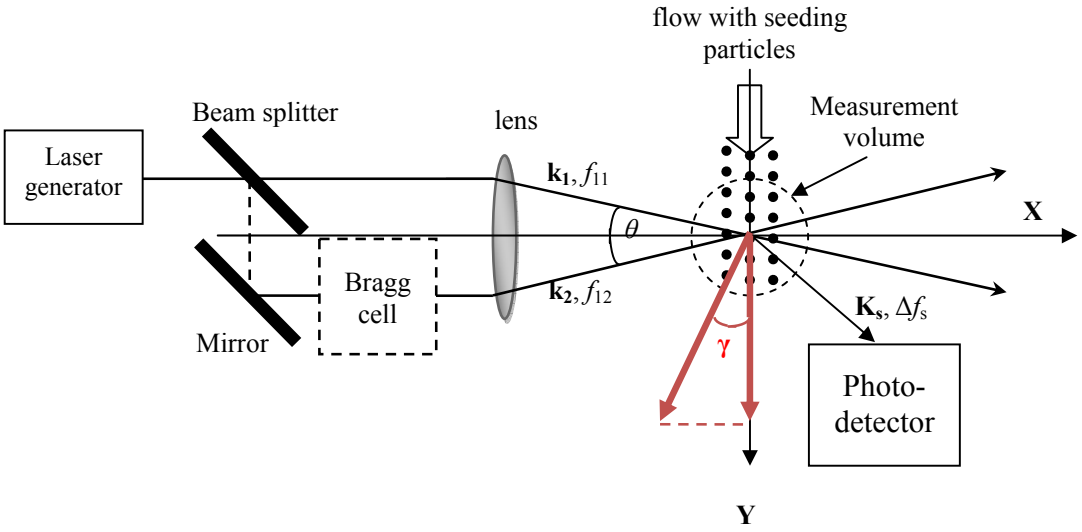

Fig. 2.7 Dual beam LDA system arrangement

The particles passing through the measurement volume scatter the incident light with different angles between the particle velocity vector and the beams. Therefore, the frequencies of the scattered lights are different and were expressed as below,

$$f_{s1} = f_{11} + \frac{\mathbf{V}(\mathbf{k}_s - \mathbf{k}_1)}{\lambda}$$
$$f_{s2} = f_{12} + \frac{\mathbf{V}(\mathbf{k}_s - \mathbf{k}_2)}{\lambda} \tag{2.12}$$

where $\mathbf{k}_1$, $\mathbf{k}_2$ are unit vectors in the direction of the incident beams, $\mathbf{k}_s$ is the unit vector in the direction of the scattered light. $\mathbf{V}$ is the particle velocity vector. Then, the beat frequency can be written as,

$$f_d = \Delta f_s = \frac{\mathbf{V}(\mathbf{k}_2 - \mathbf{k}_1)}{\lambda} = \frac{\mathbf{V}\cos\gamma}{\lambda} 2\sin\frac{\theta}{2} \tag{2.13}$$

where γ is the angle between the velocity vector $\mathbf{V}$ and the velocity component in Y direction, $\mathbf{V}_y$. θ is the angle between the incoming laser beams. The beat frequncy is so called Doppler frequency, which is much smaller than the light frequencies f_{s1}, f_{s2} and is proportional to the $\mathbf{V}_y$. Additionally, it can be found the Doppler frequency is independent of the position of the receiver.

2.4.2 The Fringe Model

In the LDA system the Bragg cell is used as a beam splitter to shift one of the two equal-power beams. When the two coherent beams having plane wave fronts intersect in space, a fringe pattern is created in the intersection region. In order to describe the LDA systems the fringe model was first proposed by Rudd [47]. It is easily visualised and also provides a basis for both quantitative and qualitative analysis of a number of features of LDA signals [39]. In Fig. 2.8, it can be seen that the two laser beams intersect in the y-z plane in the measurement volume. A fringe pattern can be created by the separation of the original source into two separate beams and then recombining them at differing angles of incidence on a viewing surface.

According to [48], the spacing between the fringes is

$$i = \frac{2\pi}{\lambda} = \frac{\lambda}{2\sin\frac{\theta}{2}} \tag{2.14}$$

Assuming the frequencies of the two incident beams are f_1 and f_2 respectively, the frequency difference between them is F_D, i.e. $F_D = |f_1 - f_2|$. The intersection angel between the beams is θ. According to the principles of Doppler Effect, the Doppler shifts of the two

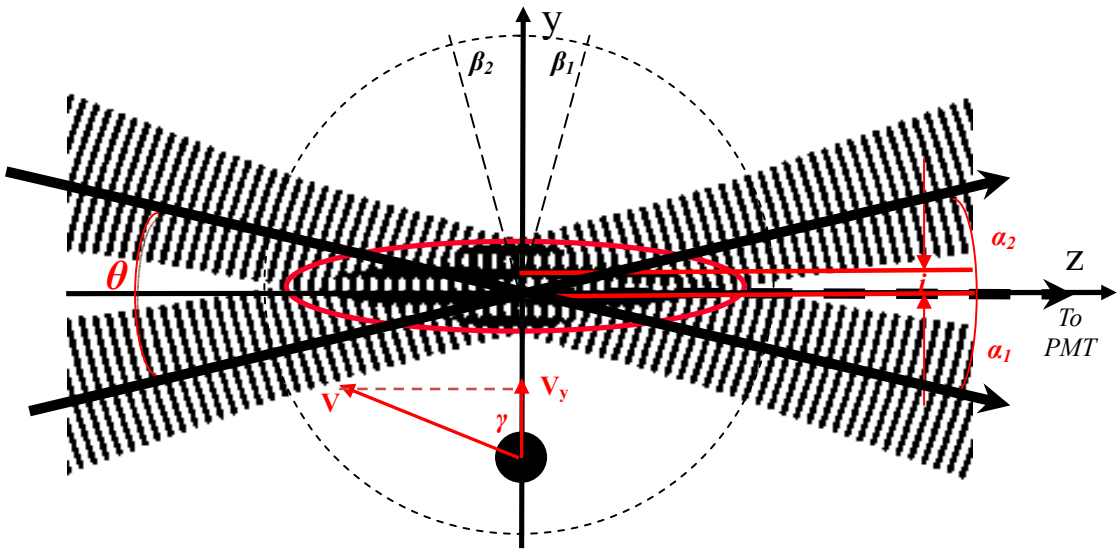

Fig. 2.8 Fringe model in the measurement volume

beams scattered by the particle can be obtained

$$f_{D1} = \frac{2V}{\lambda}\cos(-\frac{\theta}{4})\sin(-\frac{\theta}{4})$$
$$f_{D2} = \frac{2V}{\lambda}\cos\frac{\theta}{4}\sin\frac{\theta}{4} \tag{2.15}$$

So that $f_{D1} = -f_{D2}$. When there are two waves of equal amplitude and nearly equal frequency superimposed in space, a phenomenon, interference will occur. The beat signal will be generated. The frequency of the beat signal is, f_{beat} is given as

$$f_{beat} = \frac{|f_{D1} - f_{D2}|}{2} = \frac{2V\cos\gamma}{\lambda}\sin\frac{\theta}{2} \tag{2.16}$$

In the LDA terminology, the beat signal is called Doppler Burst Signal (DBS) and its frequency is called Doppler frequency, F_D, *i.e.*

$$F_D = F_B + f_D = F_s + \frac{2V\cos\gamma}{\lambda}\sin\frac{\theta}{2} \tag{2.17}$$

where F_B is also called shift frequency and f_D is called the Doppler shift [39]. V is the particle velocity and V_y is the velocity component perpendicular to bisector of beams, γ is the angle between V and V_y.

2.4.3 Directional Ambiguity

The LDA system measures the frequency of the light intensity variation resulting from a particle crossing a series of equally spaced fringes. However, there are two limitations of this technique. First, there is an ambiguity in the direction of the measured velocity. For example, two particles travelling with the same speed but opposite directions will generate the same DBSs. Secondly, if the particle keeps stable in the measurement volume, no signal will be produced.

In order to solve the problem of directional ambiguity, a frequency shift f_s should be added to one of the incoming beams. Therefore, for the other unshifted beam, the fringe pattern moves at a constant speed in the direction depending on the direction of the frequency shift f_s. The particle moving with the fringes generates DBS of higher frequency while the particle moving against the fringes generates DBS of lower frequency. Thus, the directional ambiguity is removed. The frequency of DBS with the frequency shift can be expressed as follows,

$$f_D = f_s + \frac{V_y}{i} = f_s + \frac{2V\cos\gamma}{\lambda}\sin(\theta/2) \tag{2.18}$$

According to (2.18), we can conclude that when $f_s > |\frac{2V\cos\gamma}{\lambda}\sin(\theta/2)|$, the sign of V can be determined.

In the practical applications, the frequency shift is usually generated by the Bragg cell which is introduced in the path of one of the laser beams. The transparent medium contained in the Bragg cell is composed of either liquid or solid. The laser beam passes through it. The medium is excited by passing ultrasonic sound waves through it. The

sound waves propagate through the medium in the form of density waves and therefore waves of refractive index diffract the laser beam. The movement of sound waves results in the frequency shift of the laser beam known as Bragg reflection, which is equal to the frequency of the waves, typically 40MHz in the LDA/PDA systems.

2.4.4 The Measurement Volume

The region of fringes formed by the intersection of laser beams is known as a measurement volume or a probe volume. The size of the measurement volume is one of the important parameters of the LDA system because it determines the spatial resolution of this technique. In Fig. 2.9, it can be seen that the measurement volume is an ellipsoid due to the Gaussian intensity distribution of the beams in all three dimensions.

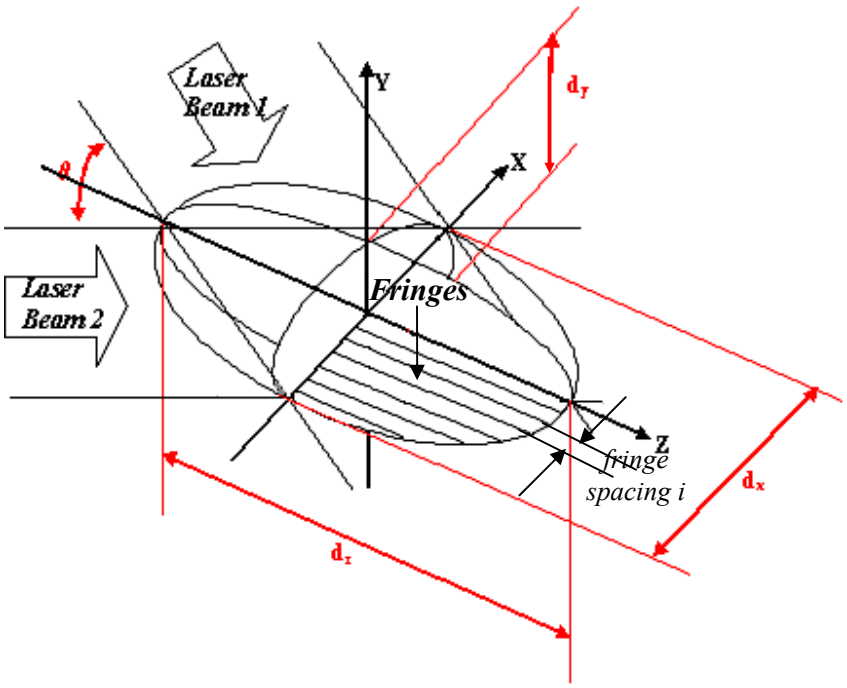

Fig. 2.9 The measurement volume dimensions

The dimensions of the measurement volume are defined by the light intensity distribution of the fringe pattern. The e^{-2} decay of the modulation amplitude was arbitrarily chosen as the dimensions of the measurement volume. In the volume, the beam intensity is higher than e^{-2} times amplitude of the maximum intensity, which occurs at the

centre of the fringe pattern. The dimensions of the measurement volume based on the e^{-2} intensity boundary are shown in Fig. 2.9. The size of the volume can be calculated from the beam waist diameter d_f of the focused laser beams and the angle between them [34].

$$d_f = \frac{4 f_L \lambda}{\pi E_w d_L} \tag{2.19}$$

$$d_z = \frac{d_f}{\sin(\theta/2)}, d_y = d_f, d_x = \frac{d_f}{\cos(\theta/2)} \tag{2.20}$$

where d_L is the diameter of the laser beam waist before expansion, E_w is the beam expansion ratio and f_L is the focal length of the front lens.

The volume from which signals are received is defined as the detection volume, which is different from the measurement volume. The size of the detection volume depends on the requirements of the signal processing system and can be smaller or larger than the measurement volume.

2.5 Theory of the Phase Doppler Anemometry

The Phase Doppler Anemometry (PDA) was first proposed in 1975 by Durst and Zaré [49]. The PDA is developed based on LDA and can be regarded as an extension of it. Besides the velocity, the PDA can measure particle size simultaneously with the range from 0.5μm to 2.5mm [50]. These particles can be droplets, bubbles or solid particles, as typically occur in sprays, liquid atomisation, bubbly two-phase flows and multiphase flows with, for example, glass beads. The block diagram of PDA system is shown in Fig. 2.10.

The main difference between PDA and LDA systems is in the number of photo detectors. The PDA uses multiple instead of one photo detector to receive the scattered light. The principles of velocity measurement by PDA system are the same as the ones used by LDA. The principles of the particle size measurements used in PDA are illustrated in Fig. 2.11. The aerosol passes through the measurement volume. Particles scatter the two incident laser beams. A receiving lens located at an off axis collection

angle projects a portion of the scattered light onto two detectors [51].

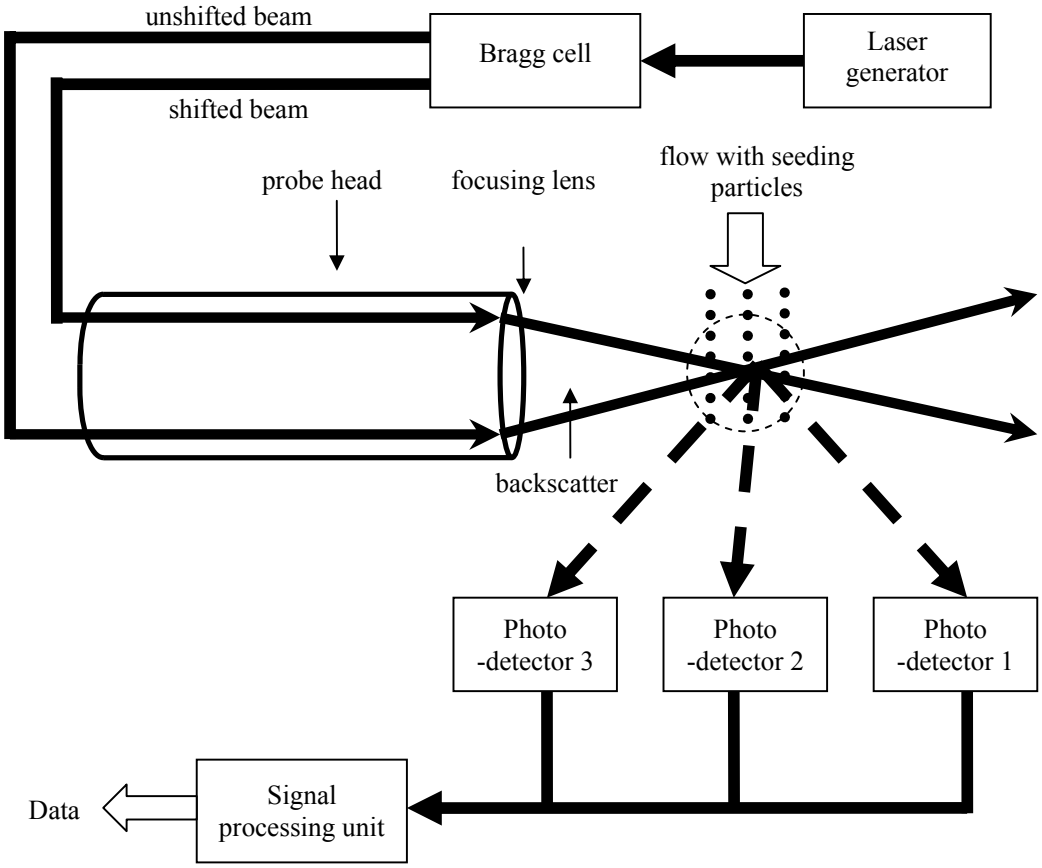

Fig. 2.10 Block diagram of Phase Doppler Anemometry system

Since more than one photo detector is employed in the PDA system, the phase difference between the signals generated by different detectors can be measured. The phase difference, Φ, is proportional to the size of the spherical particle. This relationship can be defined by the following expressions in two cases:

a. Scattering is dominated by reflection [52]

$$\Phi = \frac{2\pi D}{\lambda} \frac{\sin\theta \sin\phi}{\sqrt{2(1-\cos\theta\cos\phi\cos\varphi)}} \tag{2.21}$$

b. Scattering is dominated by refraction [52]

$$\Phi = -\frac{2\pi D}{\lambda}\frac{n_{rel}\sin\theta\sin\phi}{\sqrt{2(1+\cos\theta\cos\phi\cos\varphi)(1+n_{rel}^2-n_{rel}\sqrt{2(1+\cos\theta\cos\phi\cos\varphi)})}} \quad (2.22)$$

where, $n_{rel}=\frac{n_{particle}}{n_{medium}}$, refers to the relative refractive index, D is the particle diameter.

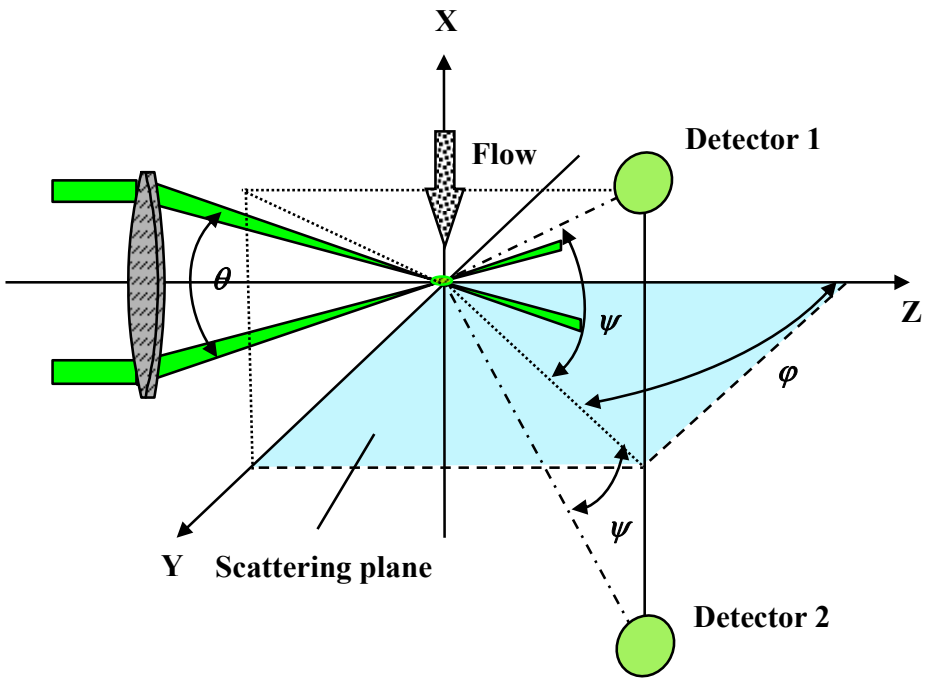

Fig. 2.11 Illustrate of standard PDA set-up. Optical parameters of a PDA set-up: Two beams intersect in the x-y plane under the intersection angle θ; the receiving systems are positioned in the x-z plane at the scattering angle φ; the detectors are titled against the y-z plane under the elevation angle Ψ [52].

Usually, the maximum particle size that can be unambiguously measured with two detectors corresponds to a phase shift smaller than 2π. If the size of a particle causes the phase difference to go beyond a 2π jump, two-detectors PDA can't unambiguously measure the particle size. Reducing the distance between the detectors can extend the measurable range of particle size. However, it will also reduce the measurement resolution [52]. Considering a large measurable size range and a high measurement resolution, three-detectors PDA is a preferred solution. All the detectors have the same scattering angle. Nowadays, three-detectors PDA are widely employed in the commercial

PDA systems to avoid the ambiguity in phase shift measurement.

2.6 Summary and Conclusions

This chapter focused on the background discussion of the underlying principles of the PCSA. In order to measure the particle charge, the particle is forced to pass through the excitation field. The relationship between the particle charge, velocity and size based on different excitation methods was given. It was shown that the charge and size measurement can be simultaneously obtained directly from the PDA system.

The theories of the LDA and PDA were introduced. The LDA is a well-established optical technique for measurement of particle velocities. The PDA can be regarded as an extension of the LDA. The PDA system is capable of measuring the size and velocity of spherical particles simultaneously. The velocity measurement principles of the LDA and PDA are based on the Doppler Effect. Both the LDA and the PDA measure particle velocity from the DBS generated by particles passing through the fringe pattern created by the interfering laser beams. In the PDA system, the particle size is measured from the phase difference between the different DBSs obtained from multiple photo-detectors.

It can be concluded that the main advantage of the DC excitation method is a straightforward relationship between the charge, size and particle velocity. Also, the DC field produces the DBS, which is relatively uncomplicated due to largely constant particle velocity inside the measurement cell. However, the main disadvantage of the DC excitation field is that significant proportion of the highly charged particles inevitably escapes the measurement volume, which subsequently leads to the underestimation of the aerosol charge profile. This is due to the fact that the particles with a high electrical mobility are deflected towards the electrodes before they can be detected by the moving measurement volume. In addition, the DC excitation system creates significant difficulties in the operation of the instrument. The measurement volume has to be moved forwards and backwards across the measurement cell in order to capture the particles of different electrical mobilities, which requires expensive and cumbersome traversing mechanism. It prolongs the measurement time and makes the instrument less suitable for measuring rapidly changing aerosols.

In contrast to the DC field, in the oscillatory field the measurement volume can be kept stationary in both the sine-wave and square-wave excitation methods. Also, since the particles are oscillating inside the measurement cell rather than traveling towards the electrodes, the highly charged particles remain inside the cell. However, the use of the oscillatory field results in much more complex DBS requiring non-standard specialized signal processing method. The specific signal processing challenges related to both oscillatory fields as well as the design of the signal processing systems will be discussed in chapter 4. First of all, however, the next chapter will discuss the mathematical modeling and the simulation of the Doppler burst signals in different excitation methods.

Chapter 3

Mathematical Modelling and Simulation of Doppler Burst Signals

3.1 Introduction

This chapter investigates mathematical modelling and simulations of the Doppler Burst Signal corresponding to different scenarios of charged particle motion via the measurement volume. Three types of particle excitation fields are considered: DC excitation field (steady and accelerated state), sine-wave excitation field and square-wave excitation field. The purpose of the chapter is twofold, firstly, to investigate the characteristics of the DBS due to various particle trajectories via the measurement volume; secondly, to assess the limitations of the spectral analysis in different excitation fields. The chapter is organised as follows. First of all, the general mathematical model of DBS in time domain is given. Next, signal models corresponding to different particle motion in the measurement volume and in different excitation fields are derived. Then, the simulation results based on different mathematical models are shown. The particle trajectory via the measurement volume and the corresponding DBS are presented, including the case of discontinuous-burst signals. In addition to time domain representation, the spectral analysis of the DBS is performed. Finally, the simulations of multi-burst signals in different scenarios are presented and the corresponding results of spectral analysis are given.

In the next chapter, the signal processing systems using different techniques and working in DC, sine-wave and square-wave excitation fields will be separately developed in order to obtain particle charge and size simultaneously in real time.

3.2 General Time Domain Description of Doppler Burst Signal

The DBS is generated when a single particle passes through the measurement volume of the PDA system. The DBS envelope reflects the characteristics of the Gaussian intensity of the laser beams and its instantaneous frequency is defined by

$$F_D(t) = F_B + f_D(t) = F_B + \frac{2\mathbf{V}_x(t)}{\lambda}\sin\frac{\theta}{2} = F_B + D\mathbf{V}_x(t) \tag{3.1}$$

where $\mathbf{V_x}(t)$ is the particle real-time velocity component perpendicular to bisector of beams, only this component contributes to the frequency of DBS, θ is the intersection angel between the beams, λ is the wavelength of the incident beams, D is called the calibration factor, $D = \frac{1}{i} = \frac{2\sin(\theta/2)}{\lambda}$,where i is the fringe spacing, F_B is called shift frequency which is a constant frequency introduced by the Bragg cell to solve the direction ambiguity in velocity estimation.

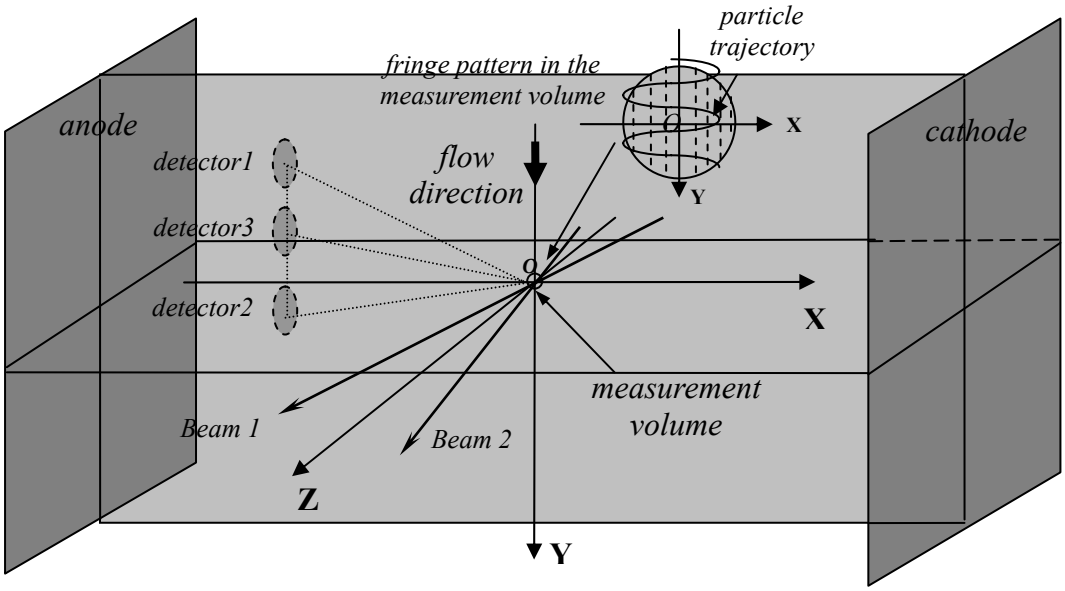

Fig. 3.1 Structure of the charge measurement cell

Fig. 3.1 shows the optical arrangement of the laser Doppler system, where two laser beams intersect in the **XZ** plane. The aerosol main flow is in the direction of the **Y** axis. There are two electrodes which are parallel to the **YZ** plane. The particle motion due to the excitation field takes place in **XY** plane. The time domain

description of DBS from the medium-sized particles is determined by the particle position within the measurement volume, fringe spacing, i, intersection angle, θ, shift frequency, F_B, laser beam radius, r_m, and some other parameters [34]. As an example, the particle trajectory in sine-wave excitation field via the measurement volume is presented.

The mathematical model of the DBS in time domain is composed of two parts, the DC part, $S_{DC}(t)$, and the AC part, $S_{AC}(t)$. The time domain description of DBS is expressed as,

$$S(t) = S_{DC}(t) + S_{AC}(t) = I_{DC} + I_{AC}\cos(\omega t + \varphi_0) \tag{3.2}$$

where I_{DC}, I_{AC} are the amplitudes of the DC and the AC part of DBS model respectively. The DBS frequency ω is defined as,

$$\omega = 2\pi F_D(t) = 2\pi[F_B + D\mathbf{V}_x(t)] \tag{3.3}$$

In order to simplify the DBS model in (3.2), it is assumed that the beam incident point and the glare point [34] coincide with the particle centre. The amplitudes of the DC and the AC parts are separately described in the following equations,

$$\begin{aligned} I_{DC} &= A_{DBS}\exp\{-\frac{[\mathbf{x}(t)\cos(\theta/2)-\mathbf{z}(t)\sin(\theta/2)]^2+\mathbf{y}^2(t)]}{r_m^2} \\ &\quad -\frac{[\mathbf{x}(t)\cos(\theta/2)+\mathbf{z}(t)\sin(\theta/2)]^2+\mathbf{y}^2(t)]}{r_m^2}\} \\ I_{AC} &= A_{DBS}\exp\{-\frac{[\mathbf{x}(t)\cos(\theta/2)-\mathbf{z}(t)\sin(\theta/2)]^2+\mathbf{y}^2(t)]}{r_m^2} \\ &\quad -\frac{[\mathbf{x}(t)\cos(\theta/2)+\mathbf{z}(t)\sin(\theta/2)]^2+\mathbf{y}^2(t)]}{r_m^2}\} \end{aligned} \tag{3.4}$$

where the vectors $\mathbf{x}(t)$, $\mathbf{y}(t)$, $\mathbf{z}(t)$ represent particle positions separately projected on **X**, **Y** and **Z** axis. The origin of the coordinate system is in the centre of the measurement volume. A_{DBS} is the amplitude of the DC and the AC parts. It is determined by the beam wavelength, light speed in the air, beam waist radius, scattering function and other parameters [34]. Given the laminar flow conditions and the particle cross flow velocity confined to XY plane, the vector $\mathbf{z}(t)$ equals to a zero vector for all the time. Therefore, the general mathematical model of the DBS in (3.2) can be rewritten as,

$$S(t) = A_{DBS} \exp[-2\frac{\mathbf{x}^2(t)\cos^2(\theta/2)+\mathbf{y}^2(t)}{r_m^2}] + A_{DBS} \exp[-2\frac{\mathbf{x}^2(t)\cos^2(\theta/2)+\mathbf{y}^2(t)}{r_m^2}]\cos\{2\pi[F_B t + D\mathbf{x}(t)]+\varphi_0\} \quad (3.5)$$

From (3.5), it can be seen that the envelope of the DBS is simultaneously affected by the particle displacement on **X** and **Y** axis. The displacement on **Z** axis has no effect on the envelope. In addition, the instantaneous frequency of the DBS is only determined by the particle displacement on **X** axis, *i.e.* $\mathbf{x}(t)$. Assuming that the particle moves in the DC excitation field and passes through the centre of the measurement volume, it can be seen from (3.5), the maximum amplitude of the Gaussian envelope of DBS appears in the middle of the signal burst. This maximum point corresponds to the time instance when the particle is passing through the measurement centre. The particle motion in the measurement volume, on the **XY** plane, is shown in Fig. 3.2.

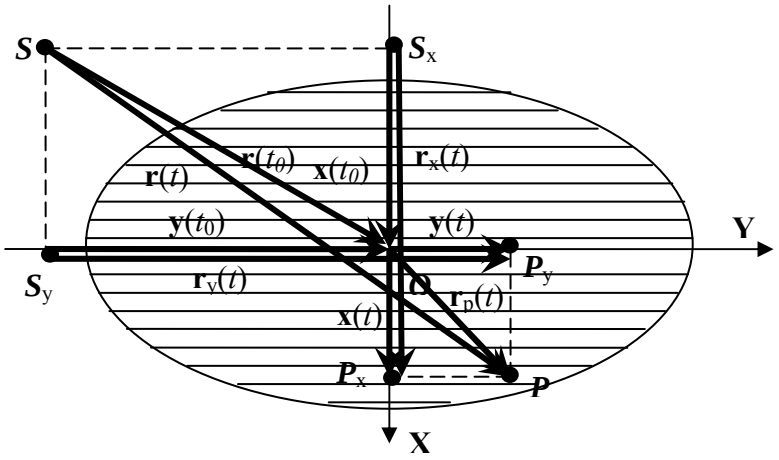

Fig. 3.2 Particle motion in the measurement volume on **XY** plane

The particle moves from the point ***S*** to point ***P***. The centre of the volume, ***O***, coincides with the origin of the coordinate system. $\mathbf{r}(t)$ is the vector from point ***S*** to ***P***, which represents the particle displacement during the movement. $\mathbf{r}_x(t)$ and $\mathbf{r}_y(t)$ is the projection of $\mathbf{r}(t)$ on **X** and **Y** axis. $\mathbf{r}_p(t)$ is the vector from ***O*** to ***P***, which is the particle position within the measurement volume during the movement. $\mathbf{r}_p(t)$ is projected on **X** and **Y** axis respectively and correspondingly generates vectors $\mathbf{x}(t)$ and $\mathbf{y}(t)$. The particle position is characterized by $\mathbf{x}(t)$ and $\mathbf{y}(t)$ in the DBS model. The vector $\mathbf{r}(t_0)$ points from ***S*** to ***O*** which denotes the particle displacement before it reaches the centre of volume. t_0 is the time when the particle reaches the

volume centre, ***O***. The projections on the two axis are $\mathbf{x}(t_0)$ and $\mathbf{y}(t_0)$. Finally, the vector equation in the **X** and **Y** direction can be given as,

$$\begin{aligned} \mathbf{X}&: \mathbf{x}(t_0) + \mathbf{x}(t) = \mathbf{r}_x(t) \\ \mathbf{Y}&: \mathbf{y}(t_0) + \mathbf{y}(t) = \mathbf{r}_y(t) \end{aligned} \tag{3.6}$$

Therefore, the position of particle $\boldsymbol{P}(\mathbf{x}(t), \mathbf{y}(t))$ within the measurement volume can be expressed as,

$$\begin{aligned} \mathbf{X}&: \mathbf{x}(t) = \mathbf{r}_x(t) - \mathbf{x}(t_0) \\ \mathbf{Y}&: \mathbf{y}(t) = \mathbf{r}_y(t) - \mathbf{y}(t_0) \end{aligned} \tag{3.7}$$

3.3 The Mathematical Models of DBS in Different Excitation Fields

3.3.1 Introduction

In the previous section the time domain description of the DBS has been introduced. In this section the discussion will focus on the effect of particle trajectory via the measurement volume on the properties of the DBS. Four kinds of particle motions will be considered: constant-particle velocity (steady state), constant-particle acceleration, particle motion in the sine-wave and particle motion in the square-wave excitation field. The specific DBS models corresponding to different particle excitation systems will be derived from the general mathematical model of the DBS in (3.5).

3.3.2 DC Excitation Field - Steady State

In the DC excitation field, the particle travels through the measurement volume with a constant velocity when the drag force and the electric force are in balance. The corresponding mathematical model of the DBS is shown below. Given the particle velocity on **X** and **Y** axis as,

$$\begin{aligned} \mathbf{V}_x(t) &= \mathbf{V}_x \\ \mathbf{V}_y(t) &= \mathbf{V}_y \end{aligned} \tag{3.8}$$

where, $\mathbf{V}_y(t)$ is the mean flow velocity, which is constant in the measurement experiments. From (3.6), there are

$$\begin{aligned}\mathbf{r}_x(t) &= \mathbf{r}_{0x} + \int_0^t \mathbf{V}_x(t)dt = \mathbf{r}_{0x} + \int_0^t \mathbf{V}_x dt = \mathbf{V}_x t \\ \mathbf{r}_y(t) &= \mathbf{r}_{0y} + \int_0^t \mathbf{V}_y(t)dt = \mathbf{r}_{0y} + \int_0^t \mathbf{V}_y dt = \mathbf{V}_y t\end{aligned} \tag{3.9}$$

where $\mathbf{r}_{0x=0}$, $\mathbf{r}_{0y}$=0.

$$\begin{aligned}\mathbf{x}(t_0) &= -\mathbf{x}_0 + \int_0^{t_0} \mathbf{V}_x(t)dt = -\mathbf{x}_0 + \mathbf{V}_x t_0 \\ \mathbf{y}(t_0) &= -\mathbf{y}_0 + \int_0^{t_0} \mathbf{V}_y(t)dt = -\mathbf{y}_0 + \mathbf{V}_y t_0\end{aligned} \tag{3.10}$$

From (3.7) and (3.10), the particle position ($\mathbf{x}(t)$,$\mathbf{y}(t)$) in the measurement volume can be obtained,

$$\begin{aligned}\mathbf{x}(t) &= \mathbf{x}_0 + \mathbf{V}_x(t - t_0) \\ \mathbf{y}(t) &= \mathbf{y}_0 + \mathbf{V}_y(t - t_0)\end{aligned} \tag{3.11}$$

As mentioned above, t_0 is the time corresponding to the particle being exactly at the centre of the measurement volume (x_0, y_0 being 0). Thus, (3.11) can be simplified as

$$\begin{aligned}\mathbf{x}(t) &= \mathbf{V}_x(t - t_0) \\ \mathbf{y}(t) &= \mathbf{V}_y(t - t_0)\end{aligned} \tag{3.12}$$

By substituting $\mathbf{x}(t)$ and $\mathbf{y}(t)$ in (3.5) by (3.12), the DBS model in the DC excitation field is obtained

$$\begin{aligned}S(t) = A_{DBS} \exp\{-2\frac{[\mathbf{V}_x(t - t_0)]^2 \cos^2(\theta/2) + [\mathbf{V}_y(t - t_0)]^2}{r_m^2}\} \\ \times\{1 + \cos\{2\pi[F_B t + D\mathbf{V}_x(t - t_0)] + \varphi_0\}\}\end{aligned} \tag{3.13}$$

3.3.3 DC Excitation Field – Constant-particle Acceleration

When a particle moves in the measurement volume, it is affected by two forces. One is the electric force, the other one is the drag force due to the viscous medium.

These two forces are defined as,

$$\mathbf{F}_e = \mathbf{E}q \tag{3.14}$$

where q is the particle charge, **E** is the excitation field vector in the direction of particle drift velocity.

$$\mathbf{F}_{drag} = -3\pi\eta d\mathbf{v}_x(t)/C_c \tag{3.15}$$

where C_c is the Cunningham slip correction factor, η is the air viscosity, $\mathbf{v}_x(t)$ is the relative real-time velocity vector between the air and particle. It can be seen that the drag force is proportional to the particle velocity and acts in the opposite direction.

The equation of particle motion in the presence of the DC excitation field-constant-particle acceleration is shown in (3.16).

$$\mathbf{F}_e\text{-}\mathbf{F}_{drag} = m\mathbf{a} \tag{3.16}$$

where **a** is the constant-particle acceleration, m is the mass of the particle.

For the particle motion with a constant acceleration, the particle velocity in the **X** and **Y** directions are,

$$\begin{aligned} \mathbf{V}_x(t) &= \mathbf{V}_{x0} + \mathbf{a}t \\ \mathbf{V}_y(t) &= \mathbf{V}_y \end{aligned} \tag{3.17}$$

where $\mathbf{V}_{x0}$ is the original velocity in the X direction.

Thus, from (3.15) and (3.17), $\mathbf{F}_{drag}$ is proportional to t, when $\mathbf{V}_{x0}$ equals to zero. From (3.14) and (3.16), it can be seen that the field strength, **E**, is directly proportional to the time,

$$\mathbf{E}=\mathbf{b}+\mathbf{k}t \tag{3.18}$$

where **b**, **k** are constant. $\mathbf{b}=m\mathbf{a}/q$, $\mathbf{k}=3\pi\eta d\mathbf{a}/(C_c q)$.

When the electric field **E** defined in (3.18) is increasing, the difference between the electric force and the drag force remains constant. Therefore, the constant acceleration of the particle can be achieved. The schematic diagram of the relationship between $\mathbf{F}_e$ and $\mathbf{F}_{drag}$ is shown in Fig. 3.3.

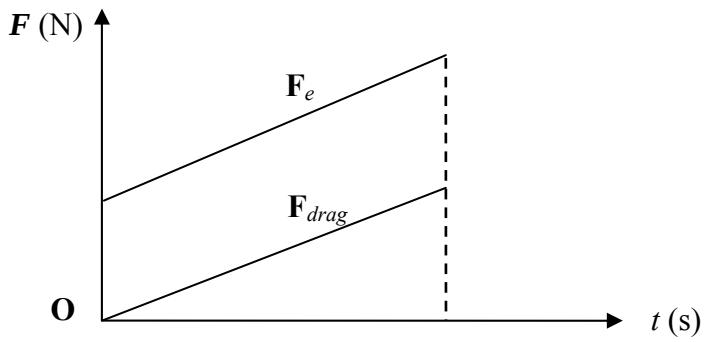

Fig. 3.3 Schematic diagram of relationship between the electric force and the drag force

From (3.6), there are,

$$\begin{aligned}\mathbf{r}_x(t) &= \mathbf{r}_{0x} + \int_0^t \mathbf{V}_x(t)dt = \mathbf{r}_{0x} + \int_0^t (\mathbf{V}_{x0} + \mathbf{a}t)dt = \mathbf{V}_{x0}t + \frac{1}{2}\mathbf{a}t^2 \\ \mathbf{r}_y(t) &= \mathbf{r}_{0y} + \int_0^t \mathbf{V}_y(t)dt = \mathbf{r}_{0y} + \int_0^t \mathbf{V}_y dt = \mathbf{V}_y t\end{aligned} \tag{3.19}$$

where $\mathbf{r}_{0x=0}$, $\mathbf{r}_{0y}$=0.

$$\begin{aligned}\mathbf{x}(t_0) &= -\mathbf{x}_0 + \int_0^{t_0} \mathbf{V}_x(t)dt = -\mathbf{x}_0 + \mathbf{V}_{x0}t_0 + \frac{1}{2}\mathbf{a}t_0^2 \\ \mathbf{y}(t_0) &= -\mathbf{y}_0 + \int_0^{t_0} \mathbf{V}_y(t)dt = -\mathbf{y}_0 + \mathbf{V}_y t_0\end{aligned} \tag{3.20}$$

Based on (3.7) and (3.20), the particle position ($\mathbf{x}(t)$,$\mathbf{y}(t)$) in the measurement volume can be obtained,

$$\begin{aligned}\mathbf{x}(t) &= \mathbf{x}_0 + \mathbf{V}_{x0}(t - t_0) + \frac{1}{2}\mathbf{a}(t^2 - t_0^2) \\ \mathbf{y}(t) &= \mathbf{y}_0 + \mathbf{V}_y(t - t_0)\end{aligned} \tag{3.21}$$

Similarly to (3.11), (3.21) can be simplified as

$$\begin{aligned}\mathbf{x}(t) &= \mathbf{V}_{x0}(t - t_0) + \frac{1}{2}\mathbf{a}(t^2 - t_0^2) \\ \mathbf{y}(t) &= \mathbf{V}_y(t - t_0)\end{aligned} \tag{3.22}$$

By replacing $\mathbf{x}(t)$ and $\mathbf{y}(t)$ in (3.5) by (3.22), the DBS model corresponding to the constant-acceleration motion is obtained.

$$S(t) = A_{DBS} \exp\{-2\frac{[\mathbf{V}_{x0}(t-t_0)+\frac{1}{2}\mathbf{a}(t^2-t_0^2)]^2\cos^2(\theta/2)+[\mathbf{V}_y(t-t_0)]^2}{r_m^2}\} \times\{1+\cos\{2\pi\{F_B t + D[\mathbf{V}_{x0}(t-t_0)+\frac{1}{2}\mathbf{a}(t^2-t_0^2)]\}+\varphi_0\}\} \quad (3.23)$$

3.3.4 Sine-wave Excitation Field

In the sine-wave excitation field, the particle trajectory is sinusoidal. The procedure of obtaining the mathematical model of DBS in sine wave excitation is shown below. The particle velocity on **X** and **Y** axis are,

$$\begin{aligned}\mathbf{V}_x(t) &= \mathbf{A}_v \sin(\omega t)\\ \mathbf{V}_y(t) &= \mathbf{V}_y\end{aligned} \quad (3.24)$$

where A_v is the maximum amplitude of the particle velocity. From (3.6), there are,

$$\begin{aligned}\mathbf{r}_x(t) &= \mathbf{r}_{0x} + \int_0^t \mathbf{V}_x(t)dt = \mathbf{r}_{0x} + \int_0^t \mathbf{A}_v \sin(\omega t)dt = \frac{\mathbf{A}_v}{\omega}[1-\cos(\omega t)]\\ \mathbf{r}_y(t) &= \mathbf{r}_{0y} + \int_0^t \mathbf{V}_y(t)dt = \mathbf{r}_{0y} + \int_0^t \mathbf{V}_y dt = \mathbf{V}_y t\end{aligned} \quad (3.25)$$

where $\mathbf{r}_{0x=0}$, $\mathbf{r}_{0y}$=0.

$$\begin{aligned}\mathbf{x}(t_0) &= -\mathbf{x}_0 + \int_0^{t_0} \mathbf{V}_x(t)dt = -\mathbf{x}_0 + \frac{A_v}{\omega}[1-\cos(\omega t_0)]\\ \mathbf{y}(t_0) &= -\mathbf{y}_0 + \int_0^{t_0} \mathbf{V}_x(t)dt = -\mathbf{y}_0 + \mathbf{V}_y t_0\end{aligned} \quad (3.26)$$

Based on (3.7) and (3.26), the particle position ($\mathbf{x}(t)$,$\mathbf{y}(t)$) in the measurement volume can be obtained,

$$\begin{aligned}\mathbf{x}(t) &= \mathbf{x}_0 + \frac{\mathbf{A}_v}{\omega}[\cos(\omega t_0)-\cos(\omega t)]\\ \mathbf{y}(t) &= \mathbf{y}_0 + \mathbf{V}_y(t-t_0)\end{aligned} \quad (3.27)$$

Similarly to (3.11), (3.27) can be simplified as

$$\begin{aligned}\mathbf{x}(t) &= \frac{\mathbf{A}_v}{\omega}[\cos(\omega t_0)-\cos(\omega t)]\\ \mathbf{y}(t) &= \mathbf{V}_y(t-t_0)\end{aligned} \quad (3.28)$$

By replacing $\mathbf{x}(t)$ and $\mathbf{y}(t)$ in (3.5) by (3.28), the DBS model in the sine-wave excitation field is given as

$$S(t) = A_{DBS} \exp\{-2\frac{\{\frac{\mathbf{A}_v}{\omega}[\cos(\omega t_0) - \cos(\omega t)]\}^2 \cos^2(\theta/2) + [\mathbf{V}_y(t-t_0)]^2}{r_m^2}\} \times\{1+\cos\{2\pi\{F_B t + D\{\frac{\mathbf{A}_v}{\omega}[\cos(\omega t_0) - \cos(\omega t)]\}\} + \varphi_0\}\} \tag{3.29}$$

3.3.5 Square-wave Excitation Field

In the square-wave excitation field, the direction of the drive excitation changes at intervals. Therefore the electric force can be expressed as below.

$$\mathbf{F}_e(t) = \begin{cases} q\mathbf{E} & 0 \le t < T/2 \\ -q\mathbf{E} & T/2 \le t < T \end{cases} \tag{3.30}$$

where T is the period of the square-wave excitation.

As mentioned before, besides the electric force, the particle is affected by the drag force due to the viscous medium. The drag force can be expressed as,

$$\mathbf{F}_{drag} = -3\pi\eta d\mathbf{v}_x(t)/C_c \tag{3.31}$$

The equation of particle motion in the presence of the square-wave excitation field can be written as,

$$\mathbf{F}_e + \mathbf{F}_{drag} = md\mathbf{v}(t)/dt \tag{3.32}$$

When the drag force, $\mathbf{F}_{drag}$, and the externally applied electric force, $\mathbf{F}_e$, come into balance, the particle is in mechanical equilibrium and a steady-state velocity of the particle relative to the air results. The time that it takes for this to occur is characterized by the relaxation time τ [7], which is defined as

$$\tau = \frac{\rho d^2 C_c}{18\eta} \tag{3.33}$$

where ρ is the particle density. From (3.33), it can be seen that the relaxation time is affected by particle diameter but has no relationship to the excitation field.

When $\tau<T/2$, the particle velocity on **X** and **Y** axis can be calculated. The solution to (3.32) is given as,

$$\begin{aligned}\mathbf{v}_x(t) &= \begin{cases}\mu\mathbf{E}(1-e^{-t/\tau}) & 0 \le t < T/2 \\ \mu\mathbf{E}[2e^{-(t-T/2)/\tau}-1] & T/2 \le t < T \\ \mu\mathbf{E}[1-2e^{-(t-T)/\tau}] & T \le t < T+\tau\end{cases} \\ \mathbf{v}_y(t) &= \mathbf{V}_y\end{aligned} \tag{3.34}$$

where $\mathbf{V}_y$ is the mean flow velocity in the **Y** direction, μ is the electrical mobility of particle,

$$\mu = \frac{q\,C_c}{3\,\pi\,\eta\,d} \tag{3.35}$$

The derivation of the particle velocity and position in the measurement volume is shown in Appendix B.

The particle motion in the period from 0 to T+τ can be divided into five segments, (*a*) ~ (*e*), as shown in Fig. 3.4.

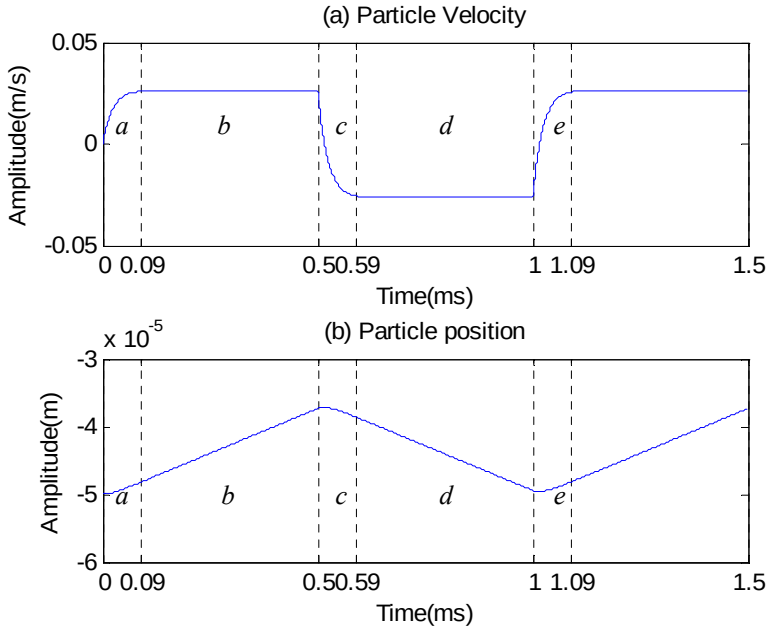

Fig. 3.4 (*a*) Particle velocity in the square wave excitation field, V_x=26.5*mm/s*, *q*=500*e*, *d*=3μ*m*, *E*=165*kV/m*, *f*=1*k*Hz, $\boldsymbol{\tau}$=0.0226*ms*, (*b*) Particle position

Assuming the direction of particle motion in the first segment is positive. *a*) When $\mathbf{F}_e+\mathbf{F}_{drag}>0$, the drag force increases and the particle is accelerated with the velocity changing from 0 to $\mu\mathbf{E}$ in the direction of the driving field. *b*) When $\mathbf{F}_e+\mathbf{F}_{drag}=0$, the particle reaches equilibrium and moves with a constant velocity, $\mu\mathbf{E}$. *c*) Due to the change of the field direction, $\mathbf{F}_e+\mathbf{F}_{drag}<0$. The particle is decelerated with the velocity changing from $\mu\mathbf{E}$ to 0 and simultaneously the drag force decreasing to 0. Next, the particle is accelerated in the negative direction with the velocity changing from 0 to $-\mu\mathbf{E}$. *d*) $\mathbf{F}_e+\mathbf{F}_{drag}=0$, the particle achieves equilibrium again and moves with constant velocity $-\mu\mathbf{E}$. *e*) The field direction is changed again. The particle is decelerated with the velocity from $-\mu\mathbf{E}$ to $\mu\mathbf{E}$.

From (3.6), there are,

$$\begin{aligned}
\mathbf{r}_x(t) &= \mathbf{r}_{0x} + \int_0^t \mathbf{V}_x(t)dt = \begin{cases} \mathbf{r}_{0x} + \int_0^t \mu\mathbf{E}(1-e^{-t/\tau})\,dt & 0 \le t < T/2 \\ \mathbf{r}_{0x} + \int_0^t \mu\mathbf{E}[2e^{-(t-T/2)/\tau} - 1]dt & T/2 \le t < T \\ \mathbf{r}_{0x} + \int_0^t \mu\mathbf{E}[1-2e^{-(t-T)/\tau}]dt & T \le t < T+\tau \end{cases} \\
\mathbf{r}_y(t) &= \mathbf{r}_{0y} + \int_0^t \mathbf{V}_y(t)dt = \mathbf{r}_{0y} + \int_0^t \mathbf{V}_y dt = \mathbf{V}_y t
\end{aligned} \tag{3.36}$$

where $\mathbf{r}_{0x=0}$, $\mathbf{r}_{0y}=0$.

$$\begin{aligned}
\mathbf{x}(t_0) &= -\mathbf{x}_0 + \int_0^{t_0} \mathbf{V}_x(t)dt \\
\mathbf{y}(t_0) &= -\mathbf{y}_0 + \int_0^{t_0} \mathbf{V}_y(t)dt = -\mathbf{y}_0 + \mathbf{V}_y t_0
\end{aligned} \tag{3.37}$$

Based on (3.7) and (3.37), the particle position ($\mathbf{x}(t)$,$\mathbf{y}(t)$) in the measurement volume can be obtained,

$$\begin{aligned}
\mathbf{x}(t) &= \begin{cases} \mathbf{x}_0 + \mu\mathbf{E}[t - t_0 - \tau(e^{-t/\tau} - e^{-t_0/\tau})] & 0 \le t < T/2 \\ \mathbf{x}(T/2) - \mu\mathbf{E}[t - T/2 + 2\tau e^{-(t-T/2)/\tau}] & T/2 \le t < T \\ \mathbf{x}(T) + \mu\mathbf{E}[t - T + 2\tau e^{-(t-T)/\tau}] & T \le t < T+\tau \end{cases} \\
\mathbf{y}(t) &= \mathbf{y}_0 + \mathbf{V}_y(t - t_0)
\end{aligned} \tag{3.38}$$

Similarly to (3.11), (3.38) can be simplified as

$$\mathbf{x}(t)=\begin{cases}\mu\mathbf{E}[t-t_0-\tau(e^{-t/\tau}-e^{-t_0/\tau})] & 0\le t<T/2\\ \mathbf{x}(T/2)-\mu\mathbf{E}[t-T/2+2\tau e^{-(t-T/2)/\tau}] & T/2\le t<T\\ \mathbf{x}(T)+\mu\mathbf{E}[t-T+2\tau e^{-(t-T)/\tau}] & T\le t<T+\tau\end{cases}$$
$$\mathbf{y}(t)=\mathbf{V}_y(t-t_0) \tag{3.39}$$

By replacing $\mathbf{x}(t)$ and $\mathbf{y}(t)$ in (3.5) by (3.39), the DBS model in the square-wave excitation field is obtained.

3.4 Simulation Results based on the Mathematical Models of DBSs in Different Excitation Fields

3.4.1 Simulation Results in DC Excitation Field – Steady State

In the DC excitation field – steady state, the particle passes through the measurement volume with a constant velocity. Therefore, the frequency of Doppler signal is constant and the particle trajectory is a straight line. In order to learn more about the characteristics of the DBS mentioned above, the simulation based on the mathematical model defined in (3.13) has been implemented and shown in Fig. 3.5. The particle motion via the measurement volume and the correspondingly generated DBS are shown in Fig. 3.5 (a) and (b), where λ is the wavelength of laser beam, θ is the intersection angle of the two beams, i is the fringe spacing, d_m is the Gaussian beam diameter, F_B is the frequency shift, A_{DBS} is the maximum amplitude of DC and AC part of DBS, V_x is the particle constant velocity in **X** direction, V_y is the mean velocity in **Y** direction, φ_0 is the original phase of DBS, t_0 is the time slot when particle passing through the measurement volume centre, N is the number of samples, f_s is the sampling frequency, σ_n is the variance of the Gaussian noise.

The relationship between particle trajectory via the measurement volume and the corresponding DBS is clearly shown in Fig. 3.5 (a) and (b). It can be seen that the envelope of the DBS which is a standard Gaussian envelope, is determined by the particle position in both the **X** and **Y** directions in the measurement volume. The envelope reaches its peak value when the particle is passing through the centre of the measurement volume. This is because the maximum intensity lies at the centre of the intersection laser beams. The measurement volume boundary is defined by the e^{-2}

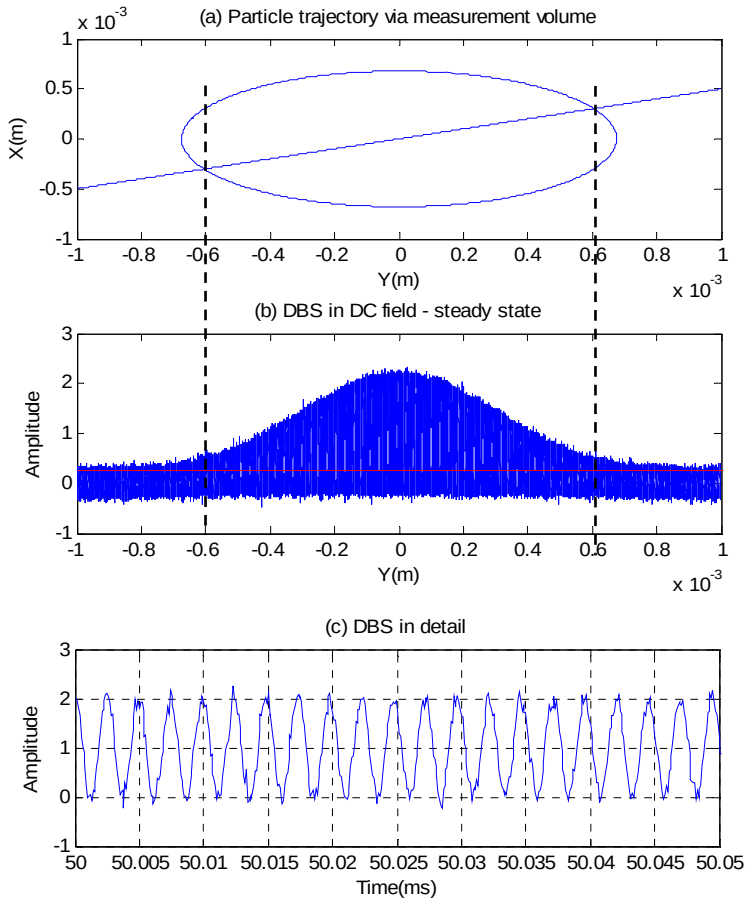

Fig. 3.5 (a) Particle trajectory via the measurement volume in the DC excitation field – steady state, (b) Corresponding DBS in the DC excitation field for λ=514.5nm, θ=0.2251rad, i=2.99μm, d_m=1.35mm, F_B=400kHz, A_{DBS}=1, V_x=10mm/s, V_y=0.05m/s, x_0=0, φ_0=0rad, t_0=0.05s, N=10^6, f_s=10MHz, σ_n^2=0.01, (c) DBS in detail.

intensity decay of the interference area in relation to its maximum value atthe centre of the volume. The red line in Fig 3.5 (b) denotes the e^{-2} decay of the maximum amplitude which is equal to $2\times e^{-2}$=0.2706. When particle moves into the measurement volume, the corresponding DBS (the part above the red line) is generated.

Additionally, it can be concluded that the frequency of the DBS is only determined by the particle velocity in the **X** direction in the measurement volume. From Fig. 3.5 (c), it can also be seen that the frequency of DBS is constant because the particle moves with a constant velocity in the **X** direction in the measurement volume.

The constant velocity in the **X** direction can be approximately estimated from the DBS spectrum. The spectrum of the DBS from Fig. 3.5 is shown in Fig. 3.6. The Doppler frequency of the DBS is equal to F_D=404.37kHz. The relationship between

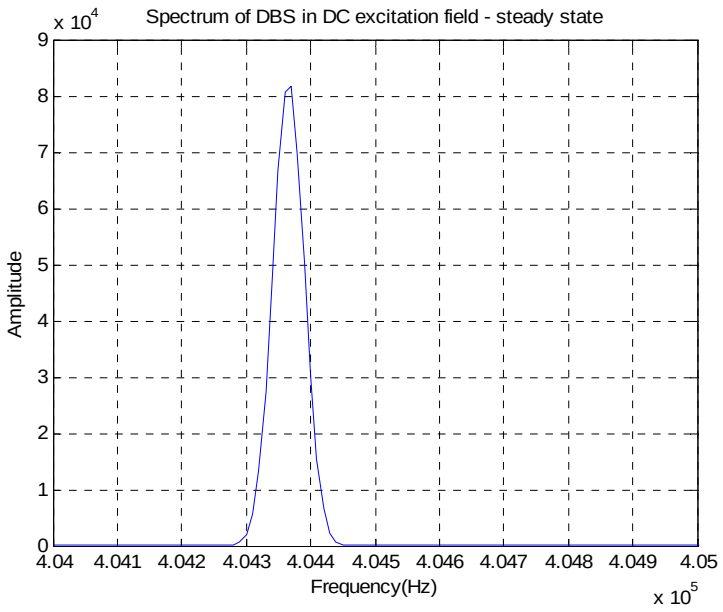

Fig. 3.6 Spectrum of Doppler Burst Signal in DC excitation field – steady state

the Doppler frequency and the particle velocity is given in (3.1). For a given simulation conditions, the constant particle velocity in the **X** direction, $V_{x,}$ can be calculated as V_x=10.0094mm/s. This result agrees very well with the simulation condition, V_x=10mm/s. It can be concluded that the spectral analysis could be effectively used to estimate the velocity of the particle in the DC excitation field – steady state. Comprehensive discussion of the accuracy of the spectral analysis in the estimation of particle velocity is provided in chapter 5.

3.4.2 Simulation Results in DC Excitation Field – Constant-particle Acceleration

In the DC excitation field – constant-particle acceleration, the particle passes through the measurement volume with a constant acceleration. Therefore, the frequency of Doppler signal increases with a constant acceleration. The particle trajectory is no longer a straight line but a parabola. In order to investigate the characteristics of DBS mentioned above, the simulation based on the mathematical model defined by (3.23) has been implemented and the simulation results are shown in Fig. 3.7.

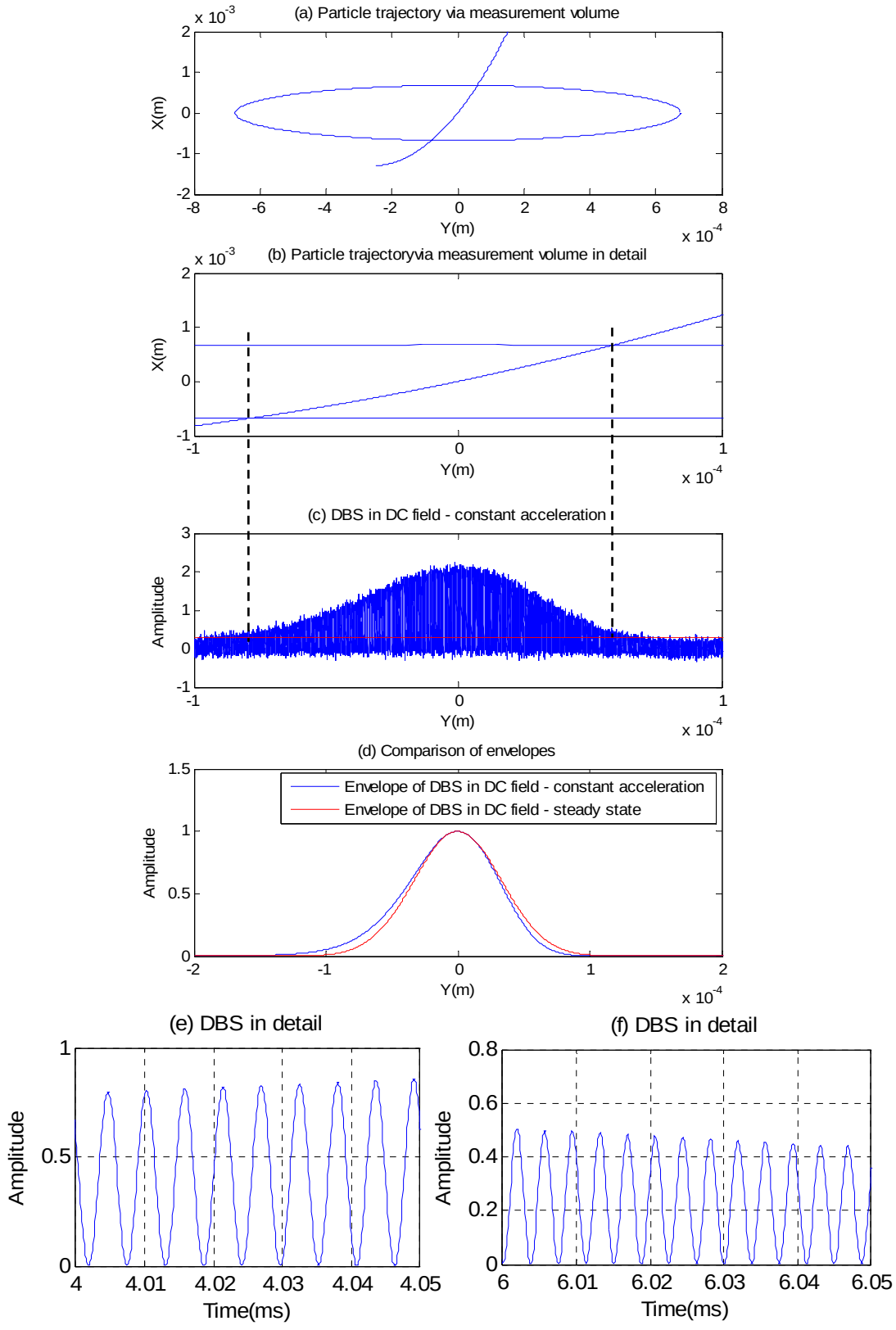

Fig. 3.7 (a) & (b) Particle trajectory and details via the measurement volume in the DC excitation field – constant acceleration, (c) Corresponding DBS for λ=514.5nm, θ=0.2251rad, i=2.99μm, d_m=1.35mm, F_B=400kHz, A_{DBS}=1, V_{x0}=0.01m/s, a=100m/s^2, V_y=0.05m/s, φ_0=0rad, t_0=0.005s, N=10^5, f_s=10MHz, σ_n^2=0.01, (d) Comparison of envelopes corresponding to different scenarios (e) & (f) DBS in detail

The relationship between particle trajectory via the measurement volume and the corresponding DBS is clearly shown in Fig. 3.7 (b) and (c). It can be concluded that the envelope of the DBS is mainly determined by the particle position in both the **X** and **Y** directions in the measurement volume. The red line in Fig 3.7 (c) denotes the e^{-2} decay of the maximum amplitude which is equal to $2\times e^{-2}=0.2706$. When particle enters the measurement volume, the corresponding DBS (the part above the red line) is generated.

Additionally, from Fig. 3.7 (d), it can be seen that the envelope of the signal is not a standard Gaussian envolope due to the particle acceleration. In order to illustrate it clearly, the envelope of the DBS in DC excitation field – steady state has been compared with the envelope of the DBS in the DC excitation field – constant acceleration. In this comparison the constant particle velocity equals to the mean velocity of accelerating particle. From Fig. 3.7 (d) it can be observed, that the shape of the envelope in DC excitation field – constant acceleration is different from the one in DC excitation field – steady state (standard Gaussian envelope) .

Moreover, it can be concluded that the real-time frequency of DBS is determined by the particle position in the **X** direction in the measurement volume. However, the instantaneouse frequency of DBS is no longer a constant as shown in Fig. 3.7 (e) and (f). In order to show the frequency difference clearly, the frequency shift F_B (400*k*Hz) and noise have been removed in Fig. 3.7 (e) and (f). The spectum of the DBS from Fig. 3.7 is shown in Fig. 3.8. The instantaneouse particle velocity can't be estimated from the spectral analysis because the real-time information is not available in the spectrum.

It can also be seen that the width of spectrum is larger than the one obtained in the DC excitation field. However, some other information, such as, the mean value of the particle velocity through the measurement volume could be estimated from the spectrum. Based on the example in Fig. 3.8, the peak value of frequency in the spectrum is equal to f=622.4*k*Hz. From (3.1), the mean velocity can be derived, $V_{mx}=0.5094m/s$. This estimated result compares well with the simulation condition, $V_{mx}=0.51m/s$.

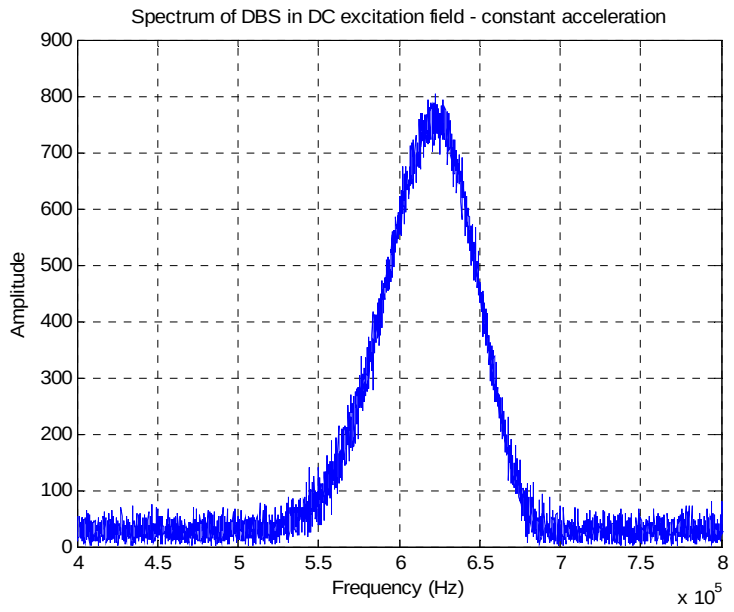

Fig. 3.8 The spectrum of Doppler Burst Signal in DC excitation field – constant acceleration

3.4.3 Simulation Results in Sine-wave Excitation Field

In the sine-wave excitation field, the particle passes through the measurement volume with a sinusoidal velocity. Therefore, the instantaneous frequency of the Doppler signal increases and decreases as a sine-wave function. In order to investigate the characteristics of DBS mentioned above, the simulation based on the mathematical model defined in (3.29) has been implemented. The simulation results and the relationship between particle trajectory via the measurement volume and the corresponding DBS are clearly shown in Fig. 3.9 (a) and (b). It can be concluded that the envelope of DBS is mainly determined by the particle position in both the **X** and **Y** directions in the measurement volume. The red line in Fig 3.9 (b) denotes the e^{-2} decay of the maximum amplitude whose value equals to $2\times e^{-2}=0.2706$. When particle enters the measurement volume, the corresponding DBS (the part above the red line) is generated.

Compared to the result in DC excitation field – steady state, it can be found from Fig. 3.9 that the envelope of the signal is not a standard Gaussian envelope due to the sine-wave particle motion via the measurement volume.

The signal details have been shown in Fig. 3.9 (c). In order to show the frequency difference clearly, the frequency shift F_B (400*k*Hz) has been removed. As shown in Fig. 3.9 (c), the instantaneous frequency of DBS sometimes increases and

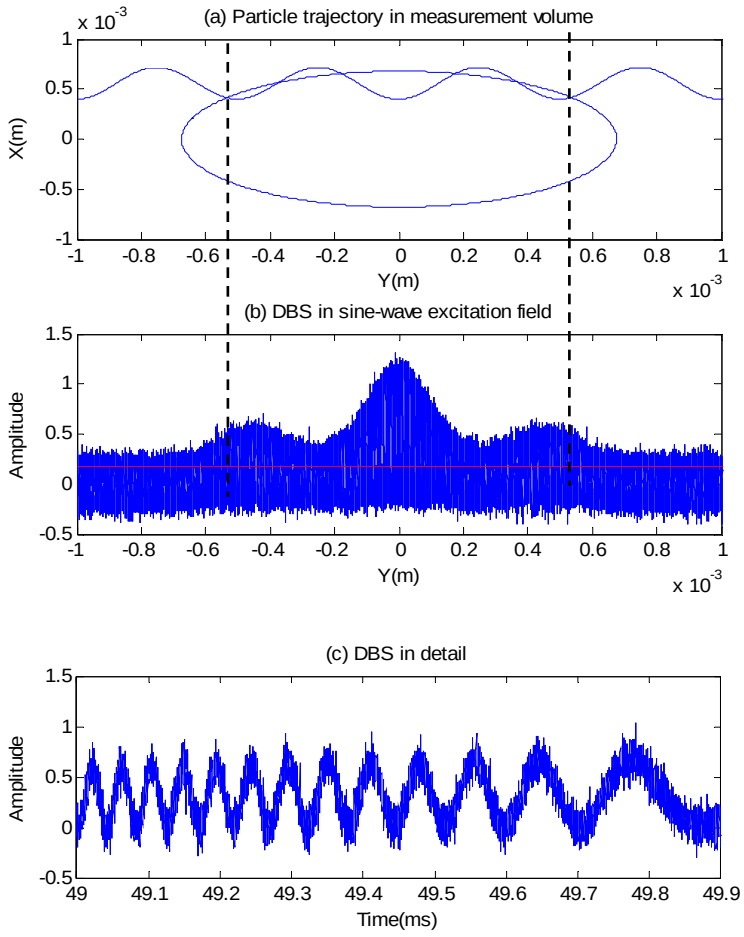

Fig. 3.9 (a) Particle trajectory via the measurement volume in the sine-wave excitation field, (b) Corresponding DBS for λ=514.5nm, θ=0.2251rad, i=2.99μm, d_m=1.35mm, F_B=400kHz, A_{DBS}=1, A_v=100mm/s, ω=200π rad/s, x_0=400μm, V_y=0.05m/s, φ_0=0 rad, t_0=0.05s, N=10^6, f_s=10MHz, σ_n^2=0.01, (c) DBS in detail

sometimes decreases, which is determined by the particle sinusoidal trajectory in the **X** direction via the measurement volume. The DBS in the sine-wave excitation field can be regarded as a Frequency Modulated (FM) signal.

The spectrum of DBS in the sine-wave excitation field has been shown in Fig. 3.10. It is clear that the instantaneouse particle velocity can't be estimated from the spectral analysis. This method is not suitable for real-time signal processing. However, from the spectrum, some other information can be derived. Because DBS can be regarded as a FM signal, DBS in the sine-wave excitation field can be analysed based on the principles of the frequency modulation. Frequency deviation is defiend as the maximum difference between frequency of an FM signal and the carrier frequency. In (3.1), F_B corresponds to the carrier frequency. The maximum instantaneous difference

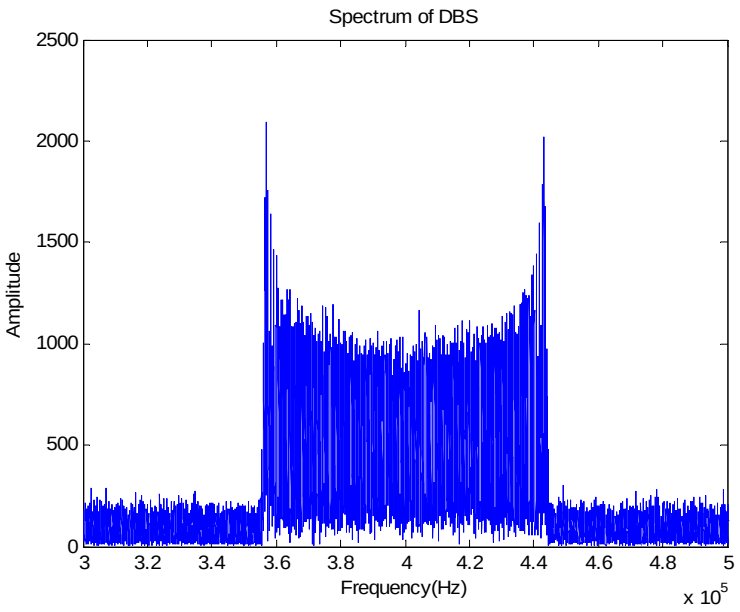

Fig. 3.10. Spectrum of DBS in the sine-wave excitation field

is the maximum value of $DV_x(t)$. In the example presented in Fig. 3.10, the peak frequency deviation is approximately equal to 4.5×10^4Hz. Therefore the bandwidth of DBS can be determined based on Carson's rule [53].

3.4.4 Simulation Results in Square-wave Excitation Field

In the square-wave excitation field, the particle passes through the measurement volume with a nearly-constant velocity. Therefore, the frequency of the corresponding DBS can be roughly regarded as a constant. The particle trajectory is a triangular wave. In order to learn more about the characteristics of DBS the simulation based on the mathematical model defined by (3.5) and (3.39) has been implemented. The simulation results are shown in Fig. 3.11.

The relationship between particle trajectory via the measurement volume and the corresponding DBS is clearly shown in Fig. 3.11 (a) and (b). The envelope of DBS is mainly determined by the particle position in both the **X** and **Y** directions in the measurement volume. The red line in Fig 3.11 (b) denotes the e^{-2} decay of the maximum amplitude whose value equals to $2\times e^{-2}=0.2706$. When particle moves into the measurement volume, the corresponding DBS (the part above the red line) is generated.

Compared to the result in DC field – steady state, it can be seen from Fig. 3.11

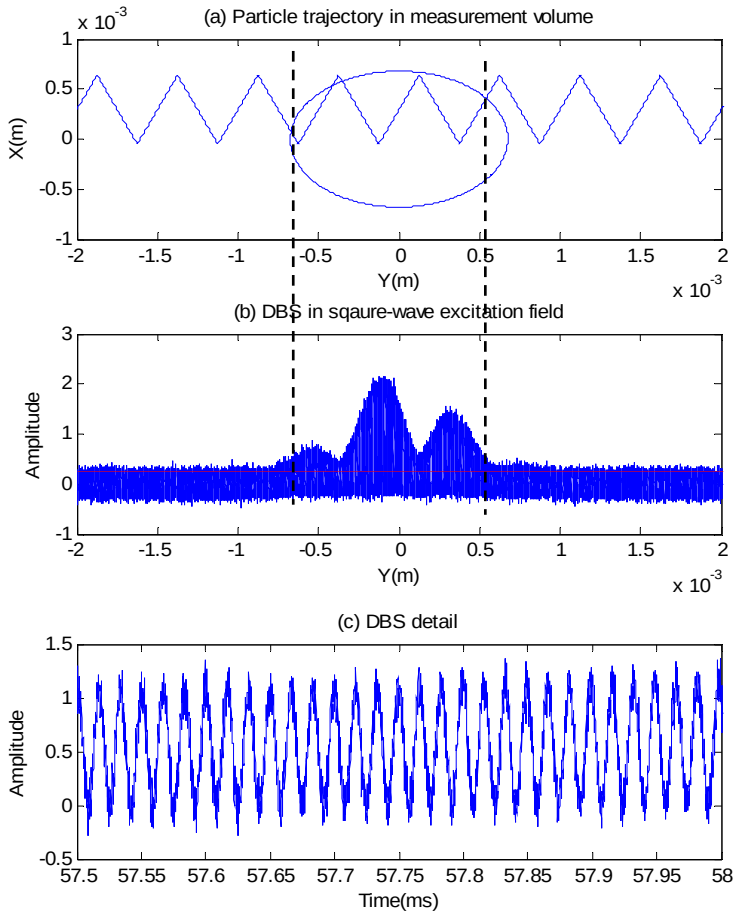

Fig. 3.11 (a) Particle trajectory via the measurement volume in square-wave excitation field, (b) Corresponding DBS for λ=514.5nm, θ=0.2251rad, i=2.99μm, d_m=1.35mm, F_B=400kHz, A_{DBS}=1, E=0.5MV/m, f_{drive}= 100Hz, q=260e, d=1μm, x_0=-50μm, V_y=0.05m/s, φ_0=0 rad, t_0=0.05s, N=10^6, f_s=10MHz, σ_n^2=0.01. (c) DBS detail.

that the envelope of the signal is not a standard Gaussian envelope due to the square-wave particle trajectory via the measurement volume. In different segments of the DBS determined by the direction of the particle velocity, the instantaneouse frequency of DBS is almost a constant as shown in Fig. 3.11 (c). In order to show the instantaneous frequency clearly, the the DBS signal has been downshifted by 400kHz. Due to the characteristics of particle motion in the square-wave excitation field, the frequency of DBS can be regarded as constant except short periods corrsponding to the particle acceleration and deceleration shown in Fig. 3.4. These period contribute to the spectral broadening of the DBS.

The spectrum of the DBS from Fig. 3.11 is shown in Fig. 3.12.

From the above figure, it can be seen that both the amplitude and the direction of the particle velocity, can be estimated from the spectral analysis. Compared to the

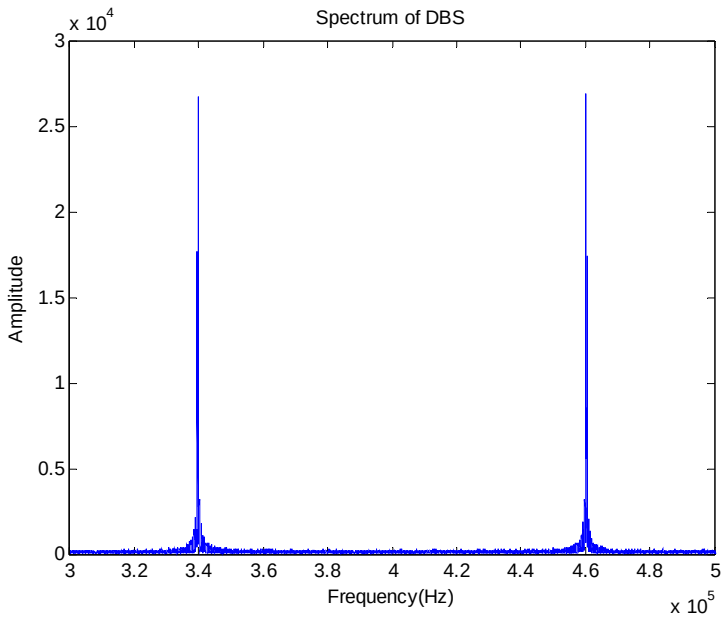

Fig. 3.12. Spectrum of DBS in the square-wave excitation field

DBS spectrum shown in Fig. 3.6, there are additional frequency components generated due to the particle acceleration and deceleration inside the measurement volume. However, as this examples illustates the velocity estimation by means of spectral analysis and peak detection could be successfully implemented. For instance, from Fig. 3.12, the estimated frequency of DBS is 460200Hz. From (3.1), the constant particle velocity in the **X** direction, $V_{x,}$ can be calculated as, V_x=0.1379*m*/*s*. This result agrees well with the simulation condition, V_x=0.1378*m*/*s*.

3.5 Discontinuous-burst Doppler Signals

Sometimes, both in the sine-wave and the square-wave excitation fields, the particle travels in and out of the measurement volume due to the oscillatory particle motion. Thus, there is a discontinuous DBS generated as shown in Fig. 3.13 and 3.14.

As shown in Fig. 3.13 and 3.14, the corresponding DBS is split into several smaller bursts because the particle moves outside of the measurement volume. The discontinuity in the DBS will creates difficulties in the signal processing. Firstly, sometimes the burst length is too short to be correctly estimated. Secondly, it creates ambiguity in the determination of the starting and ending points of the burst in the train of DBSs.

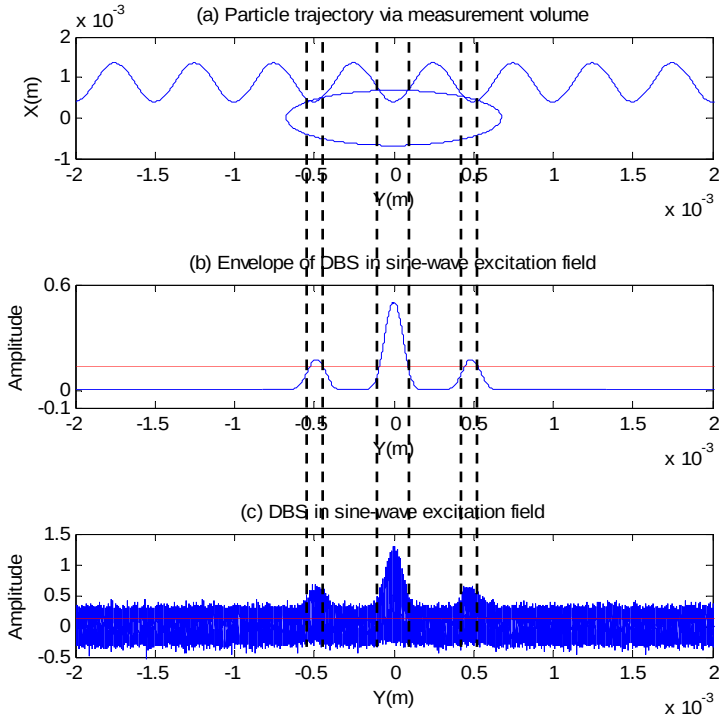

Fig. 3.13 Discontiuous DBS in sine-wave excitation field, (a) particle trajectory via the measurement volume, (b) Signal envelope, (c) DBS in sine-wave excitation field for λ=514.5nm, θ=0.2251rad, i=2.99μm, d_m=1.35mm, F_B=400kHz, ω=200π rad/s, A_{DBS}=1, x_0=400μm, A_v=300mm/s, φ_0=0, y_0=0, V_y=0.05m/s, t_0=0.05s, N=10^6, f_s=10MHz, σ_n^2=0.01.

3.6 Multi-burst Doppler Signals

3.6.1 Mathematical Model of Multi-burst Doppler Signals

As mentioned in the Section 3.2, the DBS described in (3.1) is generated by a single particle passing through the measurement volume. Sometimes, two or more particles will travel through the measurement volume at the same time. This creates an overlap of DBS, which is called the multi-burst DBS. For a given measurement volume V_{MV} and a given particle concentration number c_p, the number of particles n which are in the measurement volume at the same time can be described using Poisson distribution [54].

$$P(n) = \frac{(c_p V_{MV})^n}{n!} \exp(-c_p V_{MV}) \tag{3.40}$$

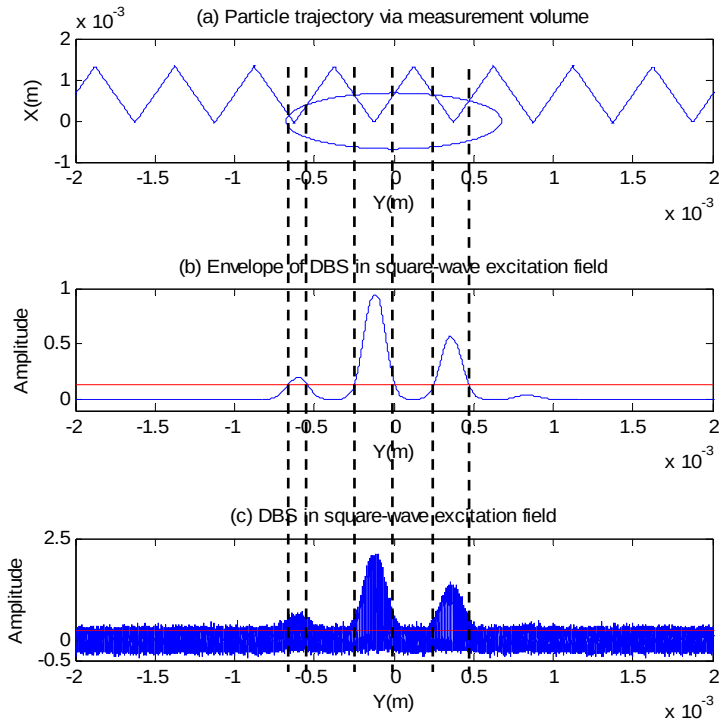

Fig. 3.14 Discontiuous DBS in the square-wave excitation field, (a) particle trajectory via the measurement volume, (b) Signal envelope, (c) DBS in the square-wave excitation field for λ=514.5nm, θ=0.2251rad, i=2.99μm, d_m=1.35mm, F_B=400kHz, A_{DBS}=1, f_{drive}=100Hz, E=1MV/m, d=1μm, q=520e, x_0=-50μm, φ=0 rad, y_0=0, V_y=0.05m/s, t_0=0.05s, N=10^6, f_s=10MHz, σ_n^2=0.01.

In this project, the measurement volume, calculated from the beam waist radius (r_w=100~200μm) and the intersection angle (θ=12.9deg), could reach up to V_{MV}=6.5×$10^{-11}m^3$. For instance, with a particle concentration number (c_p=1×$10^{10}/m^3$,), the probability of multi-burst signals (n=2) equals to 11% and can't be neglected. Therefore, it is necessary to consider dealing with the problem of multi-burst signal processing.

From (3.40), the probability of the multi-burst DBS can be reduced either by the reduction of the size of the measurement volume or the particle concentration [55].

The mathematical model of the multi-burst signal can be expressed as below,

$$S(t)=\sum_{i=1}^{N}S_i(t)$$

$$S_i(t)=A_{DBS}\exp[-2\frac{\mathbf{x}_i^2(t)\cos^2(\theta/2)+\mathbf{y}_i^2(t)}{r_m^2}] \tag{3.41}$$

$$+A_{DBS}\exp[-2\frac{\mathbf{x}_i^2(t)\cos^2(\theta/2)+\mathbf{y}_i^2(t)}{r_m^2}]\cos\{2\pi[F_Bt+D\mathbf{x}_i(t)]+\varphi_0\}$$

where N is the number of bursts in the signal, $S_i(t)$ corresponds to the burst signal generated by the i-th particle.

3.6.2 Simulation Results of Multi-burst Doppler Signals

Some examples of the dual-burst signals in different excitation fields are shown in Fig. 3.15 ~ 3.17. For the sake of clarity the different particle trajectories and the corresponding DBS envelopes are printed in different colours. First of all, the simulation results of dual-burst DBS in the DC excitation field are shown in Fig. 3.15.

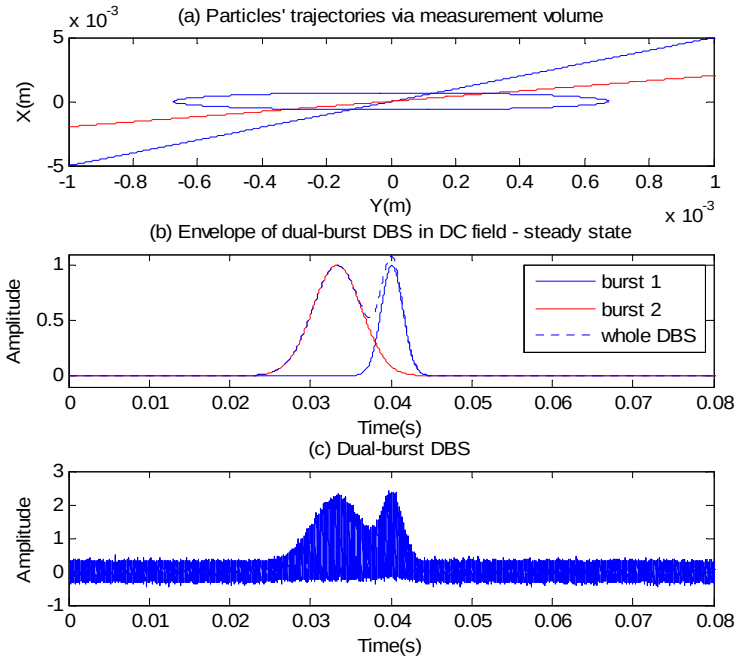

Fig. 3.15 (a) Particles' trajectories via the measurement volume, (b) Envelope of dual-burst DBS in the DC excitation field – steady state, (c) Corresponding Dual-burst DBS for λ=514.5nm, θ=0.2251rad, i=2.99μm, d_m=1.35mm, F_B=400kHz, A_{DBS}=1, x_{01}=-37.5μm, x_{02}=0, t_{01}=0.04s, t_{02}=0.0333s, V_{x1}=0.25m/s, V_{x2}=0.1m/s, φ_{01}=1.0708 rad, φ_{02}=0, y_0=0, V_y=0.05m/s, t_0=0.05s, N=10^6, f_s=10MHz, σ_n^2=0.01.

Secondly, the simulation results of dual-burst DBS in the sine-wave excitation field are presented in Fig. 3.16. Thirdly, the simulation results of dual-burst DBS in the square-wave excitation field are given in Fig. 3.17.

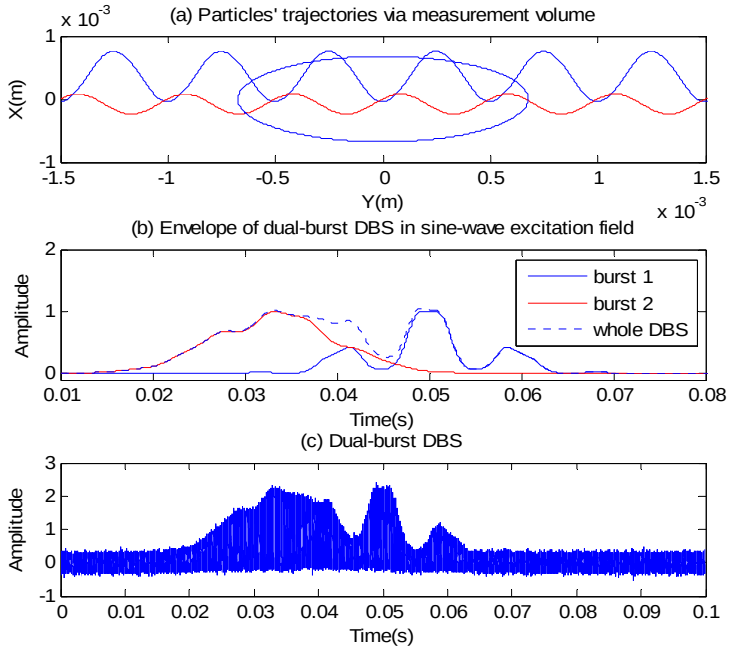

Fig. 3.16 (a) Particles' trajectories in the measurement volume, (b) Envelope of dual-burst DBS in the sine-wave excitation field, (c) Corresponding dual-burst DBS for λ=514.5nm, θ=0.2251rad, i=2.99μm, d_m=1.35mm, F_B=400kHz, ω=100rad/s, A_{DBS}=1, x_{01}=-37.5μm, x_{02}=0mm, t_{01}=0.05s, t_{02}=0.0333s, A_{v1}=0.25m/s, A_{v2}=0.1m/s, φ_{01}=1.0708 rad, φ_{02}=0 rad, y_0=0, V_y=0.05m/s, t_0=0.05s, N=10^6, f_s=10MHz, σ_n^2=0.01.

From Fig. 3.15 ~ 3.17, it can be seen that the multi-burst DBS is the superimposition of each burst of signal. Because the multi-burst signal is generated by more than one particle with different velocities, the corresponding spectrums are different from the one of the single-burst signal, and are shown in Fig. 3.18 ~ 3.20. Comparing these figures, it can be concluded that it is theoretically possible to estimate the velocities of particles by spectral analysis both in the DC excitation field and the square-wave excitation field. However, spectral analysis fails in the sine-wave excitation field because the peak value in the spectrum doesn't correspond to the Doppler frequency which is proportional to the particle velocity, as discussed in Section 3.4.3.

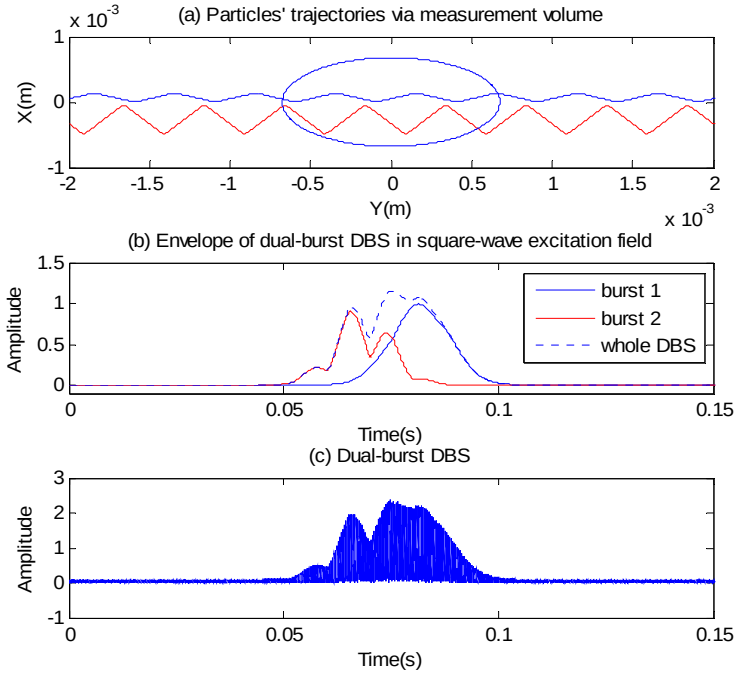

Fig. 3.17 (a) Particles' trajectories via the measurement volume, (b) Envelope of dual-burst DBS in the square-wave excitation field, (c) Corresponding dual-burst DBS for λ=514.5nm, θ=0.2251rad, i=2.99μm, d_m=1.35mm, F_B=400kHz, A_{DBS}=1, f_{drive}=100Hz, E=1MV/m, d_1=d_2=10μm, q_1=300e, q_2=1000e, x_{01}=0mm, x_{02}=-0.5mm, t_{01}=0.082s, t_{02}=0.0683s, φ_{01}=0 rad , φ_{02}=0.9292 rad, y_0=0, V_y=0.05m/s, , t_0=0.05s, N=10^5, f_s=0.5MHz, σ_n^2=0.01.

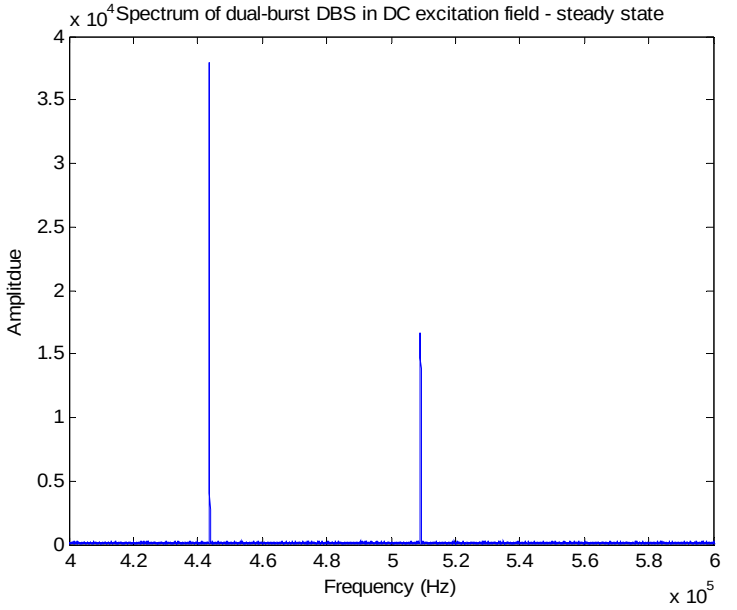

Fig. 3.18 Spectrum of dual-burst DBS in the DC excitation field – steady state

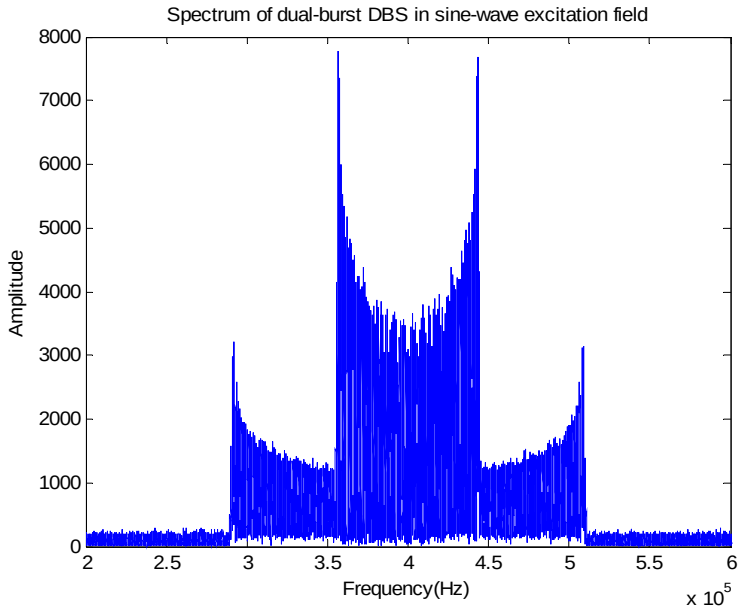

Fig. 3.19 Spectrum of dual-burst DBS in the sine-wave excitation field

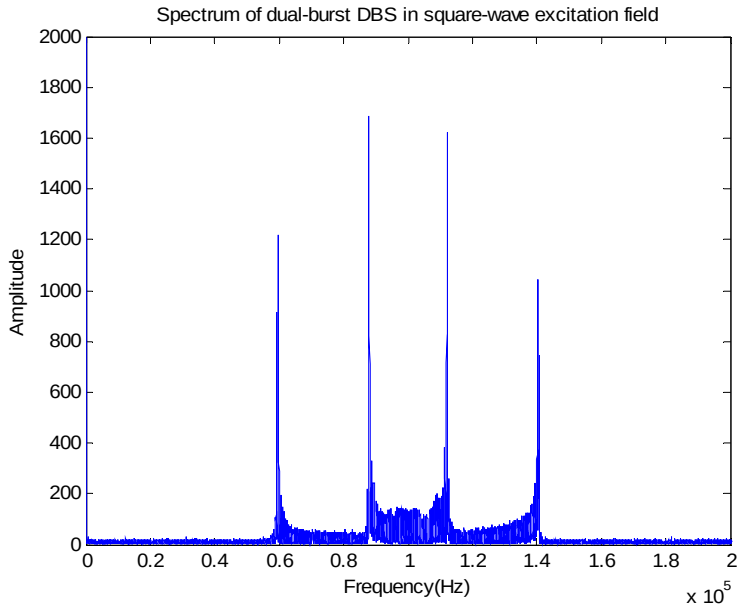

Fig. 3.20 Spectrum of dual-burst DBS in the square-wave excitation field

3.7 Summary and Conclusions

The discussion presented in this chapter focused on the derivation of mathematical models of the DBSs generated from different particle motions via measurement volume. The simulations were completed based on the derived mathematical models of DBSs in different scenarios of particle motion. The

relationship between particle trajectory via the measurement volume and the corresponding DBS was investigated. Four different types of particle motion were studied: constant velocity, constant acceleration and sinusoidal velocity which corresponded to the motion of particle in the DC, square-wave and sine-wave excitation fields. Additionally, the simulation of multi-burst DBS was also implemented. The characteristics of the DBS were investigated based on the simulation results of particle trajectory via the measurement volume and the corresponding DBS. It was demonstrated that the envelope of the DBS is determined by the particle positions in both **X** and **Y** direction. In the DC excitation field – steady state, it is a standard Gaussian envelope. However, in other excitation fields, the shape of the envelope is different because the particle doesn't move with a constant velocity in the **X** direction via the measurement volume. Even worse, sometimes, the envelope becomes discontinuous because the particle moves in and out of the measurement volume in both sine-wave and square-wave excitation field. The processing of discontinuous DBS remains a significant challenge for signal processing. Moreover, it was shown that the particle velocity in the Y direction determines width of signal burst. The envelope was shown to achieve its peak value when the particle was passing through the centre of the measurement volume. This is because the maximum intensity lies at the centre of the intersection of laser beams. The measurement volume has been defined by the e^{-2} intensity decay of the interference area.

It can be concluded that the instantaneous frequency of the Gaussian-amplitude DBS is only determined by real-time particle position in the X direction in the measurement volume. In the DC excitation field, the frequency of the Doppler signal is constant due to the constant-velocity particle motion in the measurement volume. However, introducing acceleration and oscillation into the particle motion in the measurement volume resulted in the variation of the real-time Doppler frequency. For example, the DBS generated in the sine-wave excitation field can be regarded as a FM signal whose instantaneous frequency changes as a sine-wave function. The DBS generated in the square-wave excitation field can be approximately regarded as a signal with the constant frequency except short periods of acceleration and deceleration in the particle motion. This characteristic of the DBS enables the use of spectral analysis to estimate the amplitude of particle velocity in the square-wave excitation field.

Finally, the spectral analysis of the DBS was performed in order to evaluate its limitations in velocity estimation in different excitation fields. The more nonlinear particle motion inside the measurement volume the more complex DBS spectrum becomes. Due to the characteristics of Doppler frequency, the results in the DC (steady state) and square-wave excitation field can be accurately obtained. However, this method is not suitable for real-time DBS processing in the DC excitation field (constant acceleration) and the sine-wave excitation field. The instantaneous velocity can't be obtained. Different signal processing method is necessary for real-time DBS processing. It was also highlighted that despite the lack of availability of real time frequency other information could be obtained using spectral analysis, for instance, the mean particle velocity in the DC excitation field (constant acceleration) and the frequency deviation in the sine-wave excitation field.

Depending on the particle concentration and the size of the measurement volume, sometimes, it is possible for the measurement volume to capture more than one particle at the same time. These events lead to an overlap of Doppler burst signals, known as multi-bursts. The mathematical model and simulation results of the multi-burst Doppler signals were given. In order to understand the generation of dual-burst signal, the simulation of the particle trajectories, single bursts and overlapped dual-burst DBS in different excitation fields were presented. Finally, the spectrums of corresponding dual-burst signals were shown, which illustrates that the velocity estimation in these instances can't be implemented by spectral analysis. The estimation of multi-burst DBS remains a significant challenge in the signal processing.

Chapter 4

Design of the Signal Processing System for the PCSA

4.1 Introduction

In Chapter 3, the mathematical models of the DBS corresponding to different scenarios of particle motions via the measurement volume and electric field excitation methods were presented. The simulation results of the synthesized DBS in the DC field (steady and accelerated state), sine-wave field and square-wave excitation field were given. Additionally, the characteristics of the DBS, such as the relationship between the particle position in the measurement volume, signal envelope and the instantaneous Doppler frequency were investigated.

The purpose of this chapter is to present a novel design and the implementation of the signal processing systems for the PCSA suitable for particle velocity and size estimation in the oscillatory excitation fields. Several techniques were investigated, specifically: Quadrature Demodulation (QD), PLL technique, spectral analysis, Hilbert transformation and correlation technique.

The structure of the chapter is as follows. Firstly, the design goals and the performance requirements of the signal processing system are discussed. This is followed

by the literature review of the existing signal processing techniques in different working domains. The literature review presented here is not meant to provide an exhaustive discussion of all LDA/PDA signal processing methods but rather selective critique aimed at highlighting the advantages and disadvantages of different methods with respect to the task of estimating particle velocity and phase shift in DC, square and sine wave excitation fields in real time. In order to further underpin the understanding of the proposed signal processing strategies, the fundamental principles of the FFT, PLL, QD, correlation techniques and Hilbert transform are briefly introduced. Finally, the detailed discussion of the design and implementation of signal processing systems are given. The proposed systems were designed, implemented and tested using MATLAB/SIMULINK software Version 6.4 (R2006a). After discussing the design schemes of the estimation systems, the results of the simulation and performance testing and comparison of different methods will be given and discussed in the next chapter.

4.2 Design Goals and Signal Processing Performance Requirements

The objective of this chapter is to discuss the design and implementation of the particle velocity and phase shift estimation systems in different excitation fields. The specific design objectives and performance requirements of the signal processing system are summarized in Table 4.1.

First of all, the velocity estimation range is expected to be wide enough to ensure that the corresponding charge measurement extends from several electrons to the

Gaussian limit without changing the drive frequency of the excitation field. This is an important and difficult requirement, which differentiates the PCSA from the commercially available E-SPART analyzer. For a given drive frequency, the size range of E-SPART analyzer is relatively narrow due to tangential relationship between the particle size and the phase lag. Therefore, in order to extend the estimation range of particle charge measurement, E-SPART analyzer has to be operated at multiple drive frequencies. This significantly prolongs the measurement time and makes the instrument less suitable for characterizing rapidly evolving aerosols. However, operating the PCSA at a constant drive frequency, while covering the entire charge range from several electrons to the saturation level, poses a considerable signal processing challenge. It is due to the fact that the particle velocity, which has to be measured, extends over four orders of magnitude. Also for small amplitudes, this SNR considerably decreases.

The maximum charge obtained by a particle is limited by the structural integrity of the particle or droplet as well as its ability to hold the electrical charge at its surface. Perhaps, the Gaussian limit is the most restrictive limit on a particle charge. It defines the maximum charge, which can build up on a surface, due to the breakdown strength of the air. When the electric field in air is greater than 3×10^{6}V/m, the air ionizes and the surface charge is dissipated. In addition to the Gaussian limit, there are other types of charge limit. First, the ion limit for charged solid particles due to the field emission. The ion limit is achieved as the repulsive electrostatic forces becoms sufficiently strong for spontaneous emission of an electron or a positive ion from the particle surface. Second, the Rayleigh limit for liquid droplet. This limit defines the maximum number of charges a droplet may have before the mutual repulsion of the excess charge overcomes the cohesive forces of surface tension causing disintegration of the droplet [7], [14].

Particle charge range	0 ~ Gaussian limit
Particle size estimation range	0.5 ~ 10μm
Phase shift range	0 ~ 90deg
Phase shift estimation relative	< 5%
Velocity estimation range	0 ~ 1m/s
Velocity estimation relative error	< 5%
Noise sensitivity	SNR>10dB
Real-time signal processing	Yes

Table 4.1 List of specific design objectives of signal processing system

This leads to the second requirement that the SNR of the designed signal processing system should be greater than 10dB in order to enable the measurement of noisy DBS. Noise in the PDA systems could arise from a number of factors including stochastic noise from the photodetector, electronic components as well as the scattering process itself. The DBS do not, but their nature, have a constant SNR as sometimes assumed in the literature [56]. Each burst signal will also vary in noise based on where the scattering particle is within the measurement volume. The problem is compounded by the oscillatory motion of the particle inside the measurement volume. The DBS generated from the particle may not be detected at all or wrong estimation result could be obtained from a noisy signal [57]. The challenge of the signal processing is to minimize the degradation of the performance of the estimator in the presence of noise. (The detailed discussion of the accuracy of the frequency estimation in the presence of noise depending on the particle trajectory via the measurement volume is given in Chapter 6).

In addition, the number of particles captured by the measurement volume and successfully processed by the system should be as high as possible with a minimum drop out rate in order to ensure that the measurement sample is representative of the overall charge and size distribution of the measured aerosol [58]. For example, bias towards lowly or highly charged particles will result in an incorrect measurement result. Therefore the estimation algorithm should be robust and consistent in processing DBSs across the whole range of particle charges and velocities. Due to the oscillatory nature of the particle trajectory via the measurement volume, this remains a challenge due to the presence of discontinuous-burst mentioned in Chapter 3. Sometimes, it is impossible to attain an accurate estimation result from a detected burst with a limited length. This problem, however, could be partially addressed by careful selection of the measurement system parameters, which will be discussed in Chapter 7.

Finally, the signal processing system of the DBS train has to be designed to simultaneously estimate both the instantaneous velocity and the phase shift of three DBS in real-time.

The schematic diagram of the overall DBS processing system consisting of velocity and phase shift estimation modules is shown in Fig. 4.1. There are three DBSs with the same frequency but different phases. Firstly, the particle velocity, V, and the two phase shifts, $\Delta\Phi_{13}$ and $\Delta\Phi_{23}$, are obtained by the velocity estimation module and the phase shift estimation module independently. The particle charge and size is be calculated from the velocity and the two phase shifts. The three signals are needed in order to overcome the problem of 2π, size ambiguity [59]. The additional tasks in signal processing of the train of DBS include: signal detection and validation. The bursts in the DBS train will arise at irregular and unknown time intervals, depending on the number of particles passing

through the measurement volume in a short succession.

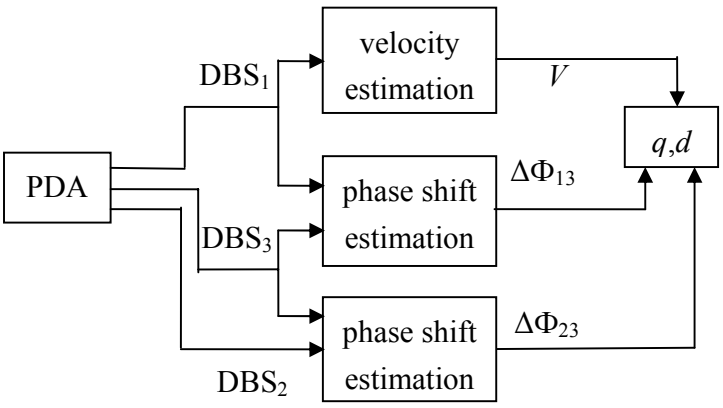

Fig. 4.1 Particle charge and size estimation system

The overall challenge of the design of the signal processing system is to meet all the design objectives in a single, low cost integrated signal processing solution.

4.3 Survey of the Existing Signal Processing Techniques of Doppler Burst Signal

4.3.1 Classification of Signal Processing Techniques

There are a number of signal processing techniques which could be employed in order to estimate the frequency of the Doppler burst signals and phase difference between the signals produced by different photo-detectors in the PDA system.

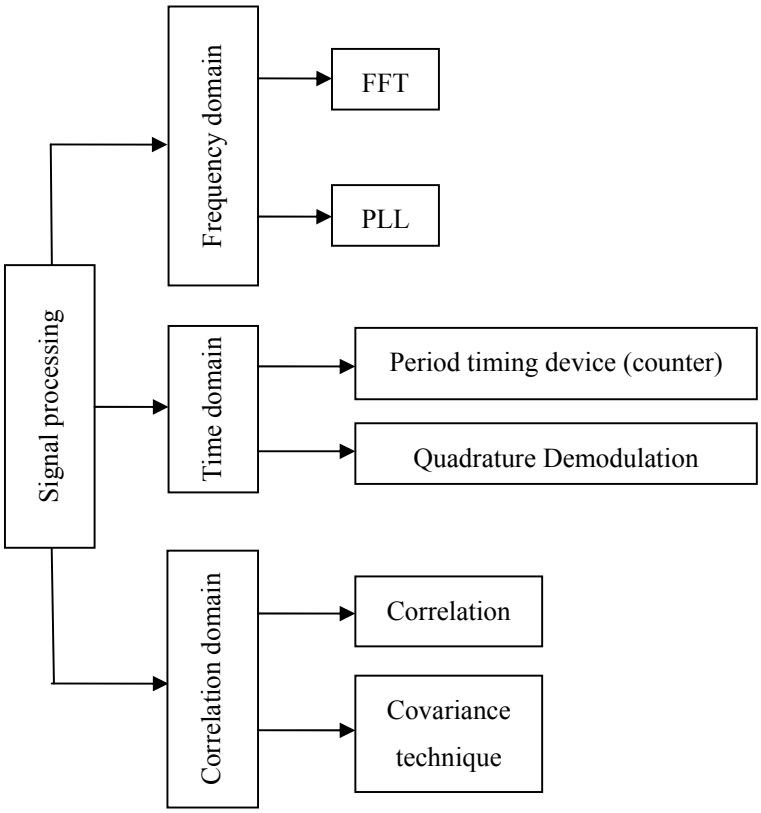

Fig. 4.2 Classification of signal processing techniques

Depending on the working domain, these signal processing techniques can be classified into three different categories: first, frequency domain techniques, e.g. analog and digital spectrum analyser, frequency-tracking demodulation technique (PLL) and burst/real-time spectrum analyser; second, time domain techniques including quadrature demodulation (QD) and period timing devices (counters); third, correlation domain techniques which include auto-correlation and auto-covariance techniques. The classification of the signal processing techniques based on the signal processing domain is shown in Fig. 4.2.

4.3.2 Signal Processing Techniques in Frequency Domain

The analog spectrum analyser was the first frequency domain signal processing technique used for the frequency estimation in Laser Doppler systems [60]. Although the analog analyser was later replaced by digital analyser and frequency tracking demodulation techniques, it can still be used as a versatile tool for diagnostic studies [31]. It can provide information when trackers failed and be able to handle poor quality signals. At low SNR, spectral analysis generally provides better estimates of particle velocity than period counters [61].

The digital spectral analysis is the most popular technique used for processing DBS and can be roughly divided into three categories: classical methods, methods based on parameter estimation and other methods. All the classical methods are based on the computation of FFT and perform well at low SNR with high computational speed [62]. The FFT analysis is one of the most frequently used tools for signal analysis which transforms the signal from the time domain to the frequency domain, thus revealing information about the signal that is hidden in the time domain. The resolution of FFT depends on the length of the data set. Although the length of the data can be increased by zero-padding, the resolution can't be improved. The low resolution result from a finite-length data set [63]. The squared output of the analyser is the power spectral density (PSD) of Doppler signal.

$$P(f) = \frac{1}{N} \left| \sum_{n=0}^{N-1} x_w[n] e^{-j\frac{2\pi kn}{N}} \right|^2 \tag{4.1}$$

where $f = \frac{k}{N} f_s$, k=0,1,…,N-1, f_s is the sapling frequency, $x_w[n]$ is the windowed time series, $w[n]$ it the time-window function, $x_w[n] = x[n]w[n]$. The objective of spectral

analysis is to obtain the power spectrum (i.e. PSD) of the Doppler signal so that the mean Doppler frequency can be determined, sometimes described as correlogram and periodogram methods. The Nuttall-Cramer Method is the computationally most efficient periodogram method [64], [65]. This algorithm is implemented by dividing the data into different non-overlapping segments and computes the mean PSD. A long data can be estimated with a low variance. But there is a drawback of this approach is that a real-time frequency can't be obtained from the frequency estimation. To solve this problem, the spectrogram approach has been proposed [66], [67], [68]. This approach estimates the time fluctuations of the velocity by investigating the bursts with a time-dependent Fourier transform. A time-varying PSD of the windowed data is computed. It can be visualized as the data sliding behind a window. This method requires a high rate of particle arrival [69]. Spectrograms are usually created by Short-Time Fourier Transform (STFT) [70], [71] sometimes by wavelet transform, called scaleograms [72], [73]. STFT uses a windowing technique to divide the whole signal into small portions assuming them to be stationary. Later, the Fourier Transform is applied on each of these portions. The main disadvantage of the STFT is the resolution tradeoff between time and frequency. Resolutions in time and frequency are determined by the width of window. In a similar way to the STFT, wavelet analysis is a windowing technique but with varying window size [74]. Usually, Wavelet analysis uses a long window at low frequencies and a short window at high frequencies [75], [76], [77]. A large window width provides good resolution in the frequency domain, but poor resolution in the time domain. Conversely, a small window width provides good resolution in the time domain and poor resolution in the frequency domain. As the instantaneous frequency of the Doppler signal increases, the number of points inside a period decreases for a given sampling frequency. It is therefore necessary

to decrease the number of windows per period to maintain frequency resolution. This complicates the design without the a priori knowledge of the periodic nature of the particle motion [78].

Advances in microelectronics technology now mean that digital analysis of frequency information using a purpose-built chip inside a signal processor is an attractive option [79]. The Doppler Burst Signal is sampled using an analogue-to-digital converter (ADC) and estimated by the spectral analysis using an efficient FFT algorithm. For instance, the Dantec Burst Spectrum Analyzer [80].

The sampling frequency of the digital spectrum analyser is determined by the Nyquist criterion and the number of samples is determined by both the signal duration and the processing speed [81]. Because it is impossible to foretell the signal duration, the buffer memory with post-optimization is necessary for variable width spectral analysis. The effect of the burst length to record length for an FFT processor working on different number of samples as a function of SNR was shown in [82]. It indicated that not the number of samples or the sampling frequency alone, but the total observation time is the important parameter. There have been several commercial implementations of FFT processors [83], [84], [85]. A transient recorder was used to realize DSP in software but decreased the processing speed. In order to improve the processing speed, a reduced number of bits, which is smaller than 4, is used in most commercial processors. Most processors operate on fixed length transforms, except a high-speed FFT processor from Aerometrics/TSI Inc. (RSA). The processor transforms the input signal at a rate of 20 million transforms per second, updated with every 8 new samples. The frequency measurement results are stored in a circular 4-cell memory buffer while a detector gate pulse appears. The measurements begin with the number of samples of 64, *i.e*. N=64.

Once the gate length exceeds N=128, the corresponding frequency values are stored and so on until four valid measurements with N=512 are obtained. For shorter burst, the four most recent frequency values are averaged and a fluctuation tolerance is applied as one validation criterion. A frequency estimation following from the power spectral density was described in [86]. This system has been developed by Hishida et al. [87] and Matovic et al. [88]. It has been proved that the current processors under frequency domain were close to the optimum estimation [89], [90]. However, these systems were not suitable for short burst signal processing. Moreover, the undesired samples which affected the results still were needed to be removed if higher order movements were computed. High-speed DSPs has been implemented. It allowed complex frequency-domain analysis performed digitally on-line and with little user intervention [91].

A burst spectrum analyzer based on a hard-wired fast FFT processor has been introduced by L. Lading in [83]. A nonlinear spectral analysis approach which hardly could be implemented in a real-time system has been tested by and Candel [92]. Both processors mentioned above, however, can't provide the phase shift information [93].

Besides the general transformation, a variety of interpolation procedures (parabolic [94], [95], Gaussian [95], [96], [97] and centroid fits [96], [98] and so on have been developed to improve the accuracy of frequency estimation [34], [98], [99], [100]. M. Gasior et al studied to enhance FFT frequency estimation resolution by using parabolic or Gaussian interpolations on the discrete magnitude spectrum. It was shown that the parabolic interpolation can improve the frequency resolution by more than one order of magnitude. However, better results can be achieved with Gaussian interpolation. A gain larger than two or even more than three orders of magnitude is possible to be obtained with employment of windows [95]. Additionally, the experimental results on the

spectrum estimation of the Japanese speech waveforms obtained by three different approaches of interpolation, Akima's approximation, the spline function approximation and Lagrange's formula are shown in [96]. The data values obtained by the investigation and comparison for the interpolated spectra indicated that Akima's method is superior to others in the calculation time.

The frequency tracking demodulator, such as PLL, can be used to track the instantaneous frequency of the continuous input signal, which means the tracker is suitable for real-time signal processing. The practical limitation of the frequency tracking method is that it requires a continuous input signal (i.e. high seeding density) and a relative high SNR [8]. Compared to the spectrum analyser, data can be collected and processed by frequency tracking demodulator more rapidly and conveniently, in addition, real-time signal processing is available [47], [101]. The PLL technique is one of the frequency tracking techniques which has been widely used for many years in tracking the signal phase or frequency. Although the working range of PLL is limited by the linear bandwidth, the range can be increased by some improvements, e.g., long loop PLL [102], [103], [104]. The performance of PLL, however, is degraded if the SNR of input signal is low [105], [106]. The SNR requirement is about 10 to 15dB [8]. However, an improved PLL technique was implemented by M. Tabiani [107]. By giving an artificial difference between input frequency and voltage controlled oscillator free running frequency, a short-duration Doppler signal (e.g. short Radar pulse) and low Doppler frequency can be detected. This improved technique can also be applied to low SNR case (as low as 3.5dB) [108]. The PLL is susceptible to noise that external signals carry and can acquire lock only if the SNR is greater than 3dB [109]. Additionally, the wavelet de-noising technique is able to effectively decrease the noise level and allows broadening of the PLL

bandwidth to track high dynamics signals [110], [111]. For the amplitude-modulated DBS [112], i.e. amplitude sensitivity, an AGC unit may be used to solve this problem in real-time processing [47].

An analog signal processing system based on PLL and QD techniques has been proposed by A. Le Duff et al [47]. The implementation of this technique turns to be well suitable for real-time measurement of acoustic signals and make the implementation of a low-cost miniature laser Doppler sensor to be possible [113]. The analog PLL system is superior to the other techniques in the design of a low-cost, integrated, real-time measurement system. However, the locking range of the common analog PLL is narrow and needed to be expanded by careful design and selection of filter parameters [56]. As the good performance in real-time signal processing of the DBS and the low cost, frequency tracking demodulation technique remains an attractive method for implementation.

4.3.3 Signal Processing Techniques in Time Domain

From 1970s to 1980s, the period timing device (counter) was widely used. The counting technique is based on the measuring the duration $\Delta\tau_N$ of a predetermined number N of the signal cycles, the frequency can be measured according to the following formula

$$\nu_D = \frac{N}{\Delta\tau_N} \tag{4.2}$$

This indicates an important property of time domain systems when applied to signal burst: time-domain analyzing systems yield frequency measurements which are

independent of the burst duration, i.e. the number of cycles in the signal burst does not influence the measurements. Conventional frequency counters with fixed gate time use an electronic clock to gate a counter which counts the zero crossings of the Doppler signals according to a fixed threshold. Hence, gate time and signal duration should be matched and this requires signal information prior to measurement. Furthermore, the gate is opened and closed simultaneously with time pulses from the clock. If the clock frequency is too low, accurate measurements can only be obtained for low Doppler frequencies.

The counting technique has been replaced by techniques operating in spectral or correlation domain because of the following disadvantages. First, it is very sensitive to noise and a high SNR is required. The inherent noise is the main cause of counting errors and the effect of noise on the measuring accuracy has to be understood and the effect reduced to an acceptable minimum [114]. Second, the measurement accuracy can be reduced due to timing errors. In practice, precise oscillators of a constant frequency generate the counting pulses. Within the time between two zero crossings of a sinusoidal signal, a number of pulses will be generated. When the pulses is counted for a large number of gate openings, the gate can open such that one pulse can be in or out, or the gate can close missing one pulse. Therefore, the timing error is produced. The optimum situation is to measure all the possible signal cycles within a burst so that the timing error can be reduced. Third, the signal pedestal must be completely removed because in practice, its presence makes the well-developed counting systems difficult in use. Thus, the elimination of signal pedestal is necessary in counting technique. There are two methods available based on electronic high pass filters and polarization properties of light beams. The counting technique can only provide a time-averaged measurement, which determines it is not suitable for real-time processing.

Until recently, the counter and FFT processors have been the standard devices for frequency measurements. However, both methods require several signal periods within an averaging time interval in order to obtain accurate measurement results. To overcome this drawback, the Quadrature demodulation (QD) technique was proposed [115]. The QD technique can give a precise frequency measurement independent of the number of signal periods available [115]~[119]. The QD technique is a quite young method but appeals to many researchers because the signal phase changes can be obtained. This method measures the time series of phase angles defined by a sine/cosine signal pair [120]. The phase angle time function corresponds to the path time function of a tracer particle in the measurement volume. Therefore, the magnitude and sign of the particle velocity can be obtained with a higher resolution compared to the conventional techniques. In other words, the high resolution in single burst evaluation and directional discrimination of velocity is the main advantage of QD technique. The QD technique has already been used with some success to estimate velocity of LDA signals [121], [122]. Because it operates in time domain, this method provides a high temporal resolution compared to the conventional techniques in the frequency domain [123], [124], [125]. Additionally, the wide velocity measurement range and acceleration evaluation on single burst are also possible as demonstrated in [126], [127]. Another system employing temperature stabilized monomode laser diodes is implemented by Muller, which enabled the realization of the compact low cost LDA sensors for directional velocity measurements [108]. The main advantages of the QD technique are the independence of the frequency determination from the occurring signal period number and the shape of the signal envelope [128]. Namely, it can measure a burst signal containing only a few signal periods or a fractional part of a burst signal period. The wide working range is

realized by a preselection of frequency shifts [122]. The statistical measuring error is only determined by the signal duration and SNR and has no relationship with other parameters, such as, the number of periods.

4.3.4 Signal Processing Techniques in Correlation Domain

The signal processing techniques in correlation domain are based on the calculation of the autocorrelation function (ACF) and autocovariance function (ACV) of the DBS [129], [130], [131].There have been several successful implementations of the ACF and ACV functions for the frequency and phase difference estimation in commercial LDA/PDA systems [132], [133], [134], [135] dealing with the standard, stationary DBS. The detailed discussion of the principles of the ACF and ACV function and its adaptation to the non-stationary DBS generated in the oscillatory field is given in section 4.7.1. In essence in the ACF and ACV technique, the Doppler signal is multiplied by a delayed version of the same signal and integrated over the burst period. The resolution of ACV technique can be increased by increasing the delay time τ. However, the larger delay time leads to the 2π phase ambiguity and adversely affects the measurement range [136].The digital correlator for signal detection has been implemented by Jensen in 1992 [120]. The amplitudes of the peaks of correlation are proportional to SNR and the frequency estimation is based on counting number of peaks. It is similar to counting method but the outlier data won't happen because noise contribution only appears at the delay time τ=0. Thus, the correlation method is able to measure low SNR signals. The burst detection is based on the level of SNR. The SNR threshold can be applied to the correlogram and validated by comparing the zero crossings to the threshold [137]. After that, the

beginning and ending of the burst can be determined. The Doppler frequency is estimated by checking the number of delay coefficients that occur between zero crossings of the first and last valid cycle in the ACF [138]. The correlation method was implemented by [139], [140], [141], [142] and exploited by [130] by using only 1-bit digitization. The designed system was able to work at the SNR of 0 dB for stationary DBS.

4.3.5 Comparison of Existing Signal Processing Techniques

The summary of the comparison of different DBS processing techniques is shown in Table 4.2. Based on the literature review it can be concluded as follows:

- In the frequency working domain, the spectrum analyser is not very sensitive to noise. Compared to the frequency tracking technique, the working range of spectrum analyser is larger. However, using standard FFT the instantaneous Doppler frequency is lost. STFT and wavelet transform could be used to obtain the real time frequency fluctuations, however both techniques are computationally expensive and suffer from the disadvantage of the resolution tradeoff between time and frequency [143]. The frequency tracking demodulator is able to track the real-time frequency. The processing speed of the tracker is also faster than the one of spectrum analyser. However, it requires higher SNR of signals.

Technique/ Device	*Working domain*	*Real-time information*	*Noise sensitivity*	*Processing speed*	*Working range(general)*
Spectrum analyser	frequency	could be available	low	slow	wide, up to 100MHz
Frequency tracking demodulator	frequency	available	high(Some improved PLL can achieve 3.5dB)	fast	narrow
Period timing device	time	unavailable	high	fast	wide
QD	time	available	Relatively high	fast	wide
Autocorrelation/ ACV	correlation	unavailable	low	fast	narrow

Table 4.2 Comparison of different signal processing techniques

- In the time working domain, the counting technique is very sensitive to noise because the random noise fluctuations result in extra zero crossings and additional periods. For this reason, multi-level crossings are used in the period counting. Counting technique, however, is not suitable for real-time signal processing since the frequency is estimated from a set number of periods or even the total number of periods in the burst. The QD, on the other hand technique is able to determine real-time frequency as well as the direction of velocity. The main advantages of QD technique are: First, the instantaneous phase difference can be continually estimated throughout the burst [34]. Second, the QD estimator can measure a burst signal containing only a few signal periods or a fractional part of a burst signal period. Compared to FFT processor

which is potentially advantageous in DBS processing with a poor SNR but have intolerably high measurement errors at low numbers of periods, QD technique can overcome this drawback [122]. This is a quite attractive for the measurement of non-stationary DBS train composed of signals randomly generated from complicated particle trajectories via the measurement volume. The likelihood of valid estimation can be improved by using QD method, which is vital for the measurement system design aiming to increase the particle count efficiency to get the most representative picture of the aerosol charge and size distribution. Third, the QD technique is able to work at a high processing speed with a high resolution compared to wavelet transforms because there is no iteration process. However, the weakness of the QD method is sensitivity to noise.

- In correlation domain, for the frequency estimation, the SNR requirement of both ACF and ACV technique is low. The resolution of the frequency estimation is affected by the choice of delay time, τ. The working range is limited when the delay time is large due to the problem of 2π ambiguity. The analog laser Doppler processor developed by Dantec Dynamics based on the covariance technique can estimate the constant frequency ranging from 120kHz to 36MHz. However, no real-time information of frequency can be obtained. For the phase estimation, the correlation technique approaches the performance of an ideal maximum likelihood processor, whereas, the performance of the frequency processor is typically in the order of 10dB below that of an ideal maximum likelihood processor [144], [145]. Compared to the conventional estimators, such as tracker and counter, burst digital correlator (BDC) is able to work effectively for stationary DBS of a low SNR within a wide dynamic range.

4.4 Velocity Estimation in DC Excitation Field – Steady State

4.4.1 Principles of the FFT

The Fourier transform is a common tool used to investigate the frequency spectra of nonperiodic waveforms. A nonperiodic waveform, given by $x(t)$ can be transformed from a function of time to a function of frequency by using following equations.

$$X(f) = \int_{-\infty}^{\infty} x(t) e^{-j2\pi ft} dt \tag{4.3}$$

$$x(t) = \int_{-\infty}^{\infty} X(f) e^{j2\pi ft} df \tag{4.4}$$

where X(f) is referred to as the Fourier transform of x(t). x(t) is the inverse Fourier transform of X(f). For discrete finite series, $x(n)$, the DFT is defined as,

$$X(k) = \sum_{n=0}^{N-1} x(n) e^{-j2\pi kn/N} \tag{4.5}$$

The inverse DFT is given by,

$$x(n) = \frac{1}{N} \sum_{k=0}^{N-1} X(k) e^{j2kn/Nt} \tag{4.6}$$

where N is the number of samples, n is the time sample index, n=0, 1, 2,..., N-1, k is the index for the computed set of discrete frequency components, k=0, 1, 2,…, N-1. As known, the computation of the DFT by the direct method is very large when N is large. Therefore, several methods have been proposed in order to improve the efficiency of the computation of the DFT. The entire set of these efficient algorithms for the digital

computation of the *N*-point DFT are called fast Fourier transform (FFT) algorithms. For more details regarding various implementations of the FFT please refer to [146], [147], [143].

4.4.2 Design of Velocity Estimation System based on Spectral Analysis

The block diagram of the velocity estimation system based on spectral analysis working in the DC excitation field is shown in Fig. 4.3.

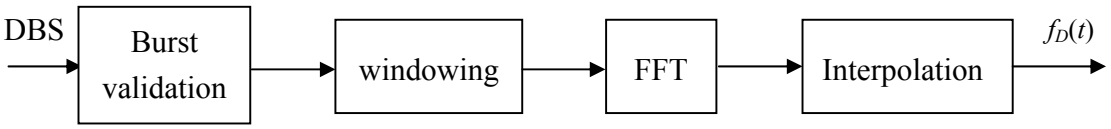

Fig. 4.3 Block diagram of velocity estimation system based on FFT

The procedure of the velocity estimation based on spectral analysis can be divided into four steps. First, the DBS in signal train are detected by a certain threshold to determine the starting and ending point of Doppler burst. The burst validation is used to determine to reject the burst with too short or too long length. Second, in order to increase the SNR and improve the performance of the frequency estimation, a Blackman window is applied to the DBS before the calculation of the spectrum. Third, the spectrum of DBS is obtained using FFT algorithm. Forth, the position of peak value in the spectrum is determined by spectrum interpolation. The frequency of the peak value in the spectrum corresponds to the Doppler frequency. The constant frequency of the DBS is estimated by interpolation using Gaussian interpolation

$$\delta = \frac{\ln(G_{k-1}) - \ln(G_{K+1})}{2[\ln(G_{K+1}) - 2\ln(G_k) + \ln(G_{k-1})} \tag{4. 7}$$

where $G_{k\text{-}1}$, G_k, G_{k+1} are coefficient values of the interpolation curve. The frequency of the peak value is determined by

$$f_D = \Delta f_s (k + \delta) . \tag{4. 8}$$

where Δf_s is the frequency resolution, $\Delta f_s k = f_k$, f_D is the frequency of the peak value, *i.e.* Doppler frequency. Finally, based on (3.1), the constant particle velocity in X direction can be obtained from Doppler frequency, f_D.

4.4.3 Principles of PLL Technique

As discussed above the frequency tracking demodulator, such as PLL, can be used to track the instantaneous frequency of the continuous input Doppler signal, which means the frequency tracker is suitable for real-time signal processing. Compared to the spectrum analyser, data can be collected and processed by frequency tracking demodulator more rapidly. In this research, the PLL technique has been used to track the instantaneous frequency of DBS. As shown in Fig. 4.4, the PLL system contains three parts, phase detector (PD), low-pass loop filter (LPF) and voltage controlled oscillator (VCO). The principles of PLL technique are described below.

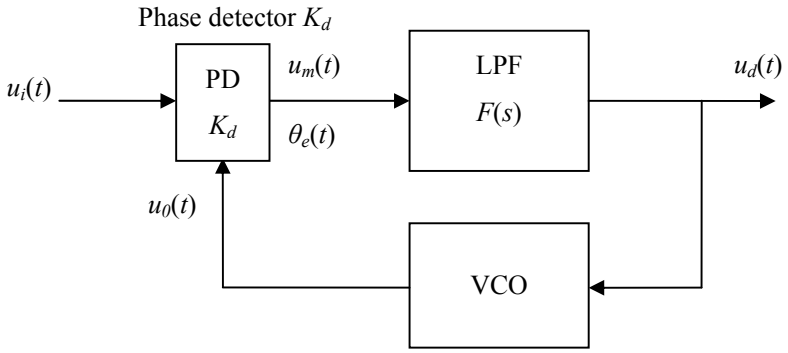

Fig. 4.4 Block diagram of Phase Locked Loop system

The PD is used to detect the phase difference $\theta_e(t)$ between the input signal $u_i(t)$ and the reference signal $u_o(t)$. The analog multiplier can be regarded as the simplest phase detector. Take the multiplier as an example to explain the principles of PD. Assume the multiplication parameter is K_d, the input DBS, $u_i(t)$, and the output signal of VCO, $u_o(t)$, have the following expressions,

$$u_i(t) = U_i \sin[\omega_i t + \theta_i(t)] \tag{4. 9}$$

$$u_o(t) = U_o \cos[\omega_o t + \theta_o(t)] \tag{4.10}$$

The input signal, $u_i(t)$ can be rewritten as

$$u_i(t) = U_i \sin[\omega_0 t + (\omega_i - \omega_0)t + \theta_i(t)] \tag{4.11}$$

Let's define the instantaneous phases of $u_i(t)$ and $u_o(t)$ respectively,

$$\theta_1(t) = (\omega_i - \omega_0)t + \theta_i(t) \tag{4.12}$$

$$\theta_2(t) = \theta_0(t) \tag{4.13}$$

$$u_i(t) = U_i \sin[\omega_0 t + \theta_1(t)] \tag{4.14}$$

$$u_0(t) = U_0 \cos[\omega_0 t + \theta_2(t)] \tag{4.15}$$

The output of PD, $u_m(t)$, is the multiplication result of the input signal $u_i(t)$ and the reference signal $u_o(t)$. It can be expressed as,

$$\begin{aligned} u_m(t) &= K_d u_i(t) \bullet u_0(t) = \\ &= K_d U_i U_0 \sin[\omega_0 t + \theta_1(t)] \sin[\omega_0 t + \theta_2(t)] = \\ &= \frac{1}{2} K_d U_i U_0 \sin[\theta_1(t) - \theta_2(t)] + \frac{1}{2} K_d U_i U_0 \sin[2\omega_0 t + \theta_1(t) + \theta_2(t)] \end{aligned} \tag{4.16}$$

where the phase difference is defined as,

$$\theta_e(t) = \theta_1(t) - \theta_2(t) \tag{4.17}$$

The LPF allows the low frequency component of the input signal pass through so that $\sin\theta_e(t)$ can be picked up by the LPF, which is called the error signal, $u_d(t)$ expressed below,

$$u_d(t) = \frac{1}{2} F(p) K_d U_i U_0 \sin\theta_e(t) \tag{4.18}$$

where $F(p)$ is the transfer factor of the LPF in time domain analysis.

The VCO is converts the voltage information into frequency information. The linear relationship between them is given as

$$\omega_{VCO}(t) = \omega_0 + K_0 u_d(t) \tag{4.19}$$

where K_0 [*rad/s* • *V*] is the gain of VCO, also called the sensitive parameter, $\omega_{VCO}(t)$ is the instantaneous frequency of $u_o(t)$, *i.e*.

$$\int_0^t \omega_{VCO}(\tau)d\tau = \omega_o t + \theta_2(t) \tag{4. 20}$$

However, in reality, the linear relationship in (4.19) is only valid in a limited range. The larger the K_0 is, the larger the linear working range of VCO is. The sensitivity of VCO will be degraded when the input voltage falls out of the range.

From (4.19) and (4.20), it can be derived,

$$\theta_2(t) = K_0 \int_0^t u_d(\tau)d\tau \text{ or } \frac{d\theta_2(t)}{dt} = K_0 u_d(t) \tag{4.21}$$

Therefore, when the PLL works in its linear working range, a linear loop equation can be given as

$$\because \theta_e(t) = \theta_1(t) - \theta_2(t)$$
$$\theta_2(t) = K_0 \int_0^t u_d(\tau)d\tau$$

$$\therefore \frac{d\theta_e(t)}{dt} = \frac{d\theta_1(t)}{dt} - K_0 u_d(t) = \frac{d\theta_1(t)}{dt} - \frac{1}{2}K_0 K_d U_i U_o F(p)\sin\theta_e(t) \tag{4. 22}$$

If the phase error $\theta_e(t)$ satisfies the condition, $|\theta_e(t)| < 30^o$, a linear approximation can be made

$$\sin\theta_e(t) = \theta_e(t) \tag{4.23}$$

Therefore, the linear loop equation of PLL can be re-expressed as,

$$\frac{d\theta_e(t)}{dt} = \frac{d\theta_1(t)}{dt} - \frac{1}{2}K_0 K_d U_i U_o F(p)\theta_e(t) \tag{4.24}$$

The function of the PLL system is aiming to minimize the error phase θ_e. When the system is in lock and the condition of $|\theta_e(t)|< 30^o$ is achieved, the equation (4.24) can be used to describe the PLL system in lock [148].

4.4.4 Design of Velocity Estimation System based on PLL Technique

The function of PLL system is to reduce the frequency difference between the input DBS and the known reference signal, which supplies the central frequency of the VCO. Therefore the frequency of the DBS can be estimated. It equals to the sum of the frequency difference and the frequency of the reference signal. A SIMULINK model has been designed and implemented in order to validate the proposed PLL system. The block diagram of the velocity estimation system based on PLL technique in the DC excitation field (steady state) is shown in Fig. 4.5. The components in the dashed blocks are the envelope detector and PLL module respectively.

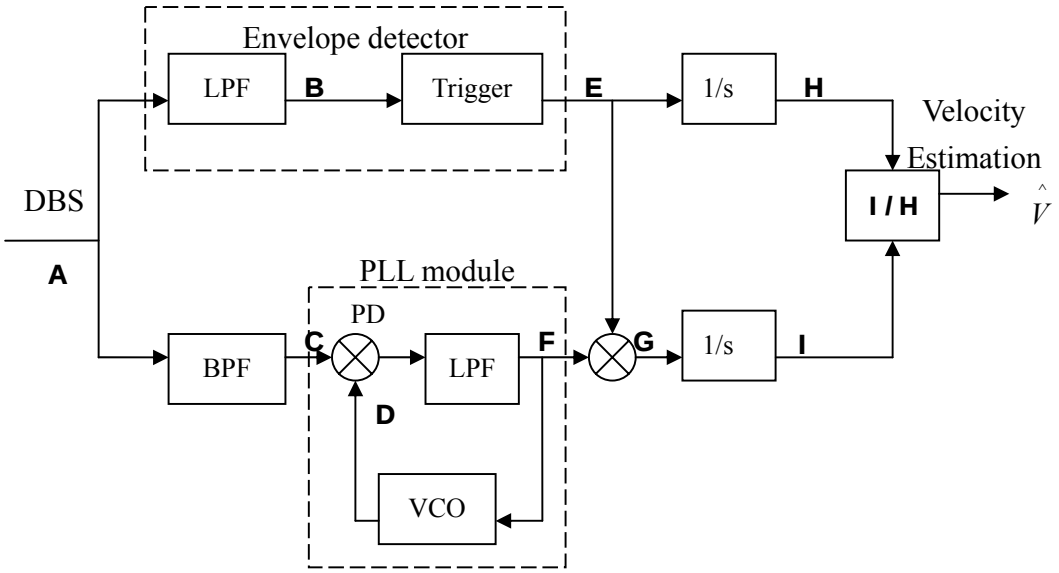

Fig. 4.5 Block diagram of velocity estimation system based on PLL in a DC field

The process of the velocity estimation in the DC excitation field includes four steps which are listed below.

The first task is to separate the AC and DC components of DBS. The DC part is used to derive the signal envelope for the signal detection. Besides, the frequency of the DBS is tracked from the AC part by the PLL system. As shown in Chapter 3 the input DBS, **A,** has the following form,

$$\begin{aligned}\mathbf{A} &= S(t) = S_{dc}(t) + S_{ac}(t) \\ &= A_{DBS}\exp[-2\frac{x^2(t)\cos^2(\theta/2)+y^2(t)}{r_m^2}] \\ &\quad + A_{DBS}\exp[-2\frac{x^2(t)\cos^2(\theta/2)+y^2(t)}{r_m^2}]\cos\{2\pi[F_B t + Dx(t)]+\varphi_0\} \\ &= A_{DBS}\exp[-2\frac{x^2(t)\cos^2(\theta/2)+y^2(t)}{r_m^2}]\{1+\cos\{2\pi[F_B t + Dx(t)]+\varphi_0\}\}\end{aligned} \tag{4.25}$$

where

$$\begin{aligned}v_x(t) &= V_x \\ x(t) &= x_0 + \int_0^t v_x(\tau)d\tau = V_x t\end{aligned} \tag{4.26}$$

In the second step, the DC part of DBS is removed by the band-pass filter (BPF) and the AC part of DBS is then derived, as shown in Fig. 4.6. Therefore the output of BPF, **C**, is expressed as,

$$\mathbf{C}=A_{DBS}\exp[-2\frac{x^2(t)\cos^2(\theta/2)+y^2(t)}{r_m^2}]\cos\{2\pi[F_B t + Dx(t)]+\varphi_0\} \tag{4.27}$$

At the same time, the DC component of the DBS, **B**, is obtained by the low-pass filter (LPF) and given as,

$$\mathbf{B} = A_{DBS} \exp[-2\frac{x^2(t)\cos^2(\theta/2) + y^2(t)}{r_m^2}] \tag{4.28}$$

The PLL module is used to track the instantaneous frequency of **C**, *i.e.* $2\pi[F_B + Dv_x(t)]$, which is the frequency of the DBS. In the PLL model shown in the dashed block in Fig. 4.6, **C** is multiplied by the output signal of VCO, **D**. The frequency difference between **C** and **D** is detected by the Phase Detector (PD) and obtained by the LPF. The output of the PLL module, **F**, equals to the frequency difference between the DBS and the known reference signal, *i.e.*, the central frequency of the VCO, ω_0.

$$\mathbf{F} = 2\pi[F_B + DV_x(t)] - \omega_0 \tag{4.29}$$

Furthermore, the envelope of the DBS is detected by the trigger based on a certain threshold in order to create an estimation window, **E**. **G** is the multiplication result of **F** and **E**. Due to the DC excitation field, the particle velocity, $V_x(t)$ is a constant. Therefore **G** is a constant. The segment within the burst period is determined by the window, **E**.

Because of the oscillations in **G** in the estimation, integrators are added into the system in order to obtain a stable result. The bound of the integration is chosen by the estimation window, **E**. After the integration, signals **H** and **I** are obtained

$$\mathbf{I} = \int_T \mathbf{G}dt = \mathbf{G}T \tag{4.30}$$

$$\mathbf{H} = \int_T \mathbf{E}dt = T \tag{4.31}$$

where T is the length of the burst period of DBS, *i.e.* the width of the window, **E**.

Finally, it can be found that the stable estimation result of the frequency difference can be obtained from **I** divided by **H**. With the addition of ω_0, the instantaneous

frequency of the DBS is obtained and therefore the velocity of the particle in real time is derived.

$$\hat{V} = \frac{\frac{I}{H} + \omega_0}{2\pi D} \tag{4.32}$$

where $\hat{V}$ is the estimation result of particle velocity.

The model of the particle velocity estimation system and subsystems designed in SIMULINK are shown in Fig. 4.6 (a) ~ (c).

The model of the envelope detector is shown in Fig. 4.6 (b). The trigger is used to detect the DBS envelope obtained by LPF from **A** based on a certain threshold. In the PLL model in Fig. 4.6 (c), the multiplier is used as the Phase Detector to detect the phase different between **C** and **D**. The output of the LPF is regarded as the output of the PLL system. The VCO is implemented by the part in dashed rectangle based on the following equation.

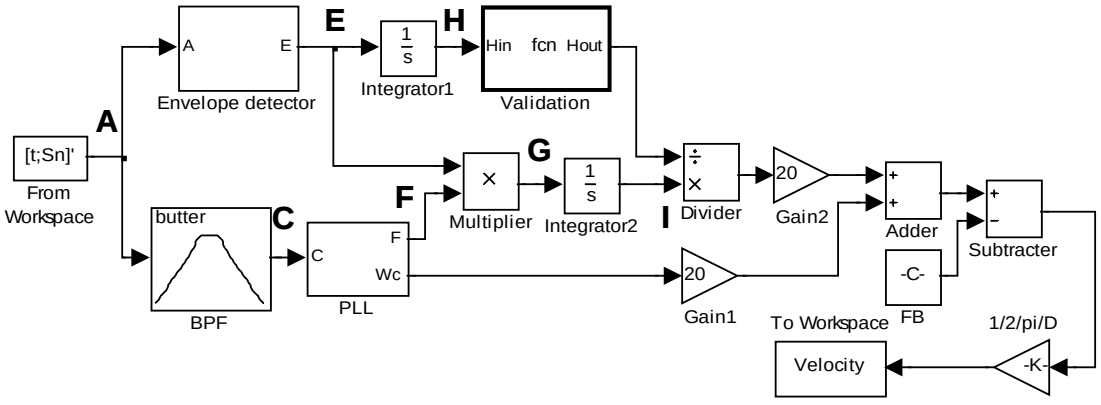

(a)

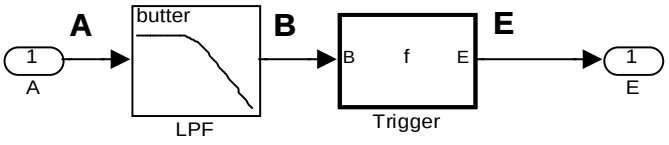

(b)

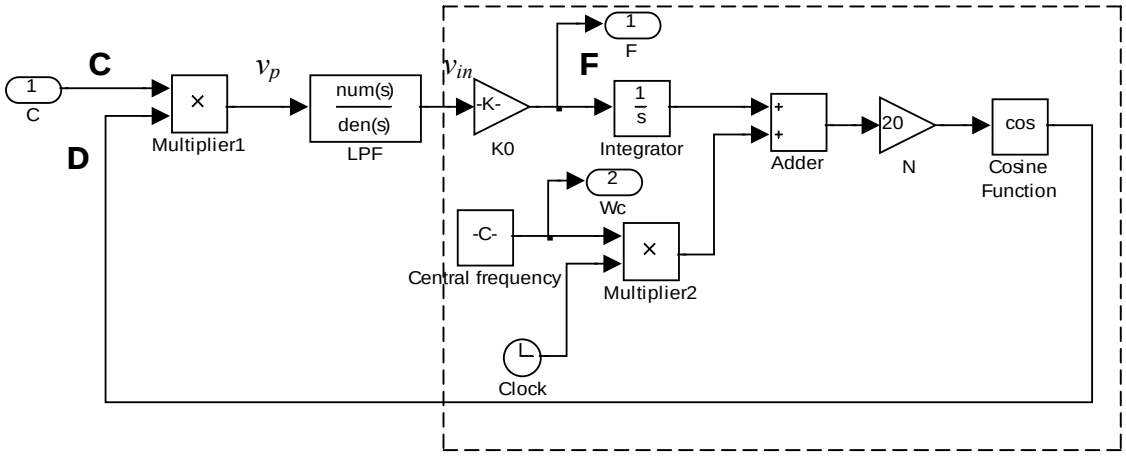

(c)

Fig. 4.6 (a) The SIMULINK model of velocity estimation system based on PLL technique in DC excitation field, (b) The SIMULINK model of envelope detector module, (c) The SIMULINK model of PLL module

$$\int_0^t \omega_{VCO}(\tau)d\tau = \omega_0 t + K_0 \int v_{in} dt \qquad (4.\ 33)$$

where $\omega_{VCO}(t)$ is the instantaneous frequency of VCO, ω_0 is the central frequency of VCO which is a constant as shown in Fig. 4.6 (c), v_{in} is the voltage of input signal of VCO, as specified in Fig. 4.6 (c). In order to enlarge the working range of PLL system, the long loop PLL is employed, *i.e.* a gain of N is added to the VCO system. Therefore, the mathematical model of PLL system in Fig. 4.6 (c) can be expressed as

$$v_p = \mathbf{C} \times \mathbf{D} = A_{DBS}(t)\cos\{2\pi[F_B + Dv_x(t)]\}A_{VCO}\cos[\int_0^t \omega_{VCO}(\tau)d\tau]$$
$$= \frac{A_{DBS}(t)A_{VCO}}{2}\{\cos\{2\pi[F_B + Dv_x(t)] + \int_0^t \omega_{VCO}(\tau)d\tau\} + \cos\{2\pi[F_B + Dv_x(t)] - \int_0^t \omega_{VCO}(\tau)d\tau\}\}$$

(4. 34)

$$v_{in} = \frac{A_{DBS}(t)A_{VCO}}{2}\{\cos\{2\pi[F_B + Dv_x(t)] - \int_0^t \omega_{VCO}(\tau)d\tau\}\} \quad (4.\ 35)$$

where v_p is the voltage of PD output, $A_{DBS}(t)$ is the envelope of input DBS, A_{VCO} is the amplitude of VCO output.

4.5 Velocity Estimation in Sine-wave Excitation Field

4.5.1 Design of Velocity Estimation System based on PLL Technique

The block diagram of the velocity estimation system based on PLL technique in the sine-wave excitation field is presented in Fig. 4.7 (a) ~ (c).

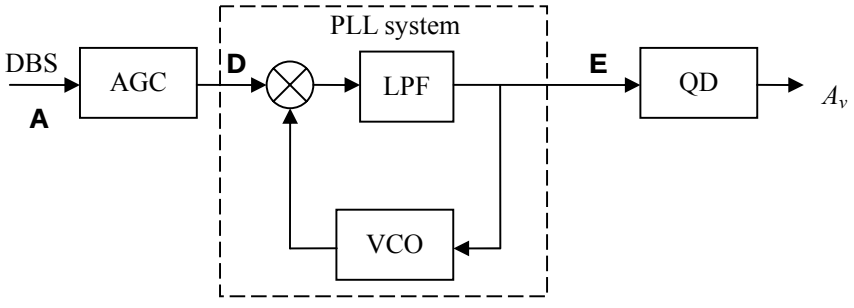

(a)

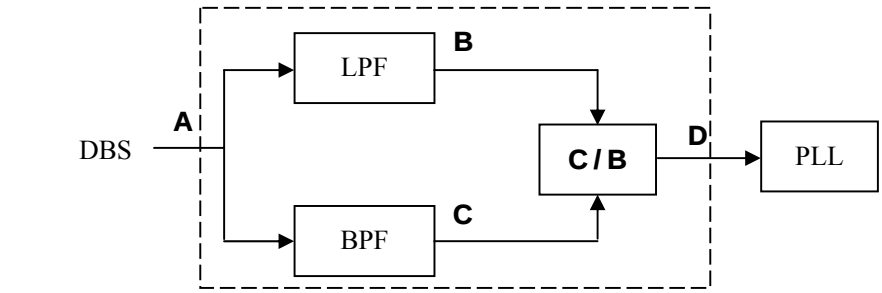

(b)

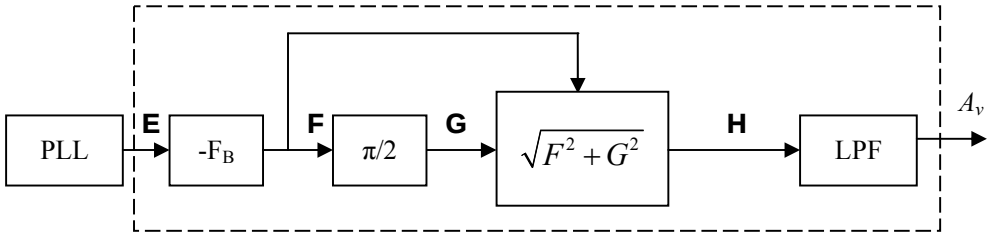

(c)

Fig. 4.7 (a) Block diagram of velocity estimation system based on PLL technique in the sine-wave excitation field, (b) Block diagram of AGC module, (c) Block diagram of QD module

The designed system proposed in Fig. 4.7 estimates the DBS based on the following steps. First of all, as shown in Fig. 4.7 (a), the first stage of the system is the AGC unit. The function of it is to compensate for the magnitude variation of DBS so that the working range of the PLL module can be improved. The structure of the AGC module is presented in Fig. 4.7 (b). The mathematical model of DBS, **A**, is shown below,

$$\begin{aligned}\mathbf{A} &= S(t) = S_{dc}(t) + S_{ac}(t) \\ &= A_{DBS}\exp[-2\frac{x^2(t)\cos^2(\theta/2)+y^2(t)}{r_m^2}] \\ &\quad + A_{DBS}\exp[-2\frac{x^2(t)\cos^2(\theta/2)+y^2(t)}{r_m^2}]\cos\{2\pi[F_B t + Dx(t)]+\varphi_0\} \\ &= A_{DBS}\exp[-2\frac{x^2(t)\cos^2(\theta/2)+y^2(t)}{r_m^2}]\{1+\cos\{2\pi[F_B t + Dx(t)]+\varphi_0\}\}\end{aligned} \tag{4. 36}$$

where

$$v_x(t) = A_v \sin(\omega t + \phi_0)$$
$$x(t) = x_0 + \int_0^t v_x(\tau) d\tau = \frac{A_v}{\omega} \cos\phi_0 - \frac{A_v}{\omega} \cos(\omega t + \phi_0) \quad (4.\ 37)$$
$$x_0 = 0$$

The outputs of LPF and BPF in AGC module are respectively expressed as,

$$\mathbf{B} = A_{DBS} \exp[-2\frac{x^2(t)\cos^2(\theta/2) + y^2(t)}{r_m^2}] \quad (4.\ 38)$$

$$\mathbf{C} = A_{DBS} \exp[-2\frac{x^2(t)\cos^2(\theta/2) + y^2(t)}{r_m^2}] \cos\{2\pi[F_B t + Dx(t)] + \varphi_0\} \quad (4.\ 39)$$

By the division operation between **B** and **C**, a compensated magnitude signal, **D**, is derived.

$$\mathbf{D}=\mathbf{C}/\mathbf{B}=\cos\{2\pi[F_B t + Dx(t)] + \varphi_0\} \quad (4.\ 40)$$

In the second stage, the frequency of DBS is tracked by the PLL system in real time.

$$\mathbf{E} = 2\pi[F_B + Dv_x(t)] \quad (4.\ 41)$$

In order to obtain the amplitude of the particle velocity, the QD module is added to the velocity estimation system. After removing $2\pi F_B$ frequency component from the output of PLL system, **E**. The result, **F**, can be expressed as,

$$\mathbf{F} = 2\pi D v_x(t) = 2\pi D A_v \sin(\omega t + \phi_0) \quad (4.\ 42)$$

Next, introducing π/2 delay to **F**. The result, **G** can be expressed as.

$$\mathbf{G} = 2\pi D A_v \cos(\omega t + \phi_0) \quad (4.\ 43)$$

Finally the amplitude of the velocity, A_v, is derived based on the following equation:

$$\mathbf{H} = \sqrt{\mathbf{F}^2 + \mathbf{G}^2} = 2\pi D A_v \tag{4. 44}$$

4.5.2 Principles of Quadrature Demodulation Technique

As mentioned in section 4.3.3 the appealing aspect of the QD technique especially in the context of processing non-stationary DBS, pursued in this research, is that it can be used to trace the signal phase changes in real time. The QD method measures the time series of phase angles defined by a sine/cosine signal pair. The pair of quadrature signals $S_s(t)$ and $S_c(t)$ with equal amplitudes and 90^o phase shift have the following forms,

$$S_s(t) = \mathrm{A}(t)\sin\Phi(t) \tag{4. 45}$$

$$S_c(t) = \mathrm{A}(t)\cos\Phi(t) \tag{4. 46}$$

where $\Phi(t) = 2\pi[F_B t + Dx(t)] + \varphi_0$

In order to generate the signal pair defined in (4.45) and (4.46) the Hilbert transform can be employed. The second signal, $S_c(t)$, is shifted 90^o in phase in relation to the first signal, $S_s(t)$. The aim of using sine/cosine signal pair is to improve the information efficiency of the phase angle measurement.

The time series of phase angle, $\Phi(t)$, also can be called phasor, which is defined as,

$$\Phi(t) = \arctan[\frac{S_s(t)}{S_c(t)}] = 2\pi[F_B t + Dx(t)] + \varphi_0 \tag{4. 47}$$

$\Phi(t)$ is measured by a bi-directional counter in order to determine the number of signal periods. Furthermore, the Doppler frequency $f_D(t)$ can be determined from the slope of the phasor with time

$$f_D(t) = \frac{1}{2\pi}\frac{d\Phi(t)}{dt} = \frac{1}{2\pi}\frac{\Delta\Phi(t)}{\Delta t} = 2\pi[F_B + DV_x(t)] \qquad (4.48)$$

Note that the sign of the particle velocity can be determined by the rotation direction of the phasor. If $d\Phi(t)/dt>0$, it means that the particle moves in the positive X direction. Additionally, the motion in the negative X direction leads to $d\Phi(t)/dt<0$. This characteristic has been exploited in a number of novel laser Doppler systems to eliminate optical frequency shifting devices.

4.5.3 Design of Velocity Estimation System based on Quadrature Demodulation Technique

The block diagram of the velocity estimation system based on QD technique in sine-wave excitation field is proposed in Fig. 4.8.

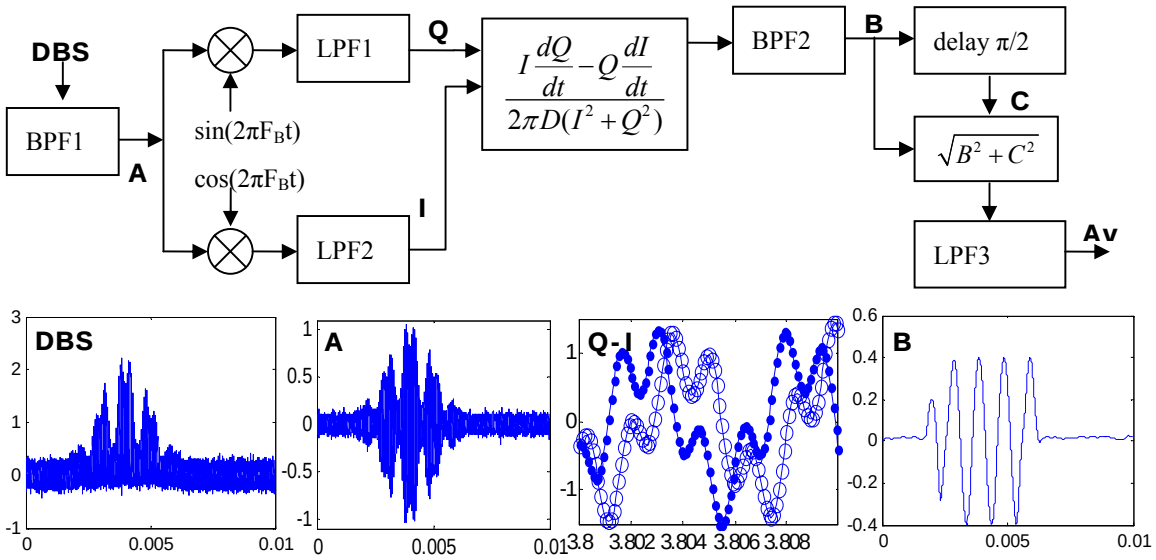

Fig.4.8. Block diagram of velocity estimation system based on QD in the Sine-Wave Excitation Field. BPF1 – Butterworth, second order, bandpass filter (Low passband edge frequency=200kHz, Upper passband edge frequency =600kHz), BPF2 – Butterworth, second order, bandpass filter (Low passband edge frequency =50Hz, Upper passband edge frequency= 300Hz), LPF1, LPF2- Butterworth, second order, low pass filters (Passband edge frequency =200kHz), LPF3- Butterworth, second order, low pass filter (Passband edge frequency =50Hz).

The input DBS is defined is given as

$$S(t) = A(t)\{1 + \cos\{2\pi[F_B t + Dx(t)] + \varphi_0\}\} \tag{4. 49}$$

where $A(t)$ is the signal envelope. $x(t)$ is the particle real-time position in the measurement volume, which equals

$$\begin{aligned} v_x(t) &= A_v \sin(\omega t + \phi_0) \\ x(t) &= x_0 + \int_0^t v_x(\tau) d\tau = \frac{A_v}{\omega}\cos\phi_0 - \frac{A_v}{\omega}\cos(\omega t + \phi_0) \\ x_0 &= 0 \end{aligned} \tag{4.50}$$

The process of the velocity measurement system in the sine-wave excitation field in by QD system can be divided into the following steps. First of all, as shown in Fig. 4.8, the DBS, **A**, is filtered by the BPF in order to remove the DC part of DBS. Therefore the output **B** is expressed as

$$\mathbf{B} = A(t)\cos\{2\pi[F_B t + Dx(t)] + \varphi_0\} \tag{4.51}$$

Next, there are two multipliers to implement the operations of multiplication which are presented below.

$$\begin{aligned} \mathbf{B} \times \sin(2\pi F_B t) &= A(t)\cos\{2\pi[F_B t + Dx(t)] + \varphi_0\}\sin(2\pi F_B t) \\ &= \frac{1}{2}A(t)\{\sin\{2\pi[2F_B t + Dx(t)] + \varphi_0\} - \sin[2\pi Dx(t) + \varphi_0]\} \\ \mathbf{B} \times \cos(2\pi F_B t) &= A(t)\cos\{2\pi[F_B t + Dx(t)] + \varphi_0\}\sin(2\pi F_B t) \\ &= \frac{1}{2}A(t)\{\cos\{2\pi[2F_B t + Dx(t)] + \varphi_0\} + \cos[2\pi Dx(t) + \varphi_0]\} \end{aligned} \tag{4.52}$$

In (4.52), there are two parts in the results of the multiplication. One is the high frequency component, the other is the low frequency component. Therefore, as shown in Fig. 4.8, the LPF is used to obtain the low frequency part from the results shown in (4.52).

The corresponding signals **C** and **D** are expressed in (4.53),

$$\begin{aligned}\mathbf{C} &= \frac{1}{2}F(p)A(t)\sin[2\pi Dx(t)+\varphi_0] \\ \mathbf{D} &= \frac{1}{2}F(p)A(t)\cos[2\pi Dx(t)+\varphi_0]\end{aligned} \tag{4.53}$$

where **C** and **D** are respectively the Q and I component of the signal. $F(p)$ is the transfer factor of the LPF in time domain analysis.

Next, the particle real-time velocity is able to be attained from (4.54) [149].

$$V_x(t)/i = [I(dQ/dt) - Q(dI/dt)]/[2\pi(I^2+Q^2)] \tag{4.54}$$

i.e. $\mathbf{E}=V_x(t)+n(t)=A_v\sin(\omega t+\phi_0)+n(t)$,where $n(t)$ is the Gaussian noise. The detailed derivation of (4.54) is presented in the Appendix C. The LPF is used to remove the noise remained in the signal **E**. The velocity amplitude is obtained by computing the absolute value of the minimum of **F**;

$$abs(\min(\mathbf{F})) = A_v \tag{4. 55}$$

4.6 Velocity Estimation in Square-wave Excitation Field

4.6.1 Design of the Velocity Estimation System based on Spectral Analysis

The diagram of the velocity estimation system based on spectral analysis in the square-wave excitation field is shown in Fig. 4.9. The processing of the train of DBSs in the square-wave excitation system can be divided into the following steps. Firstly, the

signal burst is detected by the evaluation of the burst envelope. Therefore, the starting and ending points of each burst can be determined. Secondly, the length and SNR of each burst are evaluated. The burst whose length is less than the threshold is rejected. Additionally, if SNR is lower than the threshold, the corresponding burst will be eliminated. Third, velocity of the burst which satisfies the requirements of length and SNR is estimated using FFT algorithm followed by the peak detection routine and the interpolation technique. In the square-wave excitation field, the spectrum is largely dependent on the characteristic of the excitation field such as the frequency and the magnitude as well as the particle motion inside the measurement volume.

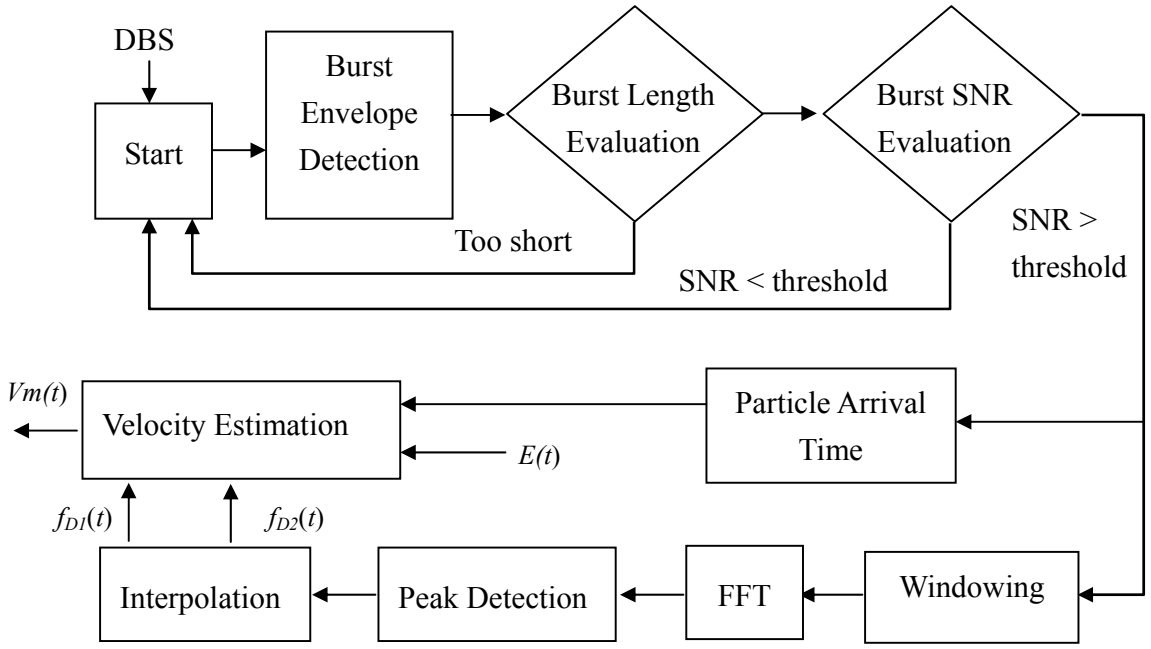

Fig. 4.9 Block diagram of velocity estimation system based on FFT

For the low frequencies of the excitation field when the particle crosses the measurement volume with the constant velocity the DBS spectrum, as demonstrated in

chapter 3, is almost the same as the one in the DC excitation field– steady state. The only exception is the small spectral broadening corresponding to the short periods of particle acceleration and deceleration inside the measurement volume. However, when the frequency of the excitation increases, several periods of particle oscillatory motion could be captured inside the measurement volume. In this case two peaks will be present in the spectrum corresponding to the particle motion in opposite directions. Each peak has to be separately evaluated. Finely, when the particle relaxation time is comparable with the period of the field excitation the effect of the particle acceleration on the spectrum becomes much more pronounced leading to spectral broadening and eventually blearing completely the peak spectral lines. The estimation results for different velocities and the level of SNR are presented in chapter 5.

4.7 Phase Shift Estimation in both Sine-wave and Square-wave Excitation Fields

4.7.1 Principles of Hilbert Transformation and Correlation Technique

The phase shift estimation system has been designed based on the correlation technique and Hilbert transformation. The phase shift is determined by the ratio of the real and imaginary part of the cross-correlation of two Doppler signals with the same frequency an different phase.

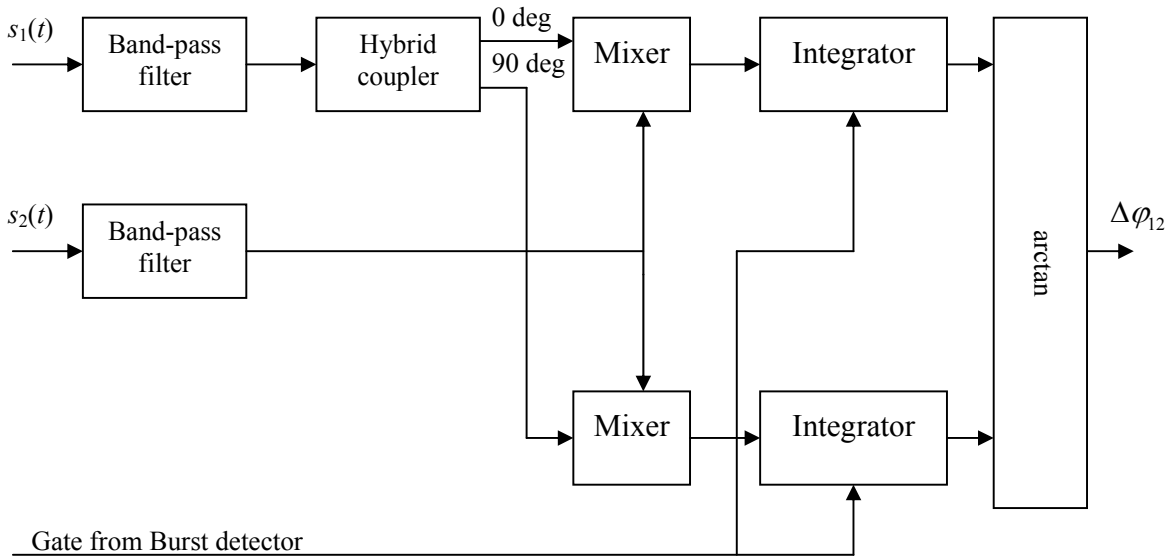

Fig. 4.10 Block diagram of a phase shift estimation based on the correlation technique

The generation of the real and imaginary part is implemented by Hilbert transformation. The block diagram of the phase shift estimation system is presented in Fig. 4.10. If the input DBS can be expressed as below,

$$s_r(t) = A_r \exp[-2\frac{x^2(t)\cos^2(\theta/2) + y^2(t)}{r_m^2}][1+\cos(2\pi f_D t + \varphi_r)] \qquad (4.56)$$

where r is the signal index equal to 1,2.

The input signal is first processed by the band-pass filter in order to remove the DC component and limit the bandwidth of the noise present in the signals. Next, the signals are fed to a hybrid coupler and to a delayer. The delay time is set to be τ. Then a multiplication and integration is performed. The 0 deg and 90 deg signals after the hybrid coupler can be expressed together in complex notation as

$$s_r(t) = A_r(t)[\cos(2\pi f_D t + \varphi_r) + j\sin(2\pi f_D t + \varphi_r)] \qquad (4.57)$$

where $A_r(t) = A_r \exp[-2\frac{\mathbf{x}^2(t)\cos^2(\theta/2)+\mathbf{y}^2(t)}{r_m^2}]$

Then the real and imaginary parts of the autocorrelation can be expressed as

$$C_{R12} = A_{12}(\tau)\cos(2\pi f_D \tau + \Delta\varphi_{12}) \tag{4. 58}$$

$$C_{I12} = A_{12}(\tau)\sin(2\pi f_D \tau + \Delta\varphi_{12}) \tag{4. 59}$$

where $A_{12}(\tau)$ is the cross-correlation of the envelope function. $\Delta\varphi_{12}$ is the phase difference between the signals, $\Delta\varphi_{12} = \varphi_1 - \varphi_2$. The ratio of these terms at τ=0 yields a quantity independent of signal amplitude and frequency, which can be used to determine the phase shift between the two input signals.

$$\Delta\varphi_{12} = \arctan\frac{C_{I12}(0)}{C_{R12}(0)} \tag{4. 60}$$

The Hilbert transform of a function $x(t)$ is defined by

$$y(t) = \aleph\{x(t)\} = \frac{1}{\pi}\int_{-\infty}^{\infty}\frac{x(\tau)}{t-\tau}d\tau \tag{4. 61}$$

The function $y(t)$ is produced by passing x(t) through a filter with the transfer function

$$H(f) = -j\,\mathrm{sgn}(f) \tag{4. 62}$$

A singularity exists at the value f=0, which, however, does not cause any computational problems. On the other hand, the infinite integral causes problems for signals that are not mean-free. Thus, when processing laser Doppler and phase Doppler signals with the Hilbert transform, it is necessary to first remove the mean, either optically or electronically.

The magnitude and phase of H(f) are

$$|H(f)|=1 \tag{4. 63}$$

For a given input signal $x(t)$ the Hilbert transform is the signal $y(t)$ which is shifted by -90 deg in phase for all frequencies.

An analytical (complex) function for a given input signal $x(t)$ can be defined as

$$z(t)=x(t)+j\aleph\{x(t)\} \tag{4. 64}$$

An example of signal and its Hilbert transform are given in Fig. 4.11.

The analytical signal $z(t)$ can be used to derive the signal envelope $A(t)$ and the instantaneous signal phase $\varphi(t)$.

$$A(t)=|z(t)| \tag{4. 65}$$

$$\varphi(t)=\arg\{z(t)\} \tag{4. 66}$$

The envelope and phase of the signal from Fig. 4.11 are shown in Fig. 4.12.

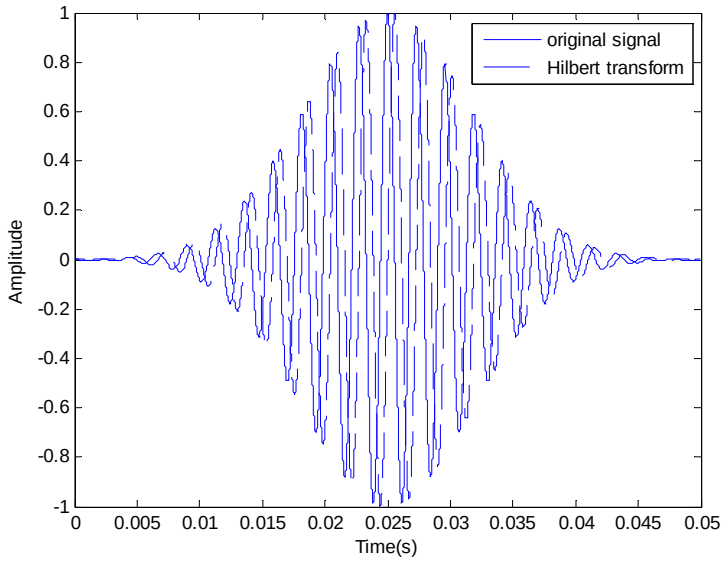

Fig. 4.11 Example of signal and its Hilbert transform (-90 deg phase shift)

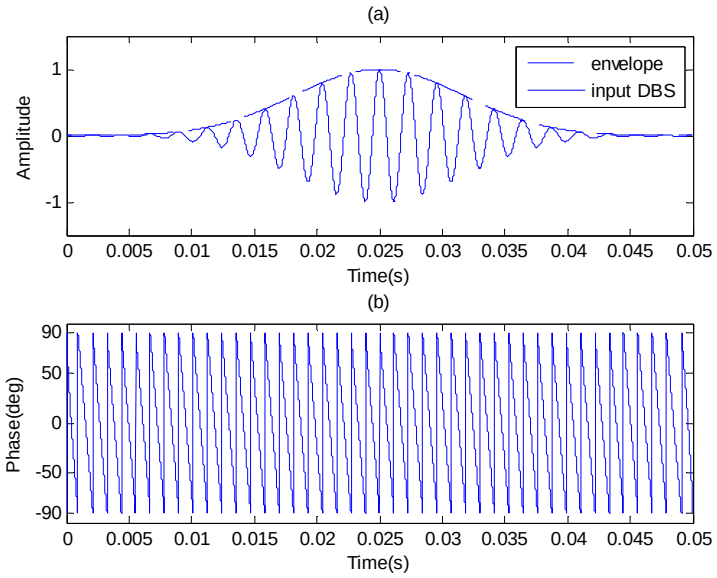

Fig. 4.12 (*a*) Input DBS and computed envelope, (*b*) Instantaneous phase of inupt DBS

4.7.2 Design of Phase Shift Estimation System based on Hilbert Transformation and Correlation Technique

The block diagram of phase shift estimation system based on the correlation technique is shown in Fig. 4.13.

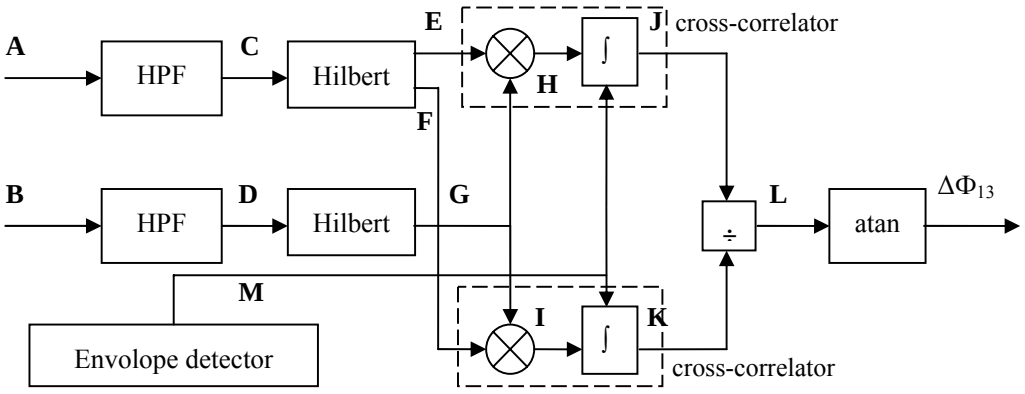

Fig. 4.13 The block diagram of phase shift estimation system

The principles of size measurement based on Hilbert transformation and the correlation technique are described below. First of all, the two DBSs, **A** and **B** received by the two different photo-detectors in the PDA system can be expressed as,

$$\begin{aligned} \mathbf{A} &= A(t)\{1+\cos\{2\pi[F_B t + Dx(t)]+\Phi_1\}\} \\ \mathbf{B} &= A(t)\{1+\cos\{2\pi[F_B t + Dx(t)]+\Phi_3\}\} \end{aligned} \tag{4. 67}$$

Next, the HPF is used to remove the DC component of input DBSs and keep the Guassian noise as much as possible.

$$\begin{aligned} \mathbf{C} &= A(t)\cos\{2\pi[F_B t + Dx(t)]+\Phi_1\} \\ \mathbf{D} &= A(t)\cos\{2\pi[F_B t + Dx(t)]+\Phi_3\} \end{aligned} \tag{4. 68}$$

The signal **C** and **D** have the same Doppler frequency but different signal phase. In order to obtain the particle size, the phase shift between **C** and **D** is going to be estimated, i.e.,

$$\Delta\Phi_{13} = \Phi_1 - \Phi_3 \tag{4. 69}$$

Then, I and Q components of **C** and **D** are generated by the Hilbert transform based on the following equations.

$$\begin{aligned} H[I_1(t)] &= \{A(t)\cos[2\pi Dx(t)+\Phi_1]+n(t)\} + j\{A(t)\sin[2\pi Dx(t)+\Phi_1]+n'(t)\} \\ H[I_3(t)] &= \{A(t)\cos[2\pi Dx(t)+\Phi_3]+n(t)\} + j\{A(t)\sin[2\pi Dx(t)+\Phi_3]+n'(t)\} \end{aligned} \tag{4. 70}$$

where $n'(t) = H[n(t)]$

Therefore, *I* and *Q* components can be obtained.

$$\begin{aligned} \mathbf{E} &= I_{1r}(t) = A(t)\cos[2\pi Dx(t)+\Phi_1]+n(t) \\ \mathbf{F} &= I_{1i}(t) = A(t)\sin[2\pi Dx(t)+\Phi_1]+n'(t) \\ \mathbf{G} &= I_{3r}(t) = A(t)\cos[2\pi Dx(t)+\Phi_3]+n(t) \end{aligned} \tag{4. 71}$$

Next, the phase shift is estimated by using the correlation method at τ=0. The cross

correlation which is defined below is implemented by integrator.

$$C_{x,y}(\tau) = \int_{-\infty}^{+\infty} x(t)y(t+\tau)dt \tag{4. 72}$$

When τ=0,

$$\begin{aligned}
\mathbf{J} &= C_{1r,3r}(0) = \int_0^T \mathbf{EG}dt = \int_0^T [I_{1r}(t)Q_{3i}(t)]dt \\
&= \int_0^T \{[A(t)\cos(2\pi Dx(t)+\Phi_1)+n(t)][A(t)\cos(2\pi Dx(t)+\Phi_3)+n'(t)]\}dt \\
&= \int_0^T \{A^2(t)\cos(2\pi Dx(t)+\Phi_1)\cos(2\pi Dx(t)+\Phi_3) \\
&\quad + A(t)n(t)[\cos(2\pi Dx(t)+\Phi_1)+\cos(2\pi Dx(t)+\Phi_3)]+n(t)n'(t)\}dt \\
&= \int_0^T \{A^2(t)\{\frac{1}{2}[\cos(4\pi Dx(t)+\Phi_1+\Phi_3)+\cos(\Phi_1-\Phi_3)]\} \\
&\quad + n(t)n'(t)+A(t)n(t)[\cos(2\pi Dx(t)+\Phi_1)+\cos(2\pi Dx(t)+\Phi_3)]\}dt
\end{aligned} \tag{4. 73}$$

$$\begin{aligned}
&\because \int_0^T \{A(t)n(t)[\cos(2\pi Dx(t)+\Phi_1)+\cos(2\pi Dx(t)+\Phi_3)]\}dt \\
&<< \int_0^T \{A^2(t)\{\frac{1}{2}[\cos(4\pi Dx(t)+\Phi_1+\Phi_3)+\cos(\Phi_1-\Phi_3)]\}+n(t)n'(t)\}dt \\
&\therefore C_{1r,3i}(0) = \int_0^T \{A^2(t)\{\frac{1}{2}[\cos(4\pi Dx(t)+\Phi_1+\Phi_3)+\cos(\Phi_1-\Phi_3)]\}+n(t)n'(t)\}dt
\end{aligned} \tag{4. 74}$$

$$\begin{aligned}
&\because x(\tau) = \int_{-\infty}^{+\infty} x(t)x(t+\tau)dt \\
&\therefore \int_0^T A^2(t)dt = A(0) \\
&\because x(\tau) = \int_{-\infty}^{+\infty} x(t)x(t+\tau)dt \\
&\therefore n(\tau) = \int_{-\infty}^{+\infty} n(t)n'(t)dt \\
&at\ \tau = 0,\ n(0) = 0
\end{aligned}$$

$$\because \int_0^T [A^2(t)\frac{1}{2}\cos(4\pi Dx(t)+\Phi_1+\Phi_3)] << \int_0^T [A^2(t)\frac{1}{2}\cos(\Phi_1-\Phi_3)+n(t)n'(t)]dt$$

$$\therefore C_{1r,3r}(0) = \mathbf{J} = C_c(0) = \frac{1}{2}A(0)\cos(\Delta\Phi_{13}) \quad (4.\ 75)$$

Based on the similar deduction, it can be derived,

$$\therefore \mathbf{K} = C_s(0) = \int (I_{1i} \times I_{1i})dt = \frac{1}{2}A(0)\sin(\Delta\Phi_{13}) \quad (4.\ 76)$$

Finally, by the mathematical operation of division and arctangent, the phase shift between the two DBSs can be obtained, *i.e*.

$$\Delta\Phi_{13} = \Phi_1 - \Phi_3 = \arctan\frac{C_s(0)}{C_c(0)} \quad (4.\ 77)$$

4.8 Summary and Conclusions

The purpose of this chapter was to present a novel design and the implementation of the signal processing systems for the PCSA suitable for the particle velocity and size estimation in the oscillatory excitation fields. A comprehensive literature review was presented aimed at highlighting the advantages and disadvantages of different methods with respect to the task of estimating particle velocity and phase shift in DC, square wave and sine wave excitation fields in real time. The comparison of existing techniques has been made with respect to the working range, SNR requirement, real-time information availability. It was concluded that spectrum analyzer, period timing device and correlation technique are not suitable for providing the real time information of the

velocity changes required for signal processing in sine-wave excitation field. However, the FFT based spectrum analyses could be successfully applied for the velocity estimation in case of the square-wave field under specific excitation conditions. This is due to the fact that in square-wave field the particle moves largely with a constant velocity through the measurements volume generating DBS signals resembling standard stationary DBS. The adequate signal processing algorithm has been designed, presented and discussed. The unique advantages of the FFT based algorithm are relative simplicity and efficiency of implementation, low SNR requirement and wide working range.

In addition to the FFT based algorithm, several other techniques were investigated, including: Quadrature Demodulation (QD), PLL technique, Hilbert transformation and correlation technique. The designs of the PLL system both in the DC field as well as sine wave excitation were presented. Although the working range of the typical PLL is limited by the linear bandwidth, the range was increased by several design improvements, including AGC and VCO unit.

Following the design of the PLL, the design of the QD technique in sine-wave excitation was investigated because of its unique advantages including the ability to provide the instantaneous phase difference throughout the burst as well as to process burst signal containing only a few periods.

In the next chapter, the simulation results and performance testing of the estimation systems mentioned in Chapter 4 are presented. The comparison of the performances of these systems and the corresponding conclusions are made.

Chapter 5

Simulation and the Performance Testing of the Signal Processing Systems

5.1 Introduction

In chapter 4, the signal processing systems for the PCSA were discussed. The different velocity and size estimation systems based on the FFT, PLL QD, correlation techniques and Hilbert transform were designed and implemented under different excitation methods using MATLAB/SIMULINK software.

This chapter focuses on the simulation and performance testing of the estimation systems. The aim of the chapter is to provide a comprehensive comparison of the systems performance with regards to the velocity, size estimation range, SNR requirement and charge measurement range.

The structure of the chapter is as follows. First of all, the procedure for the generation of the Doppler burst signals and the performance testing scheme is discussed for both velocity and phase shift estimation systems. Second, the hardware signal processing system and the processing steps are described. The noisy analog Doppler Burst Signal train was generated by TGA12101 Arbitrary Waveform Generator from signals simulated in MATLAB based on the mathematical models described in Chapter 3.

In addition to the MATLAB models of the DBS the NASA Doppler Velocimetry Simulator [150], [151], [152] was used for some performance tests and cross-validation of the results. The relationship between particle trajectory via the measurement volume and the SNR has been emphasized. Next, the simulation results of the velocity and size estimation systems based on different signal processing techniques and excitation methods are given. The performance testing of the signal processing systems was accomplished by means of Monte Carlo (MC) simulations. Following the performance testing the charge ranges of the proposed estimation systems working in different excitation fields are calculated from the estimation ranges of the particle velocity and size. Finally, the estimation systems are compared and evaluated with regards to the working range, charge range and SNR requirement.

5.2 The Doppler Burst Signal Generation and the Performance Testing Scheme for Velocity and Phase Estimation

The performance of the estimators was studied by means of Monte Carlo (MC) simulations. Several hundred trials were run on simulated signals synthesized from the signal models established in Chapter 3 for each combination of the measurement parameters. The signals were corrupted by an additive white Gaussian noise. The block diagrams illustrating the DBS generation and performance testing scheme for velocity and phase estimation are shown in Fig. 5.1 and 5.2.

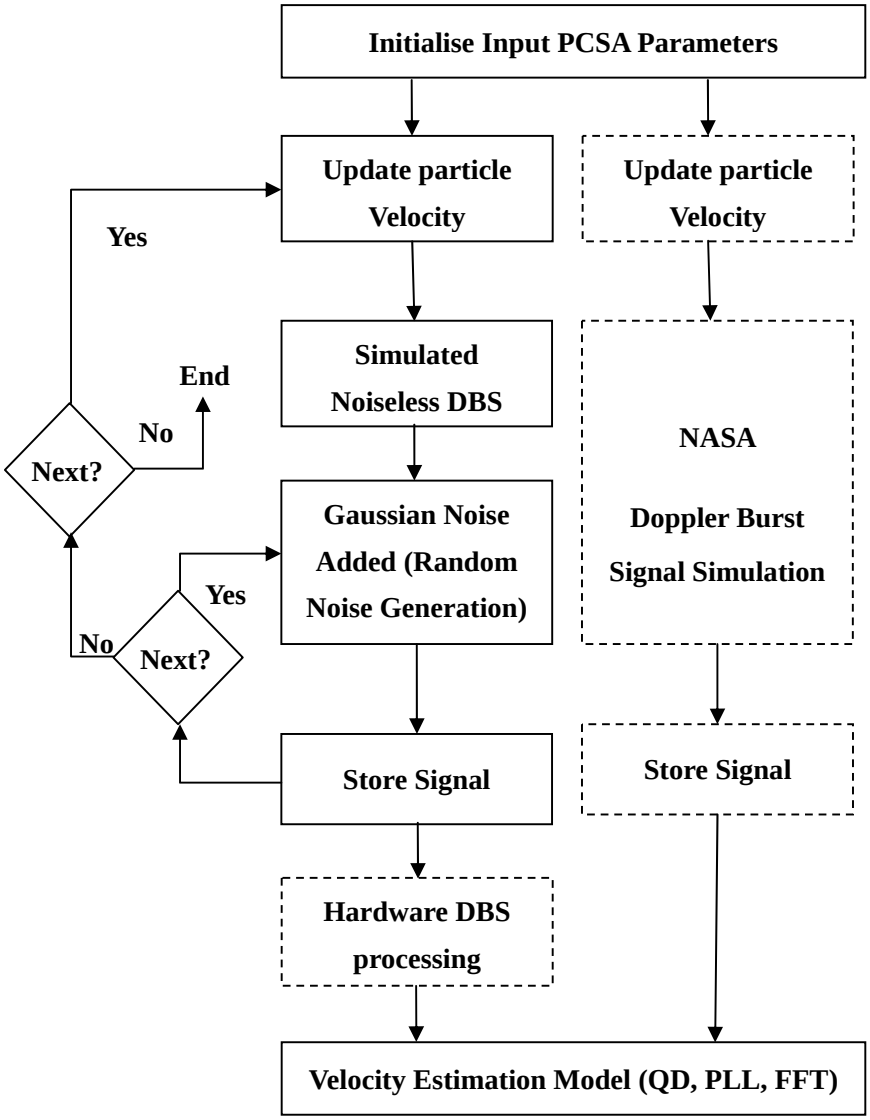

Fig. 5.1 Block diagram of the DBS generation and performance testing scheme for velocity estimation

As illustrated in Fig. 5.1, first, the input parameters of the PCSA are initialised, such as the optical parameters of the PDA (wavelength of beam, intersection angle, fringe spacing, Gaussian beam diameter, beam waist diameter, measurement volume diameter); parameters of the excitation method (drive frequency, magnitude of excitation field); the parameters of the DBS (signal phase, mean flow velocity, frequency shift, amplitude of

signal). Then, the value of particle velocity is updated in the outer simulation loop, in small increments, from 1mm/s to 800mm/s. For each generated signal corresponding to simulated particle velocity, Gaussian noise is added. Each burst of the DBS is stored composing a DBS train which simulates the signals arising from particles travelling through the measurement volume. In addition, for the purpose of cros-validation, some trains of DBSs were generated using NASA simulator (see section 5.2.2) and hardware signal processing system described in section 5.2.1. Following the DBS generation the particle velocity is obtained using the velocity estimation systems, such as QD, PLL and FFT techniques, discussed in chapter 4.

The block diagram of the DBS generation and performance testing scheme for phase shift estimation is shown in Fig. 5.2. The train of burst signals is generated in a similar fashion to the procedure discussed above and illustrated in Fig. 5.1. After initialising the input parameters of the PCSA the two DBS are generated with a predetermined phase shift corresponding to the particle size. The value of the phase shift is updated inside the outer simulation loop, in small increments, from 0 to 90 deg. The phase estimation system estimates the absolute value of the phase difference between two Doppler signals. This phase difference range corresponds to the range of arctangent function. The relationship between the particle size and phase shift was defined in (2.21). From the phase estimation range the size range can be calculated with appropriate optical system arrangement (the intersection angle, the scattering angle and the elevation angle). Each generated DBS was corrupted by Gaussian noise. The hardware signal processing system is expected to be designed and implemented in the future to provide validation of the simulation tests. Finally, the estimated phase shift is obtained by the phase estimation systems based on the correlation technique and Hilbert transformation.

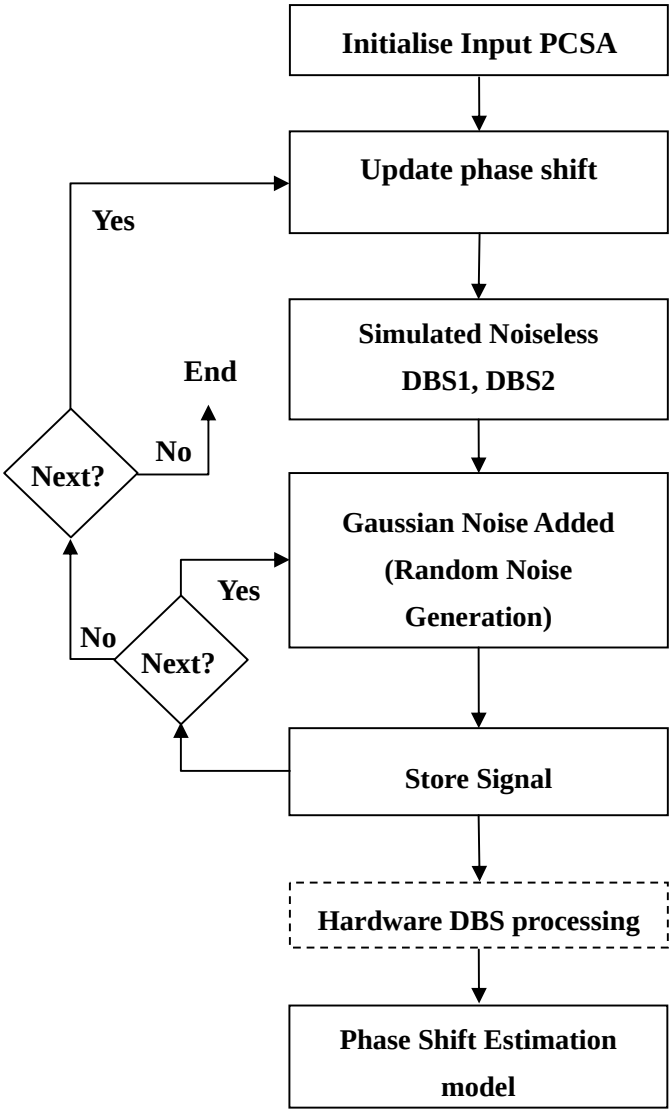

Fig. 5.2 Block diagram of the DBS generation and performance testing scheme for phase shift estimation

The details of the the simulation parameters of the DBSs in different excitation fields are given in Table 5.1 ~ 5.3.

a) DC excitation field – steady state

A_{DBS}(V)	$V_x(mm/s)$	$V_y(mm/s)$	$\mathbf{x}_0(mm)$
1	1~800	50	–3.5... 3.5
$\mathbf{y}_0(mm)$	$F_B(k\text{Hz})$	$t_0(s)$	$\varphi_0(deg)$
0	400	0.05	0

Table 5.1 Simulation parameters of the DBSs in DC excitation field – steady state

where A_{DBS} is the amplitude of DBS, V_x is the particle velocity range, V_y is the mean flow velocity, $\mathbf{x}_0$ is the original position in X direction, $\mathbf{y}_0$ is the original position in Y direction, F_B is the shift frequency, t_0 is the time slot of particle passing through the centre of the volume, φ_0 is the original phase.

b) Sine-wave excitation field

A_{DBS}(V)	$A_v(mm/s)$	$V_y(mm/s)$	$f(k\text{Hz})$	$\mathbf{x}_0(mm)$
1	1~800	50	1	–3.5... 3.5
$\mathbf{y}_0(mm)$	$F_B(k\text{Hz})$	$t_0(s)$	$\varphi_0(deg)$	
0	400	0.05	0	

Table 5.2 Simulation parameters of the DBSs in sine-wave excitation field

where A_{DBS} is the amplitude of DBS, V_x is the particle velocity range, V_y is the mean flow velocity, f is the drive frequency, $\mathbf{x}_0$ is the original position in X direction, $\mathbf{y}_0$ is the original position in Y direction, F_B is the shift frequency, t_0 is the time slot of particle passing through the centre of the volume, φ_0 is the original phase.

c) Square-wave excitation field

A_{DBS}(V)	E(MV/m)	f(kHz)	d (μm)	q (C)	V_y(mm/s)
1	0.3	1	0.5~10	1e ~ Gaussian limit	50
$\mathbf{x}_0$(mm)	$\mathbf{y}_0$(mm)	F_B(kHz)	t_0(s)	φ_0(deg)	
–3.5 to 3.5	0	400	0.05	0	

Table 5.3 Simulation parameters of the DBSs in square-wave excitation field

where A_{DBS} is the amplitude of DBS, E is the strength of the excitation field, f is the drive frequency, d is the particle diameter, q is the particle charge, V_x is the particle velocity range, V_y is the mean flow velocity, $\mathbf{x}_0$ is the original position in X direction, $\mathbf{y}_0$ is the original position in Y direction, F_B is the shift frequency, t_0 is the time slot of particle passing through the centre of the volume, φ_0 is the original phase.

The simulation of the DBS train is implemented in MATLAB under the following conditions shown in Table 5.4. The simulation of Gaussian noise is implemented by generating a pseudorandom, scalar value drawn from a normal distribution with mean 0 and standard deviation 1.

θ(deg)	λ (nm)	d_m (mm)	i (μm)	f_s (MHz)	N
12.9	514.5	1.35	2.29	10	10^6

Table 5.4 Simulation conditions of the DBS train

where θ is the intersection angle, λ is the wavelength, d_m is the beam diameter, i is the fringe spacing, f_s is the sampling frequency, N is the number of samples.

The example of the simulation the DBS train in the sine-wave excitation field is shown in Fig. 5.3. The parameters, such as particle velocity, particle charge, diameter and original position are randomly generated.

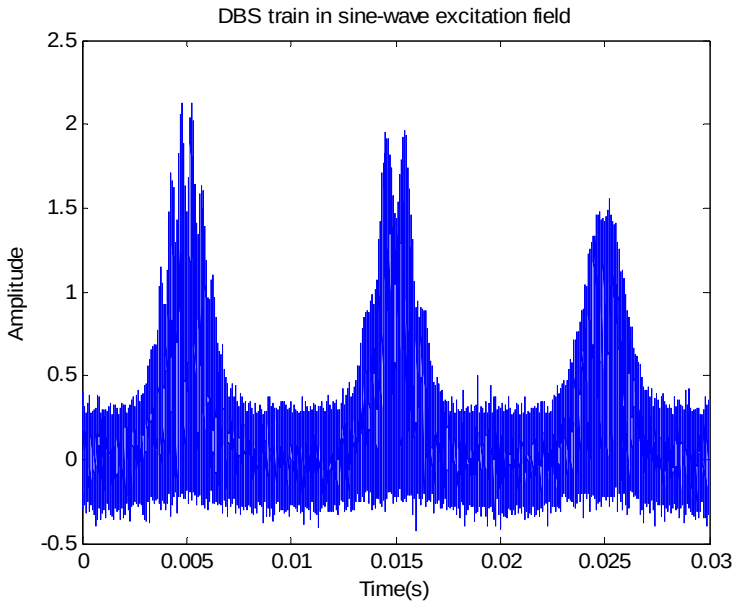

Fig. 5.3 Simulation result of DBS train in the sine-wave excitation field

5.2.1 Hardware DBS Processing System

The block diagram of the hardware signal processing system is shown in Fig. 5.4. In the hardware experiment, the analog DBS is generated using TGA12101 100MHz Arbitrary Waveform Generator based on the MATLAB data and digitized by MI30xx fast 12bit transient recorder, A/D converter board.

The procedure of signal processing in the hardware system shown in Fig. 5.1 can be divided into six steps. First of all, the simulation of noisy DBS train is implemented as

described in the previous section. Second, the data of the DBS is written into the *txt* file. Third, the data of DBS is imported from the *txt* file to the TTi Waveform Manager Plus software tool. Therefore, a new arbitrary waveform is produced and can be seen on the oscilloscope connected to the generator. Forth, this waveform is downloaded to the memory card by the generator via RS232 serial interfaces. Fifth, the analog DBS produced by the generator is sent to the PC. The type of digital data is a signed 16-bit integer.

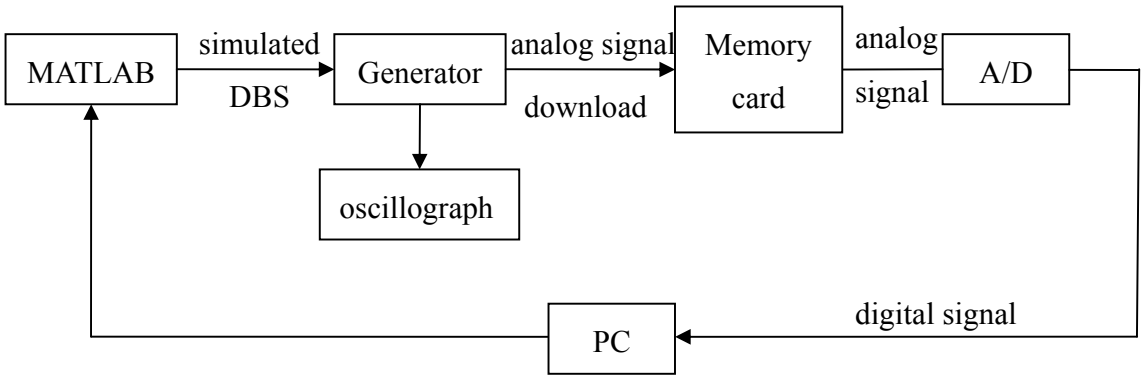

Fig. 5.4 Block diagram of hardware signal processing system

The TGA12101 100MHz Arbitrary Waveform Generator has been employed in the hardware signal processing system to generate the analog DBS. The instrument uses a combination of direct digital synthesis and variable clock techniques to provide high performance and extensive facilities in a compact instrument. It can generate a wide variety of waveform between 0.1mHz and 50MHz with high resolution and accuracy.

The sampling frequency is set to be 10MHz. The size of memory for recording is 2×10^5 samples per channel. The calibrated input range for the involved channels is set to be ±5V in order to ensure that it can cover the range of the amplitudes of input signals.

Finally, the digital signal is processed by the algorithms designed in MATLAB in order to estimate the particle velocity and size.

5.2.2 NASA Laser Doppler Velocimetry Simulator

As an alternative to the MATALB simulation of the DBS synthesized from the mathematical models and in order to provide even more realistic tests of the signal processing systems performance, NASA simulator was also used. The simulator has been developed by Dr Meyers from NASA and described in [150], [151], [152]. The numerical model used in NASA simulation software computes the DBS based on the characteristics of the laser source, the optical configuration, Mie scattering criteria for small particles, the characteristics of the photomultiplier as well as the trajectory of the particle via the measurement volume. As the particle passes through the sample volume along a given trajectory, the scattered signal is calculated based on the LV optical and electrical characteristics. The signal is mathematically high pass filtered and input to a model of a high-speed counter. The filtered signal triggers a model of a Schmidt trigger generating a corresponding digital train.

5.2.3 SNR of the Doppler Burst Signal

The SNR requirement is one of the very important criterions in the evaluation of the performance of the estimation systems. It is, therefore, necessary to calculate the SNR of the DBSs generated in different excitation fields accurately. In the literature, it is often assumed that the SNR of individual bursts is constant and equal to the square of the

maximum amplitude of the DBS divided by the square of the variance of noise. Although such simplification might be justified in some studies treating SNR as indicative of the quality of the DBS, one has to appreciate that the SNR for the DBS is not constant but varies within the individual bursts depending on the instantaneous amplitude of the DBS and the variance of noise. The problem is compounded by the fact that in addition to the Gaussian envelope of the DBS the oscillatory motion of the particle creates the oscillations in the instantaneous value of the SNR as the particle moves in and out of the volume. It is due to the fact that as the particle oscillates in the cross flow direction inside the volume the amplitude of the DBS is modulated which affects the SNR. Therefore, the definition of the DBS adopted in this study, takes into account the average power of the noise and the signal over the entire DBS and is given as

$$SNR(dB) = 10\log\frac{P_{signal}}{P_{noise}} \tag{5.1}$$

where P_{signal} and P_{noise} are the average power of signal and noise.

For discrete signal, $x(n)$ defined on $[n_1, n_2]$, its average power can be calculated from

$$P = \frac{1}{N_2 - N_1 + 1}\sum_{n=N_1}^{N_2} |x(n)|^2 \tag{5.2}$$

The following paragraphs are aimed to illustrate the effect of the particle trajectory via the measurement volume on the SNR in the DC, sine and square wave excitation fields. The calculation of the SNR of DBS can be divided into two cases. First case, the DC excitation field – steady state. Different particle trajectories and the corresponding DBSs in the DC excitation field – steady state are shown in Fig. 5.5.

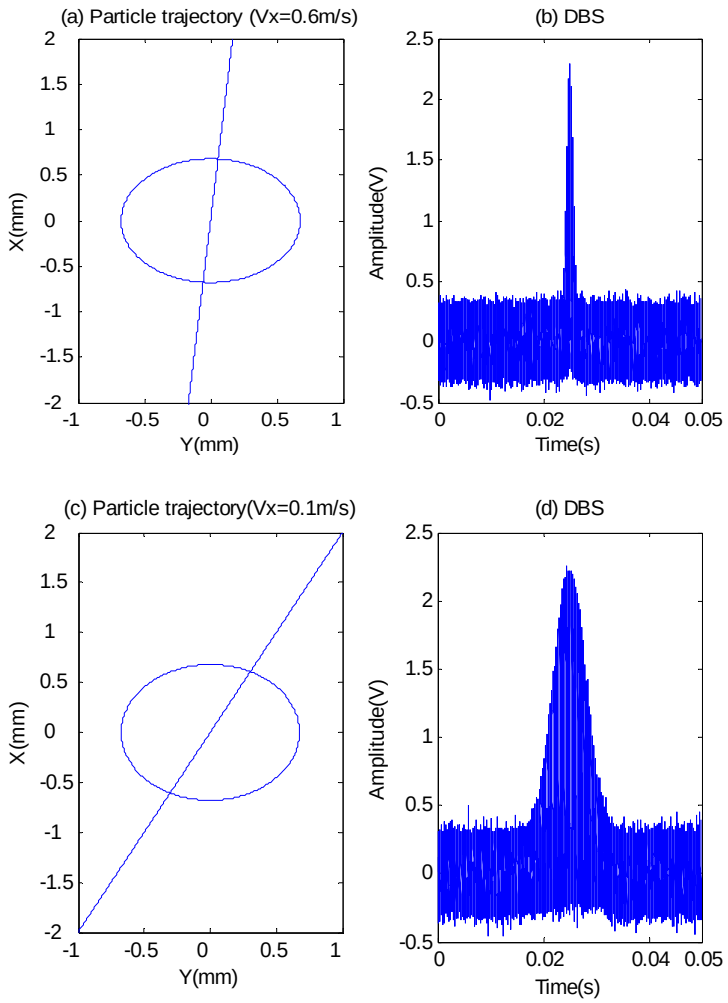

Fig. 5.5 (*a*) Trajectory of particle with velocity of $0.6m/s$, (*b*) corresponding DBS, (*c*) Trajectory of particle with velocity amplitude of $0.1m/s$, (*d*) corresponding DBS,

The SNRs of DBSs shown in Fig. 5.5 (*b*), (*d*) are 4.7dB and 12dB respectively. The powers of the noise and signal are respectively proportional to the areas of noise and signal. Therefore, the SNR can be regarded as the ratio between the areas A and B [30]. The power of the noise (noise variance) is kept the same in both Fig. 5.5 (*b*) and (*d*). However, the widths of bursts are different due to the different trajectories and the same signal amplitudes. Therefore, the signal powers are different. Thus, the SNRs of signals

are different based on (5.1). As shown in Fig. 5.5 (*b*) and (*d*), the SNR of the second DBS is greater than the one of the first one.

The second case is the sine-wave excitation field, as shown in Fig. 5.6. The SNR of DBSs shown in Fig. 5.6 (*b*), (*d*) and (*f*) are 12.5dB, 12.2dB, 3.1dB respectively. From Fig. 5.6 (*b*) and (*d*), it can be concluded that when the particle is passing through the centre of the measurement volume, the SNRs of the corresponding DBSs are almost the same although the velocity amplitudes are different. The powers of noise and signal are respectively proportional to the areas of noise and signal shown in Fig. 5.6 (*b*), (*d*) and (*f*). As mentioned before, the SNR can be regarded as the ratio between the two areas A and B. The power of the noise (noise variance) is constant during the whole period of measurement. The powers of the signals are almost the same due to the similar envelope of DBSs in Fig. 5.6 (*b*) and (*d*) (*e.g.* same width of burst, same amplitude of envelope).

From the comparison between (*d*) and (*f*), it can be seen that both the width of burst and the amplitude of envelope decreased. Therefore, the power of the signal decreased, moreover, the SNR becomes lower than before.

The same conclusion regarding to SNR of DBS can be obtained in square-wave excitation field due to the similar particle trajectory compared to the one in the sine-wave excitation field.

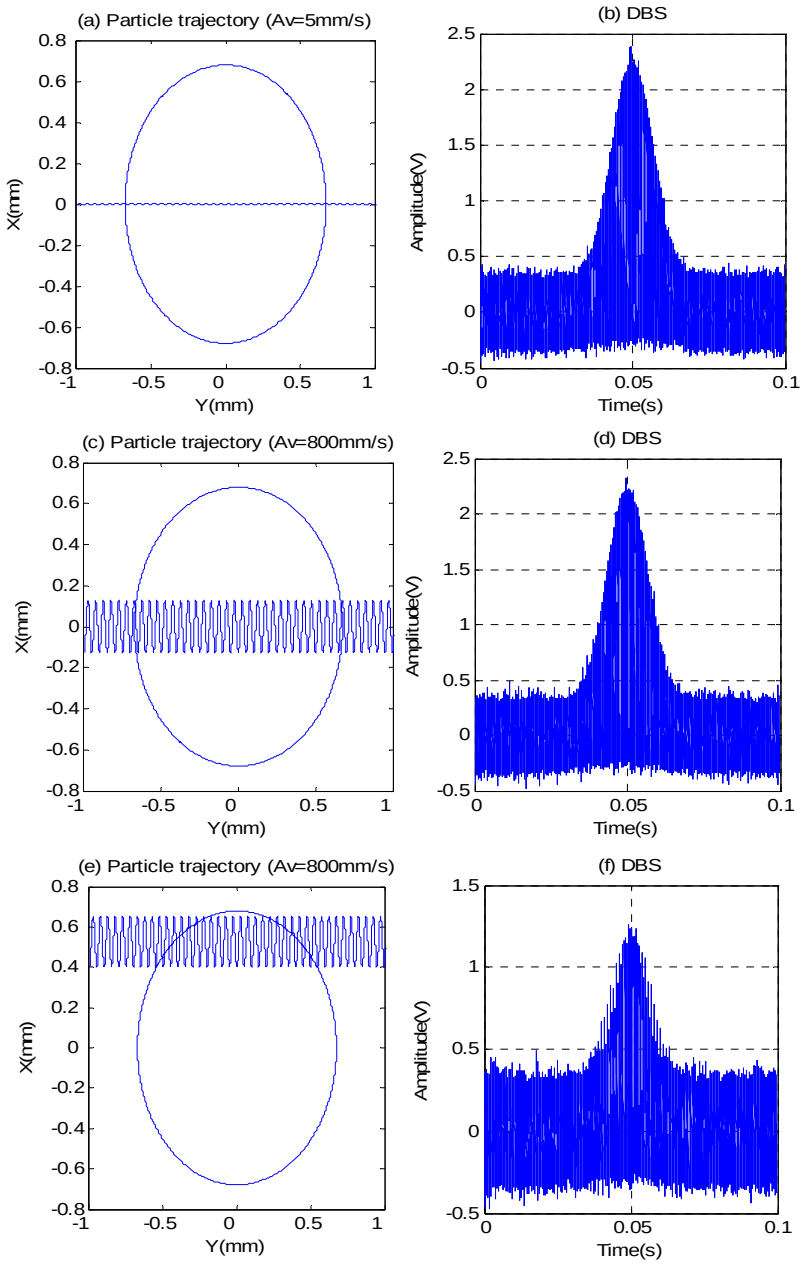

Fig. 5.6 (*a*) Trajectory of particle passing through the volume centre with velocity amplitude of 5*mm*/*s*, (*b*) corresponding DBS, (*c*) Trajectory of particle passing through the volume centre with velocity amplitude of 800*mm*/*s*, (*d*) corresponding DBS, (*e*) Trajectory of particle not passing through the volume centre with velocity amplitude of 800*mm*/*s*, (*f*) corresponding DBS.

5.3 Simulation Results of the Velocity Estimation in DC Excitation Field – Steady State

5.3.6 Simulation Results of the Velocity Estimation System based on Spectral Analysis

In the DC excitation field – steady state, the constant velocity in the X direction was obtained using FFT algorithm. This case is relatively straightforward since the particle velocity can be assumed constant throughout the measurement volume, producing standard, stationary DBS. The performance of the estimation algorithm using FFT has been improved by subsequent interpolation and windowing scheme. Fig. 5.7 shows typical example of a DBS spectrum obtained by FFT algorithm corresponding to a particle motion via the measurement volume with a constant velocity of V_x=10mm/s.

From the spectrum in Fig. 5.7, the value of normalized spectral peak offset δ can be calculated, δ= -4.1408. Thus, the Doppler frequency is obtained from (4.7), f_D = 404365.8592Hz. The relationship between the Doppler frequency and the particle velocity has been defined by (3.1). Therefore, knowing the simulation conditions, fringe spacing, i=2.29μm, F_B=40kHz, the constant particle velocity in the **X** direction, $V_{x,}$ can be calculated as Vx=9.9999mm/s. This result agrees well with the simulation condition with the relative error percentage of 7.14×10^{-6}.

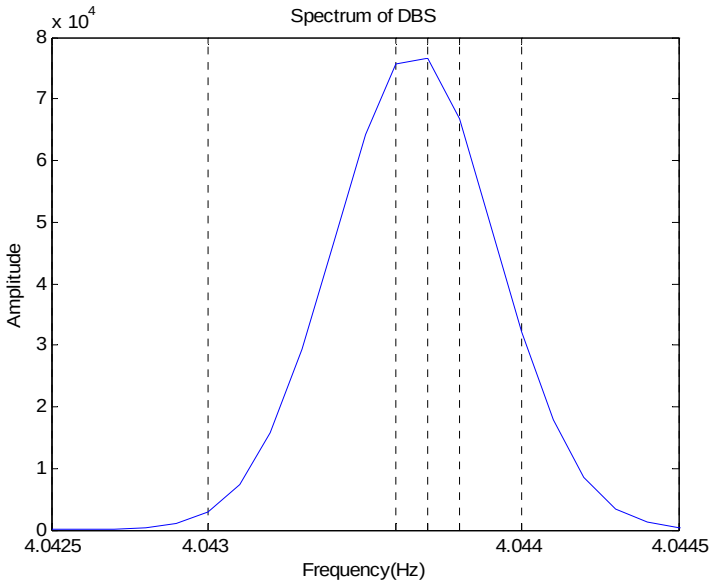

Fig. 5.7 Spectrum of Doppler Burst Signal

The comparison of the performance of the FFT algorithm and interpolation scheme used in conjunction with and without Blackman window is shown in Fig. 5.8.

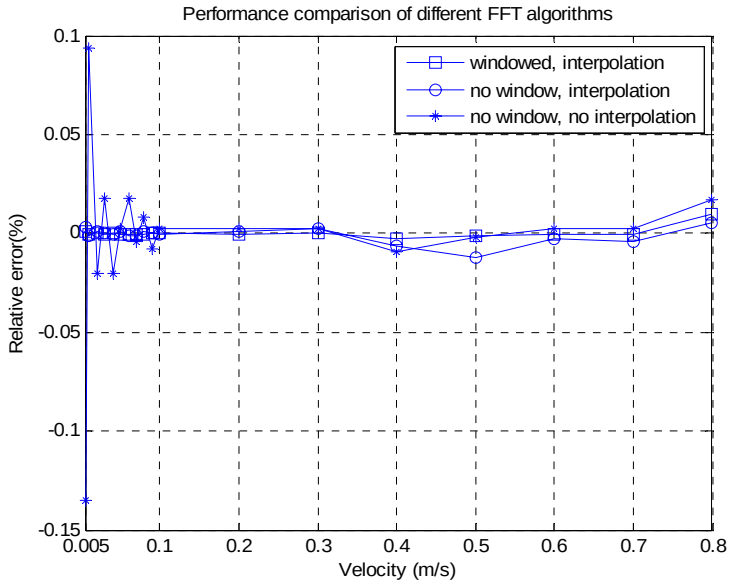

Fig. 5.8 Performance comparison of different FFT algorithms. Sampling period, T=1μs, number of samples, frequency resolution, Δf_s=5128Hz, Particle velocity, V_x=0.5m/s, noise variance, δ_n^2=0.01.

It can be concluded that in DC field the FFT algorithm performs very well in the wide range of particle velocities. However, further improvement in the accuracy of the estimation can be achieved using the time domain window and the spectrum interpolation.

5.3.2 Simulation Results of the Velocity Estimation System based on PLL Technique

This section presents the results of the PLL system performance in DC field described in section 4.4.4. The simulation conditions are shown in Table 5.5.

$\lambda(nm)$	$\theta(rad)$	$i\ (\mu m)$	$r_0(\mu m)$	$F_B(k\text{Hz})$	$V_x(mm/s)$
514.5	0.2251	2.99	675	400	100
$V_m(mm/s)$	$\varphi_0(rad)$	$t_0(s)$	N	$T\ (s)$	$x_0(m)$
50	0	0.025	5×10^5	10^{-7}	0

Table 5.5 Simulation Conditions for velocity estimation based on PLL technique in DC field

An example of the PLL system input and output signals in time domain, corresponding to the DBS generated by the particle with constant velocity $\mathbf{V}_x$=100*mm/s,* is shown in Fig. 5.9. The frequency of this noisy DBS, shown in Fig. 5.9 (*a*) equals to 4.44×10^5Hz, SNR of DBS equals to 14dB.

Fig. 5.9 (*b*), shows small oscillations in the output of the PLL gradually decreasing in amplitude over the duration of the trigger signal. Fig. 5.9 (*d*) shows the output of the velocity estimation after integration approximately equal to 100*mm*/*s* which agrees very well with the simulation condition.

In the estimation system, the long loop PLL has been adopted to enlarge the

working range. The loop range has been expanded by adjusting the loop gain of the PLL and careful design of the filters. The performance of the system was evaluated by means of the MC simulations. 100 trials were run on simulated signals synthesized from the signal model defined in (3.11).

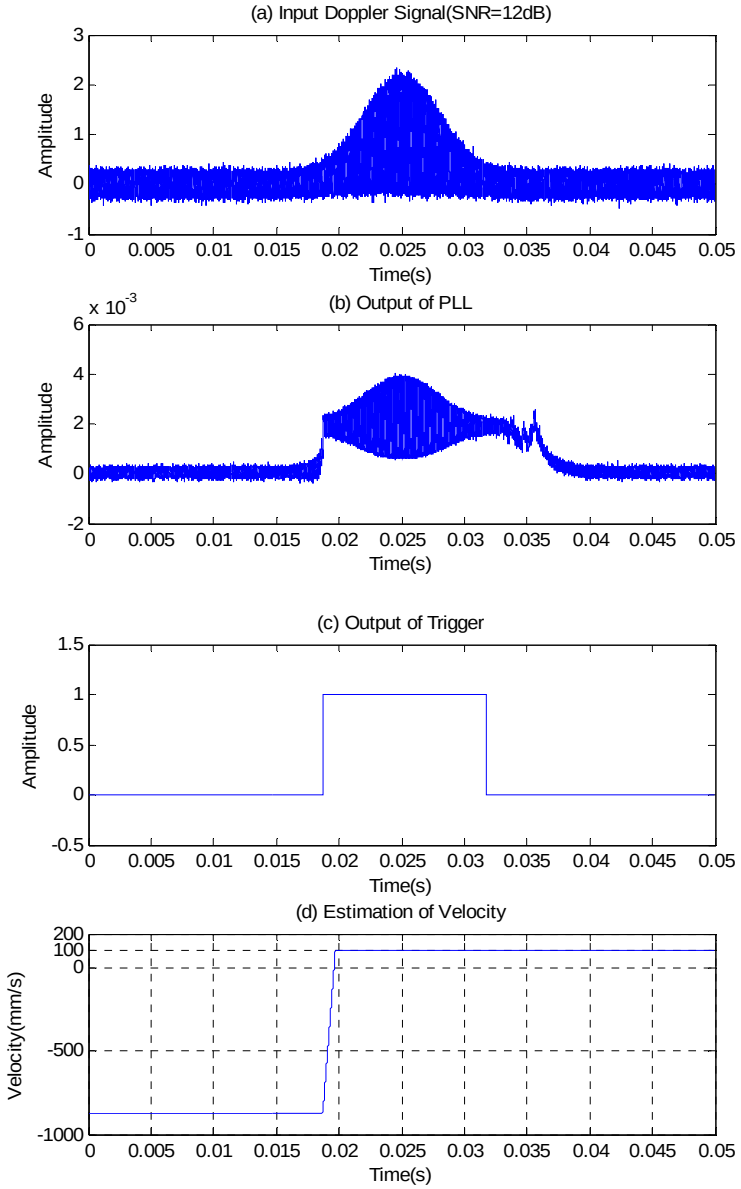

Fig. 5.9 Timing diagram of the PLL system in DC excitation field. (*a*) Doppler Signal, (*b*) Output of the PLL, (*c*) Output of the Trigger, (*d*) Velocity estimation.

The relative error and the standard deviation for the velocity estimation corresponding to different SNRs are plotted in Fig. 5.10. It illustrates that, at the noise variance of 0.01, the achievable velocity estimation range of the PLL system is from 1*mm*/*s* to 800*mm*/*s* with the error less than 5%. From Fig. 5.10 it can be seen that, the relative error is seriously affected by the noise. Therefore, it can be concluded that the PLL technique is more sensitive to noise compared to the spectral analysis.

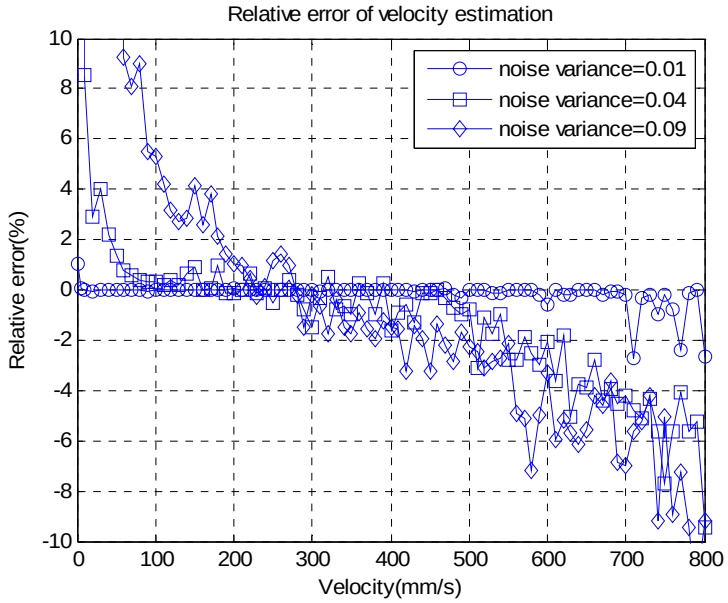

Fig. 5.10 Relative error for velocity estimation based on PLL in DC excitation field

5.4 Simulation Results of the Velocity Estimation in Sine-wave Excitation Field

5.4.1 Simulation Results of the Velocity Estimation System based on PLL Technique

This section presents the simulation results of the PLL system performance in sine-wave excitation field. The design of the system was discussed in section 4.5.1.

The simulation conditions are shown in Table 5.6.

$\lambda(nm)$	$\theta(rad)$	$i\ (\mu m)$	$r_0(\mu m)$	$F_B(kHz)$	$A_v(mm/s)$	$V_m(mm/s)$
514.5	0.2251	2.99	675	400	300	50
$\omega(rad/s)$	$\varphi_0(rad)$	$t_0(s)$	N	$T\ (s)$	$x_0(m)$	$y_0(m)$
2000π	0	0.05	10^6	10^{-7}	0	0

Table 5.6 Simulation Conditions for velocity estimation based on PLL technique in sine-wave excitation field

An example of the timing diagram showing the PLL estimator output is shown in Fig. 5.11. The DBS generated by the particle with the amplitude of velocity A_v=300mm/s is shown in Fig. 5.11 (*a*). The corresponding frequency range of this noisy DBS is from 3.96×10^5Hz to 4.04×10^5Hz. Fig. 5.11 (*b*) shows the output of the automatic gain control (AGC) device. As in discussed in section 4.5.1 the AGC compensates for magnitude variations of the Doppler signal and allows to widen the capture range of the PLL. The output of the PLL system is shown in Fig. 5.11 (*d*) with the signal following the oscillatory changes of the particle velocity inside the measurement volume.

It can be concluded from Fig. 5.11 (*d*) that the estimation result of the velocity amplitude is approximately 300mm/s. This result agrees very well with the simulation condition, A_v=300mm/s.

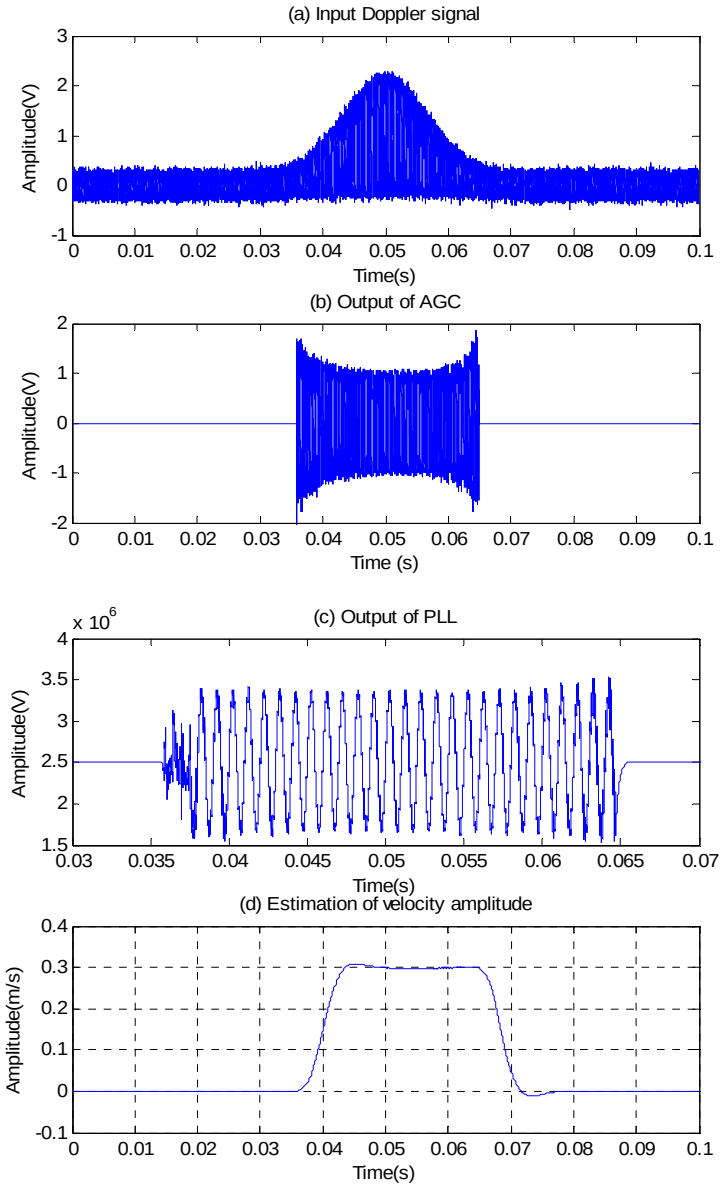

Fig. 5.11 Timing diagram of the PLL system in sine-wave excitation field. (*a*) Doppler signal, (*b*) Output of AGC, (*c*) Output of the PLL, (*d*) Velocity amplitude estimation.

Similar to the model designed in the DC excitation field, the long loop PLL has been also adopted to achieve the large working range. Additionally, the working range has been increased by employing the AGC module.

The performance of the system was evaluated by the means of Monte Carlo simulations. The relative error of the velocity estimation corresponding to different SNRs is plotted in Fig. 5.12. The results demonstrate that the achievable velocity estimation range of the system is from 30*mm*/*s* to 640*mm*/*s* with the relative error of velocity estimation less than 5%. The corresponding SNR is 12dB and the noise variance is 0.01. However, in case of more noisy signals, the estimation error rapidly escalates leading to the reduction of the estimation range.

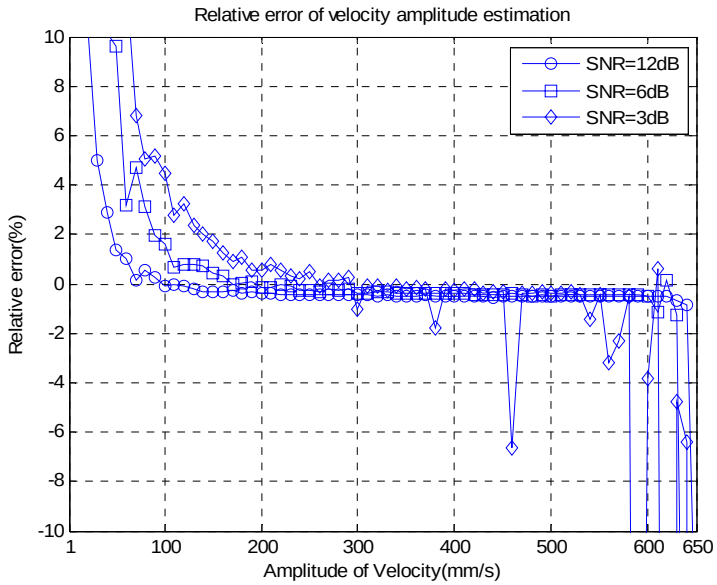

Fig. 5.12 Relative error for velocity amplitude estimation based on PLL in sine-wave excitation field

5.4.2 Simulation Results of the Velocity Estimation System based on Quadrature Demodulation Technique

This section presents the simulation results of the DQ system performance in sine-wave excitation field. The detailed discussion of the design of the system and its architecture was presented in section 4.5.3. The simulation conditions are shown in

Table 5.7.

$\lambda(nm)$	$\theta(rad)$	$i\ (\mu m)$	$r_0(\mu m)$	$F_B(kHz)$	$A_v(mm/s)$	$V_m(mm/s)$
514.5	0.2251	2.99	675	400	20	50
$\omega(rad/s)$	$\varphi_0(rad)$	$t_0(s)$	N	$T\ (s)$	$x_0(m)$	$y_0(m)$
2000π	0	0.05	10^6	10^{-7}	0	0

Table 5.7 Simulation Conditions for velocity estimatino based on QD technique in sine-wave excitation field

An example of the DBS generated by the oscillating particle with the velocity amplitude, A_v=20mm/s and a corresponding output of the QD system are shown in Fig. 5.14. The frequency range of the noisy DBS is from 3.91×10^5Hz to 4.09×10^5 Hz.

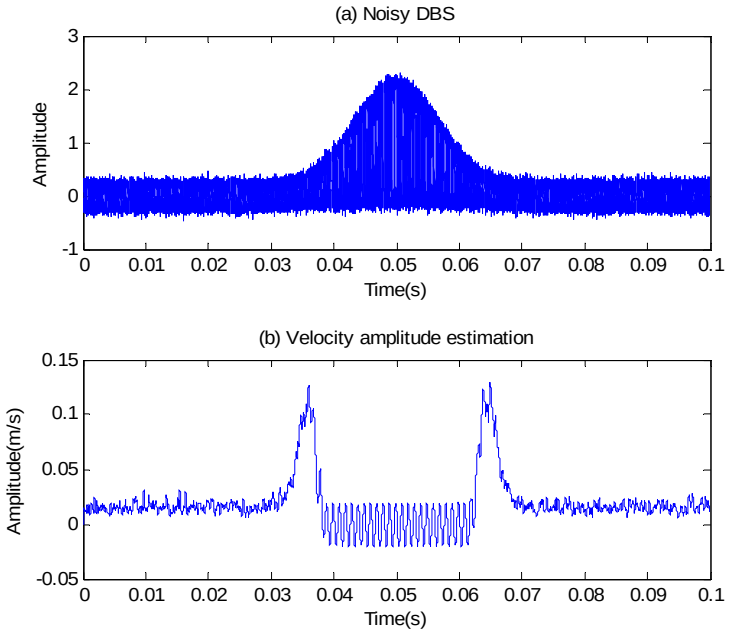

Fig. 5.13 Simulation results of QD model in sine-wave excitation field. (*a*) Noisy DBS, (*b*) Velocity amplitude estimation.

It can be seen from Fig. 5.14 (*b*) that after the initial rapid increase of the amplitude of the QD output the signal stabilizes following the oscillatory motion of the particle

velocity. The estimation result of the velocity amplitude obtained from the QD output is 20*mm*/*s*. This result agrees very well with the simulation condition.

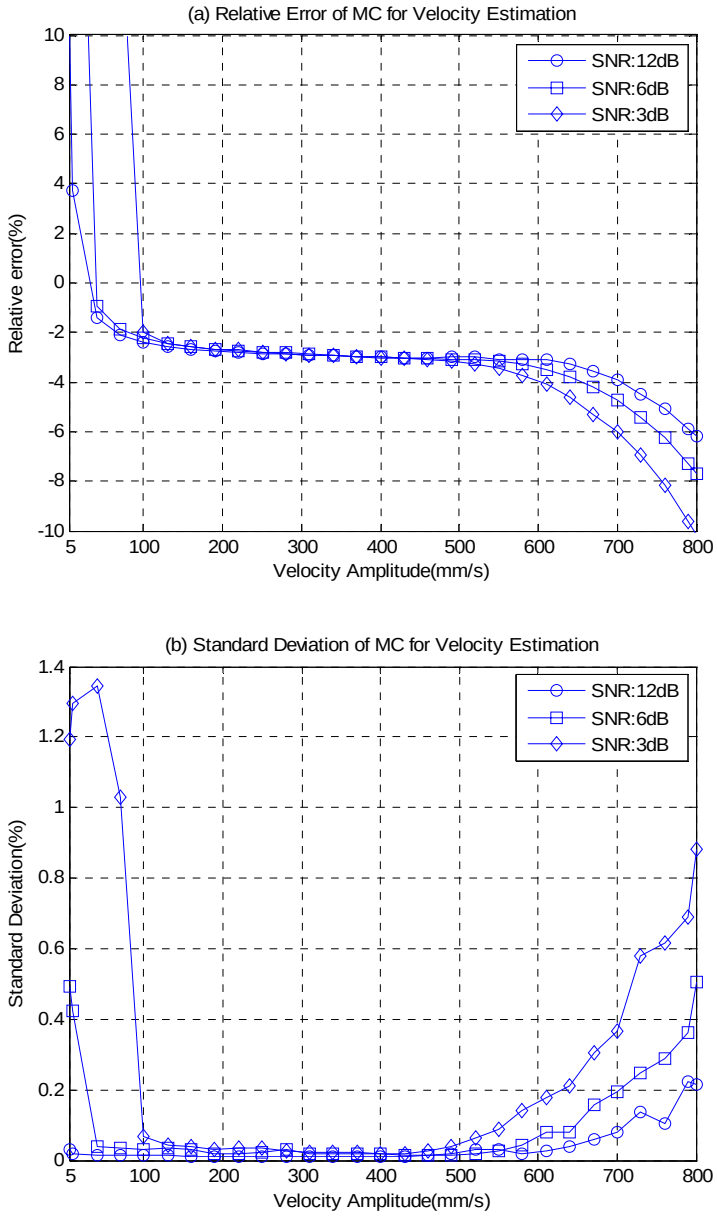

Fig. 5.14 (a) Relative error, (b) Standard deviation of MC simulations on velocity estimation in sine-wave excitation field

The performance of the system was systematically evaluated by the MC simulations. 100 trials were run on simulated signals synthesized from the signal model defined in (4.55). The relative error and the standard deviation for velocity estimation corresponding to different SNRs are plotted in Fig. 5.15. It illustrates that the achievable velocity estimation range of the system is from 10*mm*/*s* to 780*mm*/*s* in which the relative error of velocity estimation is less than 5% and the standard deviation is no larger than 1.4%. The corresponding SNR is 12dB and the noise variance is 0.01.

5.5 Simulation Results of the Velocity Estimation in Square-wave Excitation Field

5.5.1 Simulation Results of the Velocity Estimation System based on Spectral Analysis

This section presents the simulation results of velocity estimation in square wave excitation field using spectral analysis. The procedure of the spectral analysis in the square-wave excitation has been discussed in section 4.6.1. Fig. 5.15 shows an example of the velocity estimation in square-wave excitation from the DBS spectrum using peak detection and interpolation.

Based on Fig. 5.15, the value of δ can be calculated, δ= 0.0041. Thus, the Doppler frequency is obtained from (4.7), $f_D = 4.602\times10^5$Hz.

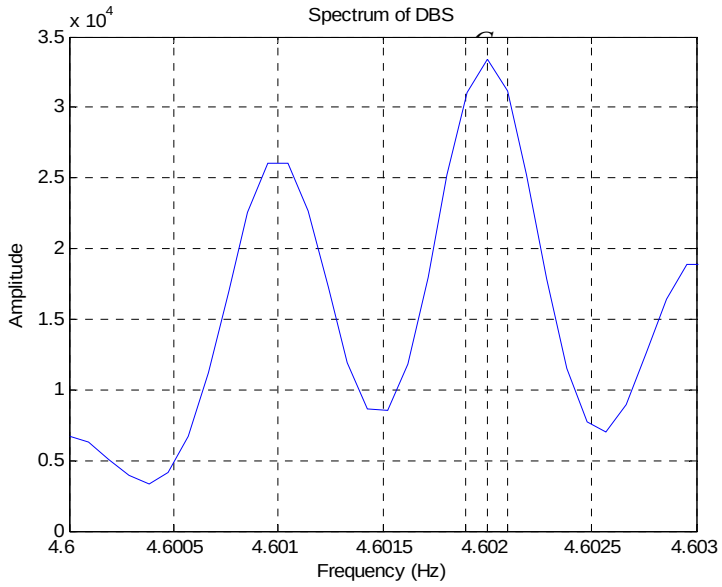

Fig. 5.15 Spectrum of Doppler Burst Signal

The relationship between the Doppler frequency and the particle velocity has been defined in (3.1). Therefore, knowing the simulation conditions, fringe spacing, D=1/i, the constant particle velocity in the **X** direction, $V_{x,}$ can be calculated from the Doppler frequency, Vx=0.1379m/s which agrees well with the simulation condition.

The velocity estimation range based on spectral analysis in the square-wave excitation field has been systematically tested by means of MC simulations and the results are shown in Fig. 5.16. The simulation conditions are shown in Table 5.8.

$\lambda(nm)$	$\theta(rad)$	$i\ (\mu m)$	$r_0(\mu m)$	$F_B(kHz)$	$V_x(mm/s)$	$V_m(mm/s)$
514.5	0.2251	2.99	675	400	1~800	50
$\omega(rad/s)$	$\varphi_0(rad)$	$t_0(s)$	N	$T\ (s)$	$x_0(m)$	$y_0(m)$
2000π	0	0.05	10^6	10^{-7}	0	0

Table 5.8 Simulation Conditions for velocity estimation based on spectral analysis in square-wave excitation field

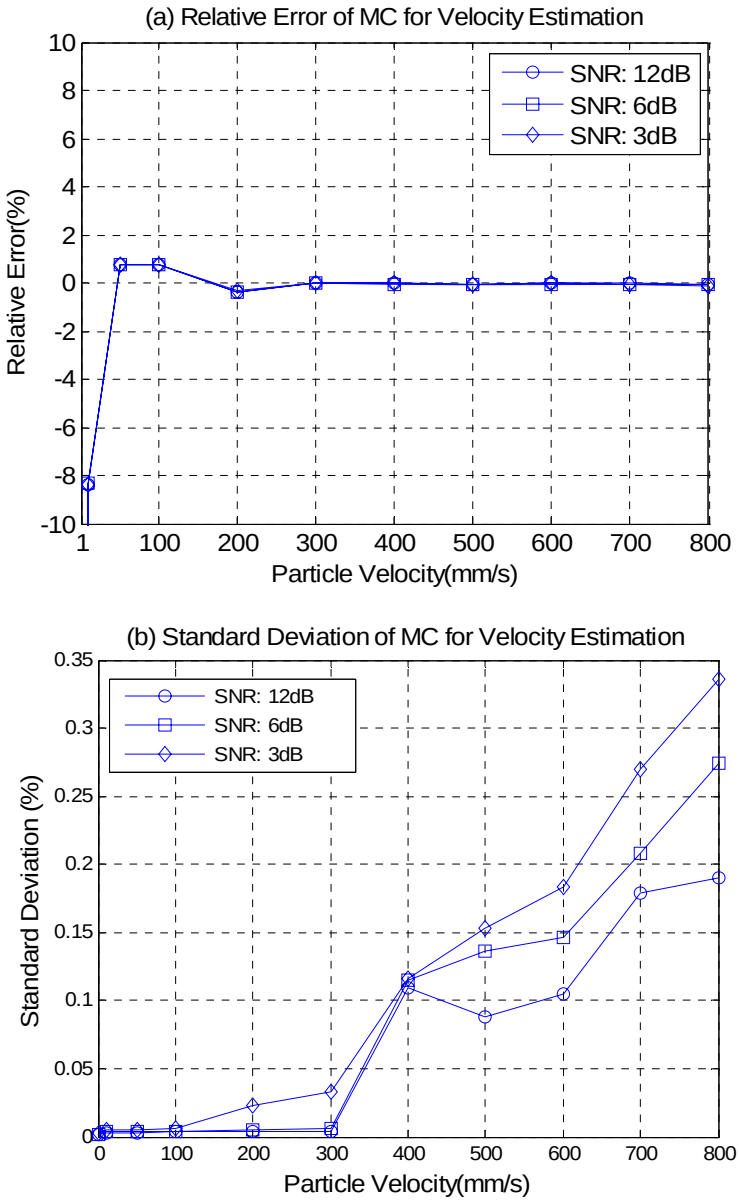

Fig. 5.16 (a) Relative error (b) Standard deviation of MC simulations on velocity estimation in square-wave excitation field

Corresponding to different SNRs, 100 trials were run on the simulated signals synthesized based on the mathematical model defined in (3.5) and (3.31). With SNR 3dB, the velocity estimation range of the spectral analysis system is from 5*mm*/*s* to 800*mm*/*s* (could be easily extended) with the relative error less than 10% and the standard

deviation smaller than 0.35%. The accuracy of velocity measurements with the FFT technique seems largely unaffected by the signal-to-noise ratio of the detected signal and depends on the sampling interval and the number of data points in the FFT. In general, the decline of the accuracy of the estimation for low velocities is largely due to the low particle displacement amplitude and therefore decreasing number of fringes crossed by the particle in its oscillatory motion. Further analysis of the effect of the number of fringes on the accuracy of the velocity estimation is given in chapter 6.

5.6 Simulation Results of the Phase Shift Estimation based on the Hilbert Transformation and the Correlation Technique

The particle size is obtained from the phase shift between DBSs received by different photo-detectors in the PDA system. The phase shift estimations of both systems are based on the correlation technique and the Hilbert transformation. The detailed discussion of the design of the signal processing system based on the Hilbert Transformation and the Correlation Technique was presented in section 4.7. The performance of the systems was tested using MC simulation and the results are given in Fig. 5.17 and 5.18. The simulation conditions are shown in Table 5.9 and 5.10.

During the performance testing, the absolute phase shift between different DBSs was estimated corresponding to different velocity amplitudes, $5mm/s$~$800mm/s$ for both the sine-wave excitation field and the square-wave excitation field. The random noise variance was maintained at 0.01. The SNR was from 15.3dB to 15.5dB for sine-wave excitation field and from 15dB to 15.5dB for square-wave excitation field.

$\lambda(nm)$	$\theta(rad)$	$i\ (\mu m)$	$r_0(\mu m)$	$F_B(kHz)$	$A_v(mm/s)$	$V_m(mm/s)$
514.5	0.2251	2.99	675	400	5~800	50
$\omega(rad/s)$	$\Delta\varphi$(Deg)	$t_0(s)$	N	$T\ (s)$	$x_0(m)$	$y_0(m)$
2000π	5~90	0.005	5×10^5	10^{-7}	0	0

Table 5.9 Simulation Conditions for phase shift estimation based on correlation technique in sine-wave excitation field

$\lambda(nm)$	$\theta(rad)$	$i\ (\mu m)$	$r_0(\mu m)$	$F_B(kHz)$	$V_x(mm/s)$	$V_m(mm/s)$
514.5	0.2251	2.99	675	400	5~800	50
$\omega(rad/s)$	$\Delta\varphi$(Deg)	$t_0(s)$	N	$T\ (s)$	$x_0(m)$	$y_0(m)$
2000π	5~90	0.005	5×10^5	10^{-7}	0	0

Table 5.10 Simulation Conditions for phase shift estimation based on correlation technique in square-wave excitation field

It can be found that for the range of phase shift estimation from 5^0 to 90^0, the relative error percentage was smaller than 8% and the standard deviation was less than 0.5% in the sine-wave excitation field. In the square-wave excitation field the relative error percentage was smaller than 3% and the standard deviation was less than 1.5%.

From Fig. 5.17 and 5.18, it can be seen that the amplitude of particle velocity has a significant effect on the estimation performance in both square-wave and sine-wave excitation field. The accuracy of the phase shift estimation decreased with the increase of the particle velocity amplitude. More research is needed to fully understand this phenomenon and improve the perfomance of the system.

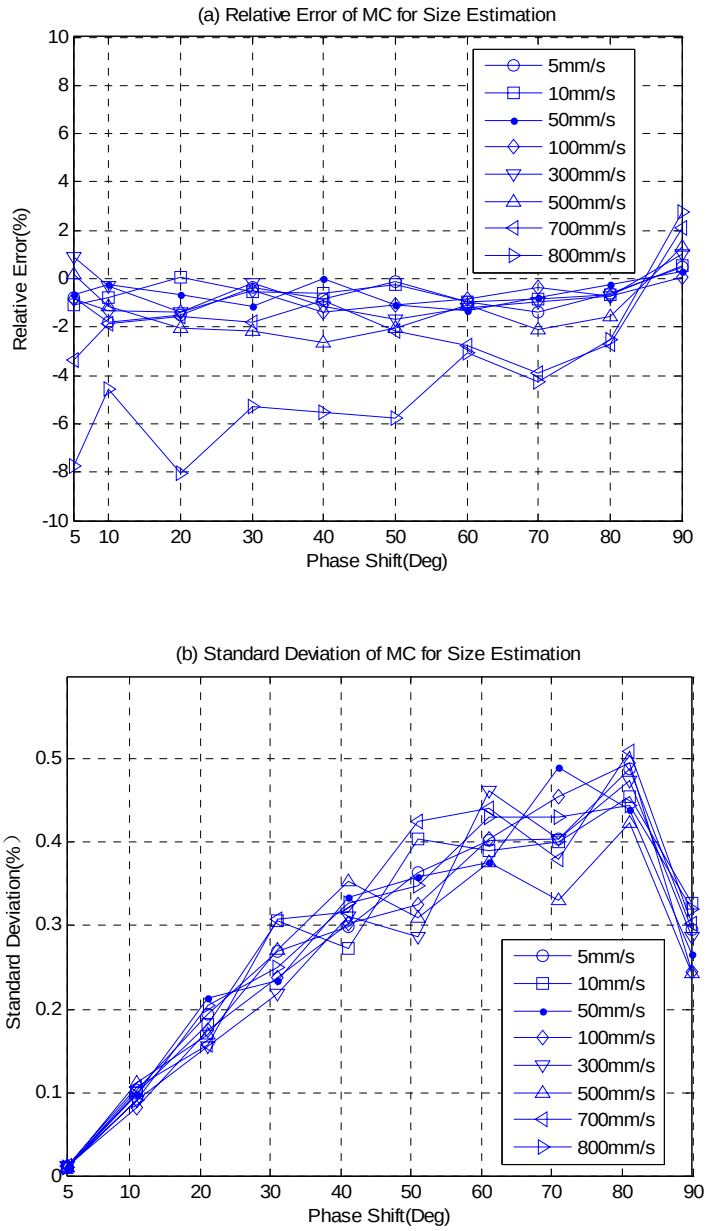

Fig. 5.17 (a) Relative error (b) Standard deviation of MC on phase shift estimation corresponding to different velocities from 5*mm*/*s* to 800*mm*/*s* in sine-wave excitation field, drive frequency *f*=1*k*Hz.

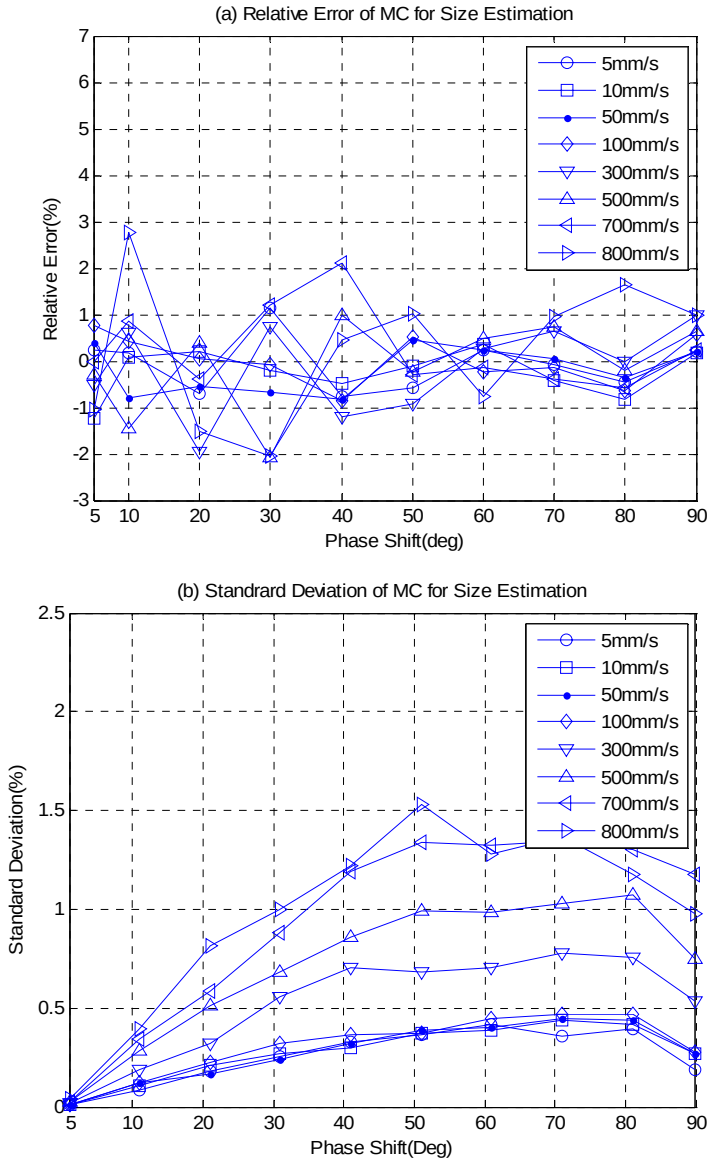

Fig. 5.18 (a) Relative error (b) Standard deviation of MC on phase shift estimation corresponding to different velocities from 5*mm*/*s* to 800*mm*/*s* in square-wave excitation field, drive frequency *f*=1*k*Hz.

5.7 Velocity and Phase Shift Estimation of the DBS Train

In order to extend the testing of the signal processing performance with single DBS,

some tests were carried our using generated and digitised trains of DBS. These trains will arise during the aerosol measurements, when a number of particles pass through the measurement volume in a short succession. There are three main challenges in signal processing of the train of DBS such as: tracking signal frequency for short bursts, signal validation for noisy signals and the presence of multiple bursts in the measurement volume. The processing of the train of DBS can be divided into the following steps. Firstly, the arrival of the DBS is detected and signaled by the trigger based on a pre-defined threshold. Secondly, velocity and phase shift corresponding to each burst is estimated using appropriate signal processing technique. Finally, the measurement is validated in order to determine whether the neighboring bursts are generated by the same particle passing through the measurement volume. An example of the train of DBS in the square-wave field is given in Fig. 5.19. Generated DBS were recorded using 12-bit Spectrum MI-3013 transient recorder. Each burst corresponds to different velocity, SNR and the trajectory of the particle. The results show that even discontinuous burst with a low SNR can be measured.

5.8 Particle Charge Range Calculation

Following on from the presentation of the results of the velocity and phase estimation systems this section discusses the calculation of the particle charge range based on the velocity and phase shift ranges in different excitation systems. The particle charge can be calculated from the following formulas (5.3) and (5.4) already introduced in chapter 2. For the sake of reader's convenience the expressions are repeated

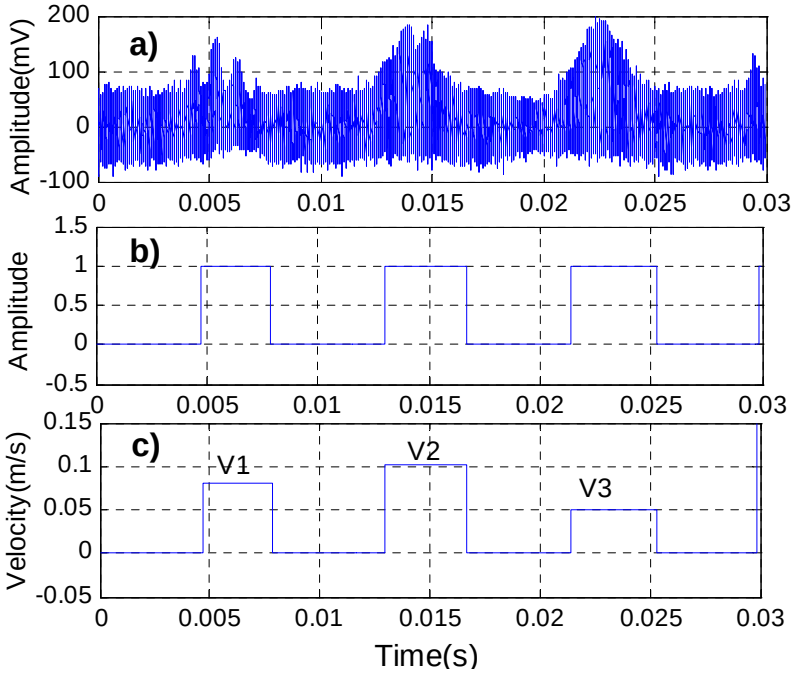

Fig. 5.19. (a) Train of DBSs, (b) Output of the trigger, (c) Velocity amplitude estimation;V_1=80mm/s, SNR_1=-3dB, $X0_1$=0.057mm; V_2=100mm/s, $X0_2$=0.025mm SNR_2=4dB;V_3=50mm/s, SNR_3=5dB, $X0_3$=0mm. X0 denotes the mean, off-axis distance of the particle from the center of the volume.

in this section.

In the DC excitation field and square-wave excitation field, the charge calculation formula can be expressed as,

$$q = \frac{3\pi\eta d V_x}{C_c E} \tag{5.3}$$

In the sine-wave excitation filed,

$$q = \frac{3\pi\eta d A_v}{C_c E}\sqrt{1+\omega^2\tau^2} \tag{5.4}$$

where V_x is the constant particle velocity, A_v is the amplitude of particle velocity, η is the air viscosity, d is the particle diameter, τ is the relaxation time, $\tau = \frac{\rho d^2 C_c}{18\eta}$, E is the

strength of the excitation field in the direction of the particle drift velocity, ω is the drive frequency and C_c is the Cunningham slip correction factor.

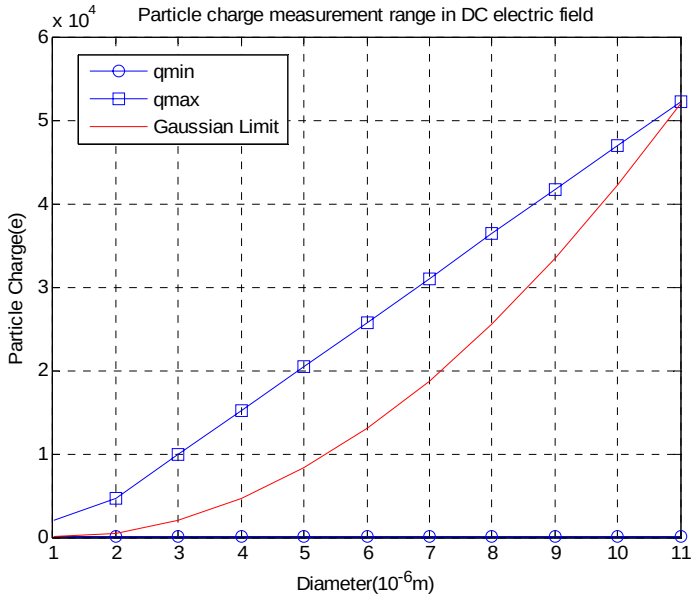

Fig.5.20 Charge range in DC excitation field, E=0.165MV/m, η=1.8616*10^{-5}, d is from 0.5μm to 10μm, V_x is from 1mm/s to 800mm/s.

The polarity of charge can be determined from the direction of particle velocity in the DC excitation field. In the sine-wave and square-wave excitation fields, the polarity of charge can be determined from the phase difference between field excitation and the particle velocity. The charge measurement limits in DC sine-wave and square-wave excitation fields are shown in Fig. 5.20 ~ Fig. 5.23.

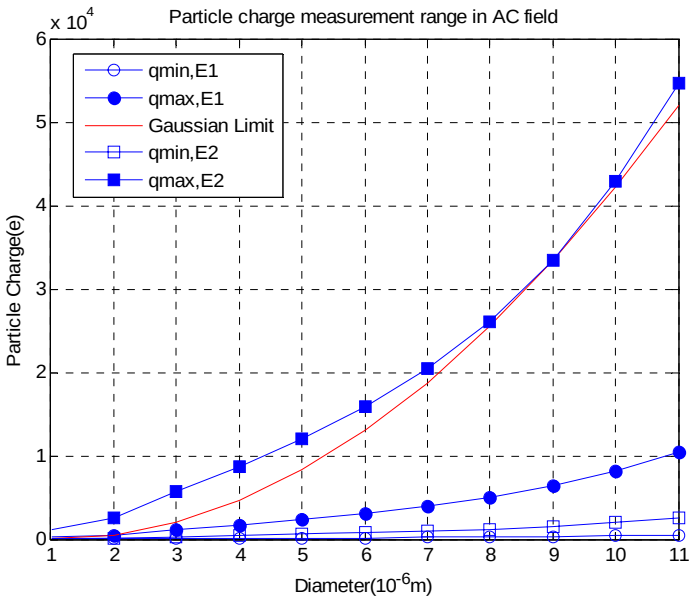

Fig. 5.21 Charge range in sine-wave excitation field based on PLL model, E_1=1.2MV/m, E_2=0.23MV/m, ω=2000π, η=1.8616*10^{-5}, d is from 0.5μm to 10μm, A_v is from 30mm/s to 640mm/s.

In the DC field, for a given field strength, E=0.165MV/m, the charge measurement range achievable using the PLL system extends from 2e to the Gaussian limit, as demonstrated in Fig. 5.20. However, in the sine-wave excitation field using the signal processing system based on the PLL technique, in order to cover the entire charge range and extend the lower limit of the measurable charge the electric field strength has to be increased from E_2=0.23MV/m to E_1=1.2MV/m between the measurements. As shown in Fig. 5.21, by combining the two ranges, the overall charge range spans from 10e to the Gaussian limit. The drawback of this approach, however, is that each measurement has to be repeated with two different values of the electric field strength.

Fig. 5.22 shows the result of the particle charge measurement range calculation in, sine-wave excitation field for the system based on QD technique. Due to the improved

performance of the QD system the achievable charge range spans from 14*e* to the Gaussian limit for a single set of parameters.

As shown in Fig. 5.23, in the square-wave excitation field, the estimation system based on spectral analysis is able to estimate the particles with the charge ranging from 12*e* to the Gaussian limit.

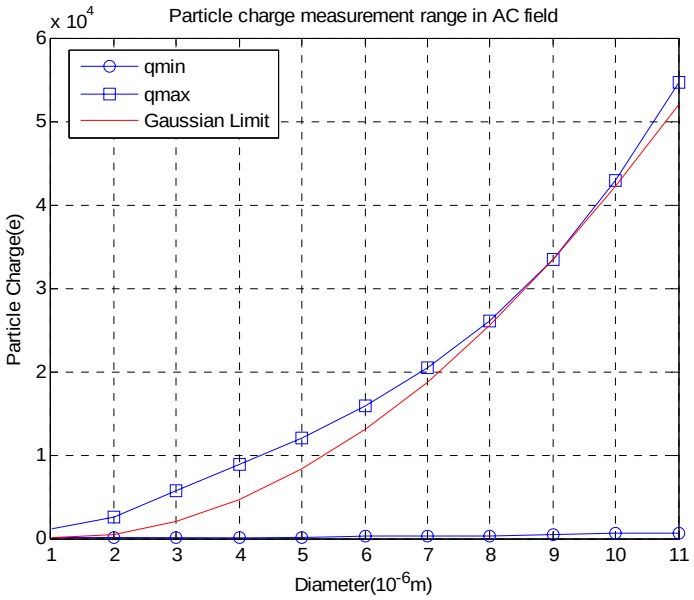

Fig. 5.22 Charge range in sine-wave excitation field based on QD model, E=0.28MV/m, ω=2000π, η=1.8616*10^{-5}, d is from 0.5μm to 10μm, A_v is from 10mm/s to 780mm/s.

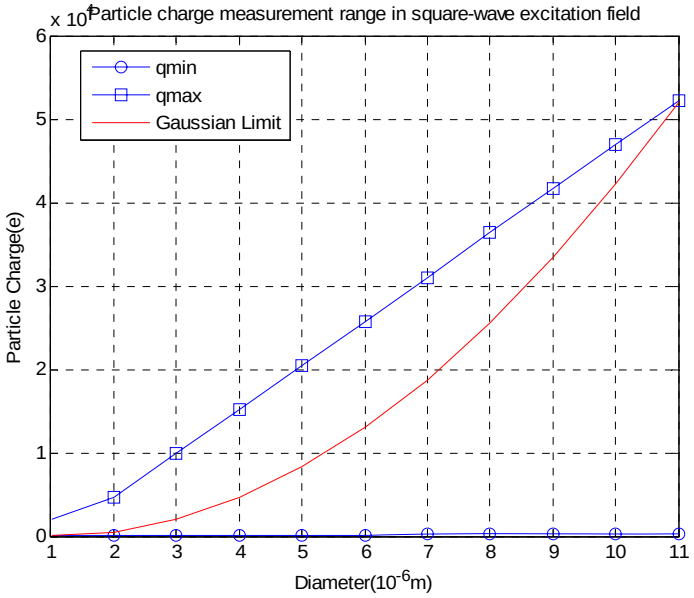

Fig. 5.23 Charge range in square-wave excitation field based on spectral analysis, E=0.165MV/m, ω=2000π, η=1.8616*10^{-5}, d is from 0.5μm to 10μm, A_v is from 5mm/s to 800mm/s.

5.9 Summary and Conclusions

This chapter presented the results of the simulation and performance testing of the estimation systems based on the QD, PLL, spectral analysis and correlation technique. First of all, the procedure for the generation of the Doppler burst signals and performance testing scheme was discussed for both velocity and phase shift estimation systems. The DBSs used in MC tests were generated from the mathematical models implemented in MATLAB. The generated DBS were subsequently corrupted with the added Gaussian noise. Cross validation of the results was performed using hardware signal processing system employing Arbitrary Waveform Generator and also NASA simulator to further confirm the validity of the estimation. Several hundreds of MC trials were run on

simulated signals synthesized from the signal models for each combination of the measurement parameters. The purpose of the chapter was to provide a comprehensive comparison of the signal processing systems performance. The comparison criteria involved velocity and phase estimation range, accuracy of the estimation, SNR requirement, and particle charge range. Based on the presented results the following conclusions have been drawn.

A. Velocity Estimation Range

The simulation results have demonstrated that the velocity estimation range of different systems designed in respective excitation fields are different for the burst signals with the same level of added noise. In the DC excitation field, the system based on the PLL technique was able to estimate the velocity from 1*mm*/*s* to 800*mm*/*s* with the relative error less than 5%. In the sine-wave excitation field, the velocity amplitude estimation range of PLL system was from 30*mm*/*s* to 640*mm*/*s* with the relative error less than 5%. In addition to the PLL system, the signal processing system based on QD technique was capable of estimating velocity amplitude from 10*mm*/*s* to 780*mm*/*s* in which the error was less than 5% and the standard deviation less than 1.4%. In the case of the square-wave excitation field, the velocity estimation range was wider and spanned from 5*mm*/*s* to 800*mm*/s, in which the relative error was less than 10% and the standard deviation was less than 0.35%.

In conclusion, the system based on PLL technique in DC field and the system based on spectral analysis in the square-wave excitation field performed better than the systems based on PLL and QD techniques in the sine-wave excitation field. Compared to the PLL system, the accuracy of the velocity estimation in the square-wave excitation

field rapidly decreased for particle velocity with and amplitude less than 5*mm*/*s*. On the other hand however, the working range of the system using spectral analyses could be easily extended without compromising the performance.

B. Phase Shift Estimation Range

The phase shift estimation system designed based on the Hilbert transform and the correlation technique was tested at the drive frequency of 1*k*Hz and with the noise variance of 0.01 in both sine and square wave excitation fields. In the sine-wave excitation field, the phase shift estimation ranged from 5^o to 90^o with an error less than 8% and the standard deviation was no larger than 0.5%. The corresponding velocity amplitude ranged from 5*mm*/*s* to 800*mm*/*s*. In the square-wave excitation field, the system was able to estimate the phase shift from 5^o to 90^o with an error less than 3% and the standard deviation was no larger than 1.5%. The corresponding velocity amplitude varied from 5*mm*/*s* to 800*mm*/*s*.

It can be concluded that the working ranges of signal processing systems in both excitation fields are very similar. In both the square-wave and sine-wave excitation field, the system performance was affected by the amplitude of velocity. More research is needed to fully understand this behavior and improve the performance of the system.

C. Charge Measurement Range

By combining the velocity and size estimation range, the charge measurement range was calculated. In the DC excitation field, the largest charge range was achieved by the PLL system. For *E*=0.165MV/m, the charge measurement range spanned from 2*e* to Gaussian limit. The PLL system in sine-wave excitation field achieved a charge range

from 10*e* to the saturation level. However, this charge range was achieved by changing the strength of the field from 1.2MV/*m* to 0.23MV/*m* between the measurements. In the sine-wave excitation, for *f*=1*k*Hz and *E*=0.28MV/*m,* the charge range from 14*e* to the Gaussian limit is achieved by QD system. In the square-wave excitation, the achievable charge range is from 12*e* to the Gaussian limit at *f*=1kHz and E=0.165MV/*m*.

In conclusion, for several combinations of the drive frequency and electric field strength, the charge range from several electrons to the Gaussian limit can be achieved without the need to change the drive frequency or the field strength, except the PLL system in the sine-wave excitation field. By comparison, the PLL system in the DC excitation field performs better in the estimation of lowly charged particles. However, the loss of some highly charged particles in DC electric field makes this system inferior. The system based on spectral analysis in square-wave excitation field provides the best results in terms of the range of measurable particle charge.

D. SNR Requirement

It can be concluded that the velocity estimation system based on spectral analysis in the square-wave excitation field has the lowest SNR requirement. When the SNR becomes smaller, the performance of all the tested systems degrades except the system based on spectral analysis working in the DC field and square-wave excitation field. In case of QD and PLL systems the estimation ranges became narrower as the SNR decreases. In the sine-wave excitation field, the PLL system is more sensitive to noise than the QD system.

Chapter 6

Bounds on the DBS Frequency Estimation Variance

6.1 Introduction

Chapter 5 presented the results of the simulation and the performance testing of the signal processing systems in different excitation methods. The comparison of systems performance with respect to velocity and phase shift estimation range, SNR requirement and the charge range was made.

In this chapter, the theoretical and numerical study of the limits of the accuracy of the Doppler frequency estimation is presented. The theoretical limit of the accuracy of the Doppler frequency estimation is an important problem with many practical implications for analyzing the performance of the frequency estimators. A lower bound on the variance of any unbiased estimator can not only provide a benchmark against which we can compare the performance of any unbiased estimator but also enables us to rule-out impossible estimators.

The new derivation of the Cramér-Rao Bound (CRB), which uses the 2D model of particle motion via the measurement volume, is presented in this chapter. The novelty of the presented approach is in the consideration of the mean flow velocity in conjunction with the cross flow velocity. Rather than assuming that the particle motion is perpendicular to the fringe pattern as in the previously published research in the literature [153]~[160], the effect of the direction of the particle velocity on the accuracy of the Doppler frequency estimation is considered. The obtained analytical expression for the CRB could be very useful in many engineering applications, e.g.

requiring the estimation of a cross flow particle velocity with a known mean flow velocity component such as the one described in [161], [15].

This chapter is organized as follows. Firstly, the LDV principles including the mathematical model of the DBS are briefly introduced. Then, the derivation of the CRB is presented. The respective influences of the size of the measurement volume, the particle velocity and trajectory and the effect of the signal to noise ratio (SNR) are illustrated. The comparison of the derived CRB with the formula from the literature [156], [157], [162]~[170] is given. Finally, the numerical results of the frequency estimation are given using FFT algorithm and Monte Carlo simulations obtained from the synthesized Doppler burst signals.

6.2 Literature Review of Cramér-Rao Bound

LDA is an optical technique ideal for non-intrusive 1D, 2D and 3D point measurement of velocity and turbulence distribution in both free flows and internal flows. The accuracy of the LDA system depends mainly upon the estimation of the frequency of the DBS, which is generated when a particle passes through the region of interference fringes of two coherent laser beams. CRB gives the lowest variance of any unbiased estimator and consequently yields theoretically the minimum uncertainties linked to the velocity estimations. Over the years several derivations have been published aimed at calculating the CRBs for LDA. In 1974, Rife *et al*. studied the CRB of the single-frequency complex signal from a finite number of noisy discrete time observations [154]. The obtained analytical bound for the circle frequency estimation is given by

$$\mathrm{var}\{\hat{\omega}\} \geq \frac{12\sigma^2}{A^2T^2N(N^2-1)} \tag{6.1}$$

where σ^2 is the zero mean variance of the Gaussian noise, T is the data sampling interval, A is the amplitude of the DBS and N the number of the total data points.

Because Rife used the single-frequency, constant amplitude signal model, the bound obtained does not provide accurate frequency estimation of DBS. Besson *et al.* calculated a CRB for the real LDA signal [162], [171]~[175]. Their derivation contained many problematic approximations and did not include the effect of the measurement time on the CRBs. In 2001 Wei-Qun Shu [153] published his calculation based on the discrete noisy complex LDA signal model and derived analytical expression of the CRB. Shu's calculation included the relationship between the number of measurement points and the Gaussian width of the DBS as a measure of the difference between the real DBS and a single frequency signal. However, the time of flight dependence on the Doppler frequency was not included in the model and the particle motion via the measurement volume was assumed perpendicular to the fringe pattern crossing the centre of the measurement volume. Sobolev *et al.* derived CRBs for frequency estimation based on the discrete model of a complex noisy LDA signal [157]. The novelty of Sobolev's calculation was to consider the dependency of the CRBs on the size of the measurement volume, defined in terms of the number of interference fringes. The effect of the measurement time as well as the dependency of the time of flight on the Doppler frequency was also incorporated in the calculation. The signal model used in [157] is given by

$$\begin{aligned} X(t) &= \sum_{-K}^{K} A\exp[-\xi^2\omega_D^2(t_k-t_0)^2]\cos[\omega_D(t_k-t_0)]+w(t_k) \\ Y(t) &= \sum_{-K}^{K} A\exp[-\xi^2\omega_D^2(t_k-t_0)^2]\sin[\omega_D(t_k-t_0)]+\breve{w}(t_k) \end{aligned} \tag{6.2}$$

where $\xi = (\pi M)^{-1}$ is the optical parameter, M denotes the number of interference fringes in the measurement volume at the e^{-1} level, t_0 is the particle arrival time at the centre of the measurement volume, $w(t)$ is the Gaussian noise and its Hilbert transform $\breve{w}(t)$. For the t_0=0 the corresponding CRB was given as

$$\mathrm{var}\{\hat{\omega}_D\} \geq \frac{\alpha\sigma^2}{A^2T^2(N-1)^3} \tag{6.3}$$

where

$$\alpha = \frac{8\eta^3}{\frac{\sqrt{\pi}}{2} erf(\eta)(1+3\xi^2) - \eta \exp(-\eta^2)\left[1+\xi^2(3+2\eta^2)\right]} \tag{6.4}$$

The $\eta = KT/T_w$ is the relative current time, T is the sampling interval, $T_w = (M\pi/\sqrt{2}\omega_D)$ is the particle time of flight and 2K+1 is the number of samples per burst. It can be concluded form (6.3) and (6.4) that both the size of the measurement volume and the measurement time significantly affect the accuracy of the Doppler frequency estimation.

In this chapter, the author presents the CRB derivation, which uses the 2D model of particle motion via the measurement volume. Rather than assuming that the particle motion is perpendicular to the fringe pattern we consider the effect of the direction of particle velocity on the accuracy of the Doppler frequency estimation. The obtained analytical expression for the CRB could be useful in many engineering applications, e.g. requiring the estimation of a cross flow particle velocity with a known mean flow velocity component such as the one described in [161], [176]~[178].

6.3 Problem formulation and CRBs Calculation

Let's consider the ellipsoidal measurement volume of the LDA, as shown in Fig. 6.1, consisting of equidistant dark and bright fringes generated by two crossing coherent laser beams. As the particle traverses the beam intersection region it alternatively encounters bright and dark fringes and the frequency of the scattered signal fluctuation depends on the particle's velocity and the interfringe distance [34]. The Gaussian shape envelope of the time-varying amplitude of the signal results from the intensity distribution of the fringes within the measurement volume. The signal is symmetric with respect to the instant where it attains its maximum value at the centre of the volume. As shown in Fig. 6.1 the duration of the signal is dependent on the size and the shape of the measurement volume as well as the magnitude and the direction

of the particle's velocity.

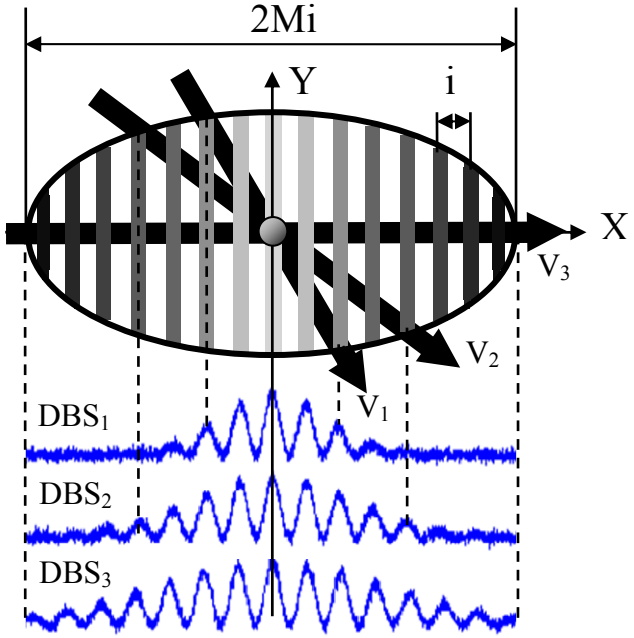

Fig. 6. 1. LDV measurement volume and the resulting DBS for three different scenarios of particle motion via the measurement volume

The mathematical model of noisy DBS employed in this study is given by

$$S(t) = A\exp[-\beta_1^2\mathbf{x}^2(t) - \beta_2^2\mathbf{y}^2(t)]\cos(\omega_D t + \varphi_0) + w(t) \tag{6.5}$$

where A is the amplitude of the DBS dependent on the particle's size, the power emitted and the optical transmission coefficients, φ_0 is the original phase, $\beta_1 = \sqrt{2}\cos(\theta/2)/\mathrm{r}_m = 2/\mathrm{iM}$ and $\beta_2 = 1/\mathrm{r}_m$ are constants determined by the optical settings of the LDA system (focused beam radius r_m and beam intersection angle θ). x(t), y(t) are particle positions projected on the X and Y axis, $w(t)$ is the Gaussian noise and $\omega_D = 2\pi\mathrm{DV_x}$ is the Doppler frequency, where D=1/i and i is the interference fringe spacing.

We now consider the following discrete model of a complex noisy DBS:

$$Z(t) = X(t) + jY(t) \tag{6.6}$$

where:

$$X(t)=\sum_{k=-K}^{K} A\exp[-\beta_1^2\mathbf{x}^2(t_k)-\beta_2^2\mathbf{y}^2(t_k)]\cos(\omega_D t_k+\varphi_0)+w(t_k)$$
$$Y(t)=\sum_{k=-K}^{K} A\exp[-\beta_1^2\mathbf{x}^2(t_k)-\beta_2^2\mathbf{y}^2(t_k)]\sin(\omega_D t_k+\varphi_0)+\check{w}(t_k) \tag{6.7}$$

$\hat{w}(t)$ is the Hilbert transform of Gaussian noise $w(t)$.

Assuming that the original particle position, x_0 and y_0, is at the centre of the measurement volume and t_0=0. The particle motion can be described as

$$\mathbf{x}(t_k)=\mathbf{x}_0+\mathbf{V}_x(t-t_0)=\mathbf{V}_x t=\omega_D(2\pi D)^{-1}t$$
$$\mathbf{y}(t_k)=\mathbf{y}_0+\mathbf{V}_y(t-t_0)=\mathbf{V}_y t \tag{6.8}$$

In (6.7) and (6.8), there are two unknown parameters composing the estimated signal parameter vector, $\theta=[\omega_D,\varphi_0]^T$. Therefore, the joint probability density function is given as

$$f(Z\mid\theta)=(\frac{1}{\sqrt{2\pi}\sigma})^{2K+1}\ \exp\{-\frac{1}{2\sigma^2}\sum_{k=-K}^{K}[(X_k-\mu_k)^2+(Y_k-\nu_k)^2]\} \tag{6.9}$$

where: $2K$+1 is the number of Doppler signal samples, μ_k,ν_k are real and imaginary noise-free Doppler signal parts and can be expressed as

$$\mu_k=A\exp[(C_1\omega_D^2+C_2)t_k^2]\cos(\omega_D t_k+\varphi_0) \tag{6.10}$$

$$\nu_k\ =A\exp[(C_1\omega_D^2+C_2)t_k^2]\sin(\omega_D t_k+\varphi_0) \tag{6.11}$$

where: $C_1=-(\beta_1/(2\pi D))^2, C_2=-\beta_2^2V_y^2$ The CRB of the unknown parameter are the diagonal elements of the inverse of the Fisher information matrix (FIM), whose elements are

$$J_{ij}=E\{H_{\vartheta_i}H_{\vartheta_j}\} \tag{6.12}$$

where E is the expectation symbol, and

$$H_{\vartheta_i}=\frac{\partial}{\partial\vartheta_i}\ln f(Z\mid\vartheta) \tag{6.13}$$

The CRB is given by

$$\mathrm{var}\{\hat{\vartheta}_i\} \geq (J^{-1})_{ii} \tag{6.14}$$

where $\hat{\vartheta}_i$ is the estimator of ϑ_i and $(J^1)_{ii}$ is the ith diagonal element of (J^1). Taking into account (6.9), the elements J_{ij} are

$$J_{ij} = \frac{1}{\sigma^2}\sum_{k=-K}^{K}\left(\frac{\partial \mu_k}{\partial \theta_i}\frac{\partial \mu_k}{\partial \theta_j} + \frac{\partial \nu_k}{\partial \theta_i}\frac{\partial \nu_k}{\partial \theta_j}\right) \tag{6.15}$$

We obtain

$$J_{11} = \frac{1}{\sigma^2}\sum_{k=-K}^{K}\left[\left(\frac{\partial \mu_k}{\partial \omega_D}\right)^2 + \left(\frac{\partial \nu_k}{\partial \omega_D}\right)^2\right] \tag{6.16}$$

From (6.16), we can find

$$J_{11} = \frac{A^2}{\sigma^2}\sum_{k=-K}^{K}\exp[2(C_1\omega_D^2 + C_2)t_k^2][(2C_1t_k^2\omega_D)^2 + t_k^2] \tag{6.17}$$

Since the sampling rate 1/T is much faster than the Doppler frequency, the summation in above equation can be substituted by the integral

$$J_{11} \approx \frac{A^2}{\sigma^2 T}\int_{-KT}^{KT}\exp(C_3t^2)(C_4t^4 + t^2)dt = \frac{A^2}{\sigma^2 T}(C_4I_4 + I_2) \tag{6.18}$$

where

$$I_n = \int_{-KT}^{KT} t^n \exp(C_3t^2)dt,\ C_3 = 2(C_1\omega_D^2 + C_2),\ C_4 = (2C_1\omega_D)^2 \tag{6.19}$$

The procedure for obtaining the integrals I_2 and I_4 is presented in the Appendix A. Finally substituting (A9) into (6.18), the CRB for the frequency estimation can be expressed as follows

$$\mathrm{var}\{\hat{\omega}_D\} \geq J_{11}^{-1} = \frac{\sigma^2 T}{A^2(C_4I_4 + I_2)} = \frac{\sigma^2\alpha_m}{A^2T^2(N-1)^3} \tag{6.20}$$

$$\alpha_m = \frac{8\eta^3}{\frac{\sqrt{\pi}}{2}[3\xi_m^2 + 1]erf(\eta) - \eta\exp(-\eta^2)[1 + \xi_m^2(2\eta^2 + 3)]} \tag{6.21}$$

where η is the relative current measurement time defined as

$$\eta = KT / T_w \tag{6.22}$$

T_w is the tracer particle time of flight. The $1/e^2$ full DBS duration equals to $\Delta t = 2\sqrt{2}T_w$. The T_w is given by

$$T_w = \sqrt{2}\pi / \left(i\beta_1 \omega_D \sqrt{1 + \left(\beta_1 / \beta_2\right)^2 \gamma^2} \right) \tag{6.23}$$

where $\gamma = V_y / V_x$ is the particle relative velocity coefficient The ξ_m parameter in (6.21) is dependent on the size of the measurement volume as well as the particle trajectory and is derived from (A8) and given by

$$\xi_m = i\beta_1 / \left(2\pi \sqrt{1 + \left(\beta_1 / \beta_2\right)^2 \gamma^2} \right) \tag{6.24}$$

Assuming that the ratio $\beta_1 / \beta_2 \simeq 1$, which is reasonable for most LDA system optical configurations because of the small beam intersection angle, and substituting for β_1, the expressions (6.23) and (6.24) can be simplified as follows

$$T_w \simeq M\pi / \left(\sqrt{2}\omega_D \sqrt{1 + \gamma^2} \right) \tag{6.25}$$

$$\xi_m \simeq \left(M\pi \sqrt{1 + \gamma^2} \right)^{-1} \tag{6.26}$$

Figs. 6.2 ~ 6.4 show the relative mean square CRB as a function of relative current measurement time η, particle relative velocity, the number of fringes and SNR. It can be concluded from Fig. 6.1 that the longer the measurement time, the more accurate the measurement becomes. It is due to the fact that more measurement samples of the DBS are acquired.

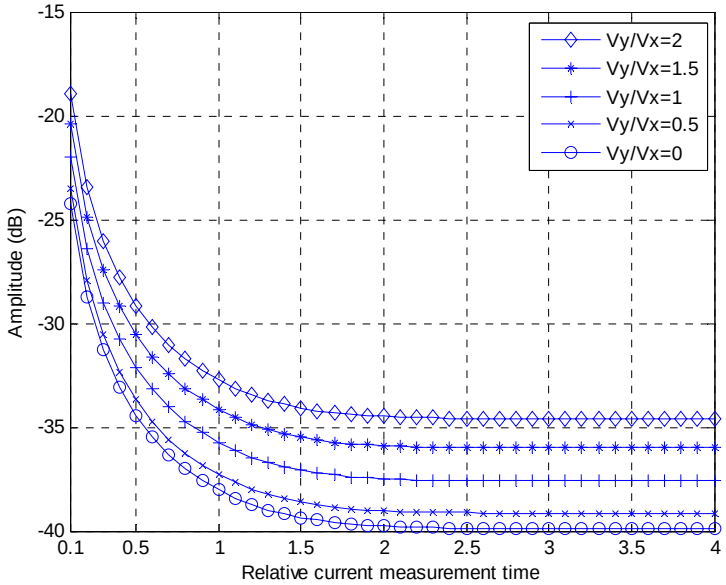

Fig. 6.2. Relative mean square CRB as a function of measurement time η and particle relative velocity γ=Vy/Vx (Vx =0.5m/s, M=100, SNR=3dB, T=0.3μs, θ=12deg, i = 2.29μm, ω_D = 1.3Mrad/s)

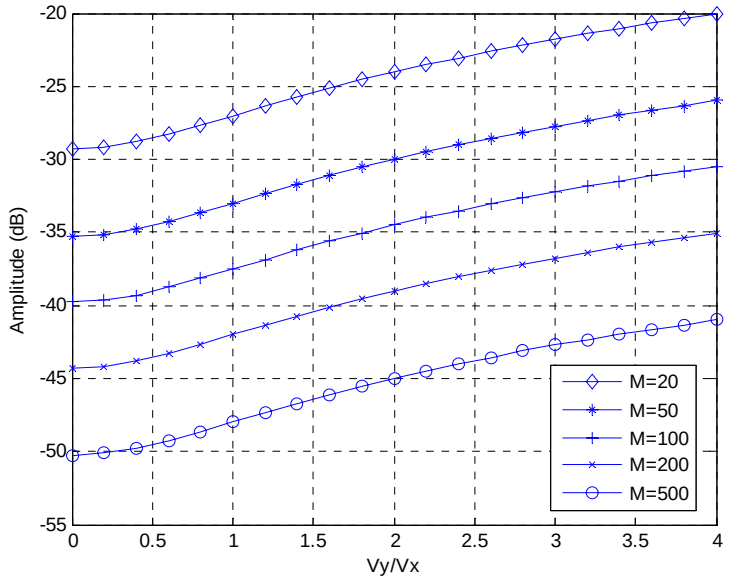

Fig. 6.3 Relative mean square CRB as a function of the number of interference fringes M and particle relative velocity γ=Vy/Vx (Vx =0.5m/s, η=2, SNR=3dB, T=0.3μs, θ=12deg, i = 2.29μm, ω_D = 1.3Mrad/s)

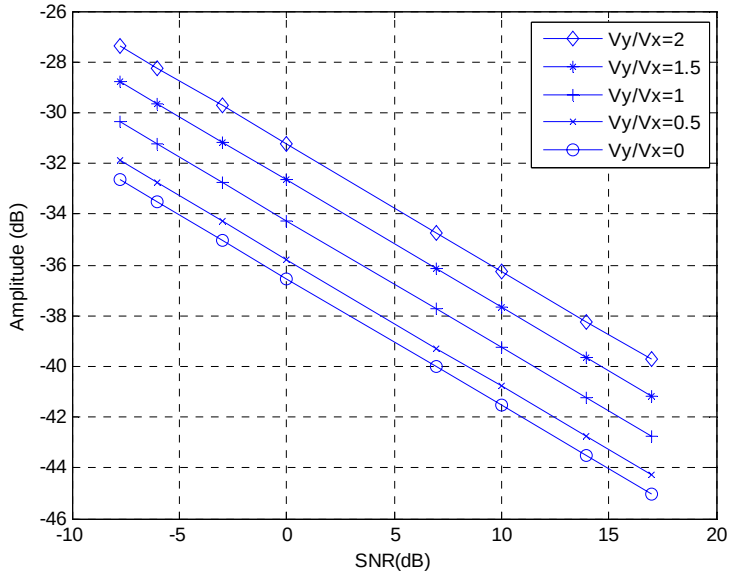

Fig. 6.4 Relative mean square CRB as a function of SNR and particle relative velocity γ=Vy/Vx (Vx =0.5m/s, η=2, M=100, T=0.3μs, θ=12deg, i = 2.29μm, ω_D = 1.3Mrad/s)

It is also evident that the accuracy of the estimation depends on both the magnitude of the particle velocity and the particle trajectory via the measurement

volume. As the particle velocity in the direction parallel to the interference fringes increases, the particle time of flight decreases, which leads to the decrease of the number of collected samples for a given burst signal. This subsequently leads to an increase in the relative variance of the frequency estimation. It is also interesting to examine the combined effect of the size of the measurement volume and the particle relative velocity as shown in Fig. 6.3. It can be noted that the increase of the size of the measurement volume increases the accuracy of the measurement.

6.4 Comparison with the CRB from Rife and Sobolev

It is important to compare the derived bound with the analytical bounds presented in the literature. The most commonly used formula for CRB_R is the one obtained by Rife *et al*. and given by (6.1). However, it is important to emphasize that this analytical bound was calculated for the single tone frequency signal instead of Gaussian weighted Doppler burst signals. The ratio of the new bound CRB_m to the one obtained by Rife is given by

$$\frac{CRB_m(\hat{\omega}_{Dm})}{CRB_R(\hat{\omega}_D)} = \frac{\alpha_m N(N^2-1)}{12(N-1)^3} \tag{6.27}$$

The expression $N(N^2-1)/(N-1)^3$ converges to 1 with an increasing N. Assuming that the number of measurement points, N is greater than 50, the (6.27) can be approximated, with an error percentage less than 5%, as

$$\frac{CRB_m(\hat{\omega}_{Dm})}{CRB_R(\hat{\omega}_D)} = \frac{\alpha_m}{12} \tag{6.28}$$

Table 6.1 shows the calculated values of α_m parameter as a function of the number of interference fringes M, relative measurement time η and particle relative velocity γ. It can be seen that when the measurement time is small in relation to the duration of the burst, i.e. $(\eta \to 0)$, α_m converges to 12.

η	M \ γ	0	0.5	1	1.5	2
0.2	1	12.2316	12.2435	12.2613	12.2727	12.279
0.2	2	12.276	12.279	12.2834	12.2863	12.2879
0.2	5	12.2884	12.2889	12.2896	12.2901	12.2903
0.2	10	12.2902	12.2903	12.2905	12.2906	12.2907
0.2	20	12.2907	12.2907	12.2907	12.2908	12.2908
0.2	50	12.2908	12.2908	12.2908	12.2908	12.2908
0.2	100	12.2908	12.2908	12.2908	12.2908	12.2908
1	1	19.0666	19.4471	20.0434	20.4426	20.6724
1	2	20.5601	20.6691	20.8338	20.94	20.9998
1	5	21.0211	21.0392	21.0664	21.0837	21.0933
1	10	21.0886	21.0932	21.1	21.1044	21.1068
1	20	21.1056	21.1067	21.1084	21.1095	21.1101
1	50	21.1104	21.1105	21.1108	21.111	21.1111
1	100	21.111	21.1111	21.1111	21.1112	21.1112
2	1	59.6601	62.3282	66.7797	69.9627	71.8739
2	2	70.9319	71.8461	73.2532	74.1787	74.7053
2	5	74.8939	75.0553	75.297	75.4519	75.5385
2	10	75.4964	75.5373	75.5983	75.6373	75.6591
2	20	75.6485	75.6587	75.6741	75.6838	75.6893
2	50	75.6912	75.6928	75.6953	75.6968	75.6977
2	100	75.6973	75.6977	75.6983	75.6987	75.6989

Table. 6.1 α_m as a function of the number of interference fringes M, relative measurement time η and particle relative velocity $\gamma = Vy/Vx$

It is to be expected, since the shorter the measurement time the closer DBS resembles a single tone waveform. On the other hand the longer η the more significant becomes the effect of the changing envelope of DBS. The measurement time has also the greatest influence on the value of α_m with the effect of the number of fringes and particle relative velocity less pronounced. It is important to bear in mind, however, that as far as CRB is concerned, the measurement time is not an independent parameter and is related to both the sampling period T, number of measurement samples N and the particle trajectory via the measurement volume (6.22)(6.23). The ratio of the new bound to CRB obtained by Sobolev *et al.* is given as

$$\frac{CRB_m(\hat{\omega}_{Dm})}{CRB_S(\hat{\omega}_D)} = \frac{\alpha_m}{\alpha} \tag{6.29}$$

Assuming a long measurement time $(\eta \to \infty)$ the (6.29) could be expressed as

$$\frac{CRB(\hat{\omega}_{Dm})}{CRB(\hat{\omega}_D)} = \frac{\alpha_m}{\alpha} = \frac{1+3\xi^2}{1+3\xi_m^2} \simeq \frac{1+3\left(M\pi\right)^{-2}}{1+3\left(M\pi\sqrt{1+\gamma^2}\right)^{-2}} \tag{6.30}$$

When the particle travels through the centre of the measurement volume in the direction perpendicular to the fringe pattern, i.e. $V_y = 0$ and $\gamma = 0$, the $\xi_m = \xi$. It this case the ratio (6.30) of the CRBs becomes unity.

6.5 Numerical Results and Discussion

Following on from the theoretical analysis presented in the previous sections and reported in [179]~[182] this section presents the numerical results of computer simulations which were performed in order to study the effect of particle trajectory via the measurement volume on the accuracy of the Doppler frequency estimation. In particular, the relative effect of the direction of the particle velocity, measurement time, the size of the measurement volume and SNR is investigated. For the estimation of the Doppler frequency the FFT algorithm has been used since it is the most

commonly applied signal processing scheme in laser Doppler measurement systems achieving good performance even for low SNRs [34], [183]~[185]. The FFT is combined with the parabolic interpolation scheme and Blackman windowing. The interpolation is necessary because the frequency resolution of the FFT is limited by the short duration of the bursts and the number of sampling points per burst [186], [187], [188]. In the process of interpolation the abscissa of the spectral peak maximum is found based on the three peak samples in the form of three bins of the magnitude spectrum nearest to the maximum [189], [190], [191]. Comparison is made between the derived CRB and the FFT estimation performance. The simulation parameters are as follows: wavelength of the laser beam, λ= 514.5nm, the intersection angle of two beams, θ =12deg, fringe spacing, i=2.99μm, Gaussian beam radius r_m=160μm, frequency shift, F_B =0Hz, original phase of the DBS, φ_0=0 and the DBS amplitude A = 1. The Doppler frequency of the simulated burst corresponding to the cross flow particle velocity V_x of 0.5m/s is 218.23 kHz. For each parameter combination, the 500 Monte Carlo simulations were run in order to estimate the relative standard deviation (RSD) and the mean relative error (MRE) of the frequency estimation. The bursts are sampled with the sampling interval T of 0.3μs. Gaussian white noise was generated and added to the simulated burst data assuming a specific SNR value defined as

$$SNR = 10\log\left(\frac{A^2}{2\sigma^2}\right) \tag{6.30}$$

where A is the DBS amplitude and the σ^2 is the zero mean variance of the Gaussian noise.

In Fig. 6.5 three of the synthesized burst signals with added noise component are plotted. Each signal represents particle passing through the measurement volume with a different velocity parallel to the fringe pattern, a) Vy=0m/s, b) Vy=0.5m/s and c) Vy=1m/s. It can be seen that although the frequency of the burst signal remains the same the characteristics of the signal both in terms of its envelope and duration becomes affected.

Figs. 6.6 ~ 6.7 show the RSD and the MRE of the frequency estimation as a

function of the measurement time and the particle relative velocity. The relatively low value of SNR of 3dB was maintained constant throughout the whole range of η. The value of η was varied from 0.1 to 4 with a stepsize of 0.1. CRB corresponding to exactly the same simulation conditions has been shown in Fig. 6.5.

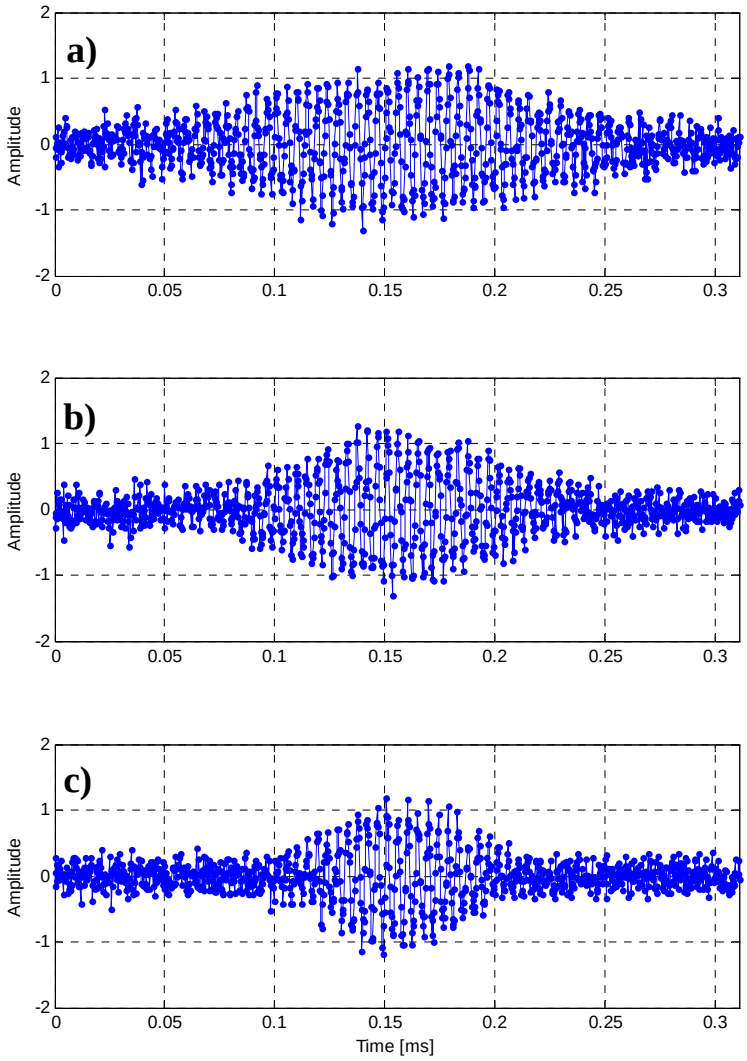

Fig. 6.5 Simulated Doppler Burst Signal for different values of particle relative velocity γ, SNR=13dB, Vx =0.5m/s, M=40, T=0.3μs, θ=12deg, i = 2.29μm, ω_D = 1.3Mrad/s a) Vy=0m/s, γ = 0, η = 3, b) Vy=0.5m/s, γ = 1, η = 4.3, c) Vy=1m/s, γ = 2, η = 6.7

From these figures, it can be seen that the absolute differences between the RSD, which have been obtained by FFT and the corresponding bounds are about 10dB.

Similar trend in terms of the mean square error difference between the FFT estimation and the CRB was reported by Besson [155], [192], [193]. Further improvement to the efficiency of the estimator could be made by using different interpolation schemes e.g., least mean squares [194], [195], [196] or interpolation using all spectral components [197]~[202]. It can also be noted that FFT performance shown in Fig. 6.6 and the CRB plotted in Fig. 6.2 exhibit similar characteristics in terms of the effect of the relative velocity on the RSD. For a given measurement time the bigger the particle relative velocity the higher the variance of the estimation and the less accurate the measurement. Fig. 6.7 shows that down to a η of 0.3 the frequency estimate is correct to 0.5 percent of the true value. In Fig. 6.8 ~ 6.9 the RSD and MRE of the frequency estimation are plotted as a function of the number of the interference fringes and the particle relative velocity. As can easily be seen, the RSD of the estimated frequency compare quite well with the CRB plotted in Fig. 6.3 in terms of the relative difference of estimates corresponding to the number of fringes in the measurement volume. As theoretically predicted, the lower the total number of fringes results in the decrease of the accuracy of the estimation. Also, the smaller the relative particle velocity coefficient the more perpendicular the motion of the particle becomes to the fringe pattern and the more accurate the estimates of the velocity. In addition, it is interesting to note that the effect of the particle trajectory via the measurement volume becomes more pronounced as the total number of fringes in the measurement volume decreases which have practical implications for the design of the optical configuration in real LDA measurements.

Finally, Figs. 6.10 and 6.11 show the RSD and MRE of the frequency estimation obtained from analyzing 500 burst signals for a given value of the noise power. The investigated SNR range was from -7dB to 18dB. The simulation results demonstrate that that the FFT method with the interpolation scheme indeed works well for laser-Doppler signals which have a very low SNR. As theoretically predicted in Section 6.4, the increasing SNR results in the improvement of the accuracy of the estimation both in terms of the RSD and MRE. In a similar fashion to the results shown in Fig. 6.4 the particle motion via the volume affects the RSD of the frequency

estimation. The greater Vy/Vx, for a given measurement time, the greater RSD becomes regardless of the value of SNR.

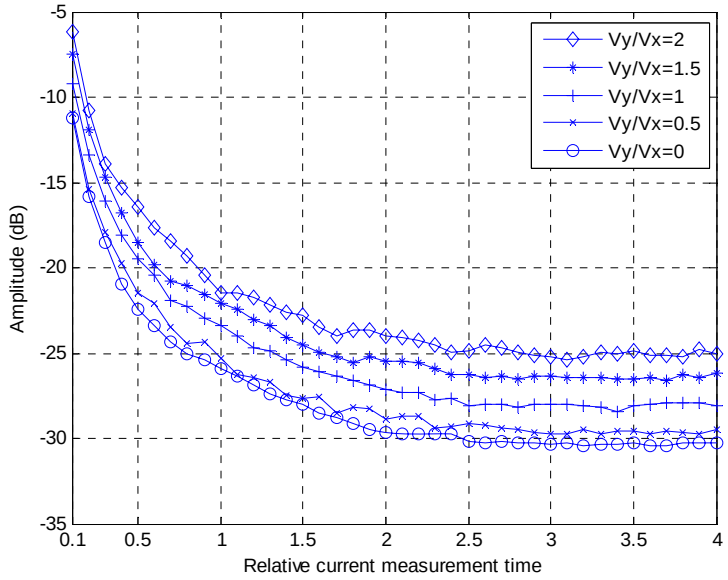

Fig. 6.6 Relative standard deviation of frequency estimation as a function of measurement time η and particle relative velocity γ=Vy/Vx (Vx =0.5m/s, M=100, SNR=3dB, T=0.3μs, θ=12deg, i = 2.29μm, ω_D = 1.3Mrad/s)

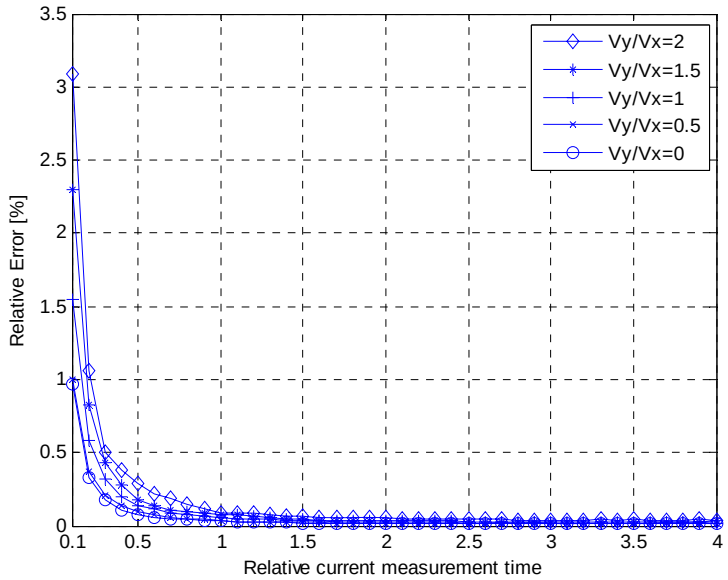

Fig. 6.7 Relative frequency estimation error as a function of the measurement time η and particle relative velocity γ=Vy/Vx (Vx =0.5m/s, M=100, SNR=3dB, T=0.3μs, θ=12deg, i = 2.29μm, ω_D = 1.3Mrad/s)

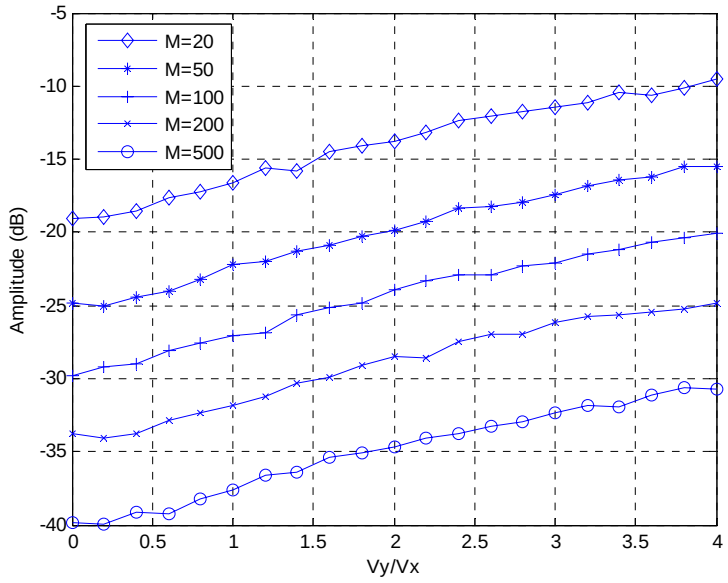

Fig. 6.8 Relative standard deviation of frequency estimation as a function of the number of interference fringes M and particle relative velocity γ=Vy/Vx (Vx =0.5m/s, η=2, SNR=3dB, T=0.3μs, θ=12deg, i = 2.29μm, ω_D = 1.3Mrad/s)

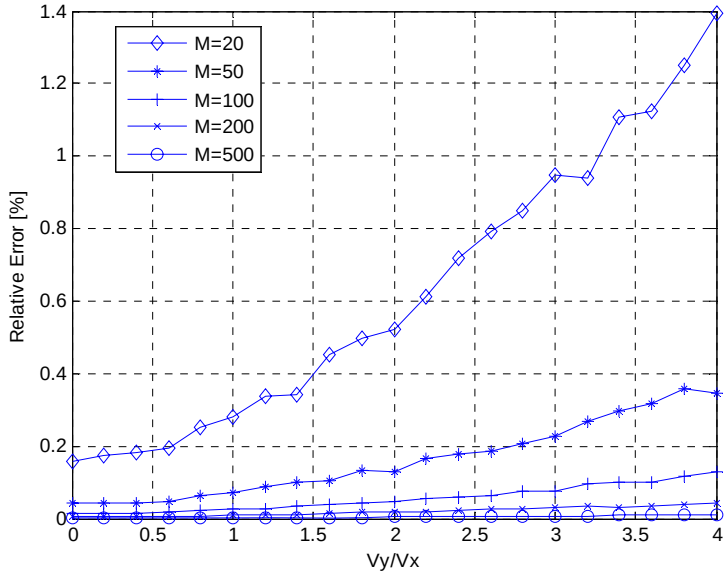

Fig. 6.9 Relative frequency estimation error as a function of the number of interference fringes M and particle relative velocity γ=Vy/Vx (Vx =0.5m/s, η=2, SNR=3dB, T=0.3μs, θ=12deg, i = 2.29μm, ω_D = 1.3Mrad/s)

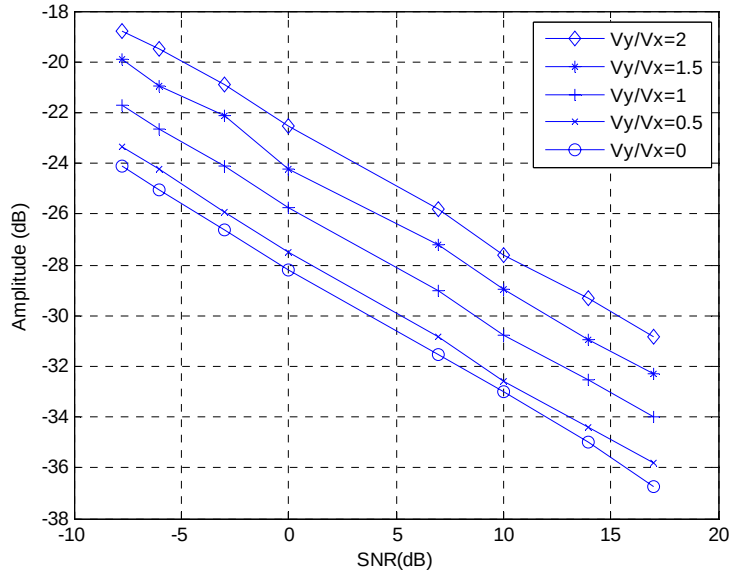

Fig. 6.10 Relative standard deviation of frequency estimation as a function of SNR and particle relative velocity γ=Vy/Vx (Vx =0.5m/s, η=2, M=100, T=0.3μs, θ=12deg, i = 2.29μm, ω_D = 1.3Mrad/s)

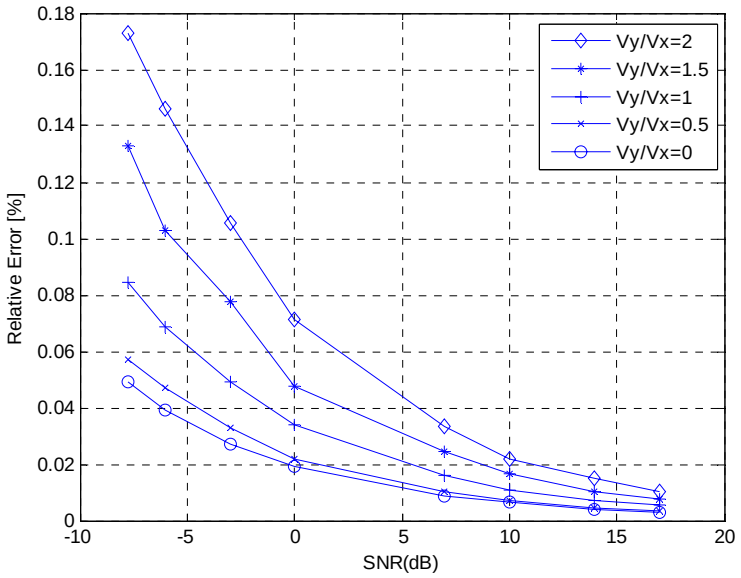

Fig. 6.11 Relative frequency estimation error as a function of SNR and particle relative velocity γ=Vy/Vx (Vx =0.5m/s, η=2, M=100, T=0.3μs, θ=12deg, i = 2.29μm, ω_D = 1.3Mrad/s)

6.6 Summary and Conclusions

This chapter derived the CRB for a model of the DBS taking into the account the 2D motion of particle tracer via the measurement volume. It was shown that as the particle velocity starts to deviate from the cross flow direction the variance of the Doppler frequency estimation increases. This can be explained in terms of the changed DBS characteristics caused by the reduced number of fringes crossed by the particle in the measurement volume. The new CRB expression was compared with the CRB obtained by Rife and Sobolev. With the increase of the particle cross-flow velocity component the new CRB asymptotically converges to the Sobolev's formula. In addition, the numerical simulations of the frequency estimation were performed using Monte Carlo simulations obtained from the synthesized Doppler burst signals. For the estimation of the Doppler frequency, the FFT algorithm has been used combined with an interpolation technique. It was shown that the numerical results confirmed the theoretical predictions in terms of the relative effect of the particle trajectory, the measurement time, the size of the volume and SNR on the accuracy of the Doppler frequency estimation. The presented analyses have practical implications for the selection of the optical configuration in real LDA/PDA measurement systems.

With the analysis of the theoretical limit of the accuracy of the estimation systems accomplished, the next chapter will discuss the measurement system parameter selection and optimization with a goal to obtain the most representative picture of the aerosol charge distribution. The optimal range of the system parameters will be determined by considering the effects of drive frequency, magnitude of the excitation field and the mean flow velocity.

Chapter 7

Measurement System Parameter Selection and Optimization

7.1 Introduction

In addition to the design and simulation of the signal processing systems presented in chapters 4 and 5 a numerical model of the measurement system has also been developed to estimate the percentage of aerosol particles arriving at the measurement volume at any given time and generating a valid DBS. The purpose of the numerical modeling was to examine various measurement system configurations and to establish the optimal range of the system parameters for both excitation methods. It is a very important problem since one can easily imagine a scenario where the measurement sample is not representative at all of the overall charge and size distribution of the measured aerosol (e.g. is significantly biased towards lowly or highly charged particles) [203].

In this chapter, a numerical model of the measurement system is discussed together with the simulation results. In order to determine the optimal range of system parameters, the effect of drive frequency, strength of field, mean flow velocity, the size of the inlet and the size of measurement volume on the particle capture percentage have been investigated based on the specific criteria in both excitation fields. The optimal range of system parameters for both excitation methods has been determined with the recommended values proposed for sine and square wave excitation systems.

7.2 Numerical Simulation of the Particle Capture Efficiency

The simulation of particle capture inside the measurement volume of the PCSA from a laminar flow field with known statistical properties of the particles was performed in a number of independent steps as represented diagrammatically in Fig. 7.1.

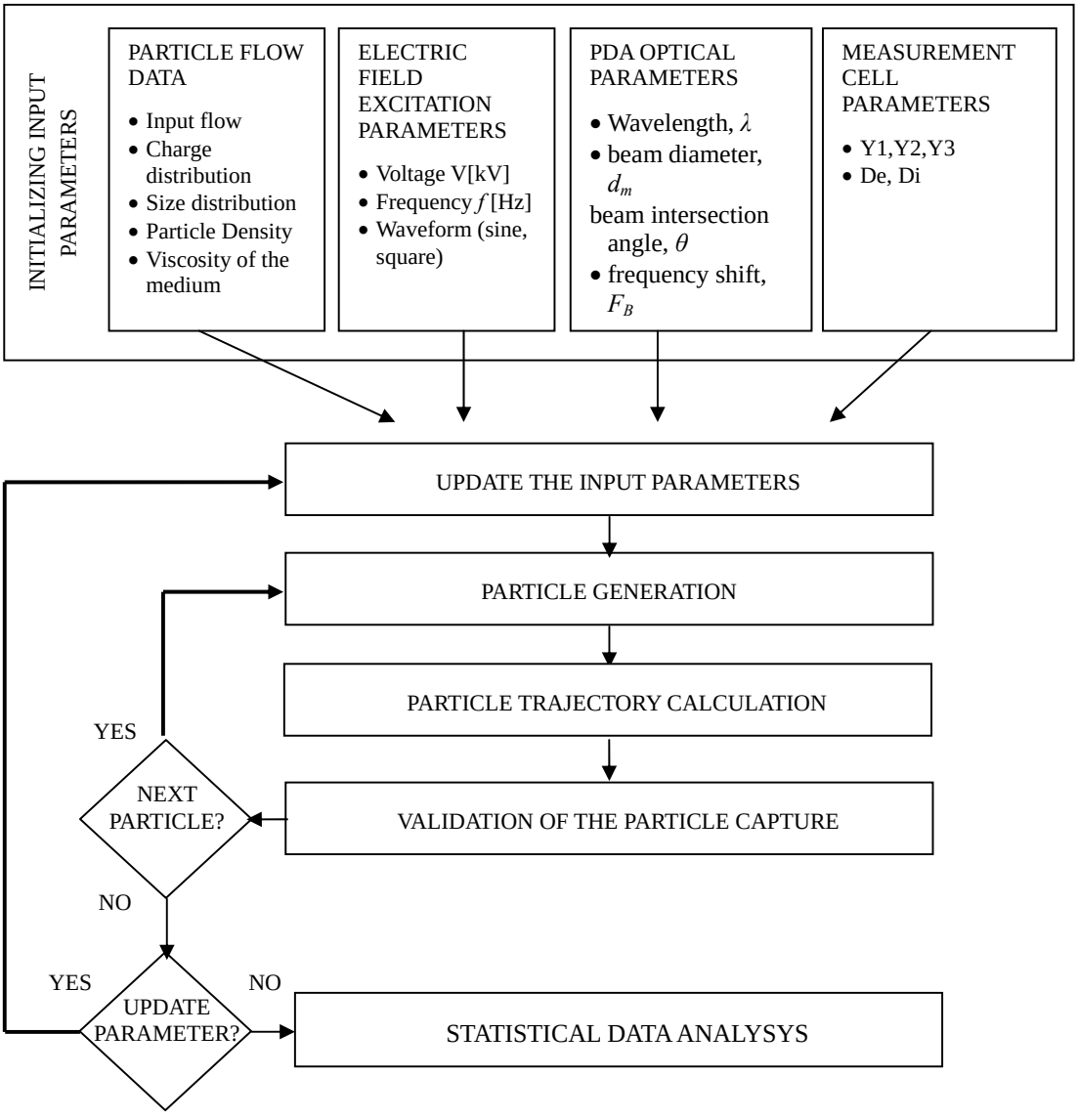

Fig. 7.1 Schematic Representation of Simulation Program

The numerical model takes into account the optical parameters of the PDA (fringe spacing, focal length of the transmitter and receiver, measurement volume

diameter, beam properties); parameters of the excitation waveform (frequency, phase, amplitude); the properties of the particle flow (particle size, charge distribution, flow rate) as well as the geometry of the inlet and measurement cell. For a given particle size, charge distribution profiles, various air flow conditions and optical configurations a number of trials were run in both sine-wave and square-wave excitation fields. For each run, trajectories of 4000 particles were computed throughout the measurement cell. It was assumed that the aerosol flow was laminar with a uniform distribution of randomly generated particles across the inlet. The simulated particle's size was from 0.5 to 10μm and charge from 0e to Gaussian limit.

As shown in Fig. 7.1, first, the input parameters of the simulation are initialized based on the predetermined configuration of the measurement cell and the excitation field. Second, the particles are randomly generated across the inlet and with a given initial velocity, charge and size distribution at regular and closely spaced points in time. Based on the distance between the inlet and the measurement volume, particle trajectory inside the volume, the arrival time and residence time are calculated. Validation of the signals generated by the individual particles consist of prescribing a particle sample scheme, including minimum number of periods of particle oscillatory motion inside the volume, the minimum number of fringes crossed by the particle, the amplitude of the particle motion in relation to the volume diameter. Finally, the statistical data analyses according to the chosen validation scheme and particle properties as well as the characteristics of the excitation field are computed and compared with the known properties of the flow. The data generated at each step can also be stored in files. Thus systematic parameter variations and their effect on particle capture can easily be investigated.

The air flow across the inlet is modeled as a uniform flow with a mean flow velocity in the vertical direction. The initial size of the detection volume is chosen as a trade off between the probability of having more than one particle occurrence at a time and getting a high particle sampling rate to enhance statistical estimates. The probability for the occurrence of coincidences reduces with decreasing measuring volume.

The particle trajectory in the measurement cell is determined by particle charge, particle diameter, drive frequency, magnitude of the excitation field and the mean flow

velocity. The effects of these parameters on the particle trajectories inside the measurement cell are illustrated in Fig. 7.2~7.5 in case of square-wave excitation field.

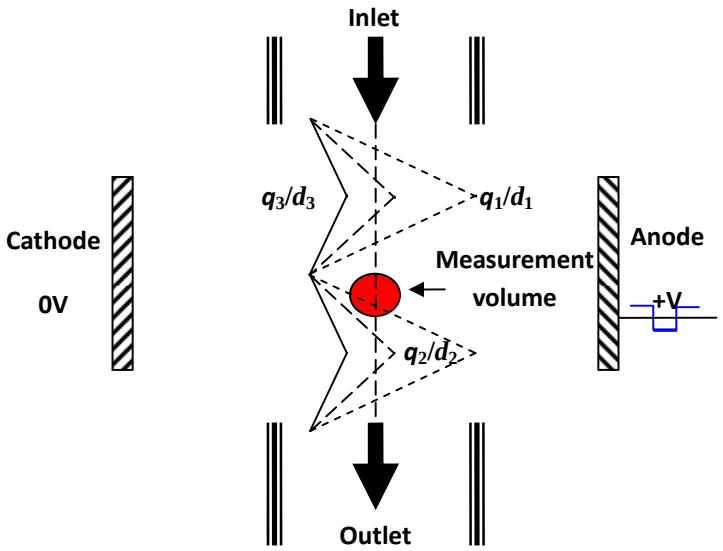

Fig. 7.2 Particle trajectories with different particle sizes and charge levels ($q_1/d_1 < q_2/d_2 < q_3/d_3$) in the measurement cell (the other system parameters are kept as constant)

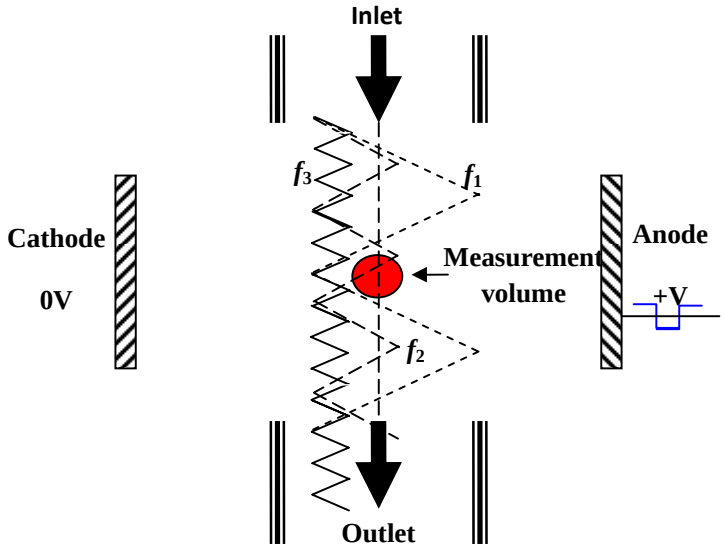

Fig. 7.3 Particle trajectories with different drive frequencies ($f_1 < f_2 < f_3$) in the measurement cell (the other system parameters are kept as constant)

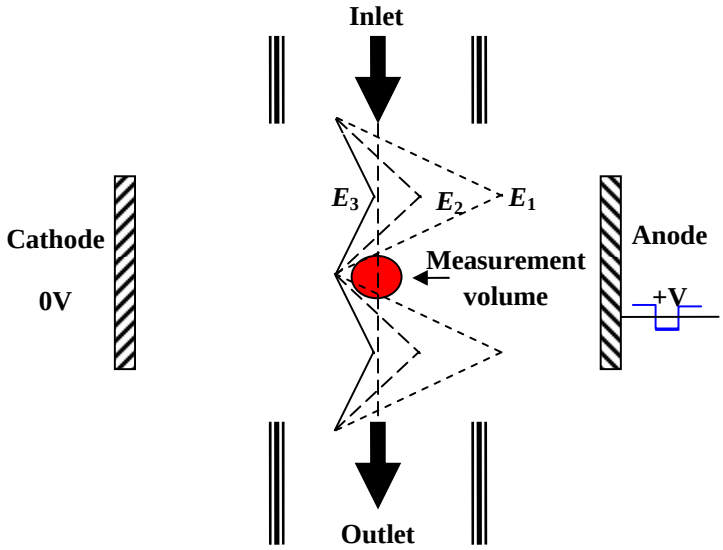

Fig. 7.4 Particle trajectories with different magnitudes of excitation field (E_1>E_2>E_3) in the measurement cell (the other system parameters are kept as constant)

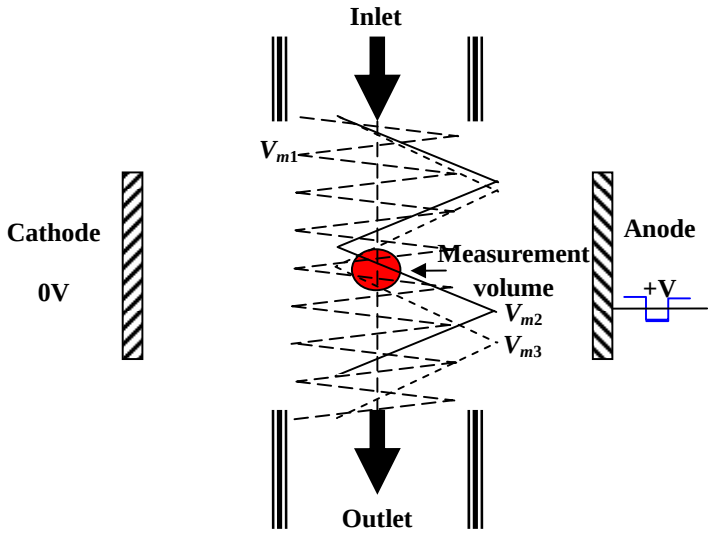

Fig. 7.5 Particle trajectories with different mean flow velocities (V_{m1}< V_{m2}< V_{m3}) in the measurement cell (the other system parameters are kept as constant)

7.2.1 Validation Criteria Applied to Detected Particles

The aim of the numerical modeling is not only to establish how many particles are captured inside the measurement volume but also to ensure that the accurate estimation results could be obtained from the generated DBSs. It means that the burst length of DBS should be large enough to ensure that a valid estimation result can be successfully obtained by the signal processing system. Additionally, the 'valid' capture percentage is also affected by the particle residence time inside the measurement volume and the number of fringes crossed by the particle motion via the measurement volume. Moreover the geometrical parameters of the cell have to be considered: such as the distance between the two electrodes, e.g it is impossible for the particle to move out of the area between the two electrodes, the distance between the inlet and the measurement cell, the length of the electrodes etc. The diagram of the measurement cell defining the geometrical parameters is shown in Fig. 7.6.

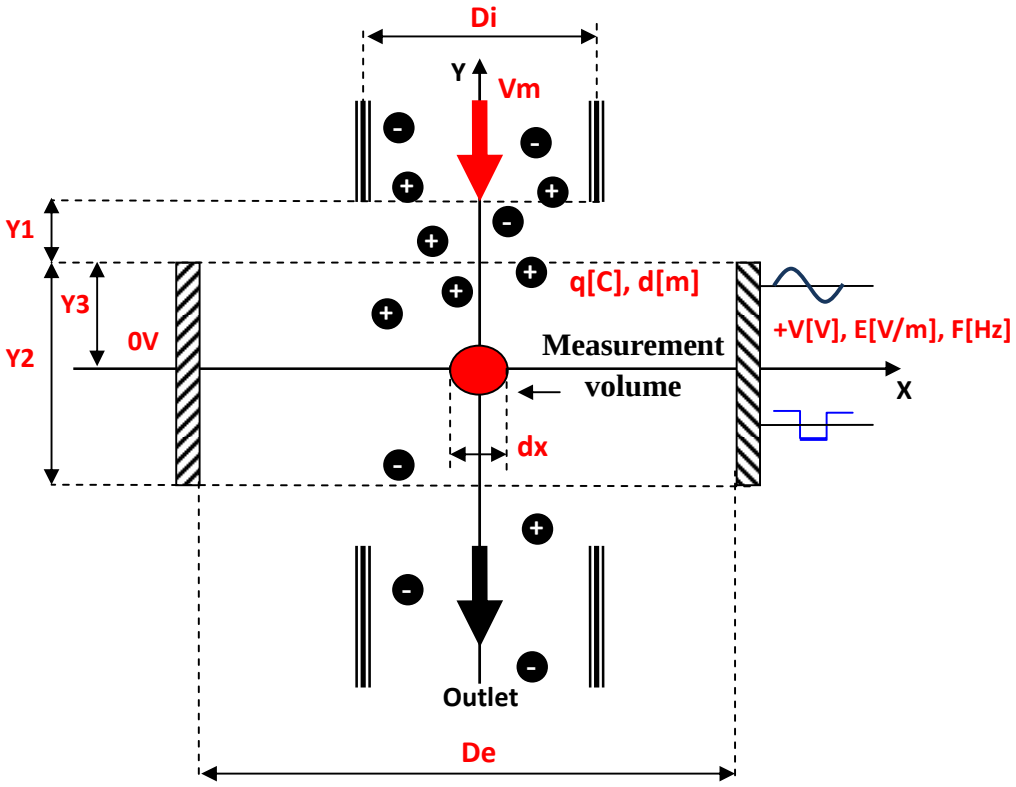

Fig. 7.6 Illustration of particle detection in the measurement cell

Different criteria are used to simulate fundamental validation requirements applied on a particle detected by the PCSA in square-wave and sine wave excitation fields. This is due to the fact that the signal processing of the DBS generated in square-wave based on FFT is less demanding in terms of the quality of the DBS, SNR and particle residence time, which increases the likelihood of the detected particles to be successfully processed. On the other hand the DBS processing in sine wave excitation is not only more sensitive to noise and the effect of the particle trajectory but also requires that the particle residence time in the measurement volume is at least equal to one period of the excitation, which effectively eliminates shorter and discontinuous burst. The specific criteria for both excitation fields are discussed below.

7.2.1.1 Square-wave Excitation Field

In the square-wave excitation system the specific validation criteria applied to the particle motion inside the measurement volume can be expressed as follows:

$$\begin{cases} 1) \quad x_{\max} > -M_x + M_{\min} i \\ 2) \quad x_{\min} < M_x - M_{\min} i \\ 3) \quad A_{pp} > M_{\min} i \\ 4) \quad |\, y(t)| < M_y \end{cases} \tag{7.1}$$

where M_x, M_y are the radius of the measurement volume in X and Y direction respectively, x_{max} and x_{min} are the maximum and minimum values of $x(t)$, $A_{pp}= x_{max}- x_{min}$, M_{min} is the minimum number of fringes crossed by the particle inside the measurement volume, $x(t)$ and $y(t)$ are the instantaneous particle positions in X and Y direction and have been defined in (3.35).

The first two requirements state that the particle's centre has to cross a certain minimum number of fringes inside the measurement volume, which is necessary to produce sufficient light scattering in a real PDA systems. In the numerical simulation M_{min} has been set equal to four, based on the recommendations from the Dantec PDA manual [204]). The third requirement states that the amplitude of the particle motion has

to be larger than $M_{min}i$, Fourth condition combined with the first two requirement ensures that the particle enters the measurement volume.

7.2.1.2 Sine-wave Excitation Field

The mathematical expression of the criterion of particle detection and validation in sine-wave excitation field can be given as:

$$\begin{cases} 1)\ x_{\max} < M_x \\ 2)\ x_{\min} > -M_x \\ 3)\ A_{pp} > M_{\min} i \\ 4)\ T_{drive} < T_{\mathrm{Re}sidence} \end{cases} \tag{7.2}$$

where T_{drive} is the period of the drive frequency, $T_{Residence}$ is time for particle staying within the measurement vloume, so called the particle residence time. x_{max} and x_{min} are the maximum and minimum values of $x(t)$, M_{min} is the minimum number of fringes crossed by the particle inside the measurement volume, $A_{pp}= x_{max}- x_{min}$, $x(t)$ and $y(t)$ are instantaneous particle positions in X and Y direction and have been defined in (3.25). In addition to the requirements already discussed for the square-wave excitation the criterion defined in (7.2) ensures that the number of fringes in the measurement volume crossed by the particle is at least M_{min} (equal to eight) and the time for particle remaining in the measurement volume should be no less than one period of drive frequency.

The simulation results showing the percentage of the total number of particles 'captured' for different system parameters and levels of charge are discussed in the following sections.

7.3 The Effect of the Drive Excitation Frequency

The simulation results showing the percentage of the total number of particles 'captured' for different excitation frequencies and levels of charge as a percentage of Gaussian limit in the square-wave excitation field are shown in Figure 7.7. It can be seen

that with the increasing drive frequency the number of particles detected inside the measurement volume initially rapidly increases reaching its peak value around 50Hz and then gradually decreases. This is mainly due to the fact that for the lower frequencies the amplitude of the particle motion is greater which increases the likelihood of the particle crossing the measurement volume.

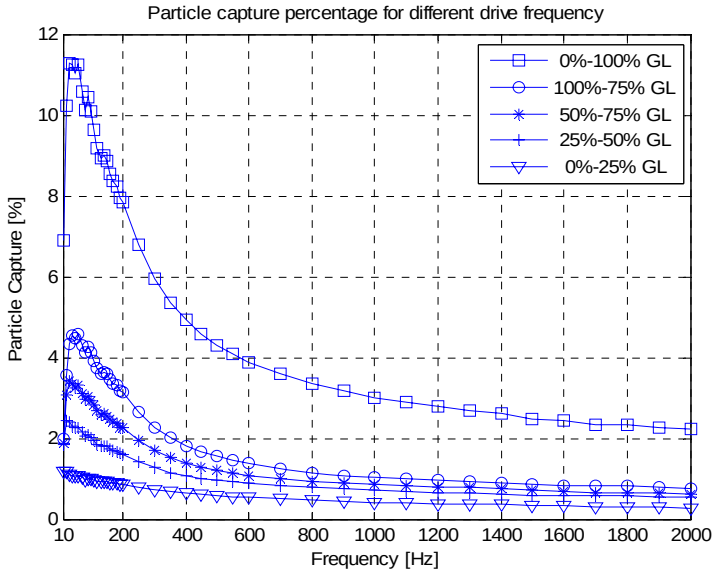

Fig. 7.7 The number of particle captured inside the measurement volume for different drive frequency and different levels of charge as a percentage of Gaussian limit in square-wave excitation field. Laser wavelength λ=514.5nm, intersection angle θ =12^0, beam waist d_w=194μm, magnitude of excitation field E=0.15MV/m, mean flow velocity V_m=0.05m/s, fringe spacing i=2.29μm, diameter of inlet L_{inlet}=7mm, size of measurement volume, M_x=97.6μm, M_y=97μm.

The amplitude of the velocity and displacement achieved in the square-wave excitation field is given by (7.3) and (7.4) respectively.

$$A_{v\_SQ} = \frac{EqC_c}{3\pi\eta d} \tag{7.3}$$

$$x_{\max\_SQ} \approx A_{v\_SQ}\frac{T_{drive}}{4} = \frac{EqC_c}{3\pi\eta d}\frac{\pi}{2\omega} \tag{7.4}$$

where the particle acceleration period is assumed to be $T_{drive}/4=\pi/2\omega$. From (7.4), it can be seen that the amplitude of particle motion in the square-wave excitation field is directly proportional to the particle charge-and-diameter ratio. Therefore, for lowly charged

particles, the amplitude of velocity is smaller and thus the capture percentage is smaller, as shown in Fig. 7.7. The number of captured particles remains almost constant at higher drive frequencies (higher than 1kHz) due to the minute amplitude of motion. In this case, the particle capture percentage is mainly determined by the size of the inlet and the measurement volume.

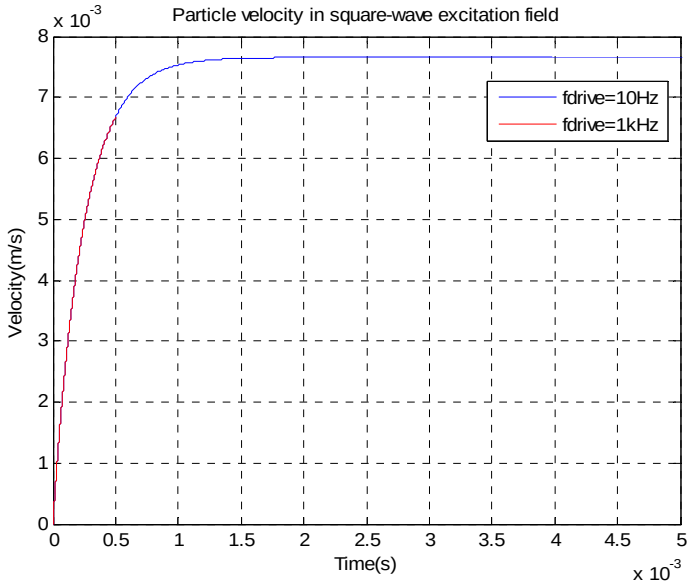

Fig. 7.8 Real-time particle velocity in the sqaure-wave excitation field, Laser wavelength λ=514.5nm, intersection angle θ =12^0, beam waist d_w=194μm, magnitude of excitation field E=0.165MV/m, mean flow velocity V_m=0.05m/s, fringe spacing i=2.29μm, diameter d=10μm, particle charge q=500e.

In addition to the effect of the frequently on the amplitude of the particle motion one needs to consider also the maximum velocity attained by the particle in its oscillatory motion. Based on (3.31), the particle velocity during one period, T, of square-wave excitation field could achieve its terminal value, μE, when there is equilibrium between drag force and electrical force. By increasing the drive frequency, the maximum value of the particle velocity for larger particles may be less than μE as shown in Fig. 7.8. It can be seen that at the drive frequency of 1kHz, 10μm particle is unable to achieve this equilibrium, which is easily reached at the lower drive frequency of 10Hz because there is enough time for the particle to accelerate and attain its terminal velocity. DBS generated by such particles for higher frequencies of drive excitation would inadvertently

lead to inaccurate charge estimates. This is one of the reasons that the particle capture efficiency becomes lower at higher drive frequency as shown in Fig. 7.7.

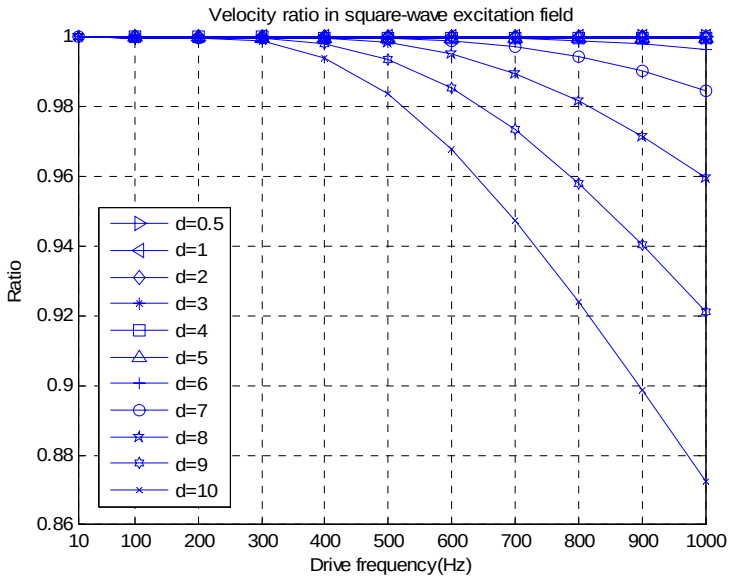

Fig. 7.9 Velocity ratio corresponding to different diameters and drive frequencies in the square-wave excitation field, Laser wavelength λ=514.5nm, intersection angle θ =12^0, beam waist d_w=194μm, fringe spacing i=2.29μm, viscosity of air η=1.8616×10^{-5}kg/ms, particle density ρ=0.8×10^3 kg/m^3, the Cunningham slip correction factor, C_c=1+2.52μ, μ is the mean free path of molecules in the air, μ=0.064μm at room temperature and atmosphere pressure.

Let's now define the velocity ratio as the ratio between the maximum value of the particle velocity and its terminal velocity μE in the electric field.

$$\gamma = \frac{(V_x)_{max}}{\mu E} = \frac{(\mu E(1-e^{-t/\tau}))_{\max}}{\mu E} \tag{7.5}$$

where V_x is the particle real-time velocity in the square-wave excitation field. The velocity ratio corresponding to different particle diameters and drive frequencies is shown in Fig. 7.9. It can be seen that at higher drive frequencies, larger particles are unable to achieve the terminal velocity value. The relaxation time of particles with larger sizes is longer [205], [206], i.e. it will take a longer time to achieve the mechanical equilibrium.

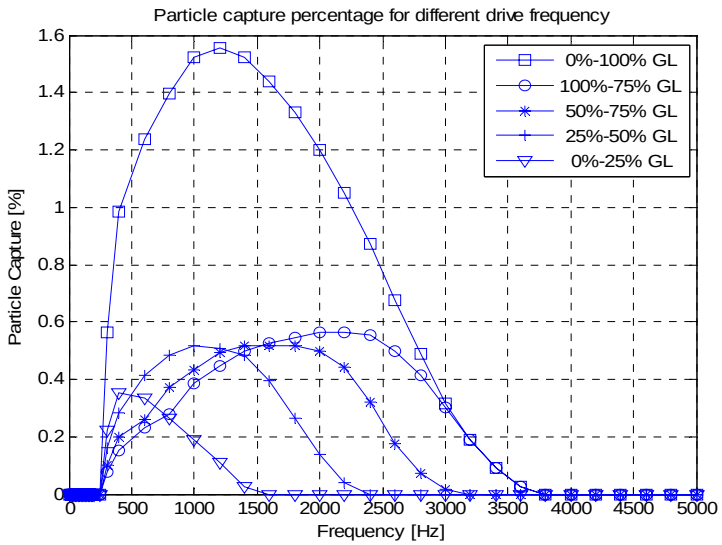

Fig. 7.10 The number of particle captured inside the measurement volume for different drive frequency and different levels of charge as a percentage of Gaussian limit in sine-wave excitation field. Laser wavelength λ=514.5nm, intersection angle θ =12^0, beam waist d_w=194μm, magnitude of excitation field E=0.15MV/m, mean flow velocity V_m=0.05m/s, fringe spacing i=2.29μm, diameter of inlet L_{inlet}=7mm, size of measurement volume, M_x=97.6μm, M_y=97μm.

The results showing the percentage of the total number of particles 'captured' for different excitation frequencies and levels of charge in the sine-wave excitation field is shown in Figure 7.10. It can be seen that the simulation results in the sine-wave exhibit similar behavior to the square-wave excitation. With an increase of drive frequency there is a rapid increase in the total number of particles captured followed by the gradual decline in the capture percentage. The amplitude of the particle velocity and displacement achieved in the sine-wave excitation field is given by (7.6) and (7.7) respectively,

$$A_{v\_SINE} = \frac{EqC_c}{3\pi\eta d\sqrt{1+\omega^2\tau^2}} \tag{7.6}$$

$$x_{\max\_SINE} = \frac{A_{v\_SINE}}{\omega} = \frac{EqC_c}{3\pi\eta d\,\omega\sqrt{1+\omega^2\tau^2}} \tag{7.7}$$

From (7.7) it can be seen the amplitude of particle motion in the sine-wave excitation field is strongly inversely proportional to drive frequency. Therefore, for

lowly charged particles and higher frequencies, the amplitude of particle velocity quickly decreases and thus the capture percentage is much reduced, as shown in Fig. 7.10.

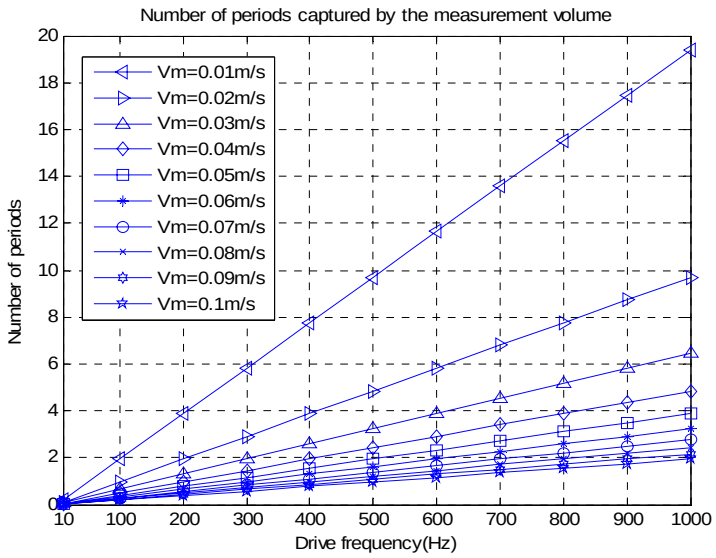

Fig. 7.11 Number of period captured by the measurement volume corresponding to different mean velocities and drive frequencies, size of measurement volume, M_x=97.6μm, M_y=97μm.

However, it is also important to emphasize the two major differences between these excitation systems. Firstly, the overall number of particles captured in sine-wave excitation is significantly smaller than in square-wave excitation. Secondly, the optimum drive frequency in sine-wave is much higher than in the square-wave excitation. This difference could be attributed to the fact that the amplitude of the particle motion is much smaller in sine-wave than in square-wave excitation. Also, the signal processing system requirement in sine-wave is that the particle has to remain inside the measurement volume for at least one period of drive excitation. This is further illustrated in Fig. 7.11 showing the number of periods of particle excitation captured by the measurement volume at different drive frequency and mean flow velocity has been shown. It can be seen that the higher drive frequency and the lower the mean flow velocity the greater number of periods of particle excitation can be captured inside the measurement volume.

From Fig. 7.7 and 7.10, it can be concluded that the optimum drive frequency, from the point of view of maximizing the number of measured particles, is between 10 and 200Hz for the square-wave and 500 to 1200Hz for sine-wave excitation. The overall

number of particles detected in the measurement volume and processed by the system was on average 10 times higher for square than sine-wave excitation.

The optimum drive frequency range for sine-wave excitation is similar to the operational frequencies used by ESPART analyzer [32]. However, the criterion for selecting the drive frequency in ESPART is different from the criteria used by the PDA system. ESPART frequency is primarily determined by the relationship between particle size and phase lag with the objective to minimize the measurement error. On the other hand, the PDA system does not have this constraint, and its operational frequency can be adjusted based on the probability of obtaining most representative sample of aerosol.

7.4 The Effect of the Magnitude of the Excitation Field

The simulation results showing the percentage of the total number of particles 'captured' for different field magnitude in the square-wave excitation field are shown in Fig. 7.12. It can be seen that increasing the magnitude of the field up to around 0.5 MV/m resulted in a significant increase of the total number of particles captured, from around 12% for 0.15MV/m to around 20% for 0.5MV/m. Although, further increase of the field strength had only limited effect on the overall particle capture percentage it significantly improved the number of lowly charged particles successfully captured. It is due to the fact that for lowly charged particles, the low amplitude of the field may not produce sufficient particle displacement in the cross flow direction – please see section 7.2.1.1 for the discussion of the validation criteria.

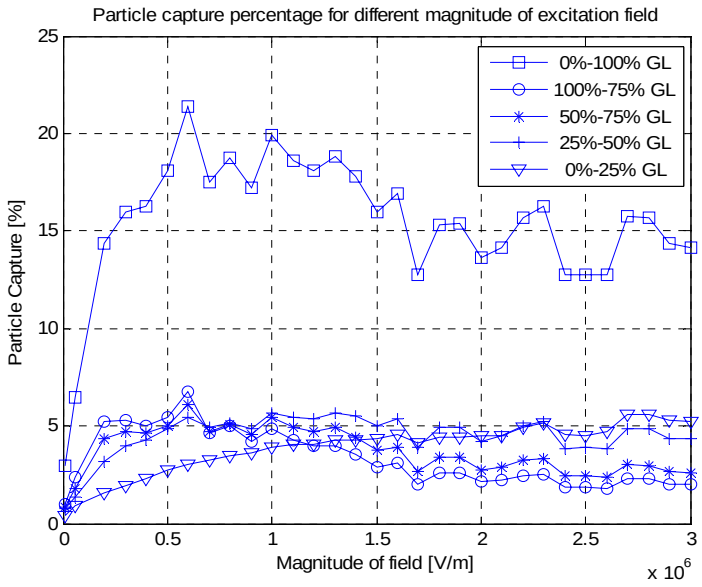

Fig. 7.12 The number of particle captured inside the measurement volume for different magnitude of excitation field and different levels of charge as a percentage of Gaussian limit in square-wave excitation field. Laser wavelength λ=514.5nm, intersection angle θ =12^0, beam waist d_w=194μm, drive frequency f=30Hz, mean flow velocity V_m=0.05m/s, fringe spacing i=2.29μm, diameter of inlet L_{inlet}=7mm, size of measurement volume, M_x=97.6μm, M_y=97μm.

The percentage of the number of particles for different electric field magnitude in the sine-wave excitation is shown in Fig. 7.13. Similarly to the square-wave field it can be observed that increasing the magnitude of the field initially resulted in a significant increase of the total number of particles captured reaching the peak value of 1.5% around 0.15MV/m. In contrast to the square-wave field excitation, however, increasing the amplitude of the electric field beyond 0.15MV/m resulted in the gradual decline of the overall number of particles captured. It is mainly because of the validation condition (7.2), stating that the particle motion in sine wave excitation has to be confined to the measurement volume. Increasing amplitude of the field increases the amplitude of the particle displacement and effectively eliminates some of the highly charged particles which tend to move in and out of the volume. This effect on lowly charged particles, however, is much less pronounced as shown in Fig. 7.13.

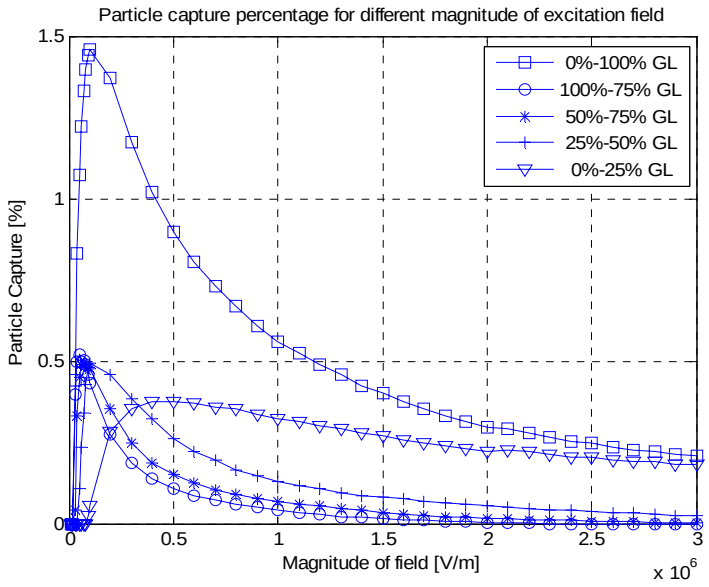

Fig. 7.13 The number of particle captured inside the measurement volume for different magnitude of excitation field and different levels of charge as a percentage of Gaussian limit in sine-wave excitation field. Laser wavelength λ=514.5nm, intersection angle θ =12^0, beam waist d_w=194μm, drive frequency f=1kHz, mean flow velocity V_m=0.05m/s, fringe spacing i=2.29μm, diameter of inlet L_{inlet}=7mm, size of measurement volume, M_x=97.6μm, M_y=97μm.

From Fig. 7.12 and 7.13, it can be concluded that the optimum magnitude of excitation field, from the point of view of maximizing the number of measured particles, is between 0.5 and 1.5MV/m for the square-wave and 0.06 to 0.3MV/m for the sine-wave excitation. The overall number of particles detected in the measurement volume and processed by the system was on average 16 times higher for square than sine-wave excitation. In both excitation fields, the capture percentage of highly charged particles decreases when the magnitude of excitation field becomes greater.

7.5 The Effect of the Mean Flow Velocity

In order to ensure the validity of the charge measurement by the PCSA the cross flow velocity of the particles inside the measurement cell should be entirely dependent on the electric field driving force. This condition can only be satisfied if strict laminar flow conditions are maintained inside the measurement cell. Any deviation from the

laminar flow or unwanted turbulence will immediately result in additional unknown flow component, which would wrongly interpreted by the signal processing system as the effect of the electrostatic charge. The laminar flow inside the inlet occurs at low Reynolds number (R_e<2300), which is defined as,

$$R_e = \frac{V_m L}{\mu} \tag{7.8}$$

where V_m is the mean flow velocity, L is the diameter of the inlet, μ is the fluid viscosity.

If the diameter of the inlet is assumed to be L=7mm, the fluid viscosity of air is $15.68\times10^{-6} m^2/s$ (27°C), the maximum mean flow velocity which could be used in the PCSA is,

$$V_m < 5 m/s \tag{7.9}$$

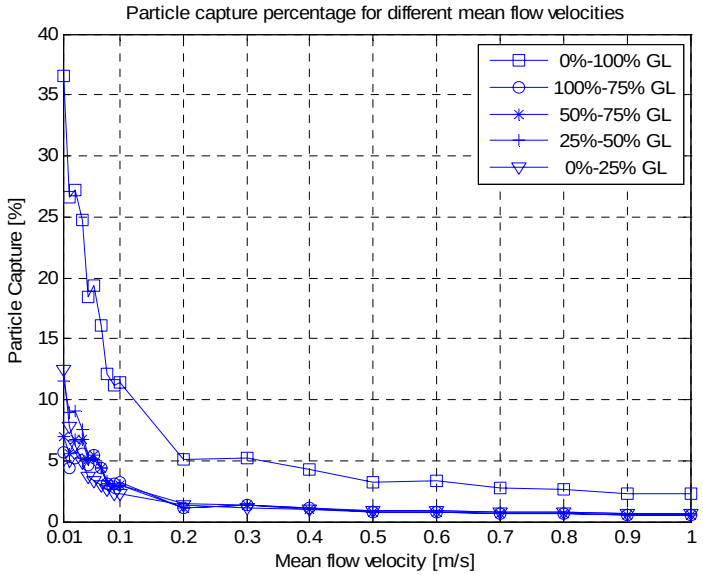

Fig. 7.14 The number of particle captured inside the measurement volume for different mean flow velocity and different levels of charge as a percentage of Gaussian limit in square-wave excitation field. Laser wavelength λ=514.5nm, intersection angle θ =12^0, beam waist d_w=194μm, magnitude of excitation field E=1MV/m, drive frequency f=30Hz, fringe spacing i=2.29μm, diameter of inlet L_{inlet}=7mm, size of measurement volume, M_x=97.6μm, M_y=97μm.

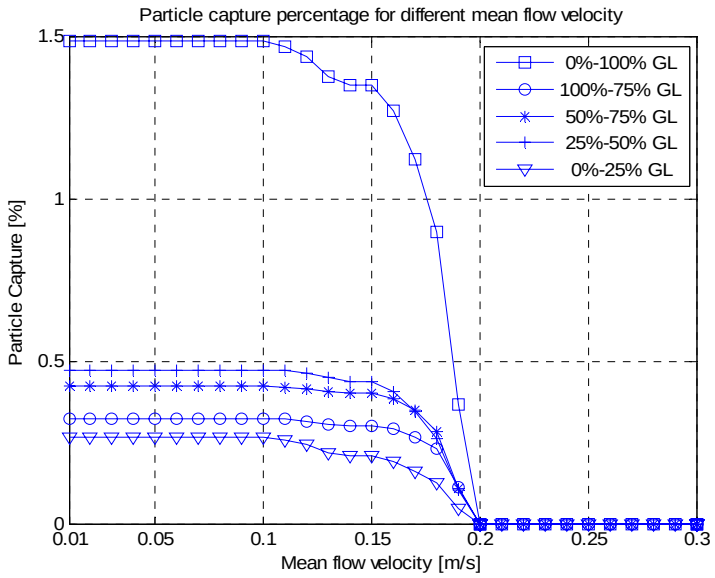

Fig. 7.15 The number of particle captured inside the measurement volume for different mean flow velocity and different levels of charge as a percentage of Gaussian limit in sine-wave excitation field. Laser wavelength λ=514.5nm, intersection angle θ =12^0, beam waist d_w=194μm, magnitude of excitation field E=0.2MV/m, drive frequency f=1kHz, fringe spacing i=2.29μm, diameter of inlet L_{inlet}=7mm, size of measurement volume, M_x=97.6μm, M_y=97μm.

The simulation results showing the percentage of the total number of particles 'captured' for different mean flow velocities and levels of charge in both fields are shown in Fig. 7.14 and 7.15. From Fig. 7.14, it can be concluded that the particle capture percentage decreases as the mean flow velocity increases in the square-wave excitation field. The main reason for that is that higher mean flow velocity increases the particle displacement in one period of the excitation in Y direction and subsequently the likelihood of particle capture. In the case of low mean flow velocity, the particles are more likely to be captured. The overall number of particles detected in the measurement volume and processed by the system is on average 10-20 times higher for square than sine-wave excitation. In the sine-wave excitation field, the capture percentage drops to zero when the mean flow velocity is higher than 0.2m/s. This is due to the fact that the particle residence time is less than one period of excitation field when the mean flow velocity is greater than 0.2m/s. No valid estimation result can be obtained from a DBS with the burst shorter than one period of excitation field, as shown in Fig. 7.15.

Additionally, in the sine-wave field, the mean flow velocity has no obvious effect on the capture percentage when the mean flow velocity is smaller than $0.1m/s$ because the particle residence time remains higher than one drive period.

7.6 The Effect of the Diameter of the Inlet

The simulation results showing the percentage of the total number of particles 'captured' for different diameters of the inlet and levels of charge in both fields are shown in Fig. 7.16 and 7.17.

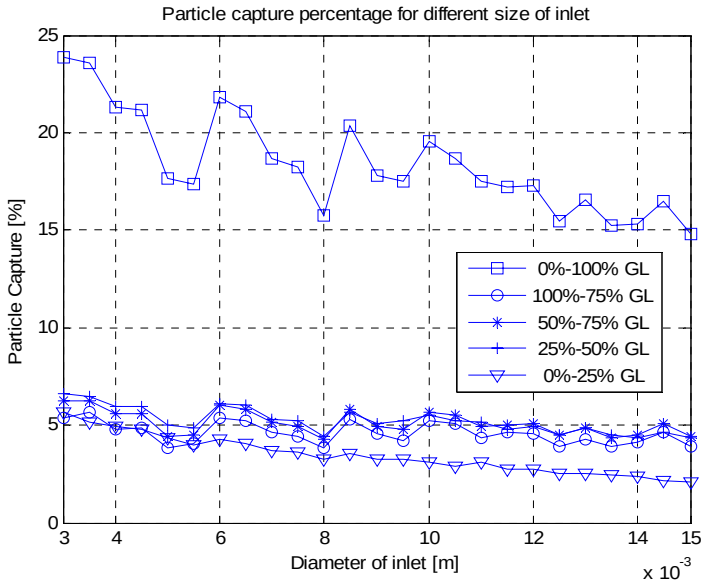

Fig. 7.16 The number of particle captured inside the measurement volume for different diameters of inlet and different levels of charge as a percentage of Gaussian limit in square-wave excitation field. Laser wavelength λ=514.5nm, intersection angle θ =12^0, beam waist d_w=194μm, magnitude of excitation field E=1MV/m, drive frequency f=30Hz, mean flow velocity V_m=0.05m/s, fringe spacing i=2.29μm, size of measurement volume, M_x=97.6μm, M_y=97μm.

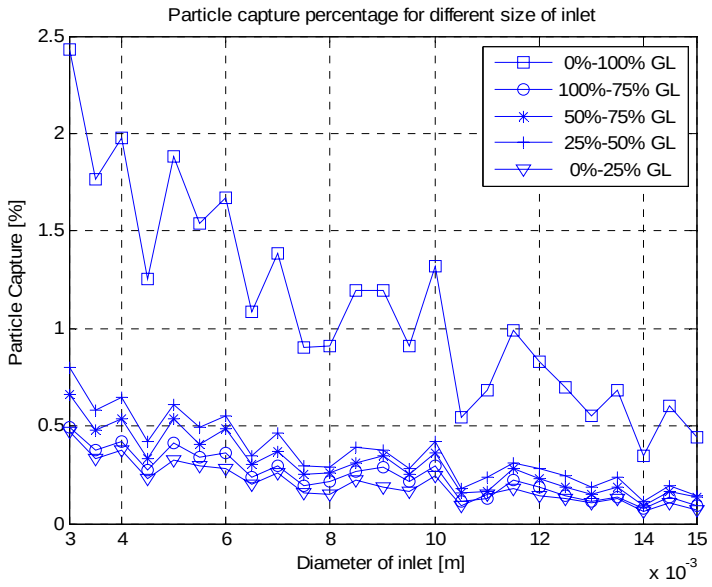

Fig. 7.17 The number of particle captured inside the measurement volume for different diameters of inlet and different levels of charge as a percentage of Gaussian limit in sine-wave excitation field. Laser wavelength λ=514.5nm, intersection angle θ =12^0, beam waist d_w=194μm, magnitude of excitation field E=0.2MV/m, drive frequency f=1kHz, mean flow velocity V_m=0.05m/s, fringe spacing i=2.29μm, size of measurement volume, M_x=97.6μm, M_y=97μm.

From Fig. 7.16 and 7.17, it can be concluded that the particle capture percentage can be improved by reducing the diameter of inlet. The smaller size of inlet, the higher the probability for the particles to get captured inside the measurement volume. The overall number of particles detected in the measurement volume and processed by the system was on average 10 times higher for square-wave than sine-wave excitation. This is because the particle achieves higher amplitude of motion in the square-wave excitation field than in the sine-wave excitation field. The effect of the inlet diameter on the particle capture percentage is more pronounced in case of the sine-wave excitation field than in the square-wave excitation field. The value of capture percentage decreases more rapidly in the sine-wave excitation field, as shown in Fig. 7.17. The greater amplitude of particle motion attained in the square-wave excitation field can compensate the decrease of particle capture percentage resulting from the increasing of the diameter of inlet.

Other factors to consider in selecting the optimum diameter of the inlet are the sampling losses and the sampling efficiency. A very small inlet diameter might lead to poor sampling efficiency due to the limited area from which the aerosol particles are drawn. Additionally too small inlet diameter might contribute to sampling losses due to the particle deposition on the surface of the inlet tube.

7.7 The Effect of the Size of the Measurement Volume

The simulation results showing the percentage of the total number of particles 'captured' for different diameters of inlet and levels of charge in both fields are shown in Fig. 7.18 and 7.19.

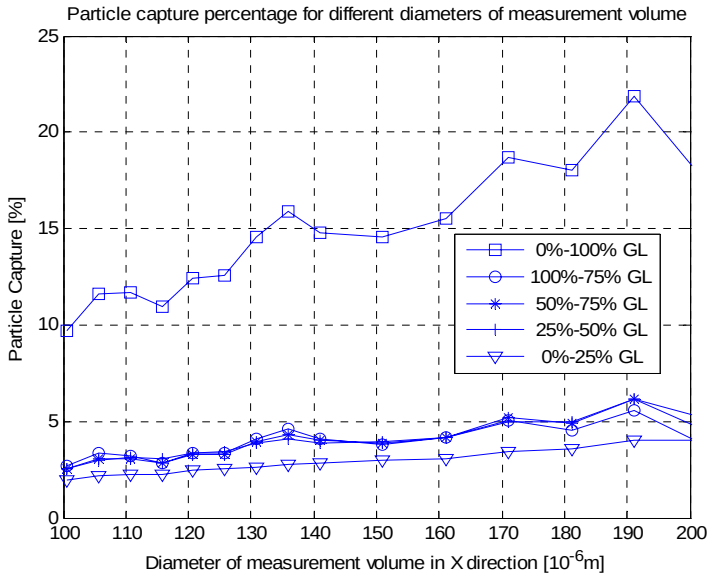

Fig.7.18 The number of particle captured inside the measurement volume for different diameters of measurement volume and different levels of charge as a percentage of Gaussian limit in square-wave excitation field. Laser wavelength λ=514.5nm, intersection angle θ =12^0, magnitude of excitation field E=1MV/m, drive frequency f=30Hz, mean flow velocity V_m=0.05m/s, fringe spacing i=2.29μm, diameter of inlet L_{inlet}=7mm.

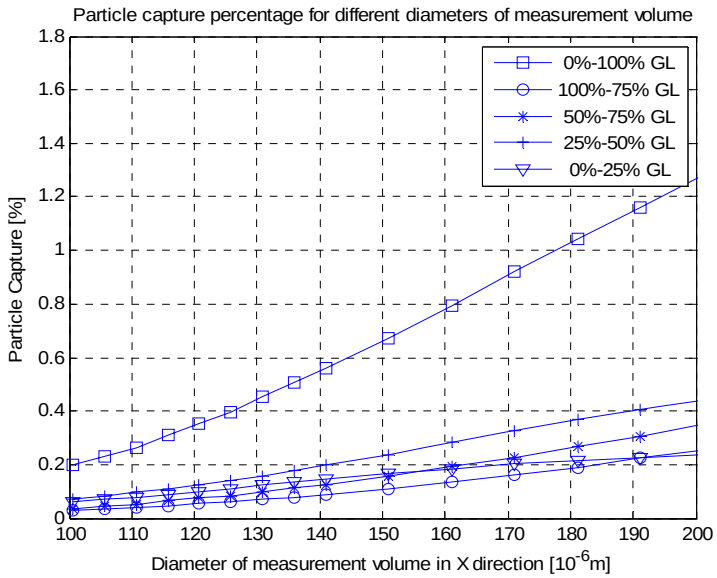

Fig. 7.19 The number of particle captured inside the measurement volume for different diameters of measurement volume and different levels of charge as a percentage of Gaussian limit in sine-wave excitation field. Laser wavelength λ=514.5nm, intersection angle θ =12^0, magnitude of excitation field E=0.2MV/m, drive frequency f=1kHz, mean flow velocity V_m=0.05m/s, fringe spacing i=2.29μm, diameter of inlet L_{inlet}=7mm.

From Fig. 7.18 and 7.19, it can be seen that the particle capture percentage can be improved by increasing the diameter of the measurement volume in both excitation fields. The measurement volume with a larger size increases the probability of the particles to be captured inside the volume, especially in the square-wave excitation field. The greater amplitude of the particle motion in the square-wave excitation field and the smaller number of fringes required in the validation criterion both contribute to the significantly larger number of particles captured inside the volume. There are small irregularities, which could be observed in the curves in Fig. 7.18, more pronounced for highly charged particles. These might be attributed to the fact that the validation criteria in square-wave is more inclusive and the particle count is more susceptible to the random distribution of the particle injection points across the inlet than small incremental changes in the size of the volume. In general, it can be concluded that, the larger the volume the higher percentage of particle capture. However, before opting for a very large measurement volume one needs to bear in mind an important tradeoff between the size of the volume and the coincidence error discussed in chapter 3. A large measurement

volume will result in a large coincidence error and a low count rate which will lead to poor statistical accuracy [7].

7.8 Summary and Conclusions

This chapter discussed the design and the implementation of the numerical simulation of the PCSA measurement system. The numerical model was developed in order to estimate the percentage of aerosol particles arriving at the measurement volume at any given time and generating a valid DBS. The purpose of the numerical modeling was to examine various measurement system configurations and to establish the optimal range of the system parameters for both excitation fields. The effect of drive frequency, strength of field, mean flow velocity, the size of the inlet and the size of measurement volume on the particle capture percentage were investigated based on the specific particle validation criteria in both excitation fields.

Based on the simulation results it could be concluded, that for the square-wave excitation, the optimal range of drive frequency is between 10 and 200Hz, the optimal range of magnitude of excitation field is between 0.5 and 1.5MV/*m*, the optimal range of mean flow velocity is between 0.01*m*/*s* to 0.1*m*/*s*. The particle capture percentage was ranging between 10-30%.

For the sine-wave excitation, the optimal range of the drive frequency is between 500 and 1200Hz, the optimal range of magnitude of excitation field is between 0.06 to 0.3MV/*m* and the optimal range of mean flow velocity is between 0.01*m*/*s* to 0.1*m*/*s*. The particle capture percentage was ranging between 1-3%.

The simulation results have demonstrated that the number of particles detected in the measurement volume and processed by the system was on average 10-20 times higher for square-wave than sine-wave excitation, which gives square-wave method a distinct advantage in obtaining more representative picture of the aerosol charge and size distribution.

Three main reasons have been identified for the superiority of the square-wave excitation over the sine-wave excitation system. Firstly, in the square-wave field particles attain higher velocities and greater amplitudes of displacement, which increases their

probability of crossing the measurement volume from various injection points. Secondly, the sine-wave excitation requires that the particle residence time in the measurement volume is at least equal to one period of the excitation, which effectively eliminates shorter and discontinuous burst. Thirdly, the signal processing in square-wave field, based on spectral analysis, is less demanding in terms of the quality of the DBS, which lead to more inclusive validation criteria and increases the likelihood of the detected particles to be successfully processed.

Chapter 8

Conclusions and Future Work

8.1 Conclusions

The main object of this research project was to design the signal processing system used in conjunction with an application of the PDA system to obtain particle size and electrostatic charge simultaneously in real time. In order to accomplish this task, during the course of the last four years of intensive studies, different estimation systems based on different signal processing strategies in different excitation fields for particle velocity and size estimation have been designed and implemented. The results of this investigation have been presented in this PhD thesis in the following structured way. After the introduction to the project given in Chapter 1, Chapter 2 discussed the underlying principles of the PCSA. Chapter 3 presented the results of the investigation of the characteristics of the DBS due to trajectory of single-particle or multi-particle via the measurement volume in different excitation fields and the study of the relationship between the real-time particle velocity and the instantaneous Doppler frequency. Chapters 4 and 5 presented the details of the design, simulation and performance testing results of the signal processing systems. Chapter 6 described the results of the theoretical study of the accuracy of the frequency estimation. The new expression for the CRB corresponding to the 2D model of DBS in DC excitation field was derived. Finally, Chapter 7 presented the results of the numerical modeling of the measurement system performed in order to estimate the percentage of aerosol particles arriving at the measurement volume at any given time and generating a valid DBS.

The main purpose of this concluding chapter is to summarize the research findings against the specific objectives of the project outlined in chapter 1, Final conclusions will be drawn on the strengths and weaknesses of the designed signal processing systems

leading to recommendations for future work in the development and refinement of the PCSA.

As discussed in Chapter 1, until now, the E-SPART Analyzer developed by Mazumder *et al.* is the only commercially available instrument for real-time measurement of the aerodynamic size and charge of particles. The instrument employs the LDA to obtain the particle instantaneous velocity from the frequency of the DBS. Although, the Analyzer presents an elegant approach, it suffers from some shortcomings. First, the size measurement range is narrow for a given drive frequency due to tangential relationship between the particle diameter and the phase lag. In order to extend the size range the E-SPART has to be operated in multiple frequencies, which prolongs the measurement and makes the instrument less suitable for characterizing rapidly evolving, unstable aerosols. Second, the E-SPART measures only the charged particles when using the AC electric drive, since the uncharged particles do not respond to the electric field. In order to capture the uncharged and lowly charged particles the acoustic drive is used, which complicates the measurement and makes it more susceptible to the unwanted acoustically generated flow disturbance. Third, the instrument suffers from relatively low particle count rate due to its sampling mechanism and signal processing constraints.

The Particle Size and Charge Analyser (PSCA) described in this project employs the PDA technique, which extends the capabilities of the LDA to the measurement of particle velocity as well as size. Different from E-SPART Analyser, the PDA measures particle size optically by measuring the phase difference between signals from different detectors. Compared to the E-SPART Analyser, the PSCA can provide both a larger range of size measurement and a more accurate result of size measurement of lowly charged spherical particles. The first study using the PDA system to measure the particle charge and size distribution on medical inhalers was reported by Kulon *et al.*[15]. The particles were subjected to a stationary DC electric field. The experimental results demonstrated the capability of the technique to handle high particle data rates in the range of more than 1000 particles per second. However, two main disadvantages of using DC field were also identified. First, the measurement volume had to be moved across the measurement cell, which required expensive, high precision traversing mechanism and prolonged the sampling time. Second, some highly charged particles were deflected towards the

electrodes before reaching the measurement volume due to their high electrical mobility, which resulted in the underestimation of their count. In order to address these shortcomings the oscillatory excitation electric field was used.

The use of the PDA in conjunction with the oscillatory field such as sine or square wave, has led to specific challenges in the signal processing, including, burst detection, instantaneous frequency tracking, processing discontinuous-burst, short-DBS, burst with limited number of fringes due to the complex particle motion via the measurement volume etc. In order to understand and study the effect of the particle oscillatory motion on the characteristics of the DBS the mathematical models of the DBS in different excitation fields have been developed and implemented. From the modeling and simulation results, presented in Chapter 3, it can be concluded that the envelope and the instantaneous frequency of the DBS are dependent on the particle position in the measurement volume in both X and Y directions. In the DC excitation field – steady state, the envelope is standard Gaussian due to the constant particle velocity in X direction. In the sine and square wave excitation fields, the shape of the envelope is distorted due to the fact that the velocity in X direction is no longer constant. Sometimes, the discontinuous-burst signal is generated from the oscillatory particle trajectory via the measurement volume, which presents a challenge for the signal detection and processing. Moreover, no valid results can be obtained from the DBS generated from the small amplitude of particle motion. It is because of the limited number of fringes crossed by the particle. Sometimes, no DBS is generated when the amplitude of particle motion is smaller than the fringe spacing. The envelope was shown to achieve its peak value when the particle was passing through the centre of the measurement volume.. Sometimes, however, the particle trajectory via the measurement volume isn't passing through the centre of the measurement volume and produces DBS with substantially smaller amplitude. This is because the maximum intensity lies at the centre of the intersection of laser beams and decays from centre to edge of the interference area. Such bursts with small amplitude will be discarded during burst detection and validation procedure. Additionally, the width of the envelope, i.e. the width of the burst, is determined by the velocity in Y direction, i.e. the mean flow velocity. It was demonstrated that the instantaneous frequency of the DBS is only determined by the real-time particle velocity

in the X direction in the measurement volume. The peak value of the DBS frequency corresponds to the amplitude of particle velocity. In the DC field – steady state, the frequency of DBS is constant. However, the acceleration and oscillation introduced into the particle motion result in the variation in Doppler frequency. In sine-wave excitation field, the DBS can be regarded as a frequency modulated signal whose real-time frequency changes as a sine-wave function. In the square-wave excitation field, the DBS can be approximately regarded as a signal with constant frequency except short periods of acceleration and deceleration in the particle motion. The estimation of the multi-burst DBS due to the high particle concentration was also identified as one of the challenges in the DBS processing.

In order to address these challenges, in the course of this research project, many different signal processing techniques have been studied and adapted for the application in the oscillatory fields. These techniques can be divided into three different categories based on working domain. Firstly, in the frequency domain, e.g. spectrum analyser, the frequency tracking demodulator. Secondly, in time domain, e.g. the period timing technique, QD technique. Finally, in the correlation domain, e.g. the correlation technique. Succinct summary of the advantages and disadvantages of various techniques with respect to the task of estimating particle velocity and phase shift in different excitation fields, in real time is given below.

- Spectrum Analysis and Wavelet analysis

  Common signal processing for the PDA and LDA commercial systems is based on the FFT as good performance even for low SNRs can be achieved. The performance of FFT algorithm can be improved by using window and interpolation. The unique advantages of the FFT based algorithm are relative simplicity and efficiency of implementation, low SNR requirement and wide working range. However, as the FFT processor searches for the peak of spectrum, it requires the particle velocity to be almost constant during one burst and therefore, does not track the frequency fluctuations. In case of the DC and square-wave excitation fields, spectral analysis can be utilized to estimate particle velocity in a wide range of frequencies of DBS. It is due to the fact that frequency remains constant for most part of the particle oscillatory cycle with the exception of the region of the reversal

of the direction of particle velocity in the square-wave excitation field. However, in the case of the sine-wave excitation, the DBS becomes frequency modulated thus rendering complex spectra spanning a wide range of frequencies. The spectrum analyser fails to provide real-time information. However, Wavelet analysis is able to solve this problem by using window with varying size to maintain the frequency resolution. This complicates the algorithm design without the a priori knowledge of the periodic nature of the particle motion

- Frequency Trackers and Periodic Counters

  The frequency tracking demodulators, such as PLL, have been also used to track the instantaneous frequency of the photo-detector signal and provide a direct real-time measurement of the velocity. However, the performance of the PLL is rapidly degrading at low SNR if the large frequency range is required. Also, the working range of the PLL is limited and it requires a continuous signal with a drop-out protection. If the signal is discontinuous as a result of low concentration of aerosol particles or if the signals from two particles interfere destructively to produce dropout, then the signal is lost for short periods of time. This becomes a problem since the output at any point which has dropout will not be proportional to the velocity. In the time domain, period timing counters have been used in the past to track the real-time frequency, but these are particularly sensitive to random noise fluctuations, which could lead to extra zero crossings and estimation errors. The counting technique can only provide a time-averaged measurement, which determines it is not suitable for real-time processing.

- QD method and Correlation Technique

  Quadrature demodulation as a means for laser Doppler frequency estimation is a relatively young technique that exhibits several features, which make it especially attractive for the application to non-stationary DBS. First, it yields time-dependent phase difference information between two signals and allows the instantaneous frequency estimation at relatively low SNR. In a manner similar to frequency determination, the QD method can be also used to determine the phase difference between two input signals which can be continually estimated throughout the burst and thus, phase difference changes can be registered. The QD method is able to

process burst signal containing only a few periods which is an important advantage for DBS frequency estimation. In addition, a wider frequency tracking range than PLL is achievable with QD technique. In commercial PDA systems, the cross-correlation of the two Doppler signals has also been successfully utilized to determine the phase difference between input signals.

Following the investigation of the signal processing methods several signal processing systems were designed and tested. These systems included: velocity estimation system using spectral analysis in DC excitation field, velocity estimation system based on PLL technique working in DC as well as sine-wave excitation fields, velocity estimation system based on QD technique under sine-wave excitation method, velocity estimation system using spectral analysis in square-wave excitation field and phase shift estimation based on Hilbert transformation and correlation technique in both sine-wave and square-wave excitation fields. The performances of these systems were evaluated using MC simulations obtained from the synthesized Doppler burst signals generated from the mathematical models implemented in MATLAB. The synthesized DBS were subsequently corrupted with the added Gaussian noise. Cross validation of the results was performed using hardware signal processing system employing Arbitrary Waveform Generator and also NASA simulator to further confirm the validity of the estimation. However, it is important to emphasize that the purpose of the present study is not to directly compare these very different signal processing schemes but rather independently demonstrate their performance in the context of the specific DBS requirements and respective excitation waveforms.

In order to extend the theoretical analysis of the accuracy of the frequency estimation. the new analytical expression of CRB for a model of the DBS taking into account the 2D motion of particle tracer via the measurement volume has been derived. It was demonstrated that the CRB expression is a function of the direction of particle velocity relative to the fringe pattern. It was shown that the variance of the Doppler frequency estimation increases as the particle velocity starts to deviate from the cross flow direction. This phenomenon was explained in terms of the changed DBS characteristics and the reduced number of fringes crossed by the particle in the measurement volume. The new CRB expression has been compared with the CRB

obtained by Sobolev [177]. With the increase of the particle cross-flow velocity component the CRB asymptotically converges to the Sobolev's formula. It can be concluded that the new Cramér-Rao Bound is more accurate and suitable for the DBS model mentioned in this thesis. In addition, the numerical simulations of the frequency estimation were performed using Monte Carlo simulations obtained from the synthesized Doppler burst signals. It was shown that the numerical results confirmed the theoretical predictions in terms of the relative effect of the particle trajectory, the measurement time, the size of the volume and SNR on the accuracy of the Doppler frequency estimation. The presented analyses have practical implications for the selection of the optical configuration in real LDA measurement systems.

Excitation method	Technique	Velocity estimation range (mm/s)	Charge range	SNR requirement	Capture efficiency	Operation	Hardware Implementation
DC	PLL	1~800	2*e*~ Gaussian limit (lose highly charged particles)	high	lowest	difficult, highly some charged particles are lost	analog, low cost
sine-wave	PLL	30~640	10*e*~ Gaussian limit	high	moderate	easy, some lowly charged particles are lost	analog, low cost
	QD	10~780	14*e*~ Gaussian limit	high	moderate	easy, some lowly charged particles are lost	analog, low cost
square-wave	Spectral analysis	5~800	12*e*~ Gaussian limit	lowest	highest	easy, some lowly charged particles are lost	digital, moderate cost

Table 8.1 Comparison of different estimation systems

Finally, the numerical modeling and simulation of the measurement system was performed leading to better understanding of the relationship between particle charge, particle diameter, particle trajectory and system characteristics, such as, the strength of

excitation field, the drive frequency, the mean flow velocity, the diameter of inlet, the size of measurement volume etc. Succinct summary of the comparison of the signal processing systems in different excitation fields is given in Table 8.1.

The research findings with regards to the velocity and phase shift estimation range, charge range, SNR requirement, particle capture percentage and the cost of hardware system can be summarized as follows:

- Particle Velocity Estimation Range

  The simulation results have demonstrated that at the same level of noise the velocity estimation system based on PLL technique is able to estimate velocity from 1*mm*/*s* to 800*mm*/*s* in the DC excitation field and from 30*mm*/*s* to 640*mm*/*s* in sine-wave excitation field with an error less than 5%. The signal processing system based on QD technique is capable of performing particle velocity estimation in the sine-wave excitation field with a good accuracy. It is able to estimate velocity amplitude from 10*mm*/*s* to 780*mm*/*s* in which the error percentage is less than 5% and the standard deviation smaller than 1.4%. In case of the square-wave excitation field, the velocity estimation range is wider and spans from 5*mm*/*s* to 800*mm*/s. In conclusion, the system based on PLL technique in the DC field and the system based on spectral analysis in the square-wave excitation field performed better than the systems based on PLL and QD techniques in the sine-wave excitation field. The system based on PLL technique in DC field provides the largest range, especially the measurement of particles with low velocity, down to 1*mm*/*s*. Compared to the PLL system working in the DC field, the accuracy of the velocity estimation in the square-wave excitation field decreased for particle velocity with and amplitude less than 5*mm*/*s*. On the other hand however, the working range of the system using spectral analyses could be easily extended upwards without compromising the performance.

- Phase Shift Estimation Range

  The phase shift estimation system was designed based on the Hilbert transform and the correlation technique. In the sine-wave excitation field, the system is able to estimate the phase shift from 5^o to 90^o with an error less than 8% and the standard deviation no larger than 0.5%. The corresponding SNR is 12dB. The corresponding velocity amplitude ranged from 5*mm*/*s* to 800*mm*/*s*. In the square-wave excitation

field, it is able to estimate the phase shift from 5^o to 90^o with an error less than 3% and the standard deviation no larger than 1.5% at the SNR of 12dB. The corresponding velocity amplitude ranged from 5*mm*/*s* to 800*mm*/*s*. It can be concluded that the working ranges of the estimation systems in both excitation fields are similar. In both fields, the relative error and the standard deviation increase as the amplitude of velocity increases.

- Charge Range

  In the DC excitation field, the largest charge range can be obtained by the PLL system. It's from 2*e* to Gaussian limit. The PLL system in sine-wave excitation field provides a charge range from 10*e* to the saturation level. However, it is achieved by changing the strength of field from 1.2MV/*m* to 0.23MV/*m*. In the sine-wave excitation, for *f*=1*k*Hz and E=0.28MV/*m*, the charge range from 14*e* to the Gaussian limit is attainable by QD system. In the square-wave excitation, at *f*=1kHz and *E*=0.165MV/*m*, the charge range from 12*e* to the Gaussian limit can be easily achieved without the need to change the drive frequency or the field strength. In conclusion, for several combinations of the drive frequency and electric field strength, the charge range from several electrons to the Gaussian limit can be achieved without the need to change the drive frequency or the field strength, except for the PLL system in the sine-wave excitation field. Using multiple frequencies prolongs the measurement and makes the instrument less suitable for characterizing rapidly evolving, unstable aerosols. By comparison, the PLL system in the DC excitation field performs better in the estimation of lowly charged particles. However, the loss of some highly charged particles in DC electric field makes this system inferior. The system based on spectral analysis in square-wave excitation field provides the best compromise in terms of the range of measurable particle charge.

- SNR Requirement

  It can be concluded that the velocity estimation system based on spectral analysis in the square-wave excitation field has the lowest SNR requirement. When the SNR becomes smaller, the performance of all the tested systems degrades except the system based on spectral analysis working in the DC field and square-wave

excitation field. Compared to the systems based on PLL technique in the DC excitation field and the sine-wave excitation field, the QD model gives a better performance at the low SNR. In the sine-wave excitation field, the PLL system is more sensitive to noise than the QD system.

- Particle Capture efficiency

  It has been concluded that in an oscillating excitation system, such as sine-wave and square-wave excitation system, more highly charged particles can be measured than in DC excitation system. The numerical modeling of sine-wave and square-wave excitation systems demonstrated that the percentage of particles detected in the measurement volume and processed by the system with valid estimation results was significantly higher for square-wave excitation which gives this system a distinct advantage in obtaining more representative picture of the aerosol charge and size distribution.

- Operation of the system and the cost of hardware implementation

  In the DC excitation field, the measurement volume has to be moved forward and backward in order to capture the moving particles of different mobilities. This creates significant difficulties in the experimental operation and require expensive, high precision traversing mechanism and prolonged the sampling time. Additionally, in the DC field, some highly charged particles will reach the electrodes before they are captured by the measurement volume. Compared to the DC field, the oscillating excitation methods, sine-wave and square-wave, make the operation easier due to the oscillation in particle trajectory. The measurement volume could be kept stationary in the middle of the cell. Moreover, the highly charged particles won't be lost. However, the accuracy of the measurement of the lowly charged particles decreases in oscillatory fields with the increase of the drive frequency. When the amplitude of motion of lowly charged particle is smaller than a certain number of fringe spacing, the correct estimation results can't be obtained from the corresponding DBS.

Based on the discussion shown above, it can be concluded that the velocity estimation system based on spectral analysis in square-wave excitation field offers the best

overall performance in terms of the working range, noise sensitivity and particle capture percentage.

The main reasons for the superiority of the square-wave excitation over the sine-wave excitation system can be summarized as: Firstly, in the square-wave field particles attain higher velocities and greater amplitudes of displacement, which increases their probability of crossing the measurement volume from various injection points. Secondly, the sine-wave excitation requires that the particle residence time in the measurement volume is at least equal to one period of the excitation, which effectively eliminates shorter and discontinuous burst. Thirdly, the signal processing based on FFT is less demanding in terms of the quality of DBS, which increases the likelihood of the detected particles to be successfully processed.

8.2 Future work

It is envisaged that the future work will focus on the following tasks:

1. **Performance evaluation of the estimation systems based on raw DBS**
   Although the system performance has been tested using MC simulations on synthesized DBS, which closely resemble the real laser Doppler signals, it is important to evaluate the performance of the PCSA based on some raw DBS obtained from experiments. Compared to the simulated DBS obtained from the mathematical model, the raw signals will provide the ultimate performance test of the systems.
2. **Implementation of the Maximum-likelihood Estimator (MLE) and a new derivation of the CRB for the oscillatory field**
   The MLE should be implemented and the results should be compared with the newly formulated CRB. In addition a new CRB should be derived using the oscillatory motion of the particle via the measurement volume and the 2D model of the particle motion via the volume. This is a very challenging task due to high mathematical complexity of the problem.
3. **The hardware implementation**
   After having completed the design and performance testing of the estimation systems, the hardware system implementation and integration are expected to be performed.

There are two comparable implementation schemes to be considered, analog and digital system. The analog system will be composed of the optical front end to generate analog DBS, the hardware circuits, the ADC for data conversion and PC. The digital system will consist of the following parts: the optical front end to generate analog DBS, ADC and DAC connected to the DSP processor for data conversion, DSP processor and PC. The developed DSP program installed on the DSP chip will sample, detect, store data. DSP board and PC will perform the data acquisition. DSP code installed on the PC will demodulate signal and calculate particle size and charge.,

4. **Evaluation of the measurement system performance using unipolarly and bipolarly charged aerosols**

Appendix A

Determination of the Integrals from the Fisher Information Matrix

$$I_2 = \int_{-KT}^{KT} t^2 \exp(C_3 t^2) dt = \frac{1}{C_3}[t \exp(C_3 t^2)|_0^{KT} - \int_0^{KT} \exp(C_3 t^2) dt] \tag{A1}$$

$$I_2 = \frac{1}{C_3}[KT \exp(K^2 T^2 C_3) - \frac{\sqrt{\pi}}{2\sqrt{-C_3}} erf(KT\sqrt{-C_3})] \tag{A2}$$

$$I_4 = \int_{-KT}^{KT} t^4 \exp(C_3 t^2) dt = \frac{1}{C_3} \int_0^{KT} t^3 d \exp(C_3 t^2) = \frac{1}{C_3}[t^3 \exp(C_3 t^2)|_0^{KT} - \frac{3}{2} \int_0^{KT} t^2 \exp(C_3 t^2) dt] \tag{A3}$$

$$I_4 = \frac{1}{C_3}\{K^3 T^3 \exp(K^2 T^2 C_3) - \frac{3}{C_3}[KT \exp(K^2 T^2 C_3) - \frac{\sqrt{\pi}}{2\sqrt{-C_3}} erf(KT\sqrt{-C_3})]\} \tag{A4}$$

Substituting for K=(N-1)/2 and $\eta = KT\sqrt{-C_3}$ in (A2) ,(A4)

$$I_2 = -\frac{(N-1)^3 T^3}{2^3 \eta^2}[\exp(-\eta^2) - \frac{\sqrt{\pi}}{2\eta} erf(\eta)] \tag{A5}$$

$$I_4 = -\frac{(N-1)^2 T^2}{2^2 \eta^2}[\frac{(N-1)^3}{2^3} T^3 \exp(-\eta^2) - 3I_2] \tag{A6}$$

Therefore,

$$C_4 I_4 + I_2 = -\frac{C_4 (N-1)^5 T^5}{2^5 \eta^2} \exp(-\eta^2) - [\frac{3C_4 (N-1)^2 T^2}{2^3 \eta^2} + 1] \frac{(N-1)^3 T^3}{2^3 \eta^2} [\exp(-\eta^2) - \frac{\sqrt{\pi}}{2\eta} erf(\eta)] \tag{A7}$$

Let's, define

$$\xi_m = \sqrt{C_4}(N-1)T/(2\sqrt{2}\eta) \tag{A8}$$

Finally, rearranging (A7) and substituting (A8)

$$C_4 I_4 + I_2 = \frac{(N-1)^3 T^3}{8\eta^3} \qquad \frac{\sqrt{\pi}}{2}[3\xi_m^2 + 1]erf(\eta) - \eta \exp(-\eta^2)[1 + \xi_m^2(2\eta^2 + 3)] \tag{A9}$$

Additionally, the derivation and simplification of tracer particle time T_w and parameter ξ_m are shown below.

$$T_w = \frac{1}{\sqrt{2}\sqrt{\beta_1^2 V_x^2 + \beta_2^2 V_y^2}} = \frac{1}{\sqrt{2}\sqrt{\beta_1^2 V_x^2 [1 + (\frac{\beta_2}{\beta_1})^2 (\frac{V_y}{V_x})^2]}} = \frac{1}{\sqrt{2}\beta_1 V_x \sqrt{1 + (\frac{\beta_2}{\beta_1})^2 (\frac{V_y}{V_x})^2}} \tag{A10}$$

Let's define

$$\gamma = \frac{V_y}{V_x}$$

which is called the particle relative velocity coefficient.

Therefore,

$$T_w = \frac{1}{\sqrt{2}\beta_1 V_x \sqrt{1 + (\frac{\beta_2}{\beta_1})^2 \gamma^2}} = \frac{1}{\frac{\sqrt{2}\beta_1 \omega_D i}{2\pi} \sqrt{1 + (\frac{\beta_2}{\beta_1})^2 \gamma^2}} = \frac{\sqrt{2}\pi}{i\beta_1 \omega_D \sqrt{1 + (\frac{\beta_2}{\beta_1})^2 \gamma^2}} \tag{A11}$$

From (A8),

$$\xi_m = \frac{\sqrt{C_4 (N-1)T}}{2\sqrt{2}\eta} = \frac{2C_1 \omega_D (N-1)T}{2\sqrt{2}\eta} = \frac{\beta_1^2 \omega_D (N-1)T}{(2\pi D)^2 \sqrt{2}\eta} \tag{A12}$$

$$\because K = \frac{N-1}{2}$$

$$\therefore \xi_m = \frac{\beta_1^2 2\pi D V_x (2K)T}{\sqrt{2}(2\pi D)^2 \eta \frac{KT}{T_w}} = \frac{\beta_1^2 V_x T_w}{\sqrt{2}\pi D} = \frac{\beta_1^2 V_x T_w i}{\sqrt{2}\pi} \tag{A13}$$

$$\because T_w = \frac{\sqrt{2}\pi}{i\beta_1 \omega_D \sqrt{1 + (\frac{\beta_2}{\beta_1})^2 \gamma^2}}$$

$$\therefore \xi_m = \frac{i\beta_1}{2\pi\sqrt{1+(\frac{\beta_2}{\beta_1})^2\gamma^2}} \tag{A14}$$

Assuming $\frac{\beta_2}{\beta_1} \approx 1$

$$\therefore T_w = \frac{\sqrt{2}\pi}{i\beta_1\omega_D\sqrt{1+\gamma^2}} = \frac{\sqrt{2}\pi}{i\frac{2}{iN_{f(e^{-1})}}\omega_D\sqrt{1+\gamma^2}} = \frac{\pi N_{f(e^{-1})}}{\sqrt{2}\omega_D\sqrt{1+\gamma^2}} \tag{A15}$$

$$\therefore \xi_m = \frac{i\beta_1}{2\pi}\frac{1}{\sqrt{1+\gamma^2}} \tag{A16}$$

$$\because \beta_1 = \frac{2}{iN_{f(e^{-1})}}$$

$$\therefore \xi_m = \frac{2}{2\pi N_{f(e^{-1})}}\frac{1}{\sqrt{1+\gamma^2}} = \frac{1}{\pi N_{f(e^{-1})}}\frac{1}{\sqrt{1+\gamma^2}} \tag{A17}$$

Appendix B

Derivation of Formulas of Particle Velocity and Position in Square-wave Excitation Field

In the square-wave excitation field, the particle is affected by two forces. One is the electric force due to the excitation field, the other one is call the drag force arised from the viscosity of the medium in the measurement cell. These two forces are defined as below.

$$\mathbf{F}_e(t) = \begin{cases} q\mathbf{E} & 0 \le t < T/2 \\ -q\mathbf{E} & T/2 \le t < T \end{cases} \tag{B1}$$

where T is the period of the square-wave excitation.

$$\mathbf{F}_{drag}(t) = -\frac{3\pi\eta d\mathbf{v}(t)}{C_c} \tag{B2}$$

The motion of particle in un-equilibrium state in square-wave excitation field will be investigated below.

a. Particle motion in the period from t=0 to t=T/2

In this period, the particle velocity is accelerated from 0 to V_x. The figure of particle motion and forces is shown in Fig. A.1.

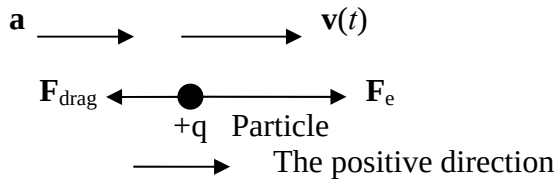

Fig. A.1

The corresponding motion equation is shown in (A.3)

$$
\begin{aligned}
&m\mathbf{a} = \mathbf{F}_e + \mathbf{F}_{drag} = \mathbf{E}q + \mathbf{F}_{drag} \\
&\because \mathbf{F}_{drag} = -\frac{3\pi d\eta \mathbf{v}(t)}{C_c} \\
&\therefore m\frac{dv(t)}{dt} = Eq - \frac{3\pi d\eta v(t)}{C_c} \\
&i.e. \frac{dv(t)}{dt} + \frac{3\pi d\eta}{mC_c} v(t) = \frac{Eq}{m}
\end{aligned}
\tag{B3}
$$

This is a 1st order linear equation with the original condition, **v**(0)=0.

Assuming $A = \frac{3\pi d\eta}{mC_c} = \frac{18\eta}{d^2 \rho C_c}, B = \frac{EqC_c}{3\pi d\eta}$

Thus, the corresponding solution is

$$\mathbf{v}(t) = B(1 - e^{-At}) \tag{B4}$$

b. Particle motion in the period from t=T/2 to t=T

In this period, the particle velocity is decelerated from V_x to 0. The figure of particle motion and forces is shown in Fig. A.2.

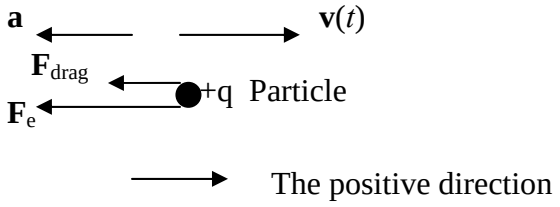

Fig. A.2

The corresponding motion equation is

$$
\begin{aligned}
&m\mathbf{a} = \mathbf{F}_e + \mathbf{F}_{rag} = \mathbf{E}q + \mathbf{F}_{drag} \\
&\because \mathbf{F}_{drag} = -\frac{3\pi d\eta \mathbf{v}(t)}{C_c} \\
&\therefore m\frac{dv(t - T/2)}{dt} = -Eq - \frac{3\pi d\eta v(t - T/2)}{C_c} \\
&i.e. \frac{dv(t - T/2)}{dt} + \frac{3\pi d\eta}{mC_c} v(t - T/2) = -\frac{Eq}{m}
\end{aligned}
\tag{B5}
$$

This is a 1st order linear differential equation, whose solution is

$$\mathbf{v}(t) = e^{-A(t - T/2)}(C - Be^{A(t - T/2)}) \tag{B6}$$

The original condition is $\mathbf{v}(T/2) = \mathbf{V}_x$

After calculation,

$$\begin{aligned} &\mathbf{V}_x = C - B \\ &\therefore C = \mathbf{V}_x + B \\ &\because \mathbf{V}_x = B \\ &\therefore C = 2B \end{aligned} \tag{B7}$$

Therefore, the particle velocity function can be expressed as

$$\mathbf{v}(t) = e^{-A(t-T/2)}(2B - Be^{A(t-T/2)}) = B[2e^{-A(t-T/2)} - 1] \tag{B8}$$

c. Particle motion in the period from t=T to t=3T/2

In this period, the particle velocity is accelerated from $-V_x$ to V_x. The calculation is similar to the case a, except the original condition, $\mathbf{v}(T) = -V_x$.

The corresponding result is

$$\mathbf{v}(t) = B[1 - 2e^{-A(t-3T/2)}] \tag{B9}$$

In conclusion, the particle velocity in the period from t=0 to t=3T/2 in the square-wave excitation field is derived. The motion from t=T/2 to t=3T/2 will be repeated from time to time.

$$\begin{aligned} \mathbf{V}_x(t) &= \begin{cases} B(1 - e^{-At}) & 0 \le t < T/2 \\ B[2e^{-A(t-T/2)} - 1] & T/2 \le t < T \\ B[1 - 2e^{-A(t-3T/2)}] & T \le t < 3T/2 \end{cases} \\ \mathbf{V}_y(t) &= \mathbf{V}_y \end{aligned} \tag{B10}$$

where $A = \dfrac{3\pi d\eta}{mC_c} = \dfrac{18\eta}{d^2\rho C_c}, B = \dfrac{EqC_c}{3\pi d\eta}$

$1/A$ is defiend as the relaxation time τ, i.e. $\tau = \dfrac{1}{A} = \dfrac{d^2\rho C_c}{18\eta}$ (B11)

Additionally, the electrical mobility of the charged particle, μ is defiend as

$$\mu = \frac{qC_c}{3\pi d\eta} = \frac{B}{E} \tag{B12}$$

By integrating (A.9), the particle position in the measurement volume can be obtained.

$$
\begin{aligned}
&\because \mathbf{V}_x(t) = B(1-e^{-At}) \qquad 0 \le t < T/2 \\
&\therefore x(t) = x_0 + \int_0^t V_x(t)dt \qquad 0 \le t < T/2 \\
&\quad = x_0 + \int_0^t B(1-e^{-At})\,dt \\
&\quad = x_0 + \int_0^t B(1-e^{-At})\,dt \\
&\quad = x_0 + B\int_0^t dt - B\int_0^t e^{-At}dt \\
&\quad = x_0 + B(t+\tau e^{-t/\tau})
\end{aligned}
\tag{B13}
$$

$$
\begin{aligned}
&\because \mathbf{V}_x(t) = B[2e^{-A(t-T/2)} - 1] \qquad T/2 \le t < T \\
&\therefore x(t) = x_0 + \int_{T/2}^t V_x(t)dt \\
&\quad = x_0 + \int_{T/2}^t B[2e^{-A(t-T/2)} - 1]\,dt \\
&\quad = x_0 + \int_{T/2}^t 2Be^{-A(t-T/2)}dt - \int_{T/2}^t Bdt \\
&\quad = x_0 - B[2\tau e^{-(t-T/2)/\tau} + t - T/2]
\end{aligned}
\tag{B14}
$$

$$
\begin{aligned}
&\because \mathbf{V}_x(t) = B[1-2e^{-A(t-3T/2)}] \qquad T \le t < 3T/2 \\
&\therefore x(t) = x_0 + \int_T^t V_x(t)dt \\
&\quad = x_0 + \int_T^t B[1-2e^{-A(t-3T/2)}]\,dt \\
&\quad = x_0 - \int_T^t 2Be^{-A(t-3T/2)}dt + \int_T^t Bdt \\
&\quad = x_0 + B\{2\tau[e^{-(t-3T/2)/\tau} - e^{T/2\tau}] + t - T\}
\end{aligned}
\tag{B15}
$$

In conclusion, the particle trajectory in the sqaure-wave excitation field from t=0 to t=3T/2 is obtained.

$$
\begin{aligned}
\mathbf{x}(t) &= \begin{cases} \mathbf{x}_0 + B(t+\tau e^{-t/\tau}) & 0 \le t < T/2 \\ \mathbf{x}(T/2) - B[2\tau e^{-(t-T/2)/\tau} + t - T/2] & T/2 \le t < T \\ \mathbf{x}(T) + B\{2\tau[e^{-(t-3T/2)/\tau} - e^{T/2\tau}] + t - T\} & T \le t < 3T/2 \end{cases} \\
\mathbf{y}(t) &= \mathbf{y}_0 + \mathbf{V}_y(t-t_0)
\end{aligned}
\tag{B16}
$$

Appendix C

Derivation of (4.54)

$$I(t) = A(t)\cos[2\pi Dx(t)] + n(t) \tag{C1}$$

$$Q(t) = A(t)\sin[2\pi Dx(t)] + n(t) \tag{C2}$$

$$\therefore \frac{dI(t)}{dt} = \frac{dA(t)}{dt}\cos[2\pi Dx(t)] - 2\pi Dv(t)A(t)\sin[2\pi Dx(t)] + \frac{dn(t)}{dt} \tag{C3}$$

$$\frac{dQ(t)}{dt} = \frac{dA(t)}{dt}\sin[2\pi Dx(t)] + 2\pi Dv(t)A(t)\cos[2\pi Dx(t)] + \frac{dn(t)}{dt} \tag{C4}$$

$$\therefore I(t)\frac{dQ(t)}{dt} - Q(t)\frac{dI(t)}{dt} = 2\pi Dv(t)A^2(t) + [A(t)\frac{dn(t)}{dt} - n(t)\frac{dA(t)}{dt}]\{\cos[2\pi Dx(t)] - \sin[2\pi Dx(t)]\}$$

(C5)

$$I^2(t) + Q^2(t) = A^2(t) + 2A(t)n(t)\{\sin[2\pi Dx(t)] + \cos[2\pi Dx(t)]\} + 2n^2(t) \tag{C6}$$

$$i.e.\ I(t)\frac{dQ(t)}{dt} - Q(t)\frac{dI(t)}{dt} = 2\pi Dv(t)A^2(t) + [\frac{dn(t)}{dt} - \frac{n(t)\frac{dA(t)}{dt}}{A(t)}][I(t) - Q(t)] \tag{C7}$$

$$I^2(t) + Q^2(t) = A^2(t) + 2n(t)[I(t) + Q(t)] + 2n^2(t) \tag{C8}$$

Therefore, when there is no noise,

$$\frac{I(t)\frac{dQ(t)}{dt} - Q(t)\frac{dI(t)}{dt}}{I^2(t) + Q^2(t)} = 2\pi Dv(t) \tag{C9}$$

Appendix D

List of Publications

D1 Journal Papers

1. L. Zhang, J. Kulon, "Comparative Study of Square and Sine Wave Excitation Methods for the Measurement of Aerosol Particles Charge and Size Distribution using Phase Doppler Anemometry, Signal Processing Strategy, System Modelling and Optimisation", *IEEE Trans. Instrum. Meas.* (In print).
2. L. Zhang, J. Kulon, "The Effect of a Particle Trajectory via the Measurement Volume on the Accuracy of the Laser Doppler Frequency Estimation", *Flow Measurement and Instrumentation* (Submitted).

D2 Conference Papers

1. L. Zhang, J. Kulon, "Cramér-Rao Bounds for a Laser Doppler Anemometer: The Effect of the Particle Trajectory via the Measurement Volume", I2MTC Int. Instrument. Measurement Technology Conf., Austin, 3~6 May 2010, pp. 300-303.
2. L. Zhang, J. Kulon, "Real-Time, Non-Invasive Measurement of Medical Aerosol Charge and Size Distribution, Signal Processing Strategy, System Modelling and Optimization," I2MTC Int. Instrument. Measurement Technology Conf., Singapore, 5~7 May 2009, pp. 457-462.
3. L. Zhang, J. Kulon, "Numerical modelling and parameter optimisation of the Particle Charge and Size Analyser", Proc. of the 4th FAT Research Workshop, University of Glamorgan, UK, 12 Mar. 2009, pp. 29-33.

4. L. Zhang, J. Kulon, “Real-Time Particle Size and Charge Estimation from Laser Doppler Burst Signals using Quadrature Demodulation and Correlation Techniques”, in *ICSP’08*, Beijing, China, 26~29 Oct. 2008, pp. 2677-2680.
5. L. Zhang, J. Kulon, “Real-time Velocity Estimation of Charged Particles using Phase Locked Loop and Quadratude Demodulation Techniques”, Proc. of the 3nd FAT Research Workshop, University of Glamorgan, UK, 6 Mar. 2008, pp. 25-29.
6. J. Kulon, L. Zhang, “PLL System Design for Simultaneous Analysis of Particle Charge and Size using Phase Doppler Anemometry,” in *9th IEEE International Conference on Applied Electronics*, Pilsen, Czech Republic, pp.117-120, 5~ 6 Sep. 2007.
7. L. Zhang, J. Kulon, “Real-Time Signal Processing Method for Obtaining Charge Distribution on Aerosols Produced by Medical Inhalers,” in *4th IEEE-EMBS International Summer School and Symposium on Medical Devices and Biosensors (ISSS-MDBS 2007)*, Cambridge, UK, pp.90-93, 19~22 Aug. 2007.
8. L. Zhang, “PLL design for real-time measurement of Particle charge,” in *the 6th Annual Doctoral Seminar, University of Glamorgan*, abstract, pp. 22, 4 May. 2007.
9. L. Zhang, “Real-time signal processing technique for the measurement of electrostatic charge by means of phase Doppler anemometry,” Proc. of the 1st FAT Research Workshop, *Faculty of Advanced Technology, University of Glamorgan*, pp. 35-39, 1 Mar. 2007.

Bibliography

[1] IMS (International Marketing Services), http://www.imshealth.com/ims/portal

[2] S. Suarez and A. Hickey, "Drug Properties Affecting Aerosol Behavior", *Respiratory Care*, vol. 45, No 6, Jun. 2000.

[3] Therapeutics 2000, Inc., http://www.therapeutics2000.com/

[4] A. G. Bailey, "The inhalation and deposition of charged particles within the human lung," *Electrostat. J.*, vol. 42, pp. 25–32, 1997.

[5] W. Balachandran, C. N. Ahmad and S. A. Barton, "Deposition of Electrically Charged Aerosol in Lung", *Inst. Phys. Conf.*, *Series no 118*, *Section 1*, pp. 57-62, 1991.

[6] A. H. Hashish, A. G. Bailey and T. J. Williams, "Drug Delivery by Inhalation of Charged Particles," in *the 6th Annual U.A.E. University Research Conference*.

[7] J. Kulon, "Real-time measurement of bipolar charge distribution on pharmaceutical aerosols and powders using phase Doppler anemometry and a bipolar charge measurement system," PhD Thesis, Dept. Systems Engineering, Brunel University, 2003.

[8] C. P. Yu and C. K. Diu, "A comparative study of aerosol deposition in different lung models," *Amer. Ind. Hygiene Assoc. J.*, vol. 43, pp. 54-65, 1982.

[9] R. C. Brown, "Tutorial review: simultaneous measurement of particle size and particle charge," *Aerosol Sci. J.* vol. 28, No. 8, pp. 1373-1391, 1997.

[10] C. P. Yu, *Ann. Occup. Hyg.*, 29,pp 219-227,1985.

[11] A. H. Hashish, A.G. Bailey and T. J. Williams, in *Proc. 2nd Conf. of Aerosol Soc.*, 1988, pp. 121-126.

[12] D. Koolpiruck, S. Prakoonwit and W. Balanchandran, *IEEE Trans. Ind. Applicat.* 40 (5), pp. 1239-1248, 2004.

[13] B. Cohen, J. Xiong and C. Fang, "Deposition of charged particles on lung airways," *Health Phys.* vol. 74, pp. 554-560, 1998.

[14] J. A. Cross, *Electrostatics: Principles, Problems and Applications*. Bristol, U.K.: Adam Hilger, 1987.

[15] J. Kulon, B. Malyan , W. Balachandran, "Simultaneous Measurement of Particle Size and Electrostatic Charge Distribution in DC Electric Field Using Phase Doppler Anemometry," *IEEE Trans. Ind. Applicat*., Vol. 39(5), 2003, pp. 1522-1528.

[16] C. J. Kenyon, L. Thorsson, L. Borgstrom and S. P. Newman, *Drug del. to lungs VII*. 1996, pp. 17-18.

[17] D. Koolpiruck, "Investigation of charged aerosol transport and deposition in human airway models," PhD thesis, Brunel University, 2005.

[18] "Solkane® 227 pharma and 134a pharma (NEW) - Markets & Applications," (2007, Aug 1) [Online]. Available:

http://www.solvay-fluor.com/product/markets_applications/0,0,-_EN-1000700,00.html

[19] J. Peart, P. Kulphaisal and J. Corban, "Relevance of electrostatics in respiratory drug delivery," *Pharmagenerics*, *Reference Section*, pp. 1-4, 2003

[20] P. R. Byron, J. Peart and J. N. Staniforth, "Aerosol electrostatics I: Properties of fine powders before and after aerosolization by dry powder inhales," *Pharmaceutical Research*, 14 (6), pp. 698–705, 1997.

[21] A. G. Bailey, "Electrostatic phenomena during powder handling," *Powder Technology J.*, vol. 37, pp. 71–85, 1984

[22] A. G. Bailey, "Charging of solids and powders," *Electrostat. J.*, vol. 30 pp. 167–180, 1993

[23] W. Balachandran, W. Machowski, E. Gaura, C. Hudson, "Control of drug aerosol in human airways using electrostatics forces," *J. Electrostat*. Vol. 40&41, pp. 579-584, 1997.

[24] W. Balachandran, S. Sivathasan, J. Kulon, "Evaluation of the Electrosatic properties of pharmaceutical powders," *Research Report Ref. No*: BCM-WB/SS/JK/12-02, Dec, 2002.

[25] D. Koolpiruck, S. Prakoonwit, W. Balachandran, "A numerical study of charged aerosol transportation in human airways," *Proc. of Drug Delivery to the Lungs XIII*, London, pp. 49-51, 12-13 Dec. 2002.

[26] D. Koolpiruck, S. Prakoonwit, W. Balachandran, "Deposition of charged aerosol in reconstructed human airways," *Proc. of ICLASS 2003*, Sorrento, Italy, 13-18 Jul. 2003.

[27] D. Koolpiruck, "Investigation of Charged Aerosol Transport and Deposition in Human Airway Models," PhD Thesis, Electronic and Computer Engineering, School of Engineering and Design, Brunel University, 2005.

[28] A. Krupa, A. Jaworek, "A method for aerosol particle charge measurements," *Electrostat. J.*, vol. 23, pp. 289-292.

[29] J. R. Greaves and B. Makin, "Measurement of the electric charge from aerosol cans," in *IAS Annual Meeting 28/9-31/10/80-Cincinnati*, pp. 1075-1080

[30] D. C. Aldred, A. F. Howe and A. Wright, "Size selective particle charge measurement," in *Filtech. Conf.* pp. 342-346.

[31] M. K. Mazumder, N. Grable, Y. Tang, S. O'Connor, R. A. Sims, "Real-time particle size and electrostatic charge distribution analysis and its applications to electrostatic processes," in *the 10th Int. Conf.*, Cambridge, 28-31, 1999.

[32] M. K. Mazumder, "Measurement of particle size and electrostatic charge distributions on toners using E-SPART analyzer," *IEEE Trans. Ind. Applicat.*, vol. 27, No. 4, 1991.

[33] W. Divito, M. K. Mazumder, J. D. Wilson, R. A. Sims, P. Louziu, A. Ojha, N. Grable, S. Chapman, "Simutaneous analysis of particle size and electrostatic charge distribution of powder with high accuracy and precision, and its applications to electrostatic processes", in *Ind. Appl. Conf., Thirty-Third IAS Annual Meeting*, vol. 3, Issue, 12-15, pp. 1892 - 1897, 1998

[34] H.-E. Albrecht, N. Damaschke, M. Borys, C. Tropea, *Laser Doppler and Phase Doppler Measurement Techniques*. Springer, 2003.

[35] D. M. Paul, D. A. Jackson, "Rapid velocity sensor using astatic confocal Fabry-Perot interferometer anda single argon laser," *J. Phys E*: Sci Instrum 4: 170-172, 1971.

[36] Naqwi A. A., Hartman R. P. A., Marijnissen J. C. M., Basic Studies of Electrohydrodynamic Atomization Spray Process Using Phase Doppler Measurement Technique, *4th International Congress on Optical Particle Sizing, Nuremburg*, 1996.

[37] De Juan L. and de la Mora J. F, Charge and size distributions of electrospray drops, *J. Colloid Interface Sci.*, vol. 186, pp. 280-293, 1997.

[38] Pitcher G., Wigley G., Saffman M. Sensitivity of drop size measurements by phase Doppler an anemometry to refractive index changes in combusting fuel sprays. *Fifth Int. Symp. On Appl. Of Laser Techniques to Fluid Mechanics*, Lisbon, Portugal, 1990.

[39] "Laser Doppler Anemometry- measurement principles," (2009, Sep 04) [Online]. Available: http://www.dantecdynamics.com/Default.aspx?ID=822

[40] F. Durst, A. Melling, J. H. Whitelaw, *Principles and Practice of Laser Doppler Anemometry*. Academic Press Inc. London Ltd. London, 1981.

[41] L. E. Drain, *The laser Doppler technique*, Chichester (etc.) Wiley, 1980.

[42] H. Komine, "System for measuring velocity field of fluid flow utilizing a laser Doppler spectral imageconverter," US Patent 4919536, Northrop Corp, Hawthorne, CA,1990.

[43] A. D. Mosedale, G. S. Elliot, C. D. Carter, T. J. Beutner, "Planar Doppler velocimetry in a large-scale facility," AIAA J 38: 1010-1024, 2000.

[44] Y. Yeh, H. Z. Cummins, "Localized fluid flow measurements with an He-Ne laser spectrometer," Appl Phys Lett 4: 176-179, 1964.

[45] J. W. Jr Foreman, E. W. George, R. D. Lewis, "Measurement of localized flow velocities in gases with a laser Doppler flowmeter," Appl Phys Lett 7: 77-78, 1965.

[46] R. J. Goldstein, D. K. Kreid, "Measurement of laminar flow development in a square duct using a laser-Doppler flowmeter," ASME J of Appl Mech 34:813-818, 1967.

[47] M. J. Rudd, "A new theoretical model for the laser Doppler meter," *J. Phys. E*, vol.2, pp. 723-726, 1969.

[48] A. L. Duff, S. Poggi, G. Plantier and J. C.Valiere, "Real-time acoustic velocity measurement in the air by means of laser Doppler Velocimetry," in *IEEE Instrumentation and Measurement, Technology Conference*, Budapest, Hungary, May21-23, 2001.

[49] Durst and ZaréM., Laser Doppler measurements in two-phase flows. In: The Accuracy of Flow Measurements by laser Doppler Methods. Proceedings of the LDA-Symposium, Copenhagen 1975, P. Buchhave, et. Al., ed., Copenhagen, 1976.

[50] "PDA HiDense Spray System," (2007, Sep 07) [Online]. Available: http://www.dantecdynamics.com/Default.aspx?ID=712.

[51] J. Kulon, *Real-time Measurement of Bipolar Charge Distribution on Pharmaceutical Aerosols and Powders Using Phase Doppler Anemometry and a Bipolar Charge Measurement System*, PhD thesis, Brunel University, Apr. 2003.

[52] "Particle dynamics analysis- Measurement principles of PDA," (2009, Sep 04) [Online]. Available: http://www.dantecdynamics.com/Default.aspx?ID=823.

[53] Leon W. Couch II, *Digital and Analog Communication Systems* (*6th ed.*), Prentice-Hall, Inc., 2001.

[54] E. J. Shaughnessy, I. M. Katz, J. P. Schaffer, *Introduction to Fluid Mechanics*, Oxford University Press, New York, Oxford, 2005.

[55] H. Nobach, "Analysis of dual-burst laser Doppler signals," *Meas. Sci. Technol*. Vol. 13, pp. 33-44, 2002.

[56] J. Xu, D. He, L. Lv, H. Gui, T. Zhao, H. Ming, J. Xie, "Improving SNR of Doppler signal and expanding dynamic measurement range of single-mode VCSEL self-mixing laser Doppler velocimetry," *Proc.SPIE*, Bellingham WA, ETATS-UNIS, 2005.

[57] Le Duff, A. Plantier, G. Gazengel, B. "Real-time particle detection and velocity measurement by means of laser Doppler velocimetry," *Proc. of IMTC 2005*, Vol. 3, pp. 2222-2225, 16-19 May 2005.

[58] M.K. Mazumder, R.E. Ware, T. Yokoyama, B.J. Rubin, and D. Kamp, "Measurement of particle size and electrostatic charge distributions on toners using E-SPART analyzer", *IEEE Trans. on Industry Appl.,* Vol.27, No.4, pp. 611-619,1991.

[59] Tan H., Loh J., "Real-time laser Doppler and phase Doppler signal processors," *Optics and Lasers in Engineering*, Vol. 17, issues 3-5, pp. 229-240, 1992.

[60] C. Tropea, G. Dimaczek, "Evaluation of the Burst Spectrum Analyser LDA Signal Processor". Proc. Int. Symp. on Appl. of Laser Anemometry to Fluid Mech., Lisbon 1988.

[61] L. Lading, "Spectral analysis versus counting," in *Proc. Int. Symp. Laser Anemometry, ASME, FED*, vol. 33, pp. 186-196, 1985.

[62] P. E. Patrick, *Digital Signal Processing Techniques for Laser Doppler Anemometry*, MSc thesis, Massachusetts Institute of Technology, Sep. 1990.

[63] R. W. Ramirez, *The FFT Fundamentals and Concepts*, Prentic Hall, Englewood Cliffs, NJ, 1985.

[64] M. Gasior, J.L. Gonzalez, "Improving FFT Frequency Measurement Resolution by Parabolic and Gaussian Spectrum Interpolation"

[65] M. Borys, *Informationsverarbeitung fur TeilchengroIJeme-Bplatze nach dem Phasendifferenz- bzw. Impulsverschiebungsverfahren.*Diplomarbeit, Universitat Rostock, Sektion Technische Elektronik, 1991.

[66] D. E. Newland, *An introduction to Random Vibrations and Spectral Analysis*, Longman Scientific and Technical, Essex, UK, 1984.

[67] A. V. Oppenheim, R. W. Schafer, *Discrete-Time Signal Processing*, Prentice Hall, Englewood Cliffs, NJ, 1989.

[68] C. Chatfield, *The Analysis of Time Series: An Introduction* (4th ed.). Chapman & Hall, 1989.

[69] F. Castanié, *Spectral Analysis: Parametric and Non-parametric Digital Methods*, London, Newport Beach, CA ISTE Ltd., 2006.

[70] Graca Cristo dos Santos Lopes Ruano, Maria da, *Investigation of real-time spectral analysis techniques for use with pulsed ultrasonic Doppler blood flow detectors*, University College of North Wales, 1992.

[71] R. Edward, *Advanced Signal Processing Techniques for Pitch Synchronous Sinusoidal Speech Coders*, PhD thesis, University of Surrey, 2007.

[72] C. K. Chui. *An Introduction to Wavelets*. San Diego: Academic Press, 1992.

[73] K. Kyriakopoulos, *Wavelet Analysis for Compression and Feature Extraction of Network Performance Measurements*, PhD thesis, Loughborough University, 2008.

[74] T. R. Downie, B. W. Silverman. "The discrete multiple wavelet transform and thresholding methods", IEEE Transactions on Signal Processing, 46(9):2558{2562, 1998. 4.3, 5.5

[75] S. Cai and K. Li. "Matlab implementation of wavelet transforms", http://taco.poly.edu/Wavelet Software/index html. Page last visited on 10/05/2007. 3.4.2, 3.4.2, 3.4.3, 3.4.3

[76] Johnson Ihyeh Agbinya. "Discrete wavelet transform techniques in speech processing", In Proceedings of the 1996 IEEE Region 10 TENCON - Digital Signal Processing Applications Conference, vol. 2, pages 514{519, Perth, Aust, Nov 26-29 1996. IEEE. 3.5, 6.2

[77] P. Abry, D. Veitch. "Wavelet analysis of long-range dependent tra_c. IEEE Transactions on Information Theory, 44(1), January 1998. 2.4.4

[78] H. R. E. van Maanen, F. J. Nijenboer, "Application of the wavelet transform to laser-Doppler processors," *Proc. 8th Int. Symp. On Applications of Laser Techniques to Fluid Mechanics*, Lisbon, paper 31.4, 1996.

[79] S. K. Mitra, M. K. Mazumder, "Performance of a DSP-based Intelligent Statistical Control System for Uncertainty Management in a Laser-based Particle Characterizing Instrument", Control'92, Perth, Nov. 1992.

[80] "Integrated solutions in Laser Doppler Anemometry", http://www.dantecdynamics.com

[81] W. O'Brian Jarrett. "Congestion Detection within Multi-Service TCP/IP Networks using Wavelets", PhD thesis, University of London, 2004. 2.4.4

[82] C. Tropea, G. Dimaczek, J. Kristensen, C. Caspersen, "Evaluation of the burst spectrum analyzer LDA signal processor," *Proc. 4th Int. Symp. on Appl. of Laser Anemom. to Fluid Mech.*, Lisbon, Portugal: paper 2.22, 1988.

[83] L. Lading, "Spectrum analysis of LDA signals," *Proc. Int. Specialists Meeting on the Use of Computers in Laser Velocimetry*, ISL, France: paper 20, 1987.

[84] JF. Meyers, JI. Jr. Clemons, "Frequency domain laser velocimeter signal processor," *NASA Techn*. Paper 2753, 1987.

[85] KM. Ibrahim, WD. Bachalo, "The significance of the Fourier analysis in signal detection and processing in laser Doppler and phase Doppler applications," *Proc. 6th Int. Symp. On Appl. of Laser Techn to Fluid Mech*, Lisbon, Portugal: paper 21.5, 1992.

[86] A. Krupa, A. Jaworek, "A method for aerosol particle charge measurements," *Electrostat. J.*, vol. 23, pp. 289-292.

[87] K. Hishida, K. Kobashi, M. Maeda, "Improvement of LDA/PDA using a digital signal processing systems processor (DSP)," *3rd Int. Conf. on Laser Anemom-Adv. and Appl.*, Swansea, UK: paper S2, 1989.

[88] D. Matovic, C. Tropea, "Spectral peak interpolation with application to LDA signal processing," *Meas. Sci. Techn. 2*: 1100-1106, 1991.

[89] K. A. Shinpaugh, R. L. Simpson, A. L. Wicks, S. M. Ha, J. L. Fleming, "Signal – processing techniques for low signal-to-noise ratio laser Doppler velocimetry signals," *Exp. Fluids*, vol. 12, pp.319-28, 1992.

[90] T. Wriedt, J. Heuermann, K. Bauckhage, A. Schone, "Performance evaluation of LDVs Fourier transform processor," *Proc. 3rd Int. Conf. on Laser Anemometry-Advances and Applications*, Swansea, paper S.6,1989.

[91] C. Tropea, "Laser Doppler anemometry: recent developments and future challenges," *Meas. Sci. Technol. J.*, vol. 6, pp. 605-619, 1995.

[92] D. Veynante, S. M. Candel, "Promising approach in laser Doppler velocimetry data processing: Signal reconstruction and nonlinear spectral analysis," Signal Proc., vol. 14, pp. 295-300, 1988.

[93] T. Wriedt, K. A. Bauchkhage, A. Schone, "Application of Fourier analysis to Phase-Doppler-Signals generated by rough metal particles," *IEEE Trans. Instrum. Meas.*, vol. 38, No. 5, 1989.

[94] H. T. Kalb, F. L. Crosswy, "Discrete Fourier transform signal processor for laser-Doppler anemometry. AEDC-TR-83-46, Arnold Engineering Development Center AAFS, Tennessee, 1983.

[95] M. Gasior, J. L. Gonzalez, "Improving FFT frequency measurement resolution by parabolic and Gaussian spectrum interpolation," AB-Note-2004-021 BDI.

[96] M. Ishihara, "Spectrum estimation by several interpolation methods," *International Journal of Computer Science and Network Security*, vol. 6, No. 2A, Feb. 2006.

[97] B. Lai, X. An, H. Yuan, Z. Chen, C. Huang, C. Liang, "A novel Gaussian interpolation formula-based IE-FFT algorithm for solving EM scattering problems", Microwave and Optical Technology Letters, Vol. 51, pp. 2233-2236, 2009.

[98] K. A. Shinpaugh, R. L. Simpson, A. L. Wicks, S. M. Ha, J. L. Fleming, "Signal-processing techniques for low signal-to-noise ratio laser Doppler velocimetry signals," *Experiments in Fluids*, vol. 12, pp. 319-328, 1992.

[99] J. Domnick, H. Ertel, C. Tropea, "Processing of phase/Doppler signals using the cross spectral density function," in *Proc. Fourth Int. Symp. Applications Laser Anemometry to Fluid Mechanics*, pp. 3.8.1-6, Lisbon, Portugal, Jul. 1988.

[100] W. D. Bachalo, D. Werthimer, R. Raffanti, R. J. Hermes, "A high speed Doppler signal processor of frequency and phase measurements," *Third Int. Conf. on Laser Anemometry-Advances and Applications (ed. Turner, J.)*, Univ. of Manchester, Swansea.

[101] V. Valeau, "Mesure de la vitesse acoustique particulaire par anémométrie laser doppler: estimation de fréquences instantanée à variation sinusoïdale, validation de la mesure," *Thèse de doctorat*, Université du Maine, 1999.

[102] A. L. Duff, G. Plantier, J. C. Valière and T. Bosch, "Analog Sensor Design Proposal for Laser Doppler Velocimetry," *IEEE Sensors J.*, vol. 4, No. 2, Apr. 2004.

[103] A. Blanchard, "Phase-Locked Loops," New York: Wiley, 1976.

[104] A. Blanchard, "Techniques des boucles d'asservissment de phase," Tech. Rep., Ěcole Supérieure d'Ělectricité, 1975.

[105] L. W. Couch II, "Digital and analog communication systems," Macmillan, 1993.

[106] M. Schwartz, "Information, transmission, modulation and noise," McGraw-Hill, 1990.

[107] M. Tabiani, F.Behnia, "Doppler detection by an improved PLL technique," *Proc. 33rd Midwest Symp. On Circuites and Systems*, pp. 909-911, 1990.

[108] H. Muller and D. Dopheide, "Direction sensitive Laser Doppler Velocimeter using the optical frequency shift of two stabilized laser diodes," *Laser anemometry advances and applications*, 1993.

[109] R. E. Ziemer, W. H. Tranter, "Principles of communications: systems, modulation and noise," 6th ed. Hoboken: Wiley, c2010.

[110] P. Lian "Improving tracking performance of PLL in high dynamic applications," *MSc. Thesis*, University of Calgary, Nov. 2004.

[111] Horowitz, Hill, *The art of Electronics*, Cambridge University Press, 1980.

[112] N. M. Wilson, "Digital signal-processing techniques for laser Doppler velocimetry," *Phys. J., E: Sci. Instrum.*, vol. 11, 1978.

[113] J. Czarske, "A miniaturized dual-fibre laser Doppler sensor," Meas. *Sci. Technol*. vol.12, pp. 1191-1198, 2001.

[114] L. Lading, "Spectral Analysis Versus Counting." Proc. Int. Symp. on Laser Anemometry, ASME 33 189-196, 1985.

[115] J. Czarske, F. Hock, H. Müller, "Quadrature demodulation – a new LDV-burst signal frequency estimator," *Proc. 5th Int. Conf. on Laser Anemometry- Advances and Applications* (Veldhoven, 23-27 August 1993) ed J Bessem et al (Bellingham, WA: SPIE), 1993.

[116] V. Strunck, H. Müller, D. Dopheide, "Time domain single-tone analysis using quadrature algorithm," *Proc. 8th Int. Symp. on Applications of Laser Techniques to Fluid Mechanics* (Lisbon) paper 6.6, 1996.

[117] J. Czarske, O. Dölle, "Quadrature demodulation technique used in laser Doppler anemometry," *Electron. Lett.* vol.43, pp. 547-549, 1998.

[118] H. Müller, V. Strunck, D. Dopheide, "The application of quadrature demodulation techniques for the investigation of flows," *Flow Meas. Instrum*. vol 7, pp. 237-245, 1996.

[119] J. Czarske, "Method for analysis of the fundamental measuring uncertainty of laser Doppler velocimeters," *Opt. Lett*. vol. 21, pp. 522-524, 1996.

[120] Leslie M. Jenson, "LDV digital signal processor based on autocorrelation," in *Proc 6th Int. Symp. on Appl. of Laser Techn. to Fluid. Meh.*, Lisbon, Portugal: paper 21.4, 1992.

[121] J. Czarske, "Statistical frequency measuring error of the quadrature demodulation technique for noisy single-tone pulse signals," *Meas. Sci. Technol. J.*, vol. 12, pp. 597-614, 2001.

[122] H. Muller, V. Strunck and D. Dopheide, "The application of quadrature demodulation techniques for the investigation of flows," *Flow Meas. Instrum. J.*, vol. 7, No. ¾, pp. 237-245, 1996.

[123] H. Tan, J. Loh, "Real-Time Laser Doppler and Phase Doppler Signal Processors". Opt. Lasers Eng. Vol. 17, pp. 229-240, 1992.

[124] Y. C. Agrawal, "Quadrature demodulation in laser Doppler velocimetry", *Appl. Opt*. Vol. 23, pp. 1185-1186, 1984.

[125] Czarske, J. Dolle, O. , "Quadrature demodulation technique used in laser Doppler velocimetry," *Electronics Letters*, Vol. 34, Issue 6, pp. 547-549, 1998.

[126] Müller H., Strunck V., Dopheide D., "The application of quadrature demodulation techniques for the investigation of flows," *Flow Measurement and Instrumentation*, Vol. 7, Issues 3-4, pp. 237-245, 1996.

[127] V. VALEAU, *Mesure de la vitesse acoustique particulaire par anémométrie laser doppler : estimation de fréquences instantanée à variation sinusoïdale, validation de la mesure*, Thèse de doctorat, Université du Maine, 1999.

[128] Czarske J. W., Doelle O., "Investigations on the frequency measuring error of laser Doppler velocimeters using the quadrature demodulation technique," *Proc. of SPIE*, Vol. 3749, 19 Jul. 1999.

[129] D. Matovic, C. Tropea, "Estimation of LDA signal frequency using the autocovariance (ACV) lag ratio method," *Phys. E: Sci. Instrum.*, vol. 22, pp. 631-637, 1989.

[130] T. Nakajima, Y. Ikeda, N. Kurihara, Y. Imanaka, R. Matsamoto, "Burst digital correlation for LDV signal processing," in *4th Int. Symp. on Appl. of Laser Anemom. to Fluid Mech.*, Lisbon, Portugal: paper 2.2 (falsely listed as paper 5.20), 1988.

[131] T. Nakajima, Y. Ikeda, M. Utsunomiya, R. Matsumoto, "Comparison of burst digital correlator with FFT processor in a numerical simulation experiment", Proceedings of the 3rd International Conference, Swansea, Wales, Sept. pp. 26-29, 1989.

[132] P. Handel, A. Host-Madsen, "Particle velocity and size estimation from two channel laser anemometry measurements", *IEEE International Conference on Acoustics, Speech and Signal Processing (ICASSP'97),* Vol. 5, Munich, Germany, Apr. 1997.

[133] Lénárd Vámos, Péter Jani, "Particle sizing by photon correlation laser Doppler anemometer in the submicron/nanometer size range," *Opt. Eng*., Vol. 49, 013602, 2010.

[134] Vamos L. Jani P. "Simulation of LDA and PDA measuring techniques in the nanometer particle size range," *Proc. SPIE 5948*, 59481Q, 2005.

[135] Seo J., Kwon H., Kim H. K., Hwang Y., "Nano-Particle Size Measurement by Photon Correlation Spectroscopy and Dielectric Loss Spectroscopy," *Flow Dynamics*, Vol. 832, pp. 229-233, 2006.

[136] Shen J., Zheng G., Li M., Sun G., “Improving methods of estimating autocorrelation function in PCS technique,” *Proc. SPIE* 4927, 586, 2002.

[137] W.J. DiVito, *Digital Acquisition and Demodulation of LDV Signal Bursts to obtain Particle Size and Charge Data*, PhD Dissertation, University of Arkansas at Little Rock, AR, 1998.

[138] Qui H-H., Jia W., Hsu C. T., Sommerfeld M., “High accuracy optical particle sizing in phase-Doppler anemometry,” *Meas. Sci. Technol*. Vol.11, pp. 142-151, 2000.

[139] H. Torp, K. Kristo_ersen, and B. Angelsen, “Autocorrelation technique in color flow imaging, signal model and statistical properties of the autocorrelation estimates," *IEEE Trans. Ultrason., Ferroelect., Freq. Contr.*, vol. 41, Sep., pp 604-612, 1994.

[140] G. T. C. Foster, M. P. Embree, and W. D. O' Brien, “Flow velocity profile via time-domain correlation: Error analysis and computer simulation," *IEEE Trans. Ultrason., Ferroelect., Freq. Contr.*, vol. 37, pp. 164-174, 1990.

[141] P. G. M de Jong, T. Arts, A. P. G. Hoeks, and R. S Reneman, “Determination of tissue motion velocity by correlation interpolation of pulsed ultrasonic echo signals," *Ultrason. Imaging*, Vol. 12, pp. 84-98, 1990.

[142] H. Torp, X. M. Lai, and K. Kristo_ersen, “Comparison between cross-correlation and auto-correlation technique in color flow image," *Proc. IEEE Int. Ultrason. Symp.*, Baltimore, MD, pp. 1039-1042,1993.

[143] A. Middleditch, *Spectral analysis in high frequency radar oceanography*, PhD thesis, University of Sheffield, 2006.

[144] X. Lai, H. Torp, and K. Kristo_ersen, “An extended autocorrelation method for estimation of blood velocity," *IEEE Trans. Ultrason., Ferroelect., Freq. Contr.*, Vol. 44, No. 6, pp. 1332-1342, Nov. 1997.

[145] Valiere J. C., Herzog P., Valeau V., Tournois G., “Acoustic velocity measurements in the air by means of laser Doppler velocimetry: Dynamic and frequency rang limitations and signal processing improvements,” *Journal of sound and vibration,* Vol. 229, pp. 607-626, 2000.

[146] D. Matovic, C. Tropea, “Spectral peak interpolation with application to LDA signal processing”, *Meas. Sci. Technol*. Vol. 2, pp. 1100-1106, 1991.

[147] Wriedt T., Bauckhage K. A., Schone A., “Application of Fourier analysis to phase-Doppler-signals generated by rough metal particles,” IEEE Trans. Instrum. Meas. Vol. 38, pp. 984-990, 1989.

[148] D. H. Wolaver, *Phase-Locked Loop Circuit Design*, PTR Prentice Hall, 1991.

[149] L. Zhang, J. Kulon, "Real-time particle size and charge estimation from laser Doppler burst signals using quadrature demodulation and correlation techniques," *Proc. 9th International Conference on Signal Processing (ICSP'08),* Beijing, China P. R., pp. 2677-2680, Oct. 26-29, 2008.

[150] G. D. Baker, R. J. Murphy, J. F. Meyers, "Database for LDV Signal Processor Performance Analysis," *13th International Congress on Instrumentation in Aerospace Simulation Facilities*, Göttingen, West Germany, Sep. 18-21, 1989.

[151] J. F. Meyers, R. J. Murphy, "Frequency Domain Laser Velocimeter Signal Processor", *Technology 2000, National Aeronautics and Space Administration* November 27-28, 1990.

[152] J. F. Meyers, M. J. Walsh "Computer simulation of a fringe type laser velocimeter," *Proc. 2nd International Workshop on laser velocimetry,* Vol. 1 (A76 10426 01-35), West Lafayette, Ind. Mar. 27-29, 1974.

[153] W.-Q. Shu, "Cramer-Rao bound of Laser Doppler Anemometer," *IEEE Trans. Instrum. Meas*., vol. 50, no. 6, pp. 1770-1772, Dec. 2001.

[154] D. C. Rife and R. R. Boorstyn, "Single-ton parameter estimation from discrete-time observations," *IEEE Trans. Inf. Theory*, vol. IT-20, no. 5, pp. 591-598, Sep. 1974.

[155] O. Besson and F. Galtier, "Estimating particles velocity from laser measurements: Maximum likelihood and Cramér-Rao bounds," *IEEE Trans. Signal Processing*, vol. 44, pp. 3056–3068, Dec. 1996.

[156] D. C. Rife and R. R. Boorstyn, "Single-tone parameter estimation from discrete-time observations," *IEEE Trans. Inf. Theory*, vol. IT-20, no. 5, pp. 591-598, Sep. 1974.

[157] V. S. Sobolev and A. A. Feshenko, "Accurate Cramer-Rao Bounds for a Laser Doppler Anemometer," *IEEE Trans. Instrum. Meas.*, vol. 55, no. 2, pp. 659-665, Apr. 2006.

[158] D. Slepian, "Estimation of signal parameters in the presence of noise," IRE Trans. Inform. Theory, PGIT-3, pp. 68-89, Mar. 1957.

[159] D. C. Rife, "Digital tone parameter estimation in the presence of Gaussian noise," PhD thesis, Polytech. Inst. Brooklyn, Brooklyn, N. Y., June 1973.

[160] H. L. Van Trees, *Detection, Estimation and Modulation Theory*, Part I. New York: Wiley, 1968.

[161] L. Zhang and J. Kulon, "Real-time, non-invasive measurement of medical aerosol charge and size distribution," in *Proc. IEEE Trans. Instrum. Meas. Conf.*, Singapore, pp. 457-462, May 5-7, 2009.

[162] O. Besson and F. Galtier, “Estimating particles velocity from laser measurements: Maximum likelihood and Cramér-Rao bounds,” *IEEE Trans. Signal Processing*, vol. 44, pp. 3056–3068, Dec. 1996.

[163] P. Handel, A. Madsen, “Estimation of velocity and size of particles from two channel laser anemometry measurements,” Measurement, Vol. 21, Issue 3, pp. 113-123, 1997.

[164] T. Wriedt, K. A. Bauckhage, A. Schone, “Application of Fourier analysis to phase-Doppler-signals generated by rough metal particles,” *IEEE Trans. Instrum. Meas.* Vol. 38, Issue 5, pp. 984-990, 1989.

[165] S. Yazdanfar, C. Yang, “Frequency estimation precision in Doppler optical coherence tomography using the Cramer-Rao lower bound,” *Optics Express*, Vol. 13, Issue 2, pp.410-416, 2005.

[166] Bailliet, H., Lotton, P., Bruneau M. and Gussev., V. “Acoustic power flow measurement in thermoacoustic resonator by means of the LDA and microphonic measurement”. Applied acoustic, 60(1) , pp 1-11, 2000.

[167]Boashash, B. and O’Shea, P. “Algorithms for instantaneous frequency estimation : A comparative study”. Proc. SPIE Conf. Advanced Acous., Speech and Sig. Process., 1348, San Diego, 1990.

[168] Nedler, J.A. and Mead, R. “A simplex method for function minimization”. Computer J., 7**,** pp.308-313, 1965.

[169] Poggi, S., Gazengel, B. and Valière, J.-C. “Evaluation of the performance of two acquisition and signal processing systems for acoustic particle velocity measurement”. 4th International Symposium of Vibration measurement by laser techniques, SPIE 4072, June 20-23, Ancona (Italy), 2000.

[170] Valeau, V., Valiere, J.-C. “Instantaneous tracking of sinusoidally frequency-modulated signal with low modulation index : application to Laser measurement in acoustics”. IEEE Trans. on Sig. Proc. submitted, 2000.

[171] Valière, J.-C., Herzog, P., Valeau, V. and Tournois, G. “Acoustic velocity measurements in the air by means of Laser Doppler Velocimetry: Dynamic and frequency range limitations and signal processing improvements”. J. Sound and Vib., 229(3), pp. 607-626.2000.

[172] Ville, J. “Théorie et application de la notion de signal analytique”. Cables et transmissions, 2A, pp**.** 61-74. 1948.

[173] Sharpe, J.P and Greated, C. “The measurement of periodic acoustic field using photon correlation spectroscopy”. J. Phys. D. : Appl. Phys., 20, pp.418-423. 1987.

[174] Taylor, K.J. “Absolute measurement of acoustic particle velocity”. J. Acoust. Soc.

Am., 59(3), pp.691-694. 1976.

[175] Valeau, V., "Mesure de la vitesse acoustique particulaire par anémométrie laser doppler : estimation de fréquence instantanée à variation sinusoïdale, validation de la mesure". PhDthesis de l'université du Maine. 1999.

[176] M. K. Mazumder, R.A. Sims, A.S. Biris, P.K. Srirama, D. Saini, C.U. Yurteri, S. Trigwell, S. De and R. Sharma, "Twenty-first Century Research Needs in Electrostatic Processes Applied to Industry and Medicine," Chemical Engineering Science, Volume 61, Issue 7, April 2006, Pages 2192-2211.

[177] Zhang L., Kulon J., "Cramér-Rao Bounds for a Laser Doppler Anemometer: The effect of the particle trajectory via the measurement volume", *I2MTC Int. Instrument. Measurement Technology Conf.*, Austin, 3-6 May 2010, pp300-303.

[178] L. Zhang, J. Kulon, "Real-time, non-invasive measurement of medical aerosol charge and size distribution—signal processing strategy, system modelling and optimization," *Proc. IEEE Instrumentation & Measurement Technology Conference 2009 (I^2MTC 2009)*, Singapore, pp. 457-462, May 5-7, 2009.

[179] Zhang L., Kulon J., "Cramér-Rao Bounds for a Laser Doppler Anemometer: The effect of the particle trajectory via the measurement volume", I2MTC Int. Instrument. Measurement Technology Conf., Austin, 3-6 May 2010, pp300-303.

[180] M. Kendal, A.Stuart, *The advanced theory of statistics*, Vol 2, Charles Griffen, London, 1963.

[181] A. Papoulis, *Probability, random variable and stochastic processes*, McGraw-Hill, New York, USA, 1965.

[182] S. M. Kay, *Fundamentals of statistical signal processing: Estimation theory*. PTR Prentice Hall, Englewood Cliffs, NJ, USA, 1993.

[183] T. Wriedt, K. Bauckhage, A. Schone, "Application of Fourier Analysis to Phase Doppler Signals Generated by Rough Metal Particles". *IEEE Trans. Instrum. Meas*. Vol. 38 pp. 984-990, 1989.

[184] K. Taylor, "Absolute measurement of acoustic particle velocity," *J. Acoust. Soc. Amer.*, vol. 59, no. 3, pp. 938–945, 1977.

[185] B. Boashash, P. O'shea, M. Arnold, "Algorithms for instantaneous frequency estimation: a comparative study", Proc. Advanced signal processing algorithms, architectures and implementations, SPIE, Vol. 1348, pp. 126-148, 1990.

[186] H. Nobach, "Advanced techniques for frequency estimation from LDA burst signals," *Proc. 8th Int. Conf. on Laser Anemometry*, Rome, pp. 311-318, 1999.

[187] Lindsey W. C., Simon M. K., *Telecommunication System Engineering*, Prentice Hall, Engle Wood Cliffs, NJ, 1973.

[188] J. Schoukens, R. Pintelon, H. V. hamme, "The interpolated Fast Fourier Transform: A comparative study," *IEEE Trans. Instrum. Meas*. Vol. 41, No. 2, Apr. 1992.

[189] Lehmann P., Schombacher E. H., "Features of a combined FFT and Hilbert tramsform for phase Doppler signal processing," *Meas. Sci. Technol*., Vol. 8, No. 4, 1997.

[190] T. Grandke, "Interpolation algorithms for discrete Fourier transform of weighted signals," *IEEE Trans. Insrrum. Meas.,* vol. 1M-32, pp.350-355, 1983.

[191] C. Offelli and D. Petri, "Interpolation techniques for real-time multifrequency waveform analysis," *IEEE Trans. Insrrum. Meas.,* vol. 39, pp. 106-111, 1990.

[192] O. Besson, F. Galtier, **"**Bounds for estimation of particle's velocity from laser measurements," *Proc. of 8th IEEE Signal Processing Workshop on Statistical Signal and Array Processing (SSAP'96)*, pp. 252, 1996.

[193] O. Besson, P. Stoica, "Estimating the parameters of a random amplitude sinusoid from its sample covariances," *Proc. of the Acoustics, Speech and Signal Processing (ICASSP'96)*, Vol. 5, 1996.

[194] O. Besson, P. Stoica, "Statistical analysis of the least-squares autoregressive frequency estimator for random-amplitude sinusoidal signals," *Signal Processing*, Vol. 46, Issue 2, 1995.

[195] G. K. Smyth, D. M. Hawkins, "Robust Frequency Estimation Using Elemental Sets," *Journal of Computational and Graphical Statistics*, Vol. 9, pp. 196-214, 2000.

[196] Atkinson, A. C., Weisberg, S. "Simulated annealing for the detection of multiple outliers using least squares and least median of squares fitting. In Directions on Robust Statistics: Part I," eds. W. Stahel and S. Weisberg, Springer, pp. 7–20. 1991.

[197] Kay, S.M., Marple, S.L. "Spectrum analysis—a modern perspective," Proc. IEEE Vol. 69, pp. 1380–1419. 1981.

[198] Mackisack, M. S., Osborne, M. R., Smyth, G. K. "A modified Prony algorithm for estimating sinusoidal frequencies". *J. Statist. Comput. Simul*. Vol. 49, pp. 111–124. 1994.

[199] Rice, J. A., Rosenblatt, M. "On frequency estimation," *Biometrika* Vol. 75, pp. 477–484.1988.

[200] Smyth, G. K. "Employing symmetry constraints for improved frequency estimation by eigenanalysis Methods," *Technometrics*. To appear.1999.

[201] Stromberg, A. J. "Consistency of the least median of squares estimator in nonlinear least squares," *Commun. Statist.—Theory Meth.* Vol. 24, pp. 1971–1984, 1995.

[202] Roussseeuw, P. J., Leroy, A. M. "Robust Regression and Outlier Detection," Wiley, New York, 1986.

[203] M. K. Mazumder, R. Ware, "Aerosol Particle Charge and Size Analyzer," US Patent 4633714, 1987.

[204] Dantec Measurement Technology A/S, Tonsbakken 18, DK-2740 Skovlunde, Denmark, *Particle Dynamic Analyser Installation and User's guide*, 1999.

[205] K. J. Kirsch, M. K. Mazumder, "Aerosol Size Spectrum Analysis using Relaxation Time Measurement," *Applied Physics Letters*, Vol. 26, No. 4, pp.193-195, 1975.

[206] R. Sharma, D. W. Clark, P. K. Srirama, M. K. Mazumder, "Tribocharging Characteristics of the Mars Dust Simulant (JSC Mars-1), *IEEE trans. on Industry Applications*, Vol. 44, No. 1, 2008.